DEVELOPMENT OF A COMPUTATIONAL
MODEL FOR PREDICTING SOLAR WIND
FLOWS PAST NONMAGNETIC
TERRESTRIAL PLANETS

by

Stephen S. Stahara and
John R. Spreiter

NEAR TR 313

October 1983

1 Report No	2. Government Accession No	3. Recipient's Catalog No

4 Title and Subtitle	5. Report Date
DEVELOPMENT OF A COMPUTATIONAL MODEL FOR PREDICTING SOLAR WIND FLOWS PAST NONMAGNETIC TERRESTRIAL PLANETS	
	6 Performing Organization Code 498/C

7. Author(s)	8. Performing Organization Report No.
Stephen S. Stahara	NEAR TR 313

	10. Work Unit No.

9 Performing Organization Name and Address	11. Contract or Grant No.
Nielsen Engineering & Research, Inc. 510 Clyde Avenue Mountain View, CA 94043	NASW-3182

	13 Type of Report and Period Covered
12 Sponsoring Agency Name and Address	Contractor Report 7/78 - 8/83
National Aeronautics & Space Administration Washington, D.C. 20546	14. Sponsoring Agency Code

15 Supplementary Notes

16. Abstract

A summary report is provided of the work performed under NASA Contract No. NASW-3182. This work relates to the development and application of a computational model for the determination of the detailed plasma and magnetic field properties of the global interaction of the solar wind with nonmagnetic terrestrial planetary obstacles. The theoretical method is based on an established single fluid, steady, dissipationless, magnetohydrodynamic continuum model, and is appropriate for the calculation of supersonic, super-Alfvénic solar wind flow past terrestrial ionospheres. This report provides a concise statement of the problems studied, a summary of all the important research results, and copies of the publications.

17. Key Words (Suggested by Author(s))	18 Distribution Statement
Solar wind/planetary interaction Nonmagnetic planets Frozen magnetic field	Unclassified - Unlimited

19 Security Classif. (of this report)	20 Security Classif (of this page)	21 No of Pages	22. Price*
Unclassified	Unclassified	147	

TABLE OF CONTENTS

DEVELOPMENT OF A COMPUTATIONAL MODEL FOR PREDICTING SOLAR WIND FLOWS PAST NONMAGNETIC TERRESTRIAL PLANETS

SUMMARY

A summary report is provided of the work performed under NASA Contract No. NASW-3182. This work relates to the development and application of a computational model for the determination of the detailed plasma and magnetic field properties of the global interaction of the solar wind with nonmagnetic terrestrial planetary obstacles. The theoretical method is based on an established single fluid, steady, dissipationless, magnetohydrodynamic continuum model, and is appropriate for the calculation of supersonic, super-Alfvénic solar wind flow past terrestrial ionospheres. This report provides a concise statement of the problems studied, a summary of all the important research results, and copies of the publications.

1. INTRODUCTION

This is the final summary report under Contract No. NASW-3182 for the National Aeronautics and Space Administration. All of the important results from the research performed under this contract have been reported in the open literature, both in scientific journals and as technical papers at scientific meetings with appropriate acknowledgement of NASA support. This summary report provides a statement of the problem studied, a descriptive summary of the most important results, a reference list and copies of all publications resulting from the research, and a list of all participating scientific personnel.

2. STATEMENT OF PROBLEM INVESTIGATED

The problem toward which the research under this contract was directed was the modeling of the three-dimensional global interaction of the solar wind with non-magnetic terrestrial planet obstacles. The viewpoint on which this was to be accomplished is based on a continuum rather than particle approach. The theoretical method employed is based on an established single fluid, steady, dissipationless magnetohydrodynamic model that is appropriate for the calculation of supersonic, super-Alfvénic solar wind flow past magneto/ionopause obstacle shapes typical of terrestrial planets. The overall objective was the enablement of rational quantitative modeling studies to be performed on the global solar wind interaction problem for non-magnetic terrestrial planets. This accomplishment would involve the development and utilization of a multi-faceted computational procedure that embodies the theoretical model and incorporates advanced numerical methods so as to enable more general and detailed theoretical studies of the plasma and field properties in the interaction region than heretofore possible. Comparisons of predictions from the model were anticipated both with existing theories where possible and with observational results where available. Additionally, the model was to be employed in several collaborative efforts with other space scientists in which predictions from the model would both augment other theoretical analysis and assist in interpreting results and comparisons with observations.

3. SUMMARY OF RESEARCH RESULTS

3.1 Development of the Basic Computational Model

The theoretical model employed here for predicting the global interaction of the solar wind with terrestrial planet magneto/ionospheres involves solution of the continuum partial

differential equations of magnetohydrodynamics of a perfect gas
having infinite electrical conductivity and zero viscosity and
thermal conductivity which express the conservation of mass,
momentum, energy, and magnetic field. The computational method
developed to solve these equations is described in detail in
Ref. 1. In summary, two separate finite-difference procedures
are employed; one to treat the flow domain encompassing the bow
shock and ionopause obstacle back to the terminator plane, and
another to treat the flow domain downstream of the terminator.
The various reasons for this combination are discussed in
Ref. 1. The net result is the achievement of a computational
efficiency not possible by any other existing means.

One of the most important tasks of this segment of the
study was verification of the accuracy and range of validity
of the computational procedure. This verification was accom-
plished through comparisons with results of other theoretical
methods, and also by exercising the procedure on computations
for obstacle shapes and solar wind flow conditions that span
the entire range of interest for applications to terrestrial
planets within the solar system. These results are reported
in Ref. 1 and demonstrate both the accuracy and robustness of
the computational procedures.

Finally, one of the most significant achievements of the
study was the incorporation of the entire computational proce-
dure embodying the theoretical method into a modular, com-
pletely-automated, user-friendly code. This organization allows
any general user access to the results of the model at very
reasonable computational cost. This feature is demonstrated in
Ref. 1 where examples are provided of detailed maps of the
global interaction region for all important plasma and field
variables.

3.2 Extended Development and Evaluation of the Model with Observations

The advanced computational model that was developed above was further refined and generalized. Detailed evaluations of the model were then made by comparisons with observational plasma and magnetic field data for Venus. These developments are detailed below.

A new family of non-magnetic terrestrial planet obstacle shapes for solar wind/ionospheric interactions were determined which take account of gravitational variation in the scale height parameter. The results are detailed and reported in Ref. 2. An extensive catalog of solar wind flows past these new shapes, consisting of contour maps of all the important flow and magnetic field properties, were obtained and are presented in Ref. 3. This catalog of results has proven extremely instrumental to a wide number of investigations engaged in related solar wind studies.

A significant refinement included in the computational model in this extended development has been the allowance of an arbitrary oncoming direction of the interplanetary solar wind. This refinement is detailed in Ref. 3. This particular feature has been instrumental in showing that the asymmetry of the bow shock at the Earth previously observed and attributed to magnetic effects is either non-existent or at a level below that measurable by current spacecraft instrumentation. These and extensive related results employing the model which further demonstrate the accuracy of both the computational procedures and the basic theory are reported in Refs. 4 and 5.

Finally, a provision for the determination of time histories of plasma and field properties along an arbitrary spacecraft trajectory has been incorporated into the computational model. This feature has proven invaluable in providing

4

theoretical results for direct comparisons with spacecraft
observations. Details of this provision and results of time
history comparisons with plasma and field data from the Pioneer-
Venus spacecraft are provided in Ref. 2. We note in particular
that model comparisons in Ref. 2 with magnetic field observa-
tions for several orbits at quiet time conditions are given and
display notably good agreement. Because determination of the
frozen magnetic field is the last step in the computational
model, its accurate prediction serves as a critical test of the
correctness and accuracy of the theoretical and computational
models.

3.3 Collaborative Studies with the Model

In conjunction with this investigation, a number of col-
laborative studies have been undertaken with other space sci-
entists in which theoretical presictions from the present model
have been employed to interpret observational plasma and field
results and to augment other theoretical analyses. These
studies are described below.

The most extensive collaborative effort has been with
Dr. James A. Slavin and Professor R. E. Holzer at the Institute
of Geophysics and Planetary Physics, U.C.L.A. Results from
the current predictive model provided the theoretical basis of
an examination of solar wind flows past all the terrestrial
planets in the solar system. The model was applied first to
extensive and successful modeling of the mean bow shock shapes
and positions about these various planets. These results are
reported in Ref. 4. Next, the model was employed to aid in
interpreting these comparisons in light of both observations
and previous analyses. Those results are given in Ref. 5 and
represent the most detailed and comprehensive study completed
to date of the global interaction phenomena of the solar wind
with all the terrestrial planets (Mercury, Venus, Earth, and

Mars) from the aspect of observations of the bow shock position and shape. A number of significant findings and conclusions, several involving ongoing controversies, emerged from this study. These included: (1) the average bow shock position of the solar wind about the Earth is predicted to within 2% of its spacial location by the present model, (2) no East-West asymmetry of the Earth's bow shock as suggested by Romanov and others is discernable within present observational error when appropriate account is taken of the average aberrated direction of the on-coming solar wind, and (3) the appropriate interplanetary Mach number to be used in such modeling studies is the sonic rather than magnetosonic one. All of these results both confirm and verify the current model's applicability to terrestrial planets.

Further studies with Dr. Slavin and Professor Holzen have also been made employing the model to investigate the asymptotic behavior of planetary Mach cones. Mach cone angles determined from observational distant bow shock shapes and positions for solar wind flows past Venus, Earth, and Mars were compared in Ref. 6 with far downstream predictions from the gasdynamic model. The results verified that the model which is already known to predict good results in regions ahead of and up to the terminator also yields good results up to certain downstream distances for all the planets; i.e., -4 R_{ob} at Venus, -6 R_{ob} at Earth, and -10 R_{ob} at Mars, where R_{ob} denotes the particular obstacle nose radius.

Discrepancies, however, appear farther downstream of these points presumably due to the difference between the MHD fast mode Mach number and the sonic Mach number inherent in the gas-dynamic model. The tendency to achieve better agreement further downstream for these various obstacles between gasdynamic theory and observation as the distance from the sun increases (i.e., Venus, Earth, Mars) is attributed to the increase in accuracy of the gasdynamic approximation with decreasing IMF strength.

These results suggest that gasdynamic theory predictions for the far-downstream flow about obstacles in the solar system will be very accurate for describing flows about the large bodies in the outer solar system.

A related collaborative effort to the previous studies that employed the current predictive model was carried out with John D. Mihalov of the Space Sciences Division at Ames Research Center. In that effort, which formed the basis of Mr. Mihalov's dissertation for Engineer's Degree from Stanford University (Ref. 7), the predictive model was employed in a series of comparative calculations involving the detailed time histories of plasma and magnetic field properties in the Venusian ionosheath region for selected quiet time interplanetary conditions. These results are summarized in Ref. 8 and again verify the correctness of the present model. They also suggest some additional phenomena not included in the model which may be occurring throughout the Venusian ionosheath to retard the flow. This includes mass loading from photoionization and charge exchange, the possible presence of a viscous boundary on the ionopause, the leakage of ionospheric material into the solar wind flow, or various combinations of these effects.

Another different series of collaborative efforts involving use of the predictive model was carried out primarily with Professor C. T. Russell and Dr. J. G. Luhmann of the Institute of Geophysics and Planetary Physics, U.C.L.A. as well as others at that institute. These studies were focused primarily on employing the magnetic field predictive capability of the present model to perform a variety of different investigations. In Ref. 9, a study was made of the magnetospheric source of energetic particles observed upstream of the Earth's bow shock. Calculations were performed in which those magnetosheath field lines predicted by the model to drape over the magnetopause were traced from the magnetopause to the bow shock in order to

locate regions at the shock that should be populated with magnetospheric particles. Subsets of those field lines that connect to potential sites of magnetic merging on the magnetopause were also traced in the event that leakage occurs preferentially where normal components of the field are present across the boundary.

In Ref. 10, the predictive model was employed to investigate patterns of magnetic field merging sites on the magnetopause. Predictions of the magnetospheric field based on the Hedgecock and Thomas model and predictions of the magnetosheath field based on the current model were used to determine the relative orientations between the two fields at locations in the vicinity of the dayside magnetopause. Areas on the magnetopause with various degrees of antiparallelness between the two fields for various orientations of the IMF were obtained for the purpose of locating potential field merging sites and displayed as contour diagrams. The results suggest that large fractions of the magnetopause surface are suitable for merging for IMF's that are primarily southward or radial in direction.

In Ref. 11, the predictive model was employed to investigate the continuing question of whether the Mars-3 spacecraft observation of January 21, 1972 was of a Martian magnetosphere or of a compressed IMF in the magnetosheath. In this study, the gasdynamic model was employed to generate the global flow field and then the magnetic field computational module was repeatedly employed to investigate whether an appropriate IMF could be determined which would produce the time history variation of magnetic field that was observed. Based upon the results, it was found that a good simulation of the observed magnetic variation could be made purely on the basis of the magnetosheath field without invoking an entry into a Martian magnetosphere to explain the observations.

A final current collaborative study is underway involving Dr. William Knudsen of Lockheed Palo Alto Research Laboratories regarding Pioneer-Venus velocity potential analyzer observations and interpretations of the Venusian ionopause. The present model is being employed to examine a more accurate shape determination of the Venusian ionopause based on measured ionospheric properties at axial locations from the subsolar point back beyond the terminator and into the wake region. Employment of the predictive model to provide details of the plasma and magnetic field properties in those regions near the ionopause is essential for understanding the key physical phenomena present in the data. Presently, flow field determinations from the model have been made for a series of new and different ionopause models.

3.4 References

1. Spreiter, J. R. and Stahara, S. S.: A New Predictive Model for Determining Solar Wind - Terrestrial Planet Interactions. Jour. of Geophy. Res., Vol. 85, No. A12, pp. 6769-6777, Dec. 1, 1980.

2. Spreiter, J. R. and Stahara, S. S.: Solar Wind Past Venus: Theory and Comparisons. Jour. of Geophy. Res., Vol. 85, No. A13, pp. 7715-7738, Dec. 30, 1980.

3. Stahara, S. S., Klenke, D., Trudinger, B. C., and Spreiter, J. R.: Application of Advanced Computational Procedures for Modeling Solar-Wind Interactions with Venus - Theory and Computer Code. NASA CR 3267, May 1980.

4. Slavin, J. A. and Holzer, R. E.: Solar Wind Flow About the Terrestrial Planets 1. Modeling Bow Shock Position and Shape. Jour. of Geophy. Res., Vol. 86, No. A13, pp. 11401-11418, Dec. 1, 1981.

5. Slavin, J. A., Holzer, R. E., Spreiter, J. R., Stahara, S. S., and Chaussee, D. S.: Solar Wind Flow About the Terrestrial Planets 2. Comparison with Gas Dynamic Theory and Implications for Solar-Planetary Interactions. Jour. of Geophy. Res., Vol. 88, No. A1, pp. 19-35, Jan. 1, 1983.

6. Slavin, J. A., Holzer, R. E., Spreiter, J. R., and Stahara, S. S.: Planetary Mach Cones: Theory and Observation. Submitted to Jour. of Geophy. Res.

7. Mihalov, J. D.: Comparison of Gas Dynamic Model for Solar Wind Flow Around Venus with Pioneer Venus Orbiter Data. Stanford University Engineers Thesis, May 1981.

8. Mihalov, J. D., Spreiter, J. R., and Stahara, S. S.: Comparison of Gas Dynamic Model with Steady Solar Wind Flow Around Venus. Jour. of Geophy. Res., Vol. 87, No. A12, pp. 10363-10371, Dec. 1, 1982.

9. Luhmann, J. G., Walker, R. J., Russell, C. T., Crooker, N. U., Spreiter, J. R., Stahara, S. S., and Williams, D. J.: Characteristics of the Magnetospheric Source of Interplanetary Energetic Particles. Institute of Geophysics and Planetary Physics, U.C.L.A. Publication No. 2442, May, 1983. Submitted to Jour. of Geophy. Res.

10. Luhmann, J. G., Walker, R. J., Russell, C. T., Crooker, N. U., Spreiter, J. R., and Stahara, S. S.: Patterns of Magnetic Field. Merging Sites on the Magnetopause. Institute of Geophysics and Planetary Physics, U.C.L.A. Publication No. 2443, May 1983. Submitted to Jour. of Geophy. Res.

11. Russell, C. T., Luhmann, J. G., Spreiter, J. R., and Stahara, S. S.: The Magnetic Field of Mars: Implications from Gas Dynamic Modeling. Institute of Geophysics and Planetary Physics, U.C.L.A. Publication No. 2468, July, 1983. Submitted to Jour. of Geophy. Res.

4. PUBLICATIONS LIST

Stahara, S. S., Klenke, D., Trudinger, B. C., and Spreiter, J. R.: Application of Advanced Computational Procedures for Modeling Solar-Wind Interactions with Venus - Theory and Computer Code. NASA CR 3267, May 1980.

Spreiter, J. R. and Stahara, S. S.: A New Predictive Model for Determining Solar Wind - Terrestrial Planet Interactions. Jour. of Geophy. Res., Vol. 85, No. A12, pp. 6769-6777, Dec. 1, 1980.

Spreiter, J. R. and Stahara, S. S.: Solar Wind Past Venus: Theory and Comparisons. Jour. of Geophy. Res., Vol. 85, No. A13, pp. 7715-7738, Dec. 30, 1980.

Mihalov, J. D., Spreiter, J. R., and Stahara, S. S.: Comparison of Gas Dynamic Model with Steady Solar Wind Flow Around Venus. Jour. of Geophy. Res., Vol. 87, No. A12, pp. 10363-10371, Dec. 1, 1982.

Slavin, J. A., Holzer, R. E., Spreiter, J. R., Stahara, S. S., and Chaussee, D. S.: Solar Wind Flow About the Terrestrial Planets 2. Comparison with Gas Dynamic Theory and Implications for Solar-Planetary Interactions. Jour. of Geophy. Res., Vol. 88, No. A1, pp. 19-35, Jan. 1, 1983.

Slavin, J. A., Holzer, R. E., Spreiter, J. R., and Stahara, S. S.: Planetary Mach Cones: Theory and Observation. Submitted to Jour. of Geophy. Res.

Luhmann, J. G., Walker, R. J., Russell, C. T., Crooker, N. U., Spreiter, J. R., Stahara, S. S., and Williams, D. J.: Characteristics of the Magnetospheric Source of Interplanetary Energetic Particles. Institute of Geophysics and Planetary Physics, U.C.L.A. Publication No. 2442, May, 1983. Submitted to Jour. of Geophy. Res.

Luhmann, J. G., Walker, R. J., Russell, C. T., Crooker, N. U., Spreiter, J. R., and Stahara, S. S.: Patterns of Magnetic Field. Merging Sites on the Magnetopause. Institute of Geophysics and Planetary Physics, U.C.L.A. Publication No. 2443, May, 1983. Submitted to Jour. of Geophy. Res.

Russell, C. T., Luhmann, J. G., Spreiter, J. R., and Stahara, S. S.: The Magnetic Field of Mars: Implications from Gas Dynamic Modeling. Institute of Geophysics and Planetary Physics, U.C.L.A. Publication No. 2468, July, 1983. Submitted to Jour. of Geophy. Res.

5. PARTICIPATING SCIENTIFIC PERSONNEL

(1) Stephen S. Stahara - Principal Investigator
(2) John R. Spreiter - Co-Principal Investigator

APPENDIX

COPIES OF PUBLICATIONS

A NEW PREDICTIVE MODEL FOR DETERMINING SOLAR WIND-TERRESTRIAL PLANET INTERACTIONS

John R. Spreiter

Division of Applied Mechanics, Stanford University, Stanford, California 94305

Stephen S. Stahara

Nielsen Engineering & Research, Mountain View, California 94043

Abstract. A computational model has been developed for the determination of the gasdynamic and magnetic field properties of the solar wind flow around a magnetic planet, such as the earth, or a nonmagnetic planet, such as Venus. The procedures are based on an established single-fluid, steady, dissipationless, magnetogasdynamic model and are appropriate for the calculation of axisymmetric, supersonic, super-Alfvénic solar wind flow past a planetary magneto/ionosphere. Sample results are reported for a variety of solar wind and planetary conditions. Some of these are new applications; others are included to show that the new procedures produce the same results as previous procedures when applied to the same conditions. The new methods are completely automated and much more efficient and versatile than those employed heretofore.

Introduction

The magnetogasdynamic model for the interaction of the solar wind and a planetary magnetosphere, or ionosphere if the planet is nonmagnetic, has been found to be of great utility in the prediction and interpretation of observations in space. The development of this model has a long history stemming from the work of Spreiter and Jones [1963], Dryer and Faye-Petersen [1964, 1966], Spreiter and Summers [1966], Alksne [1967], Dryer and Heckman [1967], Spreiter et al. [1968, 1970], Alksne and Webster [1970], Spreiter and Alksne [1969, 1970], and Spreiter and Rizzi [1974]. Although the usefulness of the original results is well established, there is much to be desired. Results have been calculated for only a limited set of solar wind and planetary conditions. Moreover, the original solutions bordered on what was barely possible at the time, required considerable hand computation, and were extremely laborious. Improvements in both numerical methods and computer capabilities have now rendered such procedures thoroughly obsolete, both from the standpoint of efficiency of calculation and generality of application.

To remedy this situation, a new, efficient procedure has been developed that provides the numerical solution for the streamlines, magnetic field lines, and contours of density, speed, temperature, and magnetic field intensity similar to those familiar from the original literature. The basic theoretical model employed is that described by Spreiter, Alksne, and their colleagues in the work cited above. The present solution makes full use of recent advances in nonlinear computational fluid dynamics. These advances include an algorithm of Beam and Warming

[1976] to determine the gasdynamic flow near the nose of the magneto/ionopause. The remainder of the flow field is calculated by using a method developed by Kutler et al. [1973] and by Chaussee et al. [1975]. The magnetic field is also calculated quite differently than it was previously, being based on the decomposition of Alksne and Webster [1970]. This paper presents an outline of the principal features of the analysis and a sample of the results. Complete details of the computational procedures are provided by Stahara et al. [1977].

Mathematical Model

The fundamental assumption of the present work and all of the geophysical work cited above is that the average bulk properties of solar wind flow around a planetary magneto/ionosphere can be described adequately by solutions of the continuum equations of magnetogasdynamics of a perfect gas having infinite electrical conductivity and zero viscosity and thermal conductivity. These equations, which express the conservation of mass, momentum, energy, and magnetic field, are given by the following expressions:

$$\frac{\partial \rho}{\partial t} + \frac{\partial}{\partial x_k}(\rho V_k) = 0 \tag{1}$$

$$\frac{\partial}{\partial t}(\rho V_i) + \frac{\partial}{\partial x_k}(\rho V_i V_k + p\delta_{ik} - \frac{B_i B_k}{4\pi}$$
$$+ \frac{B^2}{8\pi}\delta_{ik} + \frac{g_i g_k}{4\pi G} - \frac{g^2}{8\pi G}\delta_{ik}) = 0 \tag{2}$$

$$\frac{\partial}{\partial t}(\frac{\rho V^2}{2} + \rho e + \rho\phi + \frac{B^2}{8\pi})$$
$$+ \frac{\partial}{\partial x_k}\left[\rho V_k(\frac{\rho V^2}{2} + e + \frac{p}{\rho} + \phi) + S_k\right] = 0 \tag{3}$$

$$\frac{\partial B_i}{\partial t} = \frac{\partial}{\partial x_k}(V_i B_k - V_k B_i), \qquad \frac{\partial B_i}{\partial x_i} = 0 \tag{4}$$

where

$$g_i = \frac{\partial \phi}{\partial x_i}, \qquad S_k = \frac{1}{4\pi}(V_k B^2 - B_k V_i B_i) \tag{5}$$

and the equation of state of a perfect gas is given by

$$p = \frac{\rho R T}{\mu} \tag{6}$$

In accordance with standard usage the symbols ρ, p, V, T, $e = C_v T$, and $h = e+p/\rho = C_p T$ refer to the density, pressure, velocity, temperature, internal energy, and enthalpy; C_v and C_p refer to the specific heats at constant volume and pressure; $R = (C_p - C_v)\nu = 8.31 \times 10^7$ ergs/g °K is the universal gas constant, and ν represents the mean molecular weight nondimensionalized so that $\nu = 16$ for atomic oxygen. For fully ionized hydrogen, ν is thus 1/2. The magnetic field $\underline{B}$ and the Poynting vector $\underline{S}$ for the flux of electromagnetic energy are in Gaussian units. The gravitational potential ϕ and acceleration g are assumed to be due to massive fixed bodies so that their time derivatives are zero. Because of the omission of dissipative terms in these equations, surfaces of discontinuity may develop in the solution, across which the fluid and magnetic properties change abruptly, but in such a way that mass, momentum, magnetic flux, and energy are conserved. These are approximations to comparatively thin layers across which similar changes in the fluid and magnetic properties occur in the corresponding theory of a dissipative gas and correspond physically to the bow wave, magneto/ionosphere boundary, and possible other thin regions of rapidly changing properties.

The shape of the magneto/ionospheric obstacle, assumed to be axisymmetric about a line through the planet center extending parallel to the free-stream solar wind velocity vector, may be specified in either of two ways: by a numerical table of coordinates or by use of simplified models from the cited references, which enable the calculation of approximate magneto/ionopause shapes upon specification of a small number of solar wind and planetary magnetic field or ionospheric parameters.

For the earth or other magnetic planets having a dipole field this shape is obtained by rotating the equatorial trace of the three-dimensional magnetosphere surface determined by balancing the Newtonian pressure $p = K\rho_\infty V_\infty^2 \cos^2\psi_0$ against the magnetic pressure due to $2f$ times the tangential component of the dipole field. Here, K and f are constants usually taken to be unity (see Spreiter [1976] for a discussion), ρ and V are the density and velocity of the solar wind, the subscript ∞ refers to conditions in the incident stream upstream of the bow wave, and ψ_0 is the angle between V_∞ and the normal to the magnetopause. These considerations lead to the following differential equation for the geocentric distance to the magnetopause r_m as a function of geomagnetic longitude ϕ, measured in such a way that ϕ is equal to $\pi/2$ at the magnetosphere nose and increases to $3\pi/2$ as one moves around the flank of the magnetosphere to the remote tail [Beard, 1960]:

$$\frac{d\bar{r}_m}{d\phi} = \bar{r}_m \left[\frac{\bar{r}_m^6 \sin\phi \cos\phi + \sqrt{\bar{r}_m^6 - 1}}{\bar{r}_m^6 \cos^2\phi - 1} \right] \quad (7)$$

$$\pi/2 \leq \phi \leq 3\pi/2$$

In this equation, $\bar{r}_m = r_m/D$,

$D = a_e(f^2 E_{eq}^2 / 2\pi K \rho_\infty V_\infty^2)^{1/6}$ is the geocentric

distance to the magnetosphere nose, where a_e refers to the radius of the earth, and E_{eq} is the average intensity of the field at the geomagnetic equator.

For a nonmagnetic planet having a sufficiently dense ionosphere to withhold the solar wind, such as Venus appears to be most of the time, the ionopause shape is determined by balancing the Newtonian pressure and the ionospheric pressure approximated by

$$p = p_R \exp\left[-\frac{r-r_R}{H}\right] \quad (8)$$

derived from (1)-(5) by assuming steady conditions, negligible velocity and magnetic field, and a constant ionospheric scale height $H = kT/mg$, where $k = 1.38 \times 10^{-16}$ ergs/°K is Boltzmann's constant, m is the mean molecular mass, and p_R is the pressure at some reference radius r_R. These considerations lead to the following differential equation for the coordinates r_i of the ionopause as a function of angle ξ from the ionopause nose as measured at the planetary center [Spreiter et al., 1970]:

$$\frac{dr_i}{d\xi} = r_i \left[\frac{\sin 2\xi - 2\Lambda\sqrt{\Lambda^2 - \Lambda^2}}{2(\Lambda^2 - \sin^2\xi)} \right] \quad 0 \leq \xi \leq \pi$$

$$(9)$$

in which $\Lambda = \exp[-(r_i - R_0)/H]$, where R_0 is the value of r_i at the ionopause nose where $\xi = 0$. A family of ionopause shapes can be obtained by integrating (9) for different values of H/R_0. Appropriate values of H/R_0 for application to Venus and Mars appear to be in the range from 0.01 to 0.30.

Two important parameters which characterize the solar wind flow in the magnetogasdynamic model are the free-stream values for the Mach number $M = V/a$ and the Alfvén Mach number $M_A = V/A$, in which $a = (\gamma p/\rho)^{1/2}$ is the speed of sound, A is the Alfvén speed $A = (B^2/4\pi\rho)^{1/2}$, and γ is the ratio of specific heats, usually taken to be 5/3 in solar wind applications. Because $M_{A\infty}$ is typically greater than 5 in the solar wind, an important simplification may be introduced on the basis that for large $M_{A\infty}$ the magnetic terms in the momentum and energy equations (2) and (3) are generally sufficiently small compared with the gasdynamic terms that they may be disregarded therein. This decouples the solution for the fluid motion from the magnetic field, which may be calculated subsequently by using the induction equation (4) and values for V already calculated.

Although few detailed comparisons have been made, other than those of Spreiter and Rizzi [1974], which made use of their complete magnetogasdynamic numerical solution for the special case of aligned flow, it is generally regarded that the magnetic field calculated in this way reproduces the broad characteristics of observations. However, the process indicates magnetic field strengths that may be too large immediately outside the magnetopause. Zwan and Wolf [1976] have made an interesting analysis of conditions in this region and concluded that the strong

magnetic fields would drive the plasma out along the field lines and produce a thin region of depleted plasma density. Crooker and Siscoe [1977] have shown further that an observed anisotropy of the magnetosheath pressure occurs naturally from a mirror instability of the resulting flow along the magnetic flux tubes. Neither of these properties nor any representation of the long discussed possibility of magnetic merging at the magnetopause are captured by the present model, but the ready ability to generate our solutions for any specified conditions should aid in further study of such phenomena.

Calculation of the Gasdynamic Flow Properties

The gasdynamic equations for supersonic flow past a blunt-nosed obstacle representative of a planetary magneto/ionosphere are solved most effectively by using one method for the nose region, where the flow accelerates from subsonic to supersonic speeds, and another for the remaining region, where the flow is purely supersonic. In the present work the solution for the nose region is calculated by using a new axisymmetric implicit unsteady Euler equation solver (IMF), which determines the steady state solution by a time-marching procedure. The remainder of the solution is calculated by using a shock-capturing marching procedure (SCT), which spatially advances the solution downstream as far as required by solving the steady Euler equations.

Implicit Unsteady Euler Equation Solution for the Nose Region

The partial differential equations employed in the implicit code are the unsteady gasdynamic Euler equations derived from (1)-(3) by deleting the magnetic and gravitational terms and specializing for axisymmetric flows. Upon introduction of the generalized independent variable transformation $\tau = T$, $\zeta = \zeta(T,X,R)$, these equations may be written as

$$(U/J)_\tau + [(\zeta_T U + \zeta_X E + \zeta_R F)/J]_\zeta$$

$$+ [(\eta_T U + \eta_X E + \eta_R F)/J]_\eta + G = 0 \quad (10)$$

where

$$U = \begin{bmatrix} \rho \\ \rho u \\ \rho v \\ \rho e_t \end{bmatrix} \quad E = \begin{bmatrix} \rho u \\ p+\rho u^2 \\ \rho u v \\ (\rho e_t+p)u \end{bmatrix} \quad (11)$$

$$F = \begin{bmatrix} \rho v \\ \rho u v \\ p+\rho v^2 \\ (\rho e_t+p)v \end{bmatrix} \quad G = \frac{1}{RJ}\begin{bmatrix} \rho v \\ \rho u v \\ \rho v^2 \\ (\rho e_t+p)v \end{bmatrix}$$

and $J = \zeta_X \eta_R - \zeta_R \eta_X$ is the transformation Jacobian. In these equations, T denotes time, X the axial downstream coordinate, and R the

cylindrical radial distance; u and v are the velocity components in the X and R directions; $e_t = p/[\rho(\gamma-1)] + (u^2 + v^2)/2$ and subscripts denote partial derivatives with respect to the indicated variable.

The analysis commences by introducing a computational mesh in polar (r,β) coordinates such that one family of coordinates consists of rays from the planetary center spaced at equal increments of β measured from the obstacle nose and the other of curved lines intersecting each ray so as to divide the portion of it between the magneto/ionopause and the shock wave into a fixed number of equal segments. The coordinate transformation equation is then used to map the portion of the X,R,T physical space bounded by (1) the bow wave, (2) the downstream outflow boundary at $\beta = \pi/2$, (3) the obstacle surface, and (4) the stagnation streamline at $\beta = 0$ into a rectangle in the ζ, η, τ computational space as illustrated in Figure 1. Generally, the transformation metrics at each time step are not known beforehand and must be determined numerically as part of the solution. Integration step size is established by using the eigenvalues of the Jacobian matrices $\bar{A}$ and $\bar{B}$, where $\bar{A} = \partial\bar{E}/\partial\bar{U}$, $\bar{B} = \partial\bar{F}/\partial\bar{U}$, and also where $\bar{U} = U/J$, $\bar{E} = (\zeta_T U + \zeta_X E + \zeta_R F)/J$, and $\bar{F} = (\eta_T U + \eta_X E + \eta_R F)/J$.

Boundary conditions for a properly posed mathematical problem are that the flow satisfy the axisymmetric Rankine-Hugoniot shock relations derivable from equation (10) along item 1 above, be entirely supersonic along item 2 above, be parallel to items 3 and 4 above, and be symmetric about item 4 above. Initial conditions are determined by use of an approximating formula for the coordinates of the bow shock wave, dependent on γ, M_∞, and the shape of the obstacle, and by prescribing a Newtonian pressure distribution on the obstacle. The remainder of the initial properties on the obstacle surface can then be determined from the conditions that the flow must be tangential to the surface and possess constant entropy. A linear variation for the flow properties between the bow shock and the obstacle is then prescribed. This provides the initial flow field, which is then integrated in a time asymptotic fashion until the steady state solution is obtained.

The basic numerical algorithm used in the IMF code was developed by Beam and Warming [1976] and is second-order accurate, noniterative and
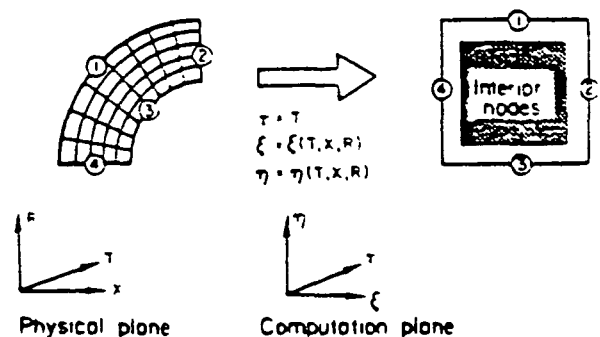

Physical plane   Computation plane

Fig. 1. Transformation from physical domain to rectangular domain.

Sphere

$M_\infty = 4.926$ $\gamma = 1.4$

- Implicit
- o Experiment (Xerikos and Anderson, 1965)
- --- Explicit (Moretti, 1967)
- △ Explicit (Bohachevsky, 1971)
- □ Explicit (Chaussee, 1975)
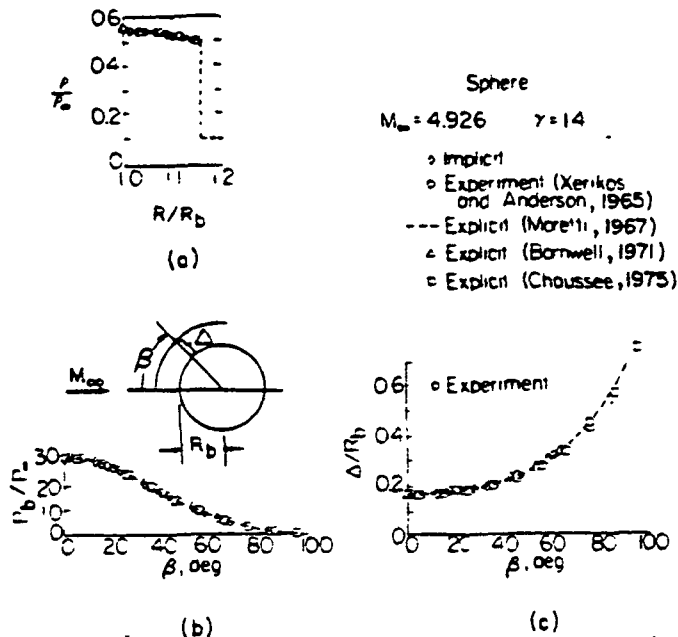
(a)

o Experiment

(b)   (c)

Fig. 2. Comparison of flow properties predicted by present implicit method with other techniques and experiment for supersonic flow past a sphere; $M_\infty = 4.926$, $\gamma = 1.4$. (a) Stagnation line density. (b) Surface pressure. (c) Shock standoff distance.

S is a fourth-order smoothing term introduced to eliminate nonlinear stabilities that may arise, since the use of central differences in the spatial directions results in a neutrally stable algorithm.

At the boundaries, modification of the differencing algorithm to account for the particular conditions described above is accomplished as follows. The obstacle surface flow tangency condition is incorporated through the use of Kentzer's [1970] scheme, while at the symmetry plane the variables are reflected according to whether they are odd or even. At the outflow boundary, where the flow is entirely supersonic, the dependent variables are determined by extrapolation from the adjacent interior points. For the upstream boundary, formed by the bow shock wave, the sharp discontinuity approach of Thomas et al. [1972] is used. The interior flow field bounded by these various boundaries is treated in shock-capturing fashion and therefore allows for the correct formation of secondary internal shocks should any occur.

Shock-Capturing Marching Solution for the Downstream Solution

The shock-capturing technique of Kutler et al. [1973] and Chaussee et al. [1975] employed herein is based on the set of four equations for steady axisymmetric flow obtained from (10) and (11) by

spatially factored. In particular, the 'delta form' with Euler time differencing is employed. When applied to (10), the algorithm assumes the form

$$(I + \Delta\tau\delta_\xi\bar{A}^n)(I + \Delta\tau\delta_\eta\bar{B}^n)(\hat{U}^{n+1} - \hat{U}^n)$$

$$= -\Delta\tau(\delta_\xi\hat{E}^n + \delta_\eta\hat{F}^n + G) \qquad (12)$$

where $\bar{A}$ and $\bar{B}$ are the Jacobian matrices, I is the identity matrix, δ_ξ and δ_η are second-order, central difference operators, $\hat{U}^{n+1} = O(n\Delta\tau)$, and $\Delta\tau$ is the integration step size.

Equation (12) is solved at the interior points only. It requires two 4×4 block tridiagonal inversions at each time step of the integration. The solution proceeds as follows:

1. Define $\Delta\hat{U} = \hat{U}^{n+1} - \hat{U}^n$.

2. Form the right-hand side of (12), and store results in the $\hat{U}^{n+1}$ array.

3. Apply smoothing $\hat{U}^{n+1} = \hat{U}^{n+1} - (\varepsilon/8)S/J$.

4. Define $\bar{U} = (I + \Delta\tau\delta_\eta\bar{B}^n)\Delta\hat{U}$, and solve the matrix equation $(I + \Delta\tau\delta_\xi\bar{A}^n)\bar{U} = \hat{U}^{n+1}$ for $\bar{U}$, storing the result in the $\hat{U}^{n+1}$ array.

5. Solve the matrix equation $(I + \Delta\tau\delta_\eta\bar{B}^n)\Delta\hat{U} = \hat{U}^{n+1}$ for $\Delta\hat{U}$.

6. Obtain the values of $\hat{U}^{n+1}$ from the relation $\hat{U}^{n+1} = \Delta\hat{U} + \hat{U}^n$.

7. Transfer the contents of $\hat{U}^{n+1}$ to $\hat{U}^n$, and repeat all steps until satisfactory convergence is attained.
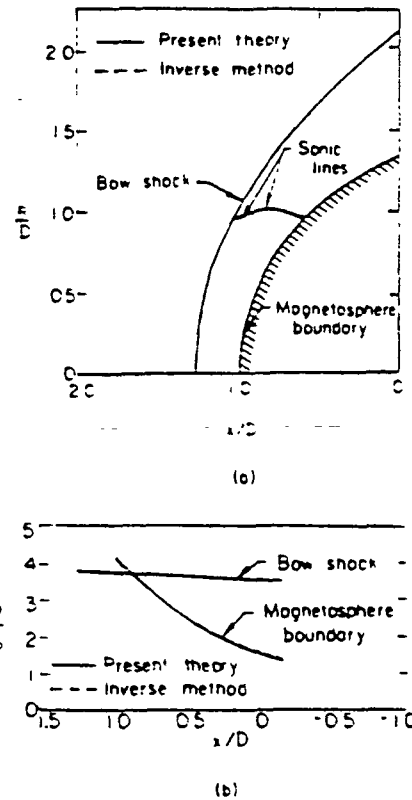

(a)

(b)

Fig. 3. Comparison of implicit and inverse methods for shock shape and sonic line location and density distribution along bow shock and magnetosphere boundary for $M_\infty = 8$, $\gamma = 5/3$ flow past the rotated equatorial trace of the magnetopause. (a) Shock shape and sonic line location. (b) Density distribution.

setting the τ derivatives to zero. The fourth of this set of equations, which represents conservation of total energy ρe_t, can be integrated to obtain the relation $h_t = e_t + p/\rho = $ const for the total enthalpy per unit mass.

The computational mesh is defined by lines of constant X and $(r-r_b)/(R_s-R_b)$, where R_b and R_s are functions of X that describe the radial cylindrical coordinates of the magneto/ionopause and bow shock wave at the same X as the field point (X,R) illustrated in Figure 1. The three remaining partial differential equations for conservation of mass and of axial and radial momentum are then transformed to a rectangular computational space by $\zeta = X$, $\eta = (R-R_b)/(R-R_b)$ to obtain

$$\frac{\partial \tilde{E}}{\partial \zeta} + \frac{\partial \tilde{F}}{\partial \eta} + \tilde{G} = 0 \qquad (13)$$

where

$$\tilde{E} = E$$

$$\tilde{F} = \{F - [\frac{\partial}{\partial \zeta} R_b + \eta \frac{\partial}{\partial \zeta} (R_s - R_b)]\}/(R_s - R_b)$$

$$\tilde{G} = G + \frac{E}{R_s - R_b} \frac{\partial}{\partial \zeta} (R_s - R_b)$$

$$(14)$$

The finite difference counterpart of (13) is integrated with respect to the hyperbolic coordinate ζ to yield values for the conservative variable E. Subsequent to each integration step the physical flow variables p, ρ, u, and v must be decoded from the components e_i of E. This necessitates the solution of four simultaneous, nonlinear equations and is facilitated by using the relations $v = e_3/e_1$, $p = e_2 - e_1 u$, $\rho = e_1/u$,

Fig. 5. Magnetopause pressure coefficients for the principal meridian magnetopause shapes shown in Figure 4.

and $h = \gamma/(\gamma-1)(p/\rho)$ to determine the following quadratic equation for u:

$$\frac{u^2}{2} + \frac{\gamma}{\gamma-1}\left[\frac{e_2 - e_1 u}{e_1}\right]u - h_t + \left(\frac{e_3}{e_1}\right)^2$$

$$= -\frac{\gamma+1}{2(\gamma-1)}u^2 + \left(\frac{\gamma}{\gamma-1}\right)\frac{e_2}{e_1}u - h_t + \left(\frac{e_3}{e_1}\right)^2 = 0 \quad (15)$$

Two roots exist; one corresponds to subsonic flow and is discarded, since u is always supersonic in the present application, while the other corre-

(a)

(b)

(c)

Fig. 6. Variation of shock standoff distance with oncoming Mach number and ratio of specific heats for various magneto/ionopause traces as determined by the present implicit procedure. (a) Magnetopause equatorial trace. (b) Ionopause trace $-B/R_0 = 0.01$. (c) Ionopause trace $-B/R_0 = 0.5$.
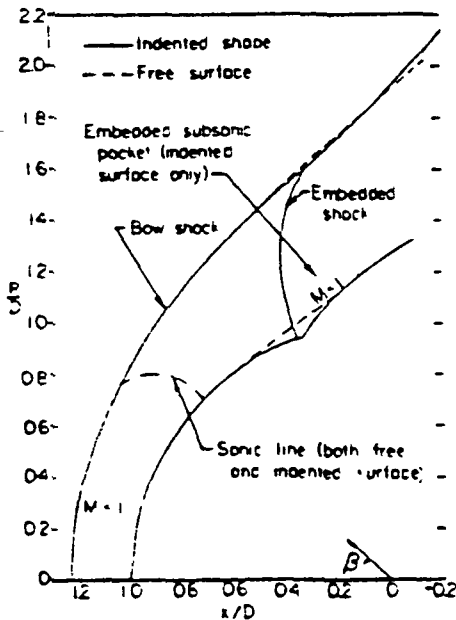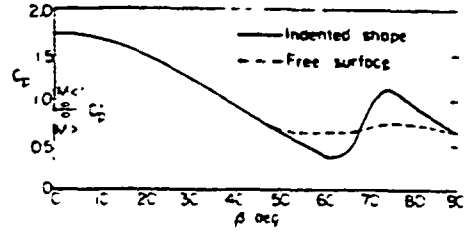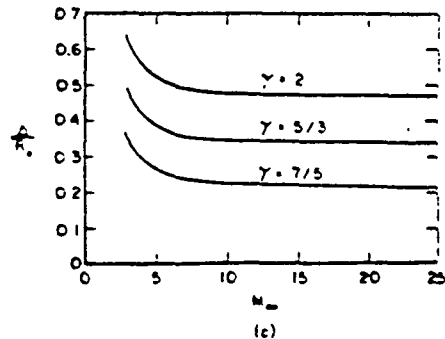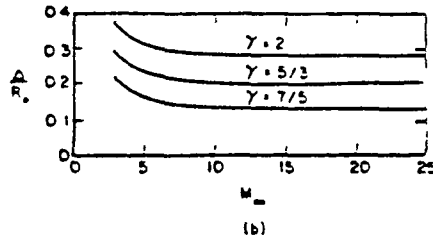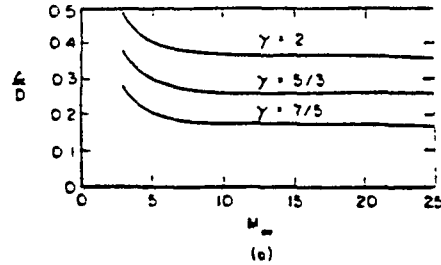

Fig. 4. Bow shock and embedded shock locations for solar wind flow with $M_\infty = 5$, $\gamma = 5/3$ past the rotated principal meridian of the magnetopause.
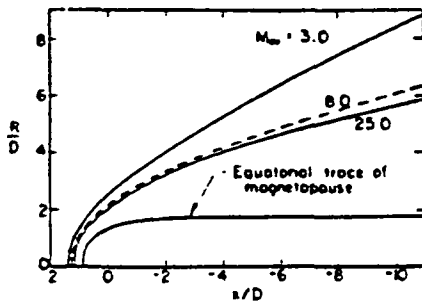
Fig. 7. Shock shapes for various supersonic flows past the rotated equatorial trace of the magnetopause; combined near (blunt body) and far (marching) solutions.

sponds to supersonic flow and gives the desired solution.

Since only the bow shock wave is treated as a sharp discontinuity and any others that may be present are 'captured' by the difference algorithm, selection of the appropriate finite difference scheme to advance the calculation in the ξ direction is of prime importance. As in the blunt body aerodynamic analysis of Kutler et al. [1973] and Chaussee et al. [1975], the numerical integration of (13) is accomplished by using the finite difference predictor-corrector scheme of MacCormack [1969], the most efficient second-order algorithm for shock-capturing calculations.

Calculation of the Streamlines

The streamlines are determined by integrating trajectories through the known velocity field, as this procedure was found to be more accurate than the alternative mass flow calculation. The calculation of a particular streamline is initiated at the bow shock, where its slope is calculated with an exact gasdynamic relation contained implicitly in both the blunt body (IMP) and marching (SCT) solution, and continued by stepwise integration in X using a modified third-order Euler predictor-corrector method. Bivariate linear interpolation from the flow field grid points is employed to obtain the velocity components (u,v) required at the stepwise points along the streamline trajectory.

Calculation of the Magnetic Field

With the flow properties known from the gasdynamic solution, calculation of the magnetic field B proceeds by integrating the steady state counterpart of (4), commonly interpreted as indi-
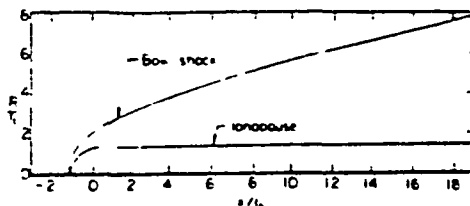

Fig. 8. Shock shape for $M_\infty = 8$, $\gamma = 5/3$ flow past an ionopause shape with $B/R_0 = 0.1$: combined near (blunt body) and far (marching) field solutions.
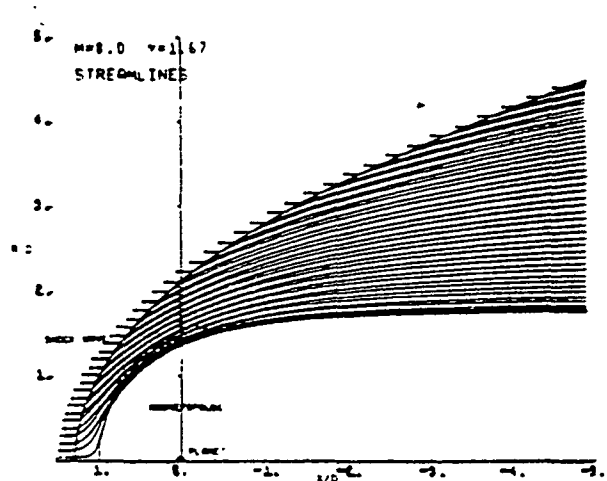

Fig. 9a. Streamline map for $M_\infty = 8.0$, $\gamma = 5/3$ flow past the rotated equatorial trace of the magnetopause: combined blunt body and marching flow field.

cating that the field lines move with the fluid. This leads to a straightforward calculation in which the vector distance from each point on an arbitrarily selected field line to its corresponding point on an adjacent field line in the downstream direction is determined by numerically integrating $\int V\, dt$ over a fixed time interval δt. Once the coordinates of the field lines are determined, the magnetic field at any point may be calculated from the relation $B/|B_\infty| = \rho\Delta\ell/(\rho_\infty|\Delta\ell_\infty|)$, where $\Delta\ell$ is the vector length of a small element of a flux tube.

Such a procedure is valid generally, but its use in the present calculations is confined to only one component of the magnetic field. The other components are determined by use of the Alksne and Webster [1970] decomposition dependent upon the axisymmetric properties of the gasdynamic solution and the linearity of the magnetic equations.

Calculation of the Contour Lines

Contours are calculated for nondimensionalized velocity $|V|/V_\infty$, density ρ/ρ_∞, and magnetic field
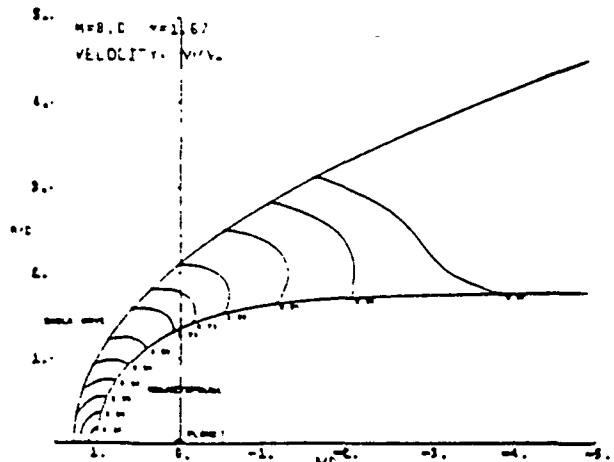

Fig. 9b. Velocity map for $M_\infty = 8.0$, $\gamma = 5/3$ flow past the rotated equatorial trace of the magnetopause: combined blunt body and marching flow field.

:components $(B/B_\infty)_{||}$ and $(B/B_\infty)_\perp$ by application of
a searching procedure. After a value for the
contour line is specified, the shock boundary is
searched for intervals which bracket the selected
value. After one such point is located by inter-
.ation, the remainder of the contour is deter-
.: by 'walking' around the contour, searching
each step for the interval and then interpo-
.ng to find the point through which the contour
, passes. This is repeated until a boundary
-: is reached. The closed contours are
.. in a similar manner. Linear interpolation
.. used throughout the process. The coordinates
: the contour lines are output as listings, pen
-::s. or both.

Results and Discussion

To verify the correctness of the new procedures
a.: to demonstrate their capability for calcula-
ting solar wind flows for a variety of conditions,
a large number of test cases have been run, and
a sample have been evaluated by comparison with
previously available theoretical and experimental
results. Figure 2 presents such a comparison for
supersonic flow of air ($\gamma=1.4$) past a sphere at
$v_\infty = -.926$. The variation of density along the
stagnation streamline is provided in Figure 2a,
while the variations of surface pressure p_b and
shock standoff distance Δ with angular distance
::x the nose are given in Figures 2b and 2c. In
these and similar comparisons the results provided
b. the new procedures are in essentially perfect
agreement with those of previous numerical solu-
tions and experiment.

Figure 3 exhibits a comparison of results
predicted by the present method with those
originally calculated by Spreiter et al. [1966,
1968] for the same solar wind and magnetosphere
conditions, using the inverse method of Inouye
and Lomax [1962] for the blunt nose region and
the method of characteristics for the downstream
supersonic region. Figure 3a displays the loca-
tions of the bow wave and sonic line for flow
past the equatorial trace of the magnetopause
for $M_\infty = 8$ and $\gamma = 5/3$. The density distribution
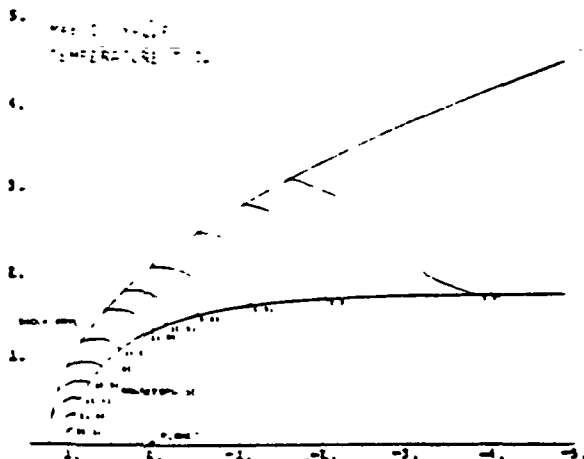along the magnetosphere boundary and along the

Fig 9c. Temperature map for $M_\infty = 8.0$, $\gamma = 5/3$
flow past the rotated equatorial trace of the
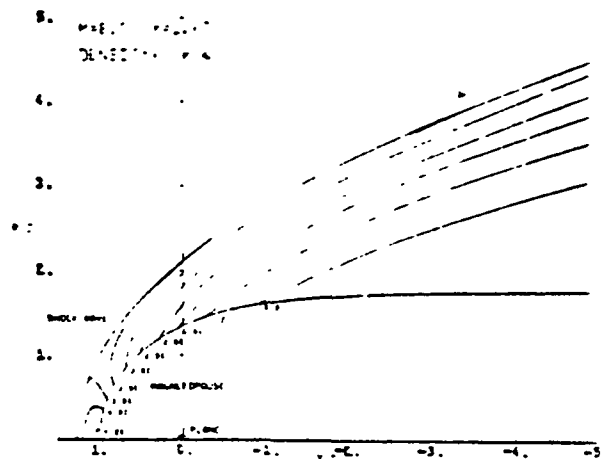magnetopause: combined blunt body and marching
flow field.

Fig. 9d. Density map for $M_\infty = 8.0$, $\gamma = 5/3$ flow
past the rotated equatorial trace of the magneto-
pause: combined blunt body and marching flow
field.

shock wave are given in Figure 3b. Essentially
perfect agreement is obtained between the present
implicit technique and the inverse method.
Similarly perfect agreement has been obtained
with all of the results presented previously in
the cited references by Spreiter and his
colleagues. The present method is, however, both
more efficient and more versatile.

Figures 4 and 5 present new results that illus-
trate the geometric flexibility of the present
solution and its ability to capture embedded
shock waves as well as the bow shock, a feature
which the inverse method cannot duplicate. This
case is for $M_\infty = 5$ and $\gamma = 5/3$ flow around the
axisymmetric shape generated by rotating the
principal meridian of an indented magnetopause
about its axis and may be compared with an experi-
mental test by Spreiter et al. [1968]. This
particular profile shape, derived by Spreiter
and Briggs [1962] from the Beard [1960] approxi-
mation to the classical Chapman and Ferraro [1931]
theory, contains a pronounced dent with a concave
corner in the vicinity of a magnetic neutral
point. Spreiter and Summers [1967] argued that
the presence of an embedded shock wave would make
it impossible for the magnetosheath plasma to
follow such an indented contour and that there
would form instead a free surface approximating,
in the meridian plane, a tangent line across the
indentation and capping an embedded cusp region.
Figure 4 presents results for both the indented
and the free surfaces, denoted by solid and dashed
lines. For the indented surface a shock wave
is located on the body at approximately $\xi = 80^\circ$,
just as in the experiment, while for the free
surface the pressure coefficient displays an
approximately constant value as anticipated.
Finally, we note that the calculation of a
supersonic flow with an embedded shock and subse-
quent subsonic pocket provides a severe test for
any blunt body procedure. The ability of the
present code to provide convergent results for
such a flow demonstrates the capability for
further extension and application to more general-
ized profiles than was heretofore possible.

As a final illustration of the range of condi-
tions for which the implicit code has been tested,
Figure 6 summarizes results for the shock standoff

distance provided by the gasdynamic calculations for three values for γ for three different magneto/ionopause shapes and a range of values for M_∞ from 3 to 25. These conditions span the range of interest of geometrical and solar wind conditions for which the computer programs developed herein would be normally applied.

In order to confirm the ability of the marching code to continue the solution to some arbitrarily specified downstream location, solutions have been carried far downstream for a wide variety of cases typical of solar wind interactions. Figure 7 exhibits the location of the bow wave downstream from the nose region to $x/D = -11$ for flows with $\gamma = 5/3$ and $M_\infty = 3$, 8, and 25 past the rotated equatorial trace of the magnetopause. For this calculation, starting conditions for the marching code (SCT) are provided by the blunt body (IMP) code on the line $x/D = 0.0$, which is the usual location at which the two solutions are joined by the computer program. The marching code then determines the remainder of the flow field back to the specified downstream location. Since for the shapes considered herein the downstream flows are quite smooth, the marching calculation is very efficient (less than 30s, CDC 7600, OPT=2 compiler). Similar results are presented in Figure 8 for $M = 8$ and $\gamma = 5/3$ flow past an ionopause shape with

$D/R_0 = 0.1$. Those results have been carried to $x/R_0 = -20$ in keeping with the observation that R_0 for Venus and Mars is only slightly greater than the planetary radius, whereas for the earth, D is of the order of 10 earth radii.

To illustrate the capability of the present procedures to determine streamlines, contour maps of various flow properties, and magnetic field lines and contours, as well as to demonstrate the automated plotting capability for displaying these results, Figures 9 and 10 have been prepared. Figure 9 illustrates the computer-generated streamline locations and contour maps of velocity ratio V/V_∞, temperature ratio T/T_∞, and density ratio ρ/ρ_∞ for the complete near- and far-field flow about the equatorial trace of the magnetosphere for $M_\infty = 8$ and $\gamma = 5/3$. Based on this gasdynamic solution, Figure 10 exhibits the corresponding results for the magnetic field $(B/B_\infty)_\perp$ and $(B/B_\infty)_{||}$ in the plane of magnetic symmetry for B_∞ parallel and perpendicular to V_∞. In addition to demonstrating the overall smoothness of the computed results these two figures illustrate the ability of the present techniques to provide the completely automated production of report quality plots of both gasdynamic and magnetic field properties for solar wind flows past axisymmetric magneto-ionopause shapes.

Concluding Remarks

Advanced numerical techniques have been applied to produce an efficient operational computer solution for the well-established dissipationless magnetogasdynamic model for axisymmetric, supersonic, super-Alfvénic solar wind flow past either magnetic or nonmagnetic terrestrial planets. The solution consists of the following assemblage of computer codes; (1) blunt body code, to determine the gasdynamic solution near the magneto/ionopause nose, (2) marching code, to determine the gasdynamic solution downstream of the magneto/ionopause nose, (3) streamline code, to determine coordinates of flow field streamlines, (4) magnetic field code, to determine frozen-in magnetic field, (5) contour code, to determine coordinates of contour lines of flow and magnetic field properties, and (6) plotting code, to plot selected flow and magnetic field results.

Comparisons are reported which demonstrate the accuracy of the present techniques by comparison with previously established theoretical methods and with experimental data. New results are presented for a variety of solar wind flows which illustrate the flexibility and generality of the methods.

References

Alksne, A. Y., The steady-state magnetic field in the transition region between the magnetosphere and the bow shock, Planet. Space Sci., 15, 239, 1967.
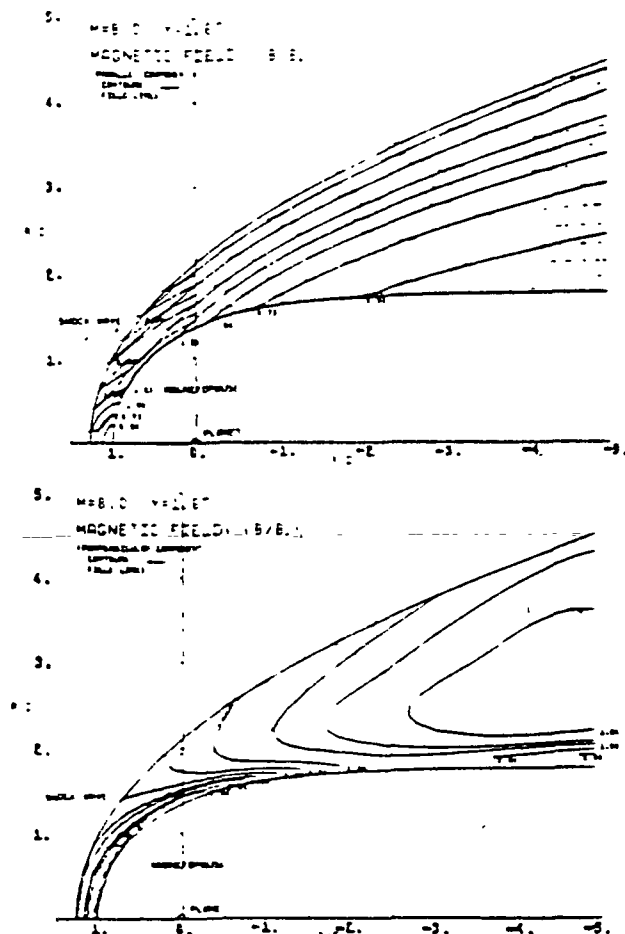
Alksne, A. Y., and D. L. Webster, Magnetic and

Fig. 10. Contours and field line locations of the magnetic field components $(B/B_\infty)_\perp$ and $(B/B_\infty)_{||}$ in the plane of magnetic symmetry for $M_\infty = 8.0$ and $\gamma = 5/3$ flow past the rotated equatorial trace of the magnetopause.

electric fields in the magnetosheath, Planet. Space Sci., 18, 1203, 1970.

Barnwell, R. W., A time-dependent method for calculating supersonic angle-of-attack flow about axisymmetric blunt bodies with sharp shoulders and smooth nonaxisymmetric blunt bodies, NASA Tech. Note, TN D-6283, 1971.

Bear. R. M., and R. F. Warming, An implicit finite-difference algorithm for hyperbolic systems in conservation-law form, J. Comput. Phys., 22, 1, 1976.

Beard, L. B., The interaction of the terrestrial magnetic field with the solar corpuscular radiation, J. Geophys. Res., 65, 3559, 1960

Chapman, S., and V. C. A. Ferraro, An outline of a theory of magnetic storms, J. Geophysics Res., 36, 77, 171, 1931.

Chaussee, D. S., T. Holtz, and P. Kutler, Inviscid supersonic/hypersonic body flow fields and aerodynamics from shock-capturing technique calculations, AIAA Pap. 75-837, 1975.

Crooker, N. V., and G. L. Siscoe, A mechanism for pressure anisotropy and mirror instability in the dayside magnetosheath, J. Geophys. Res., 82, 185, 1977.

Dryer, M., and R. Faye-Petersen, Some observations from an approximate solution of the direct blunted body problem in hypersonic flow, Proceedings of the 1964 Heat and Transfer and Fluid Mechanics Institute, edited by W. H. Giedt and S. Levy, p. 160, Stanford University Press, Stanford, Calif., 1964.

Dryer, M., and R. Faye-Petersen, Magnetogasdynamic boundary condition for a self-consistent solution to the closed magnetopause, AIAA J., 4, 246, 1966.

Dryer, M., and G. R. Heckman, Application of the hypersonic analogy to the standing shock of Mars, Sol. Phys., 2, 112, 1967.

Inouye, M., and H. Lomax, Comparison of experimental and numerical results for the flow of a perfect gas about blunt-nosed bodies, NASA Tech. Doc., TD-1426, 1962.

Kentzer, C. P., Discretization of boundary conditions on moving discontinuities, Lect. Notes Phys., 8, 108-113, 1970.

Kutler, P., W. A. Reinhardt, and R. F. Warming. Multi-shocked, three-dimensional supersonic flow fields with real gas effects, AIAA J., 11, 657, 1973.

MacCormack, R. W., The effect of viscosity in hypervelocity impact cratering, AIAA Pap., 69-354, 1969.

Moretti, G. and G. Bleich, Three dimensional flow around blunt bodies, AIAA J., 5, 1557, 1967.

Spreiter, J. R., Magnetohydrodynamic and gasdynamic aspects of solar-wind flow around

terrestrial planets: A critical review, NASA Spec. Publ., SP 397, 1976.

Spreiter, J. R., and A. Y. Alksne, Plasma flow around the magnetosphere, Rev. Geophys., 7, 11, 1969.

Spreiter, J. R., and A. Y. Alksne, Solar wind flow past objects in the solar system, Annu. Rev. Fluid Mech., 2, 1970.

Spreiter, J. R., and B. R. Briggs, Theoretical determination of the form of the boundary of the solar corpuscular stream produced by interaction with the magnetic dipole field of the earth, J. Geophys. Res., 67, 37, 1962.

Spreiter, J. R., and W. P. Jones, On the effect of a weak interplanetary magnetic field on the interaction between the solar wind and the geomagnetic field, J. Geophys. Res., 68, 3555, 1963.

Spreiter, J. R., and A. W. Rizzi, Aligned magnetohydrodynamics solution for solar wind flow past the earth's magnetosphere, Acta Astronaut., 1, 15, 1974.

Spreiter, J. R., and A. L. Summers, On conditions near the neutral points on the magnetosphere boundary, Planet Space Sci., 15, 787, 1967.

Spreiter, J. R., A. Y. Alksne, and A. L. Summers, External aerodynamics of the magnetosphere, in Physics of the Magnetosphere, edited by R. L. Carovillano, J. F. McClay, and H. R. Radoski, p. 301, D. Reidel, Bingham, Mass., 1968 (also available as NASA Tech. Note TN 4482, 1968).

Spreiter, J. R., A. L. Summers, and A. Y. Alksne, Hydromagnetic flow around the magnetosphere, Planet. Space Sci., 14, 223, 1966.

Spreiter, J. R., A. L. Summers, and A. W. Rizzi, Solar wind flow past nonmagnetic planets - Venus and Mars, Planet. Space Sci., 18, 1281, 1970.

Stahara, S. S., D. S. Chaussee, B. C. Truddinger, and J. R. Spreiter, Computational techniques for solar wind flows past terrestrial planets - Theory and computer programs, NASA Contract. Rep., CR 2924, 1977.

Thomas, P. D., M. Vinokur, R. Bastionon, and R. J. Conti, Numerical solution for the three-dimensional hypersonic flow field of a blunt delta body, AIAA J., 10, 887, 1972.

Zwan, B. J., and R. A. Wolf, Depletion of solar wind plasma near a planetary boundary, J. Geophys. Res., 81, 1636, 1976.

Xerikos, J., and W. A. Anderson, An experimental investigation of the shock layer surrounding a sphere in supersonic flow, AIAA J., 3, 451, 1965.

SOLAR WIND FLOW PAST VENUS: THEORY AND COMPARISONS

John R. Spreiter

Division of Applied Mechanics, Stanford University, Stanford, California 94305

Stephen S. Stahara

Nielsen Engineering & Research, Inc., Mountain View, California 94043

Abstract. Advanced computational procedures are applied to an improved model of solar wind flow past Venus to calculate the locations of the ionopause and bow wave and the properties of the flowing ionosheath plasma in the intervening region. The theoretical method is based on a single-fluid, steady, dissipationless, magneto-hydrodynamic continuum model and is appropriate for the calculation of axisymmetric supersonic, super-Alfvénic solar wind flow past a nonmagnetic planet possessing a sufficiently dense ionosphere to stand off the flowing plasma above the subsolar point and elsewhere. Determination of time-histories of plasma and magnetic field properties along an arbitrary spacecraft trajectory and provision for an arbitrary oncoming direction of the interplanetary solar wind have been incorporated in the model. An outline is provided of the underlying theory and computational procedures, and sample comparisons of the results are presented with observations from the Pioneer Venus orbiter.

Introduction

The magnetohydrodynamic model of Spreiter et al. [1970] for solar wind flow around the Venus ionosphere, stemming from the closely related earlier studies for the earth and its magnetosphere [Spreiter, 1976; Spreiter and Jones, 1963; Spreiter and Rizzi, 1974; Spreiter et al., 1966, 1969, 1970; Dryer and Faye-Peterson, 1966; Dryer and Heckman, 1967], provides a theoretical basis for the understanding and interpretation of observations from the viewpoint of a fluid rather than a particle description of the flow. The basic pattern for the associated calculations using this model was established by Spreiter et al. [1966] for the case of the earth, or any other planet with a dominant dipole magnetic field; and by Spreiter et al. [1970] for the case of Venus and Mars, or any other planet with no significant magnetic field but a sufficiently dense ionosphere to stand off the solar wind above the planetary surface. This consists of (1) representing the magnetopause or ionopause by a magnetohydrodynamic tangential discontinuity, (2) solving for the shape of the magnetospheric or ionospheric obstacle using simplified approximations for the pressure of the deflected solar wind flow at the obstacle boundary and for the planetary magnetic and atmospheric properties, (3) solving for the location of the bow wave and for the density, velocity, pressure, and temperature throughout the flow as a gasdynamic problem, disregarding the electromagnetic forces because of the characteristically high values of the free-stream

Alfvén Mach number, and finally (4) calculating the magnetic field as a frozen-in convected field assuming that the other fluid properties are provided sufficiently accurately by the gasdynamic solution.

Prior to the work reported recently by Stahara et al. [1977], the utility of this model was severely restricted because results were available only in the form of plots in archival journals for a limited set of solar wind and planetary conditions. Results for intermediate points or for other conditions had to be determined by interpolation. Stahara et al. [1977] improved on the basic model in many significant ways. New and more effective algorithms were introduced to perform the calculations, enabling the determination of results for a wide range of specific conditions typical of solar wind/ terrestrial planet interactions for both magnetic and nonmagnetic planets.

In the current work summarized here, that model has been extended and generalized in several important directions. These include (1) extension of the gasdynamic capability for treating free-stream Mach numbers as low as $M_\infty = 2$, (2) development of a new family of ionopause shapes which includes the effect of gravitational variation in scale height of the ionosphere, and (3) development of the capability for readily determining the plasma properties along an arbitrary spacecraft trajectory, simultaneously accounting for an arbitrary direction for the incident solar wind relative to a chosen coordinate system.

The Mathematical Model – Formulation of the Fluid Representation

The fundamental assumption underlying the present work and that reported in all of the references cited above is that many properties of solar wind flow around a planetary magneto/ ionosphere can be adequately described by the continuum equations of magnetohydrodynamics for a single-component perfect gas having infinite electrical conductivity and zero viscosity and thermal conductivity.

Governing Equations

The magnetohydrodynamic equations for the conservation of mass, momentum, energy, and magnetic field are as follows:

$$\frac{\partial \rho}{\partial t} + \frac{\partial}{\partial x_k}(\rho v_k) = 0 \tag{1}$$

$$\frac{\partial}{\partial t}(\rho v_i) + \frac{\partial}{\partial x_k}\left(\rho v_i v_k + p\delta_{ik} - \frac{B_i B_k}{4\pi}\right.$$

$$+ \frac{B^2}{8\pi} \delta_{ik} + \frac{g_i g_k}{4\pi G} - \frac{g^2}{8\pi G} \delta_{ik} \Bigg) = 0 \qquad (2)$$

$$\frac{\partial}{\partial t}\left[\frac{\rho v^2}{2} + \rho e + \rho \phi + \frac{B^2}{8\pi}\right]$$

$$+ \frac{\partial}{\partial x_k}\left[\rho v_k\left(\frac{v^2}{2} + e + \frac{P}{\rho} + \phi\right) + S_k\right] = 0 \qquad (3)$$

$$\frac{\partial B_i}{\partial t} = \frac{\partial}{\partial x_k}(v_i B_k - v_k B_i), \qquad \frac{\partial B_i}{\partial x_i} = 0 \qquad (4)$$

where

$$g_i = -\frac{\partial \phi}{\partial x_i}, \qquad S_k = \frac{1}{4\pi}\left(v_k B^2 - B_k v_i B_i\right) \qquad (5)$$

and the equation of state of a perfect gas is given by

$$p = \frac{\rho \overline{R} T}{\overline{M}} \qquad (6)$$

In these equations and those to follow, the symbols ρ, p, v, T, $e = C_v T$, and $h = C_p T$ refer to the density, pressure, velocity, temperature, internal energy, and enthalpy, and C_v and C_p refer to the specific heats at constant volume and pressure in the usual way. The symbol $\overline{R} = (C_p - C_v)\overline{M} = 8.3 \times 10^7$ erg/g°K is the universal gas constant, and $\overline{M}$ is the mean molecular weight nondimensionalized so that $\overline{M} = 16$ for atomic oxygen. For fully ionized hydrogen, $\overline{M}$ is thus 1/2. The magnetic field $\underline{B}$ and the Poynting vector $\underline{S}$ for the flux of electromagnetic energy are expressed in terms of Gaussian units. The gravitational potential ϕ and acceleration of gravity $\underline{g}$ are assumed to be due to massive fixed bodies so that their time derivatives are zero. $G = 6.67 \times 10^{-8}$ cm³/g s² is the gravitational constant. These equations apply in the region exterior to the ionosphere boundary, as shown in Figure 1, and also in a degenerate sense in the ionosphere.

Because of the omission of dissipative terms in these equations, surfaces of discontinuity may develop in the solution, across which the fluid magnetic properties change abruptly, but in such a way that mass, momentum, energy, and magnetic

flux are conserved. These are approximations to comparatively thin surfaces across which similar but continuous changes in the fluid and magnetic properties occur in the corresponding theory of a dissipative gas, and they correspond physically to the bow wave, ionosphere boundary, and possibly other thin regions of rapidly changing properties. The conservation of mass, momentum, energy, and magnetic flux lead to the following relations between the quantities on the two sides of any such discontinuity:

$$[\rho v_n^*] = 0 \qquad (7)$$

$$[\rho \underline{v} \cdot v_n^* + (p + B^2/8\pi)\hat{n} - B_n \underline{B}_t/4\pi] = 0 \qquad (8)$$

$$\left[v_n^*\left(\frac{1}{2}\rho v^2 + \rho e + p + \frac{B^2}{4\pi}\right)\right.$$

$$\left. + q_n \cdot \left(p + \frac{B^2}{8\pi}\right) - \frac{B_n(\underline{v} \cdot \underline{B})}{4\pi}\right] = 0 \qquad (9)$$

$$[\underline{B}_t \cdot v_n^* - B_n \cdot \underline{v}_t] = 0 \qquad (10)$$

Here, (n, t) denote unit vectors normal and tangential to the discontinuity surface, where q_n represents the local normal velocity of the discontinuity surface and $v_n^* = v_n - q_n$ is the fluid normal velocity component relative to the normal velocity q_n of the discontinuity surface. The square brackets are used to indicate the difference between the enclosed quantities on the two sides of the discontinuity, as in $[Q] = Q_2 - Q_1$, where subscripts 1 and 2 refer to the conditions on the upstream and downstream sides, respectively, of the discontinuity. Correspondingly, the average of Q_1 and Q_2 is represented by $<Q> = (Q_1 + Q_2)/2$.

Five classes of discontinuities are described by (7)-(10). Of these, only two, the fast shock wave and the tangential discontinuity, are of significance in the present analysis. The former, having properties that satisfy the relations

$$v_n^* \neq 0 \quad [\rho] > 0 \quad [p] > 0 \quad [B_n] = 0$$

$$\qquad (11)$$

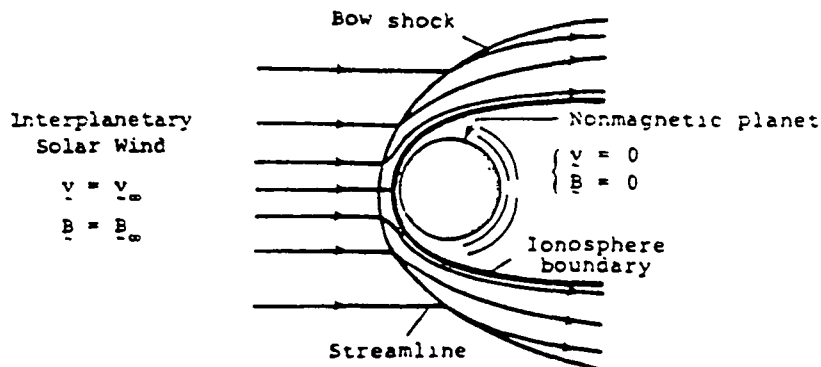$$[\underline{B}_t] > 0 \quad [B^2] > 0 \quad (\rho v_n^*)^2 > B_n^2/(4\pi <1/\rho>)$$

Fig. 1. Illustration of overall features of solar wind interaction with nonmagnetic terrestrial planets.

is appropriate for representing the bow wave; and the latter, having properties given by

$$v_n^* = B_n = 0 \qquad [v_t] \neq 0 \qquad [B_t] \neq 0$$

$$[\rho] \neq 0 \qquad [p + B^2/8\pi] = 0 \tag{12}$$

is appropriate for representing the ionopause that separates the flowing solar wind and the planetary ionosphere.

High Alfvén Mach Number Approximation

Two important parameters that characterize steady magnetohydrodynamic flow past a stationary obstacle are the free-stream Mach number $M_\infty = v_\infty/a_\infty$ and the Alfvén Mach number $M_{A\infty} = v_\infty/A_\infty$, in which $a = (\gamma p/\rho)^{1/2}$ is the speed of sound and $A = (B^2/4\pi\rho)^{1/2}$ is the speed of a rotational or Alfvén wave along the direction of the magnetic field, and $\gamma = C_p/C_v$ is the ratio of specific heats of the plasma.

For typical solar wind conditions at Venus, both M_∞ and $M_{A\infty}$ are high, values of the order of 10 being representative. As a result, important simplifications of the equations may be introduced. Since the order of magnitude of the momentum flux term in (2) and the kinetic energy flux term in (3) is related to that of the magnetic terms in the same equations by the square of $M_{A\infty}$, consideration of the magnetic terms may be decoupled from the solution of the gasdynamic portions of those equations. The equations for the fluid motion thereby reduce approximately to those of gasdynamics, and the magnetic field $\underline{B}$ can be determined subsequently by solving the remaining equations using the values for ρ and $\underline{v}$ so determined. Furthermore, because of the large value for M_∞, the terms involving g and $\mathfrak{C}$ can be disregarded in the solar wind flow because of the relatively small effects of gravity on the flow. This is not true, of course, in the ionosphere, where the comparative stationarity of the gases results in a very nearly hydrostatic variation of the pressure with altitude.

The precise specification of the range of usefulness of the decoupled approximation remains elusive in the absence of exact solutions of the complete magnetohydrodynamic equations. The only such solutions for the present category of flows are those of Spreiter and Rizzi [1974] for the special case in which $\underline{B}_\infty$ is aligned with $\underline{v}_\infty$. They indicate results virtually identical to those of the simpler decoupled theory when $M_{A\infty}$ is about 10 or greater and notably differing results as $M_{A\infty}$ is decreased below 5.

For other magnetic field alignments one can only make estimates of the relative magnitudes of the divergences of the neglected magnetic terms $B_i B_k/4\pi + B^2 \delta_{ik}/8\pi$ and S_{ik} compared to the terms $\rho v_i v_k + p\delta_{ik}$ and $\rho v_k(v^2/2 + e + p/e)$ retained in the gasdynamic analysis and then speculate about how large the magnetic terms can become before they invalidate the solution. In regions where the momentum flux and kinetic energy terms are large in comparison with the pressure and enthalpy terms, the square of the local Alfvén Mach number $M_A^2 = (\rho v^2/2) \div (B^2/8\pi)$

may be considered to provide a rough measure of the dominance of the gasdynamic terms in the calculation of the fluid motion. Since this quantity is related to $M_{A\infty}^2$ by $M_A = (\rho/\rho_\infty)(v/v_\infty)^2 \cdot (B_\infty/B)^2 M_{A\infty}^2$, and ρ/ρ_∞, v/v_∞, and B/B_∞ are independent of $M_{A\infty}$ at large $M_{A\infty}$, it follows that M_A tends to remain large for large $M_{A\infty}$ except where $\rho v^2 \ll \rho_\infty v_\infty^2$ or where $B^2 \gg B_\infty^2$. These conditions are most likely to be encountered near the stagnation point, where v vanishes; but ρ reaches a maximum value comparable to $\rho_\infty v_\infty^2$ there, and that contravenes the initial premise upon which the estimate is predicated. A localized region of small M_A does not therefore necessarily signal a failure of the approximation.

As a further consideration in making such estimates, it should be noted that the orientation of $\underline{B}_\infty$ is very important in the determination of B^2/B_∞^2 throughout the flow. In particular, near the stagnation point, $B^2/B_\infty^2 \gg 1$ if $\underline{B}_\infty$ makes a substantial angle with $\underline{v}_\infty$; whereas B^2/B_∞^2 vanishes at the stagnation point when $\underline{B}_\infty$ is parallel to $\underline{v}_\infty$, since $\underline{B}$ is everywhere proportional to ρv [Spreiter and Rizzi, 1974]. For this case therefore $M_A^2 = (\rho_\infty/\rho)M_{A\infty}^2$, and M_A does not vanish even at the stagnation point because ρ/ρ_∞ is about 4–5 for representative conditions.

A definitive theoretical evaluation of the decoupled approximation will have to await the development of more advanced methods for the solution of the complete magnetohydrodynamic equations. In the meanwhile, considerable insight can be gained by comparing the predictions with conditions actually measured in space during appropriately steady conditions. The small scale of the Venus flow field compared with that of the earth's magnetosphere makes the data from Pioneer Venus particularly valuable for this purpose; and the results presented here show our initial efforts to carry out such comparisons. This should be considered no more than a beginning, however, as we only have data from two orbits; many additional comparisons should be carried out to obtain a more comprehensive understanding of the relation between the theoretical and observational results.

Under the conditions outlined above, (2), (3), (8), and (9) are thus simplified to the following:

$$\frac{\partial}{\partial t}(\rho v_i) + \frac{\partial}{\partial x_k}(\rho v_i v_k + p\delta_{ik}) = 0 \tag{13}$$

$$\frac{\partial}{\partial t}\left(\frac{\rho v^2}{2} + \rho e\right) + \frac{\partial}{\partial x_k}\left[\rho v_k\left(\frac{v^2}{2} + e + p/\rho\right)\right] = 0 \tag{14}$$

$$[\rho \underline{v} \cdot v_n^* + p] = 0 \tag{15}$$

$$\left[v_n^* \cdot \left(\frac{1}{2}\rho v^2 + \rho e + p\right)\right] = 0 \tag{16}$$

These equations, together with (1) and (7), are just those of gasdynamics and must be solved for the location of the bow wave and the gasdynamic properties $\underline{v}$, p, ρ, and T of the flow field about the ionospheric obstacle. With these properties so determined, (4) and (10) can be used to determine the magnetic field $\underline{B}$. Although all of the solutions described here are for the steady state
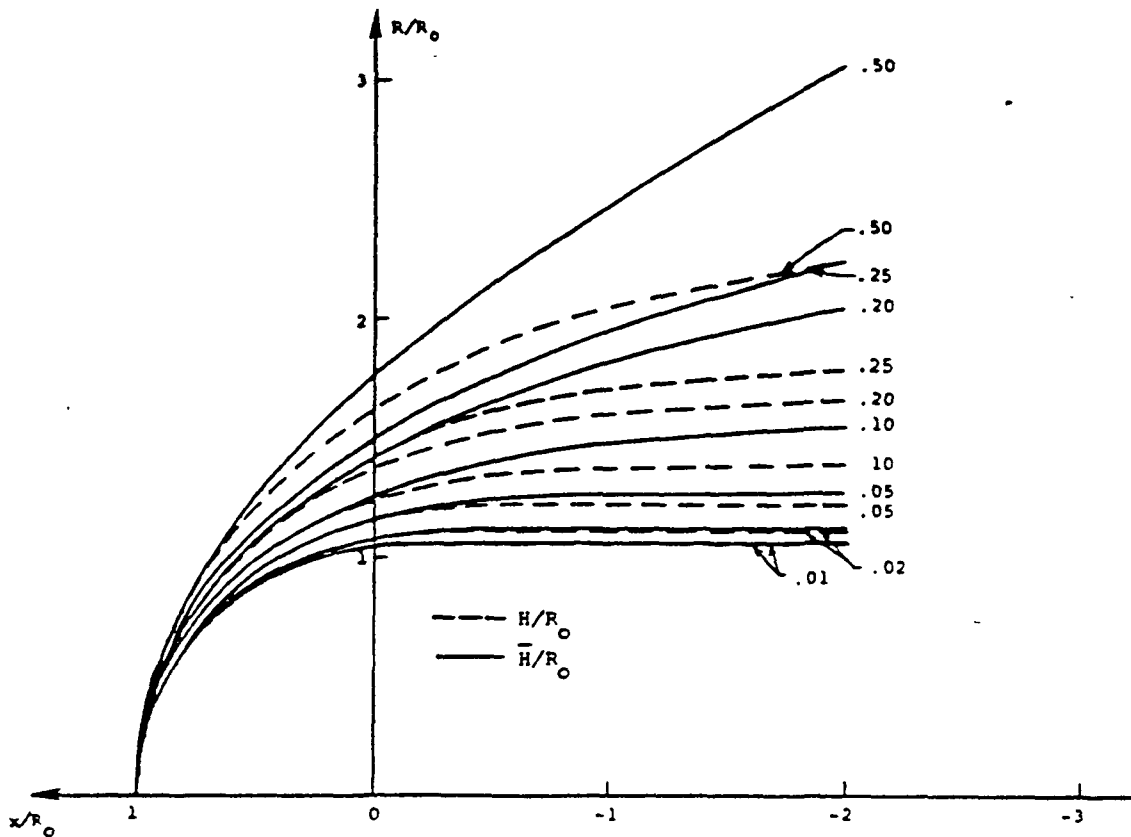
Fig. 2. Illustration of ionopause shapes for atmospheres with various (1) constant scale heights H/R_o and (2) gravitationally varying scale heights associated with a constant T/M atmosphere and characterized by $\bar{H}/R_o$.

obtained by setting $\partial/\partial t = 0$, and $v_n^* = v_n$, i.e., $q_n = 0$, the unsteady equations are presented in the foregoing because one of the computational methods used to determine the gasdynamic solution employs an unsteady procedure, integrating in time until the steady state solution is obtained asymptotically.

Determination of the Ionosphere Boundary

The determination of the ionosphere boundary, or ionopause, makes use of the idealization that the ionospheric plasma is spherically symmetric, hydrostatically supported, infinitely electrically conducting, devoid of any magnetic field, gravitationally bound to the planet, and incapable of mixing with the solar wind plasma, as sketched in Figure 1. This interior plasma is considered to be separated from the flowing solar wind plasma by a tangential discontinuity across which the relations of (12) apply. Because the magnetic pressure $B^2/8\pi$ is much smaller than the ionized gas pressure p in the ionopause, the relation $[p + B^2/8\pi] = 0$ of (12) may be simplified to

$$p_{atm} = (p + B^2/8\pi)_{flow} \qquad (17)$$

The variation of the pressure with radial distance from the planet center is given according to the hydrostatic equation by

$$dp/dr = -\rho g \qquad (18)$$

where p and ρ are the ionized gas pressure and density, r is the radial distance measured from the center of the planet, and $g = |g| = g_s(r_s/r)^2$, where subscript s denotes values at the surface of the planet. Combination of (18) and the perfect gas law given by (6) provides

$$p = p_R \exp\left(-\int_{R_R}^{r} \frac{dr}{H}\right) \qquad (19)$$

where p_R is the pressure at some reference radius R_R and $H = RT/Mg$ represents the local scale height of the ionospheric plasma.

If H is regarded as constant, i.e., if variations of g and T with r are disregarded, (19) can be integrated directly to obtain

$$p = p_R \exp\left(-\frac{r - R_R}{H}\right) \qquad (20)$$

Because of limited knowledge of the ionospheric properties of Venus at the time, the simple variation of p with r given by (20) was adopted in the initial study of Spreiter et al. [1970] and also in the more recent analysis of Stahara et al. [1977] involving the initial application of advanced computational methods to this problem. Data from the Pioneer Venus spacecraft [Knudsen et al., 1979a, b] have provided much additional knowledge of conditions in the Venus ionosphere and, in particular, have shown that the assumption of an isothermal (T = const) ionosphere at the heights of concern here is quite reasonable. With this assumption, including the variation of

gravity with height, the following result for the pressure is obtained:

$$p = p_R \exp\left[-\frac{R_R \cdot (r - R_R)}{\bar{H} \cdot r}\right] \qquad (21a)$$

where

$$\bar{H} = H_s \cdot (R_R/R_s)^2 \qquad (21b)$$

R_s being the planetary radius and $H_s = \bar{R}T/\bar{M}g_s$. Equations (20) and (21) provide the two models employed in this study for the ionosphere pressure variation required in the pressure balance relation of (17).

On the basis of the typically hypersonic values for M_∞ it has been assumed in all the previous analyses cited above that the pressure of the solar wind plasma on the ionopause could be represented adequately by the Newtonian approximation

$$p = K\rho_\infty v_\infty^2 \cos^2 \psi$$

$$K = \frac{1}{\gamma}\left[\frac{[(\gamma+1)/2]^{\gamma+1}}{\gamma-(\gamma-1)/2M_\infty^2}\right]^{\frac{1}{\gamma-1}} \qquad (22)$$

where ψ is the angle between the outward normal to the ionopause and the flow direction of the undisturbed solar wind incident on the bow wave and K is a constant usually taken as one but whose actual value to provide the correct gasdynamic stagnation pressure at the nose of the ionopause is as indicated.

The Newtonian approximation stems from gasdynamic analysis of hypersonic flows and is appropriate in the range of ψ from $0°$ to somewhat less than $90°$. In view of the close association between the magnetic pressure $B^2/8\pi$ and the gas pressure p in magnetohydrodynamics, it seems equally plausible to assume that the corresponding relation

$$p + B^2/8\pi = K\rho_\infty v_\infty^2 \cos^2 \psi \qquad (23)$$

is an appropriate, if not superior, relation for the combined magnetic and gas pressure of solar wind plasma on a planetary ionopause or magnetopause.

For the high Mach number flows typical of solar wind conditions, K approaches 0.881 for $\gamma = 5/3$ and 0.844 for $\gamma = 2$. A discussion of effects of minor constituents, such as ionized helium, in the solar wind and of some differences between a fluid and collisionless particle representation has been given by Spreiter [1976], but the most important effect of the introduction of the Newtonian approximation is that the calculation of the shape of the ionopause decouples from the calculation of the properties of the external flow. In this way we arrive at the following equation for the pressure balance at the ionopause location R_i:

$$K\rho_\infty v_\infty^2 \cos^2 \psi = p_R \Lambda(R_i) \qquad (24)$$

where

$$\Lambda(R_i) = \exp\left[-\left(\frac{R_i - R_R}{H}\right)\right] \qquad (25a)$$

$$g, T = \text{const}$$

or

$$\Lambda(R_i) = \exp\left[-R_R\left(\frac{R_i - R_R}{\bar{H} \cdot R_i}\right)\right] \qquad (25b)$$

$$g = g_s\left(\frac{r_s}{r}\right)^2, \; T = \text{const}$$

depending upon whether or not the gravitation variation is included in the scale height. It is convenient to choose the reference radius R_R to be the distance R_0 from the center of the planet to the nose of the ionopause. Then $p_R = p_0 = K\rho_\infty v_\infty^2$, and

$$\cos^2 \psi = \Lambda(R_i) \qquad (26)$$

at all points along the ionopause. To proceed, $\cos^2 \psi$ must be expressed in terms of R_i and β, where $R_i(\beta)$ represents the radial coordinate of the ionopause and β is the angle measured at the center of the planet with respect to a line that extends directly upstream. The appropriate expression is [Spreiter et al., 1970]

$$\cos^2 \psi = \left(\frac{dY_i}{dS}\right)^2 = \frac{(R_i d\beta \cos\beta + dR_i \sin\beta)^2}{dR_i^2 + (R_i d\beta)^2} \qquad (27)$$

Substitution of this expression into (26) results in the following ordinary differential equation for the ordinates of the ionosphere boundary:
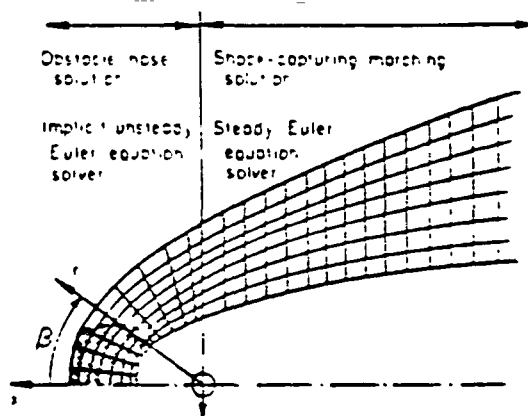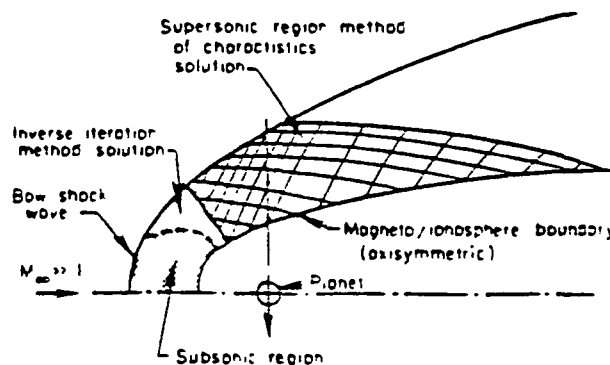

Fig. 3. Comparison of former and present computational procedures for determining the gasdynamic flow properties of solar wind-magneto/ionopause interactions.

$$\frac{dR_1}{d\beta} = R_1 \left[\frac{\sin 2\beta - 2\sqrt{\Lambda - \Lambda^2}}{2(\Lambda - \sin^2 \beta)} \right] \quad 0 \leq \beta \leq \pi \qquad (28)$$

Results for various ionopause shapes obtained by integrating (28) for different values of H/R_0 using the constant scale height model equation (25a) were provided by Spreiter et al. [1970]. Similar results using the isothermal model equation (25b) in the range $0.01 \leq \bar{H}/R_0 \leq 0.5$ are provided in Figure 2, where for comparison the constant scale height shapes for corresponding $\bar{H}/R_0$ values are also illustrated. Data from Pioneer Venus indicate that the range of interest for application to Venus appears to be $0.01 \leq \bar{H}/R_0 \leq 0.10$. They also indicate that the theory provides a good representation of the ionopause shape on the dayside but that conditions on the nightside are both more complex and variable than presently accounted for by the theory (see, for example, Brace et al. [1979], Russell et al. [1979b], or Brace et al. (this issue). To provide insight into some of the changes to be encountered in the theory, some results are also included herein in which the nightside ionopause is arbitrarily flared in and out from the calculated shapes of Figures 1 and 2.

Calculation of the Gasdynamic Flow Properties

Determination of the gasdynamic flow properties is the most difficult and time-consuming portion of the numerical solution of the foregoing equations. As sketched in Figure 3, two different methods are used in the calculations: one for the nose region, where both subsonic and supersonic flows occur, and another downstream of that region, where a more computationally economical procedure can be employed, since the flow is everywhere supersonic. In the original analysis of Spreiter et al. [1970] an inverse iteration method was used for the nose region, and the method of characteristics was employed for the remaining supersonic region. Both of these procedures are inferior to more recently developed methods and have been superseded in the current model. The nose region is treated using a new axisymmetric implicit unsteady Euler equation solver specifically developed for the present application. That procedure determines the steady state solution in the nose region by an asymptotic time-marching procedure. The downstream solution is determined by a shock capturing marching procedure which spatially advances the solution downstream as far as required by solving the steady Euler equations. Inasmuch as these methods are complex and lengthy to describe, only an outline of the procedures is provided here.

The Nose Region Solution

The nose region procedure solves the unsteady gasdynamic equations (1), (6), (7), and (13)-(16) for axisymmetric flow. The analysis commences by mapping the portion of the ionosheath bounded by the stagnation streamline, the bow wave, the ionopause, and a line through the terminator ($\beta = \pi/2$) into a rectangle. The physical boundary conditions are also transferred appropriately. Initial flow field conditions are prescribed by

using a linear variation of the flow properties between those calculated at an assumed location for the bow wave and those calculated at the ionopause, using a Newtonian pressure distribution approximation on the latter boundary. Starting with this initial flow, the unsteady equations are integrated in a time-asymptotic fashion until the steady state solution is obtained.

The basic numerical algorithm employed was developed by Beam and Warming [1976] and is second-order accurate, noniterative, and spatially factored. At the ionopause and bow shock boundaries a modification of the differencing algorithm is introduced to account for the particular features of the present application. The tangency condition at the ionopause is treated using the method of Kentzer [1970], and the sharp discontinuity approach of Thomas et al. [1972] is used at the bow wave. Any secondary shocks which may occur in the nose region are automatically determined via the shock-capturing characteristics of the algorithm.

In our earlier work [Stahara, et al., 1977] it was found that for certain ionopause shapes which have a significant amount of lateral flaring at the dawn-dusk terminator, for example, constant scale height shapes for $H/R_0 \gtrsim 0.5$, and/or cases involving low free-stream Mach numbers $M_\infty \leq 3$, the axial component of velocity at some points on the terminator plane $\beta = \pi/2$ may become subsonic. Although this has no effect on the nose region solver, the downstream solution cannot be obtained for these cases, since the marching-region solver which determines the solution downstream of this starting plane requires supersonic axial velocities in order to proceed. In the present effort this limitation has been removed by developing the capability for adding an additional portion of the flow field, located downstream of the terminator, to the blunt body solution as illustrated in Figure 4. This effectively generalizes the capability of the present procedures to treat a wide variety of ionopause shapes, including all of the shapes described by the constant scale height and constant temperature models found using (25a) and (25b), as well as to treat lower free-stream Mach numbers down to about $M_\infty = 2$.

The Downstream Region Solution

The solver for the downstream supersonic region is based on the original work of Kutler et al. [1972, 1973] and Chaussee et al. [1975] and solves for axisymmetric flow the steady state gasdynamic equations in conservation law form indicated by (1), (6), (7), and (13)-(16) with the time derivatives set to zero. Of these, (14), which represents the conservation of energy, can be integrated for the steady flow to yield the following equation for the total enthalpy:

$$h_t = h + (u^2 + v^2)/2 = const \qquad (29)$$

where $h = e + p/\rho = C_p T$ is the enthalpy per unit mass. This relation also holds in the nose region in the limit as the steady state flow solution is approached. The computational mesh defined by lines of constant X and $(R - R_b)/(R_s - R_b)$, where R_s and R_b are functions of X that describe the radial cylindrical coordinates of the bow shock
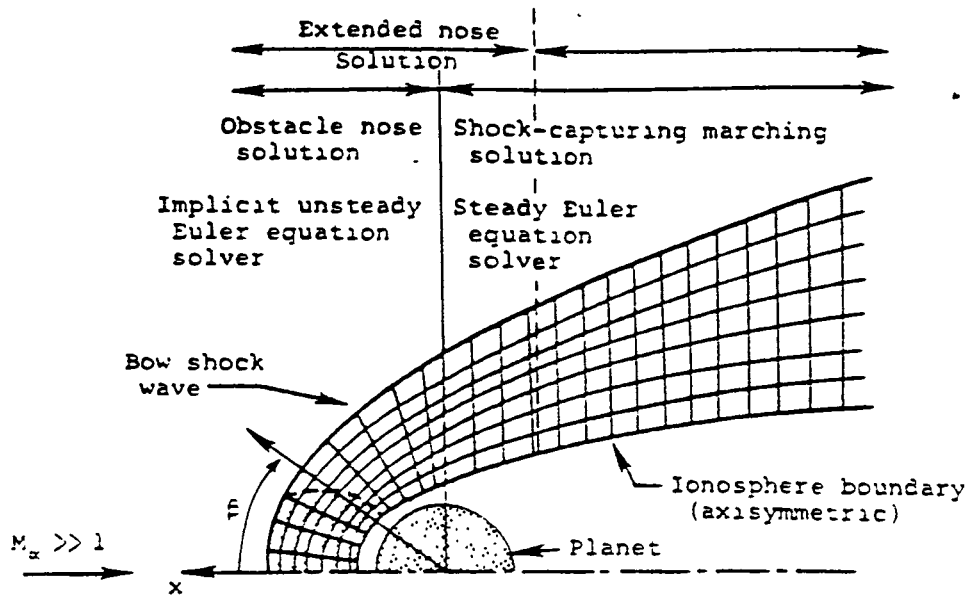
Fig. 4. Illustration of additional flow field segment to the obstacle nose-solution for determining the gasdynamic flow properties of solar wind-ionopause interactions.

wave and ionopause at the same X as the field point (X, R), is transformed into a rectangular computational grid. The gasdynamic equations are similarly transformed and integrated numerically to obtain the solution. Since only the bow shock wave is treated as a sharp discontinuity and any others that may be present are 'captured' by the difference algorithm, selection of the appropriate finite difference scheme to advance the calculation in the X direction is of prime importance. Following the analysis of Kutler et al. [1972, 1973] and Cnaussee et al. [1975] the method used is the finite difference predictor-corrector scheme of MacCormack [1969], the most efficient second-order algorithm for shock-capturing calculations.

Calculation of the Streamlines

The accurate determination of the gasdynamic streamlines is crucial, since they provide the basis for the frozen magnetic field calculation described in the following section. The streamlines are determined by integrating fluid particle trajectories through the known velocity field, since this procedure was found to be more accurate than the alternative mass flow calculation. The calculation of a particular streamline is initiated at the point where the streamline crosses the bow shock. At that point, exact values of the streamline slope dR_S/dX are given by the following relation involving M_∞, γ, and the angle ϵ_s between the free-stream direction and the tangent to the shock wave:

$$\frac{dR_S}{dX} = \frac{(2\cot\epsilon_s)(M_\infty^2\sin^2\epsilon_s - 1)}{2 + M_\infty^2(\gamma + 1 - 2\sin^2\epsilon_s)} \quad (30)$$

which is contained implicitly in both nose and marching region gasdynamic solutions. At other points, the local streamline slope is given by the ratio

$$dR_S/dX = v/u \quad (31)$$

and the streamline determination is made by step-wise integration in X using a modified third-order Euler predictor-corrector method. Bivariate linear interpolation between the flow field grid points is employed to obtain the velocity components (u, v) required at the stepwise points along the streamline.

Calculation of the Magnetic Field

With the flow properties known from the gas-dynamic calculations, the magnetic field $\underline{B}$ may be determined by integrating (4) and (10); or alternatively, the following equations may be derived from them:

$$\frac{D}{Dt}\iint_S \underline{B}\cdot d\underline{S} = 0 \qquad \frac{D}{Dt}\left(\frac{\underline{B}}{\rho}\right) = \frac{1}{\rho}(\underline{B}\cdot\nabla)\underline{v} \quad (32)$$

in which S is an arbitrary surface moving with the fluid and D/Dt is the material or substantial derivative $dD/Dt = \partial/\partial t + (\underline{v}\cdot\nabla)$. These equations are commonly interpreted as indicating the field lines move with the fluid. For the steady state in which $\partial/\partial t = 0$ and $v_n^* = v_n$, these equations lead to a straightforward calculation in which the vector distance from each point on an arbitrarily selected field line to its corresponding point on an adjacent field line in the downstream direction is determined by numerically integrating $\int \underline{v}\, dt$ over a fixed time interval Δt as indicated in Figure 5. Once the magnetic field lines are
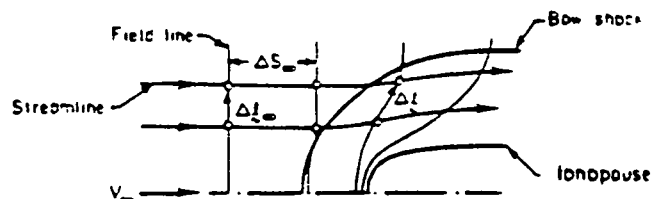

Fig. 5. Illustration of quantities used for magnetic field line calculation in the plane of magnetic symmetry.

determined, the magnetic field at any point may be calculated from the relation

$$\frac{B}{|B_\infty|} = \frac{\rho}{\rho_\infty} \frac{\Delta \ell}{|\Delta \ell_\infty|} \tag{33}$$

where $\Delta \ell$ is the vector length of a small element of a flux tube.

Such a procedure is valid generally, but its use is confined in the present calculation to only the component of the magnetic field $(B)\perp$ that lies in the plane of magnetic symmetry defined by the plane containing the axis of symmetry of the iono-pause and the magnetic field lines upstream of the bow wave and furthermore is associated with only the component of the interplanetary magnetic field that lies in the plane of magnetic symmetry and is perpendicular to v_∞. The remainder of the magnetic field calculation makes use of a decomposition due to Alksne and Webster [1970] in which the axisymmetric properties of the gasdynamic solution and the linearity of the magnetic field equations (4) and (10) or (32) are employed to derive the following relationship for the magnetic field B_p at any point P:

$$B_p = \left(\frac{B_p}{B_\infty}\right)_{||} B_{\infty||} + \left(\frac{B_p}{B}\right)_\perp B_{\infty\perp} + \hat{e}_n \left(\frac{B_p}{B_\infty}\right)_n B_{\infty n} \tag{34}$$

As illustrated in Figure 6, subscripts ", $\perp$, and n refer to contributions associated with the component $B_{\infty||}$ of B_∞ parallel to v_∞; the component $B_{\infty\perp}$ perpendicular to v_∞ in the plane that contains the point P, the center of the planet, and the vector v_∞; and the component $B_{\infty n}$ normal to the latter plane, where $\hat{e}_n$ is a unit vector in the latter direction. The unit ratios $(B_p/B_\infty)_{||}$ and $(B_p/B_\infty)_n$ can be calculated directly from the gasdynamic solution by the expressions

$$\left(\frac{B_p}{B_\infty}\right)_{||} = \frac{\rho_p v_p}{\rho_\infty |v_\infty|}, \quad \left(\frac{B_p}{B_\infty}\right)_n = \frac{R_p \rho_p}{R_{p_\infty} \rho_\infty} \tag{35}$$

where R_p is the radial cylindrical coordinate of the streamline through P, as indicated in Figure 6.

In carrying out the determination of $(B_p/B_\infty)_\perp$ using (33), values for $\Delta \ell / |\Delta \ell_\infty|$ are determined initially at the points where the streamlines and perpendicular-component field lines intersect. A generalized quadrilateral interpolation scheme followed by a fifth-order smoothing is then employed to determine the corresponding values at the computational grid points where .values for ρ/ρ_∞ are available for calculation of $(B_p/B_\infty)_\perp$. At the bow shock, exact formulas are used for the magnitude and direction of $\Delta \ell$:

$$(|\Delta \ell| / |\Delta \ell_\infty|)^2 = 1 + \cot^2\theta(1+D^2)$$
$$- 2D \times \csc\theta \times \cot\theta \times \cos(\theta-\delta) \tag{36}$$

$$\psi = \theta + \sin^{-1}\{[D \times \cot\theta$$
$$\times \sin(\theta-\delta)]/(|\Delta \ell| / |\Delta \ell_\infty|)\}$$

where

$$D^2 = 1 - 4(M_\infty^2 \sin^2\theta - 1)$$
$$\times (\gamma M_\infty^2 \sin^2\theta + 1)/[(\gamma+1)^2 M_\infty^4 \sin^2\theta]$$

$$\cot\delta = \left[(\gamma+1)M_\infty^2/\{2(M_\infty^2\sin^2\theta - 1)\} - 1\right]\tan\theta \tag{37}$$

$$\theta = \tan^{-1}\left(\frac{dR_s}{dX}\right)$$

and ψ is the angle between the free-stream direction and the $\Delta \ell$ vector.

Finally, the resultant magnetic field vector can be expressed in terms of components relative to any orthogonal (X, Y, Z) coordinate system. If the coordinate system is oriented so that the point P lies in the (X, Y) plane, the magnetic components are

$$B_X/B_\infty = [(|B|/B_\infty)_{||} \cos\phi \cos\alpha_p$$
$$+ (|B|/B_\infty)_\perp \cos\psi \sin\alpha_p)]\cos\alpha_n$$

$$B_Y/B_\infty = [(|B|/B_\infty)_{||} \sin\phi \cos\alpha_p \tag{38}$$
$$+ (|B|/B_\infty)_\perp \sin\psi \sin\alpha_p)]\cos\alpha_n$$

$$B_Z/B_\infty = (B/B_\infty)_n \sin\alpha_n$$

where ϕ is the local flow angle given by

$$\phi = \tan^{-1}\left(\frac{v}{u}\right) \tag{39}$$

and the interplanetary magnetic field angles α_p and α_n indicated in Figure 6 are defined by

$$\alpha_p = \tan^{-1}\left[\frac{B_{\infty\perp}}{B_{\infty||}}\right] = \tan^{-1}\left[\frac{B_{Y_\infty}}{B_{X_\infty}}\right] \tag{40}$$
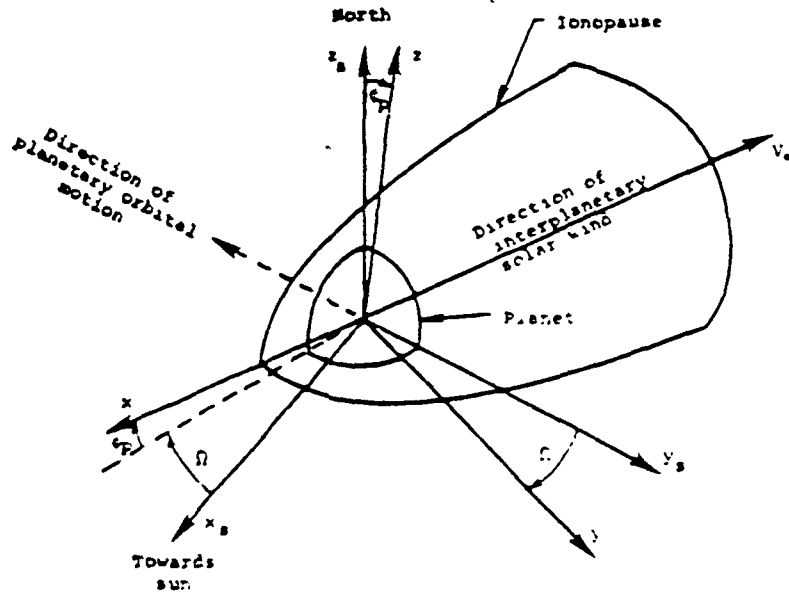

Fig. 6. Illustration of the components of the three-dimensional magnetic field.

Fig. 7. Illustration of sun-planet (x_s, y_s, z_s) and solar wind (x, y, z) coordinate systems and the azimuthal (Ω) and polar (ϵ_p) solar wind angles, both shown in a positive sense.

$$\alpha_n = \tan^{-1}\left[\frac{B_{\infty_n}}{\sqrt{(B_{\infty_{\parallel}})^2 + (B_{\infty_{\perp}})^2}}\right]$$

$$= \tan^{-1}\left[\frac{B_{Z_{\infty}}}{\sqrt{(B_{X_{\infty}})^2 + (B_{Y_{\infty}})^2}}\right] \quad (41)$$

The generalization of these results when the point P is at some arbitrary (X, Y, Z) point not in the (X, Y) plane are provided below in the spacecraft trajectory section.

Calculation of the Contour Lines

In order to provide convenient summary information of the detailed plasma and magnetic field properties determined by the above model, contour and field line maps are determined for the important field properties. Contours are calculated for nondimensionalized velocity $|\underline{v}|/v_\infty$, density ρ/ρ_∞, and magnetic field components $(|\underline{B}|/B_\infty)_{\parallel}$, $(|\underline{B}|/B_\infty)_{\perp}$ and $(B/B_\infty)_n$. Details of these calculations are provided by Stahara et al. [1980]. Since the temperature is a function of $|\underline{v}|/v_\infty$ only for a specified M_∞ and γ, i.e.,

$$T/T_\infty = 1 + \left(\frac{\gamma-1}{2}\right) M_\infty^2 \left[1 - \left(\frac{|\underline{v}|}{v_\infty}\right)^2\right] \quad (42)$$

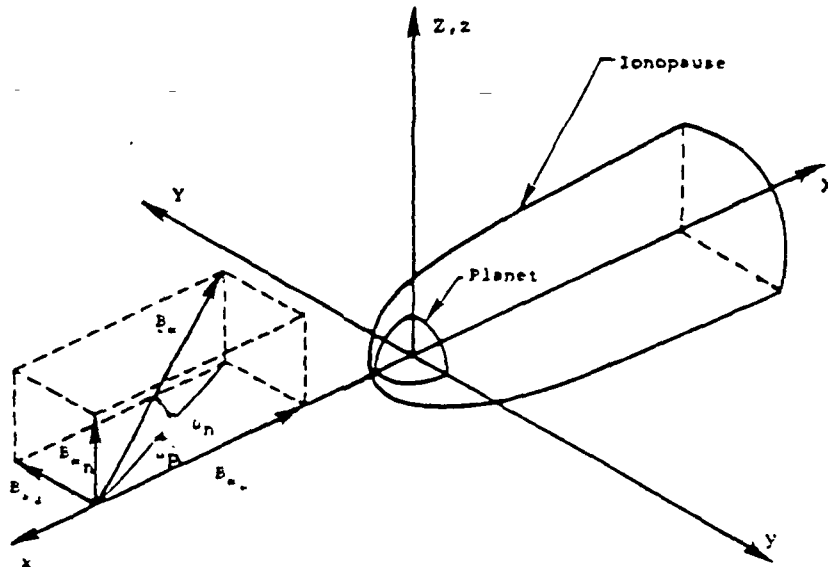
Fig. 8. Illustration of solar wind (x, y, z) and (X, Y, Z) coordinate systems and the interplanetary magnetic field and magnetic field angles (α_p, α_n).

M=8.0   γ=1.67   H̄/R.=0.10
STREAMLINES

(a)

M=8.0   γ=1.67   H̄/R.=0.10
VELOCITY, |v|/v_

(b)
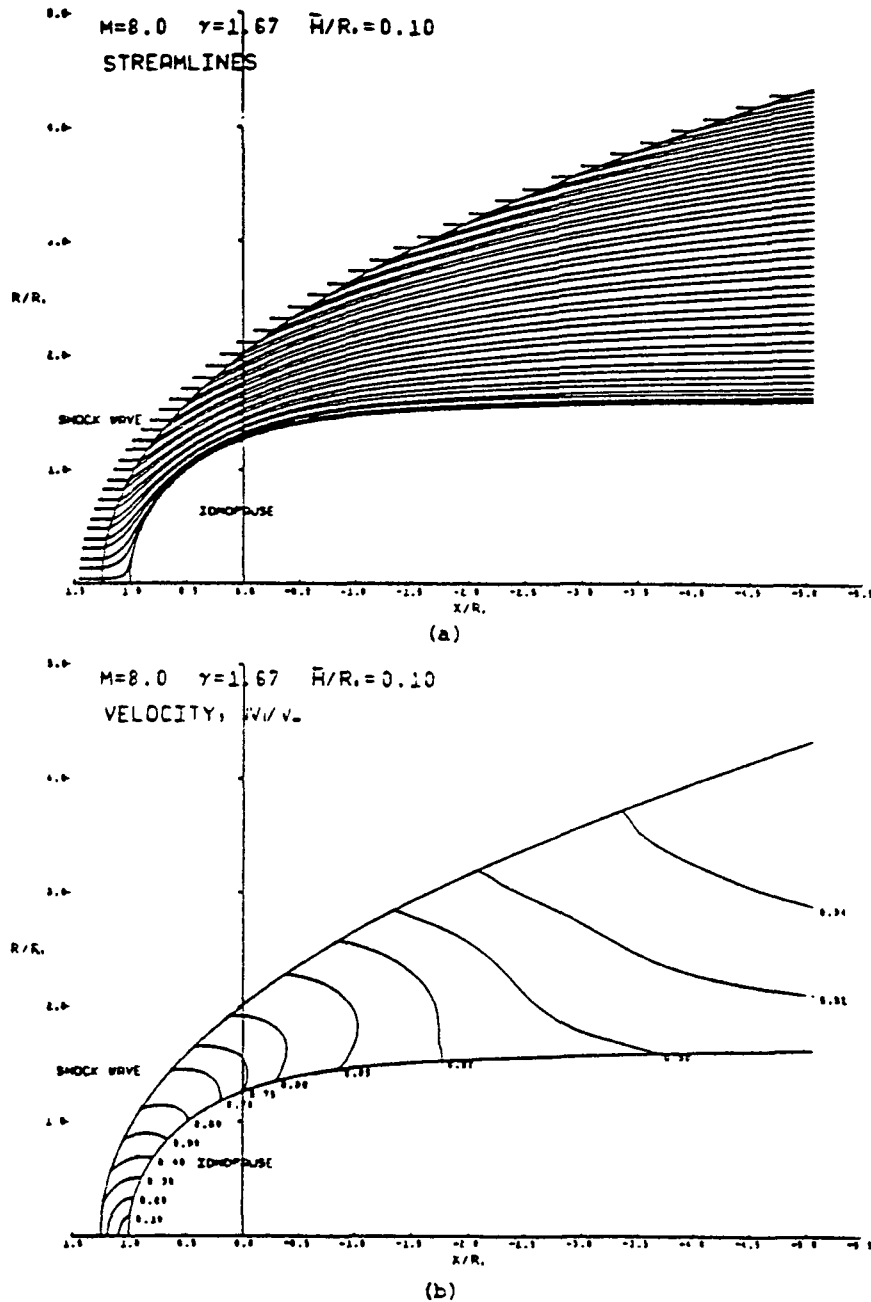
Fig. 9. Calculated ionopause and bow shock locations and ionosheath properties for $M_\infty = 8.0$, $\gamma = 5/3$, $\bar{H}/R_0 = 0.10$, and $\underline{B}_\infty$ either parallel or perpendicular to $\underline{v}_\infty$. (a) Streamline map. (b) Velocity map. (c) Density map. (d) Temperature map. (e) Parallel magnetic field map. (f) Perpendicular magnetic field map.
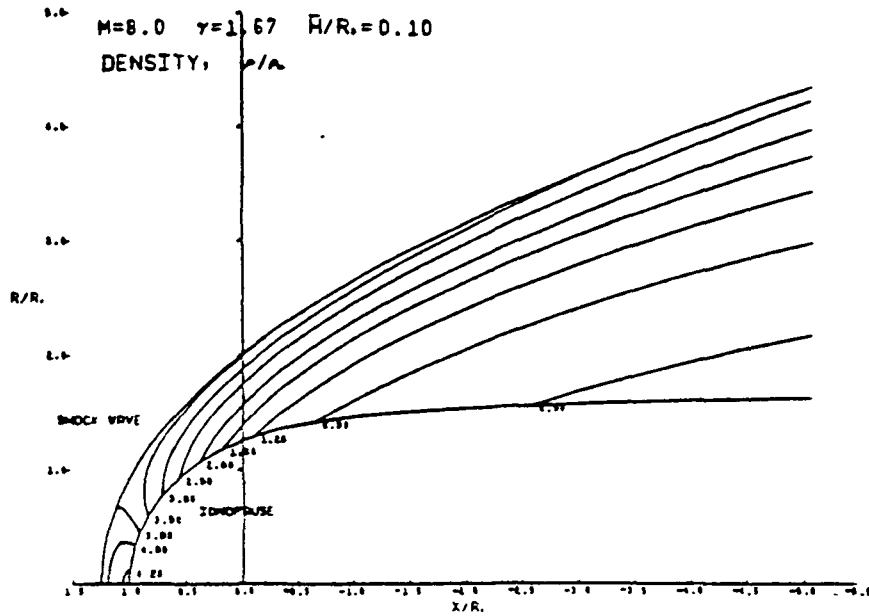
velocity contours may also be considered as temperature contours with only a relabeling required.

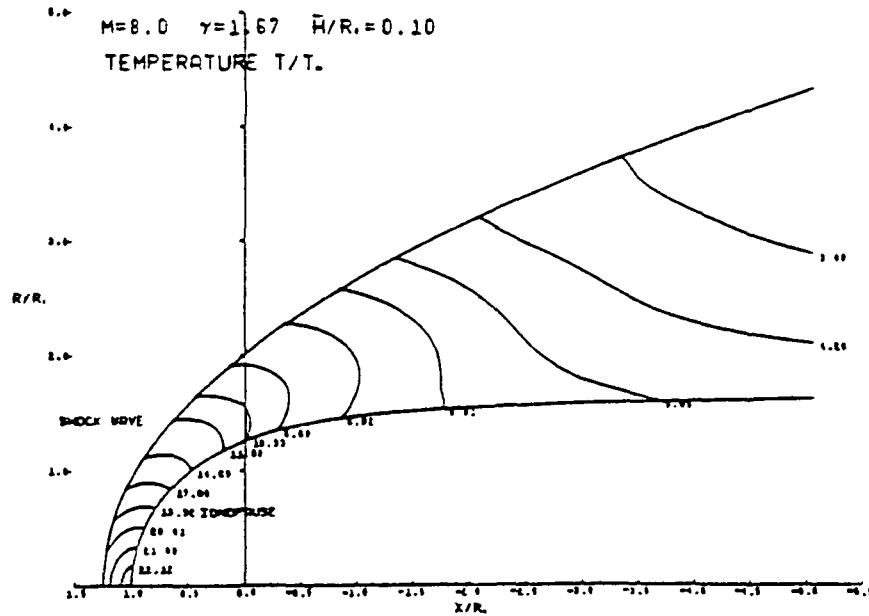### Solar Ecliptic/Solar Wind Coordinate Transformation

To compare results of the present calculations with observational data, it is necessary to consider the appropriate transformations between the spacecraft and solar wind coordinate systems. Part of the data required as input to the theoretical model consists of oncoming interplanetary values of solar wind temperature, density, and velocity and magnetic field vector components. These are usually reported in a sun-planet or

solar ecliptic reference frame, whereas the natural coordinate system for the theoretical model is one which aligns the axial direction with the oncoming solar wind, since the gasdynamic calculation is assumed to be axisymmetric about this direction. Thus the interplanetary input data must be transformed to the solar wind system to initiate the theoretical determination. Once the gasdynamic and magnetic field calculations in the solar wind system are complete, those results must then be transformed back to the sun-planet system to allow direct comparison with the spacecraft data obtained as a function of time along its trajectory.

For the sun-planet system (x_s, y_s, z_s) the

$M=8.0$ $\gamma=1.67$ $\bar{H}/R_*=0.10$
DENSITY, ρ/ρ_*

R/R.

SHOCK WAVE

IONOPAUSE

X/R.

(c)

$M=8.0$ $\gamma=1.67$ $\bar{H}/R_*=0.10$
TEMPERATURE T/T_*

R/R.

SHOCK WAVE

IONOPAUSE

X/R.

(d)

Fig. 9.   (continued)

origin is placed at the planetary center, the x_s axis is directed toward the sun, the y_s axis is directed opposite to the planetary orbital motion, and the z_s axis is orthogonally northward. The direction of the oncoming solar wind is such that the azimuthal angle, including aberration effects due to planetary motion, of the solar wind velocity vector in the planetary orbital plane is Ω, and the out-of-orbital plane polar angle is ϕ_p. The positive sense of the azimuthal angle is for west-to-east flow, and that of the polar angle is for north-to-south flow, as indicated in Figure 7. Also illustrated is the solar wind (x, y, z) coordinate system defined by (Ω, ϕ_p). This system is somewhat inconvenient because the direction of solar wind flow is in the negative x direction; therefore the internal gasdynamic and magnetic field calculations are performed in the (X, Y, Z) system illustrated in Figure 8.
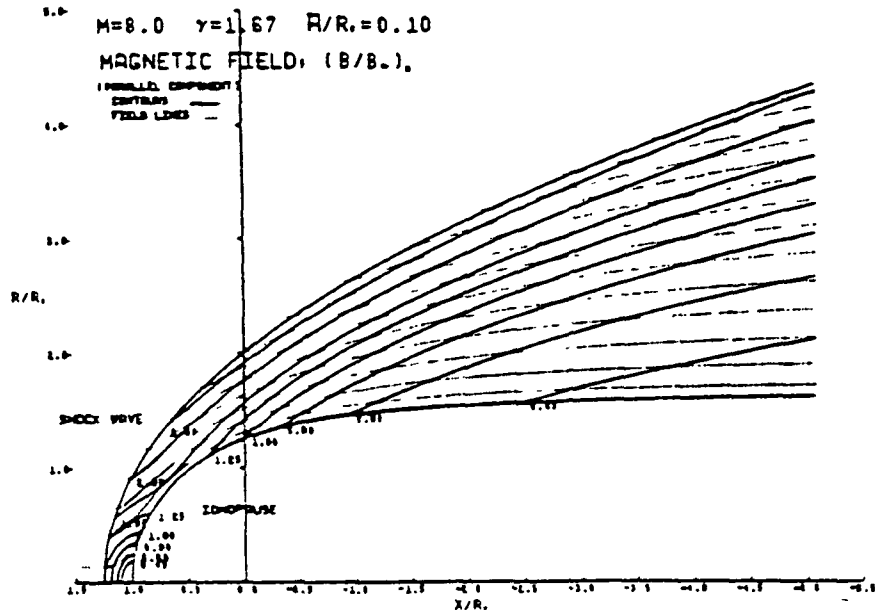
The coordinates and vector transformations from

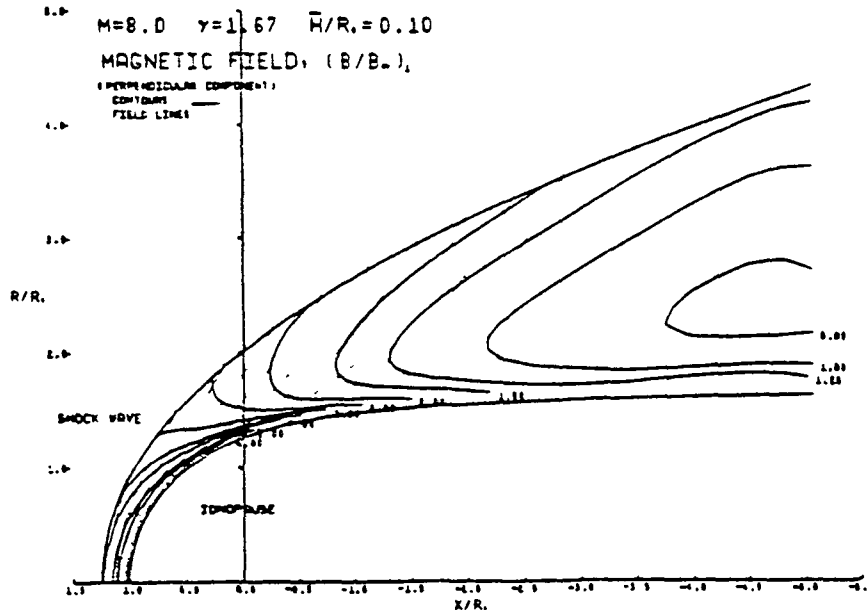the ecliptic sun-planet (x_s, y_s, z_s) system to the (X, Y, Z) solar wind system are given by

$$\begin{pmatrix} Q_X \\ Q_Y \\ Q_Z \end{pmatrix} = \begin{pmatrix} -\cos\Omega\cos\phi_p & -\sin\Omega\cos\phi_p & \sin\phi_p \\ \sin\Omega & -\cos\Omega & 0 \\ -\cos\Omega\sin\phi_p & \sin\Omega\sin\phi_p & \cos\phi_p \end{pmatrix} \begin{pmatrix} Q_{x_s} \\ Q_{y_s} \\ Q_{z_s} \end{pmatrix} \quad (43)$$

where (Q_X, Q_Y, Q_Z) represents the Cartesian components of any vector referred to the (X, Y, Z) system, and $(Q_{x_s}, Q_{y_s}, Q_{z_s})$ represents the corresponding vector in the (x_s, y_s, z_s) system. Thus for a transformation of coordinates,

$$(Q_X, Q_Y, Q_Z) = (X, Y, Z)$$
$$(Q_{x_s}, Q_{y_s}, Q_{z_s}) = (x_s, y_s, z_s) \quad (44)$$

M=8.0 γ=1.67 R/R.=0.10
MAGNETIC FIELD, (B/B.).

(e)

M=8.0 γ=1.67 H̄/R.=0.10
MAGNETIC FIELD, (B/B.).

(f)

Fig. 9. (continued)

while for a vector transformation of, say, the magnetic field,

$$(Q_x, Q_y, Q_z) = (B_x, B_y, B_z)$$

$$(Q_{x_s}, Q_{y_s}, Q_{z_s}) = (B_{x_s}, B_{y_s}, B_{z_s})$$

(45)

The inverse transformation from the solar wind to the sun-planet system is given by

$$
\begin{pmatrix} Q_{x_s} \\ Q_{y_s} \\ Q_{z_s} \end{pmatrix} =
\begin{pmatrix}
-\cos\Omega\cos\phi_p & \sin\Omega & -\cos\Omega\sin\phi_p \\
\sin\Omega\cos\phi_p & -\cos\Omega & \sin\Omega\sin\phi_p \\
\sin\phi_p & 0 & \cos\phi_p
\end{pmatrix}
\begin{pmatrix} Q_X \\ Q_Y \\ Q_Z \end{pmatrix}
$$

(46)

Properties Along a Spacecraft Trajectory

One of the primary aims of the present effort has been to develop the capability to determine plasma and magnetic field properties, as predicted by the theoretical model, at locations specified along an arbitrary spacecraft trajectory, and in such a form as to enable comparisons to be made directly with actual spacecraft data. To accomplish this, the following procedure has been developed and implemented in the current model. First, from the known oncoming interplanetary conditions provided in a sun-planet reference frame, the azimuthal and polar solar wind angles (Ω, ϕ_p) are employed in (43) to establish both the location (X_p, Y_p, Z_p) of the trajectory point and the interplanetary magnetic field components $(B_{X_\infty}, B_{Y_\infty}, B_{Z_\infty})$ in the solar wind (X, Y, Z) frame.
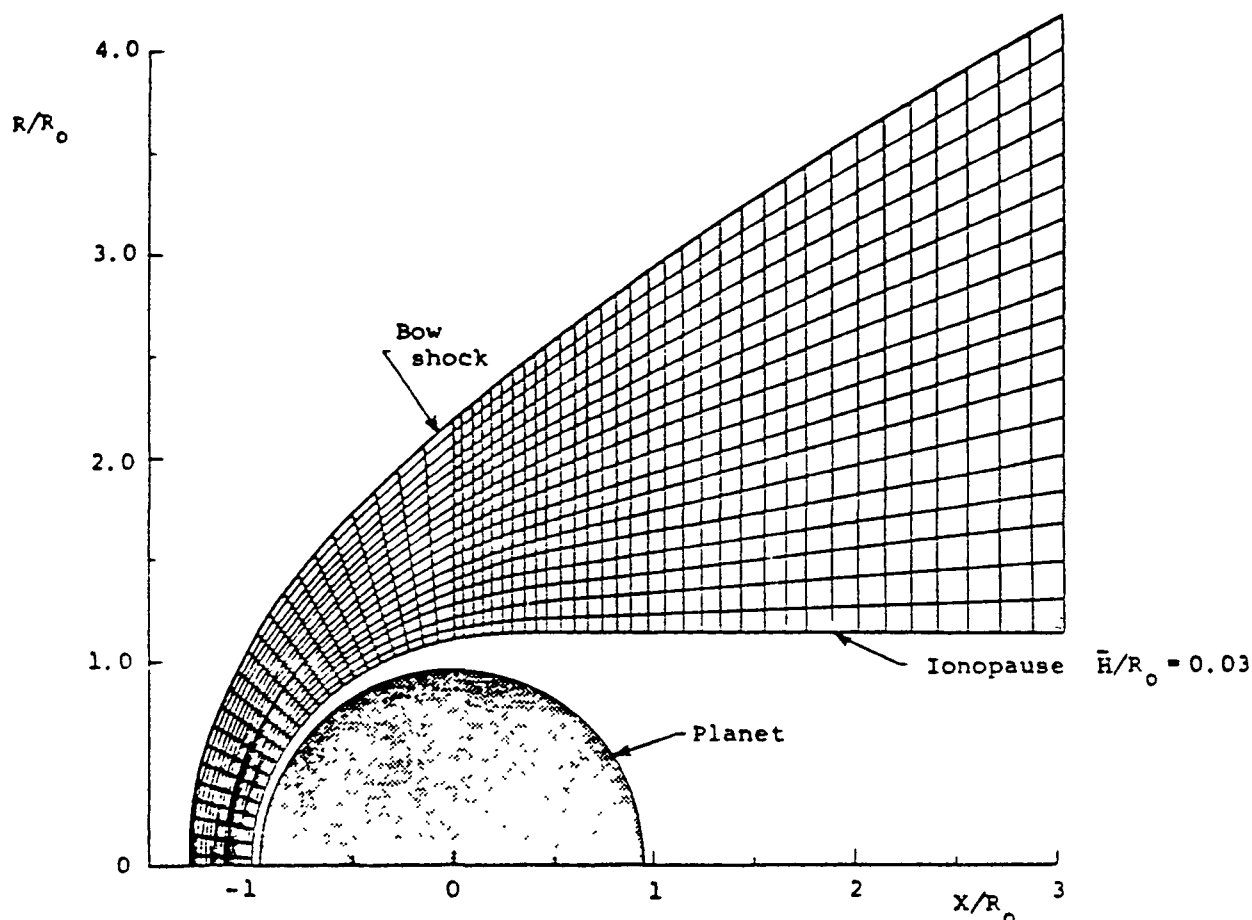
Fig. 10. Illustration of typical flow field grid density for gasdynamic solution; $M_\infty = 3.0$, $\gamma = 5/3$.

In the next step, in which the axisymmetric gasdynamic and unit magnetic field calculations are carried out, it is convenient to take advantage of the axisymmetric property of the gasdynamic flow and introduce still another coordinate system (X, y', z') related to the (X, Y, Z) system by a rotation about the X axis by an angle θ such that the y' axis passes through the point P. This rotation defines a new coordinate system (x', y', z'), where

$$\begin{bmatrix} x' \\ y' \\ z' \end{bmatrix} = \begin{bmatrix} 1 & 0 & 0 \\ 0 & \cos\theta & \sin\theta \\ 0 & -\sin\theta & \cos\theta \end{bmatrix} \begin{bmatrix} X \\ Y \\ Z \end{bmatrix} \qquad (47)$$

in which

$$\theta = \tan^{-1}\left[\frac{Z_p}{Y_p}\right] \qquad (48)$$

and

$$x' = X_p$$

$$y' = \sqrt{Y_p^2 + Z_p^2} \qquad (49)$$

$$z' = 0$$

Thus the (x', y') plane which contains the X axis and the arbitrary point P corresponds directly to the plane $(X, R) = (X_p, \sqrt{Y_p^2 + Z_p^2})$, in which the axisymmetric gasdynamic flow properties are calculated. In particular, the velocity magnitude v, density ρ, and flow angle ϕ at the point P are found by bilinear interpolation through the (X, R) flow field grid. The vector velocity in the (X, Y, Z) system is then given by the transformation

$$\begin{bmatrix} v_X \\ v_Y \\ v_Z \end{bmatrix} = \begin{bmatrix} 1 & 0 & 0 \\ 0 & \cos\theta & -\sin\theta \\ 0 & \sin\theta & \cos\theta \end{bmatrix} \begin{bmatrix} v\cos\phi \\ v\sin\phi \\ 0 \end{bmatrix} \qquad (50)$$

and then in the solar ecliptic system by the transformation indicated by

$$\begin{bmatrix} v_{x_s} \\ v_{y_s} \\ v_{z_x} \end{bmatrix} = \begin{bmatrix} -\cos\Omega\cos\phi_p & \sin\Omega & -\cos\Omega\sin\phi_p \\ \sin\Omega\cos\phi_p & -\cos\Omega & \sin\Omega\sin\phi_p \\ \sin\phi_p & 0 & \cos\phi_p \end{bmatrix} \begin{bmatrix} v_X \\ v_Y \\ v_Z \end{bmatrix} \qquad (51)$$

Calculation of the magnetic field at an arbitrary point is somewhat more complicated, since these components are dependent upon the orientation of the incident interplanetary mag-
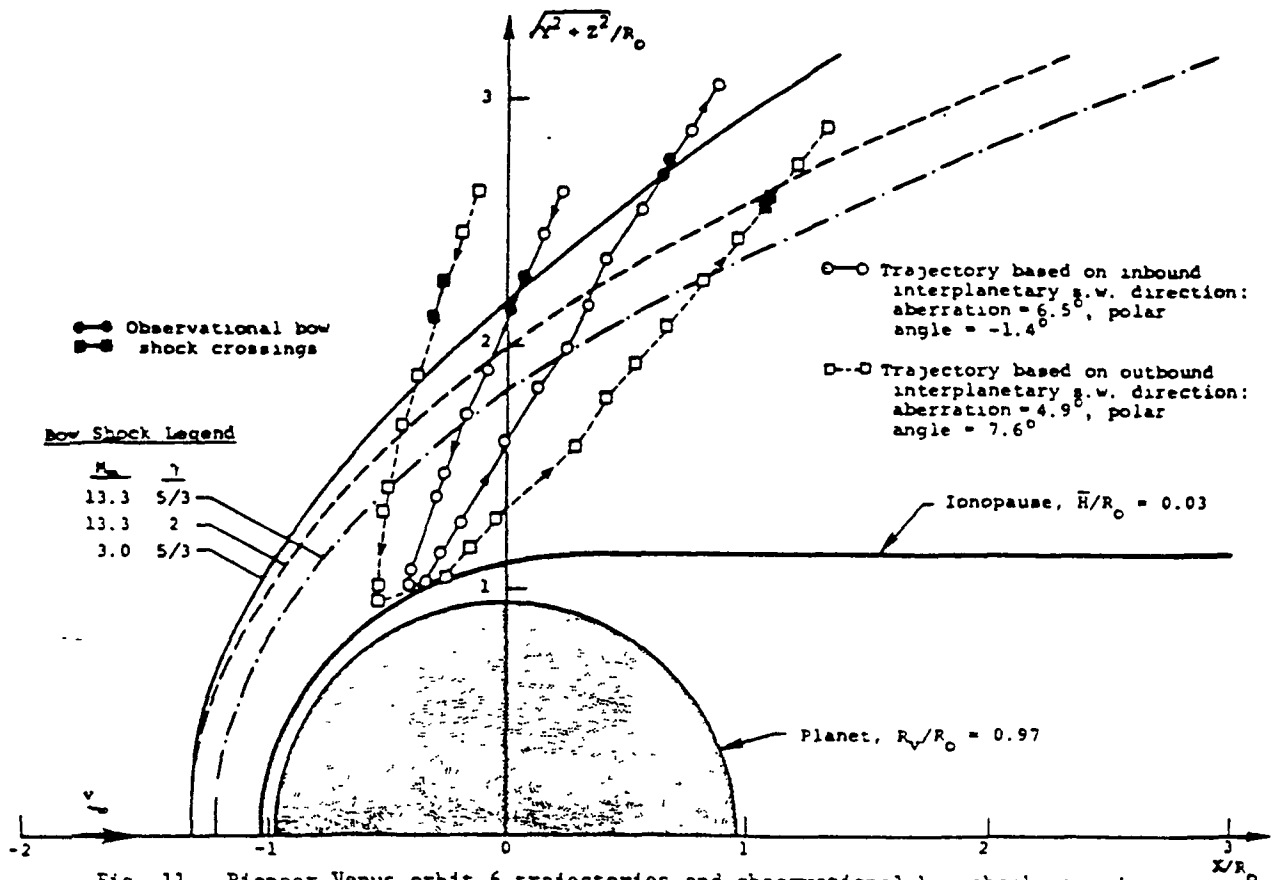
Fig. 11. Pioneer Venus orbit 6 trajectories and observational bow shock crossings as viewed in solar wind coordinates based on inbound and outbound interplanetary solar wind directions; also, various bow shock shapes for different interplanetary solar wind conditions.
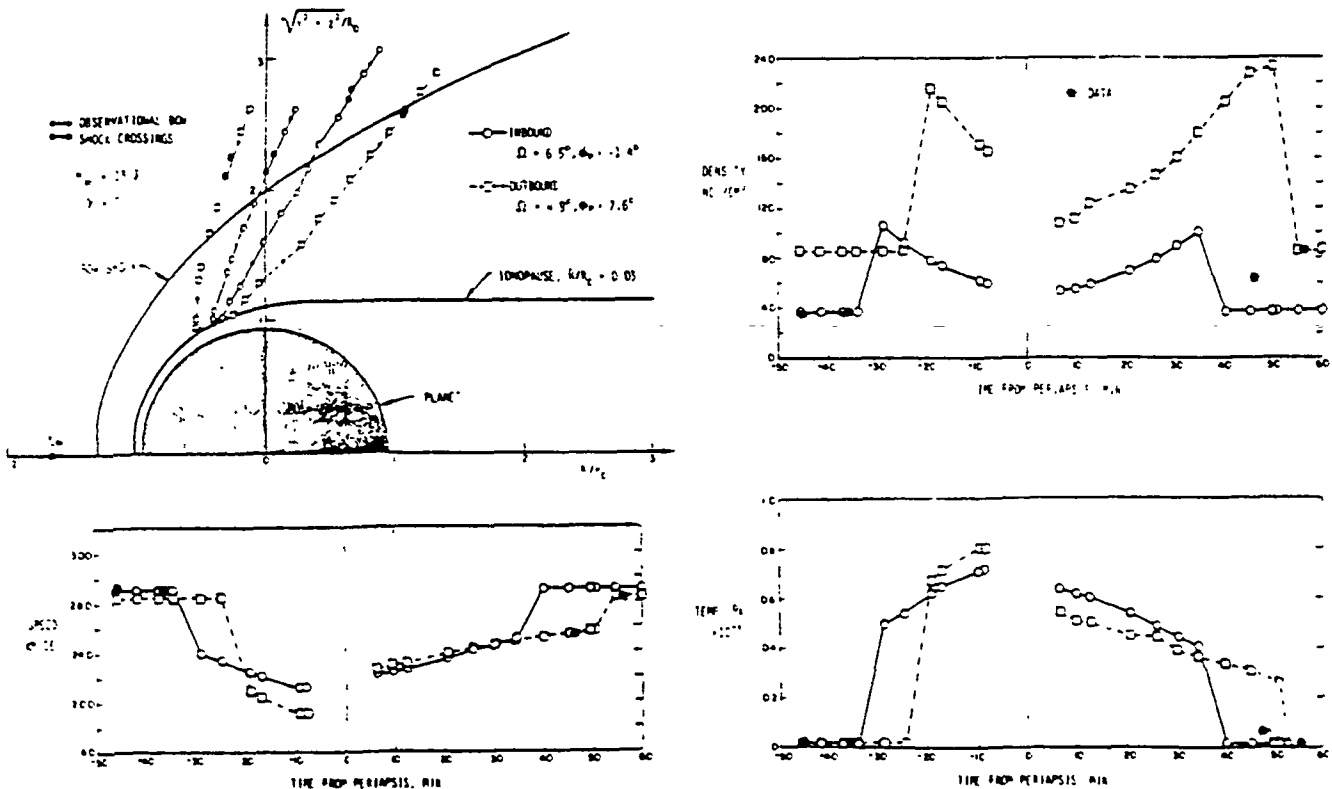

Fig. 12. Comparison of observed (OPA) and theoretical time histories of ionosheath plasma properties for Pioneer Venus orbit 6 based on inbound and outbound interplanetary solar wind conditions using a gasdynamic solution for $M_\infty = 13.3$, $\gamma = 2.0$.
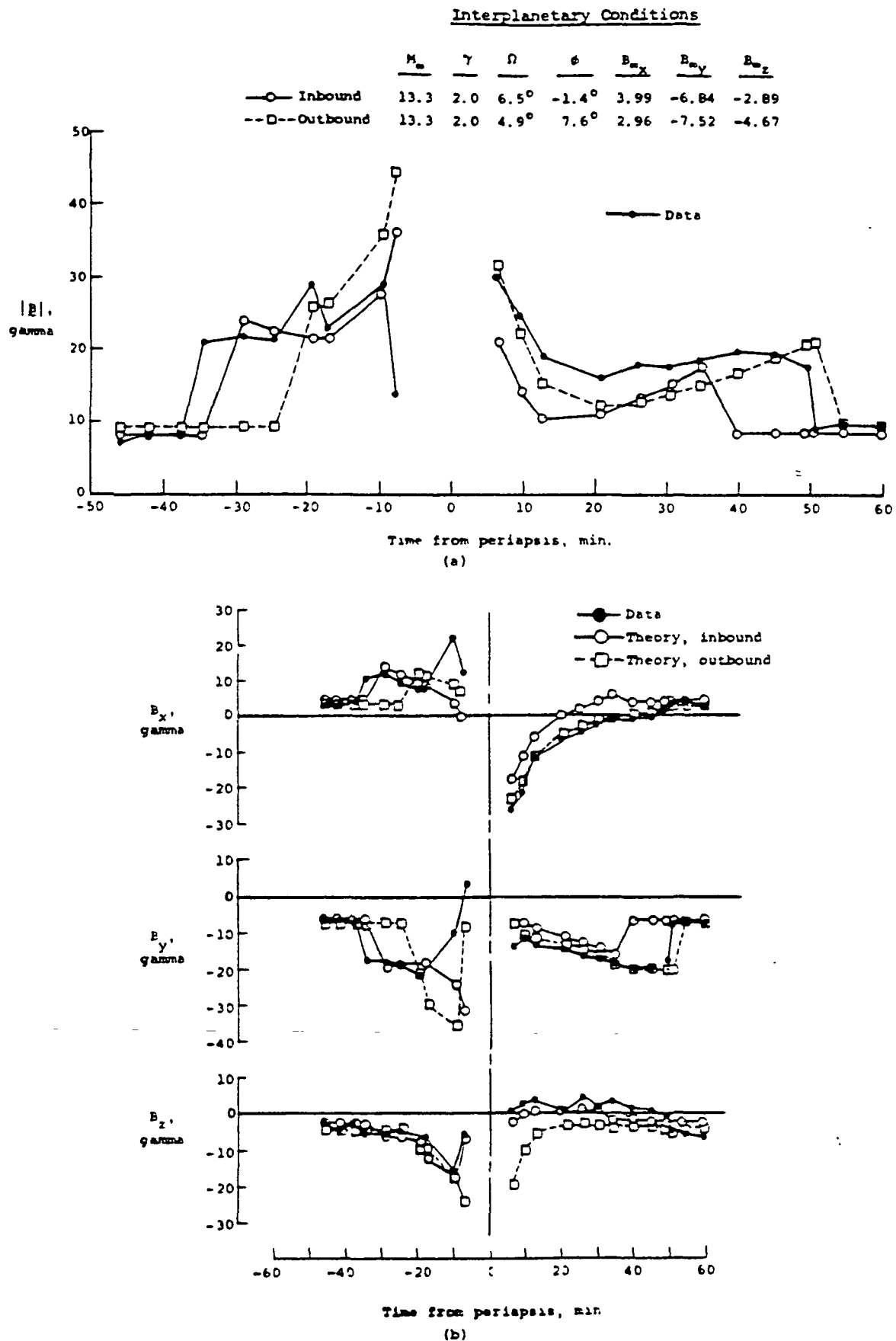
Interplanetary Conditions

	M_∞	γ	Ω	ϕ	$B_{\infty x}$	$B_{\infty y}$	$B_{\infty z}$
—O— Inbound	13.3	2.0	6.5°	-1.4°	3.99	-6.84	-2.89
--□--Outbound	13.3	2.0	4.9°	7.6°	2.96	-7.52	-4.67

Fig. 13. Comparison of observed (OMAG) and theoretical time histories for the magnitude of the magnetic field for Pioneer Venus orbit 6 based on inbound and outbound interplanetary conditions using gasdynamic solution for M_∞ = 13.3, γ = 2.0. (a) Magnetic field magnitude. (b) Magnetic field components.
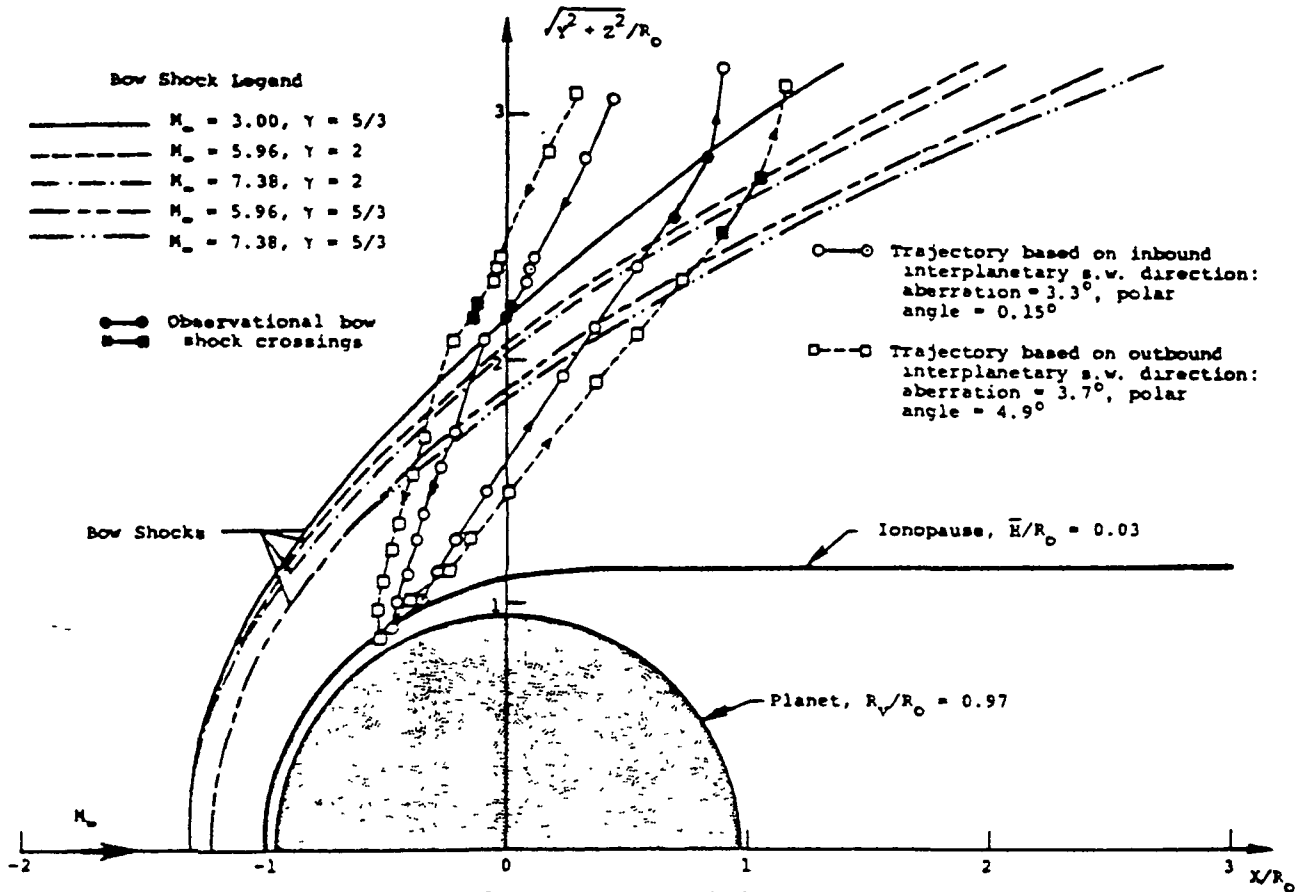
Fig. 14. Pioneer Venus orbit 3 trajectories and observational bow shock crossings as viewed in solar wind coordinates based on inbound and outbound interplanetary solar wind directions; also, various bow shock shapes for different interplanetary solar wind conditions.

netic field. With the known (B_X, B_Y, B_Z) components the corresponding components $(B'_{x_\infty}, B'_{y_\infty}, B'_{z_\infty})$ in the rotated system are given by

$$\begin{pmatrix} B'_{x_\infty} \\ B'_{y_\infty} \\ B'_{z_\infty} \end{pmatrix} = \begin{pmatrix} 1 & 0 & 0 \\ 0 & \cos\theta & \sin\theta \\ 0 & -\sin\theta & \cos\theta \end{pmatrix} \begin{pmatrix} B_{X_\infty} \\ B_{Y_\infty} \\ B_{Z_\infty} \end{pmatrix} \quad (52)$$

In this reference frame the parallel, perpendicular, and normal interplanetary components are identified as

$$B_{\infty_{\shortparallel}} = B'_{x_\infty}$$

$$B_{\infty_\perp} = B'_{y_\infty} \quad (53)$$

$$B_{\infty_n} = B'_{z_\infty}$$

The magnetic field angles α'_p and α'_n in the rotated system are given by

$$\alpha'_p = \tan^{-1}\left[\frac{B_{\infty_\perp}}{B_{\infty_{\shortparallel}}}\right] = \tan^{-1}\left[\frac{B'_{y_\infty}}{B'_{x_\infty}}\right] \quad (54)$$

$$\alpha'_n = \tan^{-1}\left[\frac{B_{\infty_n}}{\sqrt{(B_{\infty_{\shortparallel}})^2 + (B_{\infty_\perp})^2}}\right]$$

$$= \tan^{-1}\left[\frac{B'_{z_\infty}}{\sqrt{(B'_{x_\infty}) + (B'_{y_\infty})^2}}\right] \quad (55)$$

The magnetic angle ψ associated with the incident perpendicular component and the unit magnetic field ratios $(|B|/B_\infty)_{\shortparallel}$, $(|B|/B_\infty)_\perp$, and $(B/B_\infty)_n$ in the rotated system are next determined by bilinear interpolation through the flow field grid. Then the magnetic field components (B'_X, B'_Y, B'_Z) in the rotated system are calculated from

$$B'_X = \cos\alpha'_n\left(\cos\zeta \cdot \cos\alpha'_p \cdot \left|\frac{B}{B_\infty}\right|_{\shortparallel}\right.$$
$$\left. + \cos\psi \cdot \sin\alpha'_p \cdot \left|\frac{B}{B_\infty}\right|_\perp\right) \cdot B_\infty \quad (56)$$

$$B'_y = \cos\alpha'_n\left(\sin\zeta \cdot \cos\alpha'_p \cdot \left|\frac{B}{B_\infty}\right|\right.$$
$$\left. + \sin\psi \cdot \sin\alpha'_p \cdot \left|\frac{B}{B_\infty}\right|_\perp\right) \cdot B_\infty \quad (57)$$
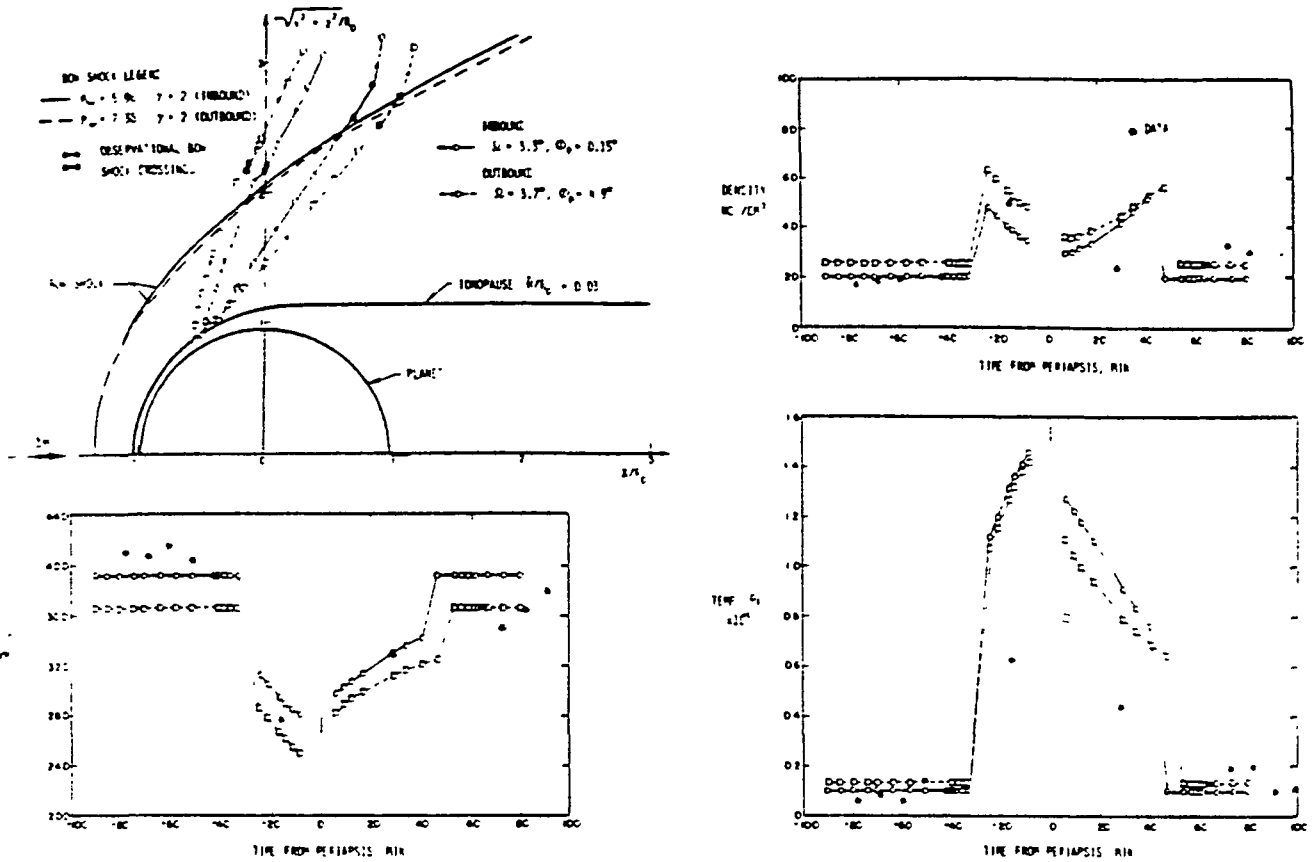
Fig. 15. Comparison of observed and theoretical time histories of ionosheath plasma properties for Pioneer Venus orbit 3 based on inbound and outbound interplanetary solar wind conditions.

$$B_z' = \sin\alpha_n' \cdot \left(\frac{B}{B_\infty}\right)_n \cdot B_\infty \tag{58}$$

The magnetic field components in the solar wind (X, Y, Z) system are then determined from the rotational transformation

$$\begin{pmatrix} B_X \\ B_Y \\ B_Z \end{pmatrix} = \begin{pmatrix} 1 & 0 & 0 \\ 0 & \cos\theta & -\sin\theta \\ 0 & \sin\theta & \cos\theta \end{pmatrix} \begin{pmatrix} B_X' \\ B_Y' \\ B_Z' \end{pmatrix} \tag{59}$$

and finally in the sun-planet system from

$$\begin{pmatrix} B_{X_s} \\ B_{Y_s} \\ B_{Z_s} \end{pmatrix} = \begin{pmatrix} -\cos\Omega\cos\phi_p & \sin\Omega & -\cos\Omega\sin\phi_p \\ \sin\Omega\cos\phi_p & -\cos\Omega & \sin\Omega\sin\phi_p \\ \sin\phi_p & 0 & \cos\phi_p \end{pmatrix} \begin{pmatrix} B_X \\ B_Y \\ B_Z \end{pmatrix} \tag{60}$$

Results

Using the computational procedures described above, a large number of solutions have been calculated for a wide variety of conditions representative of those that might be experienced at Venus. A sample of these results is illustrated in Figure 9 for $M_\infty = 8$, $\gamma = 5/3$, and $\bar{B}/R_0 = 0.10$

with B_∞ either parallel or perpendicular to v_∞. These and similar determinations for the following 35 other sets of conditions have been included in a catalog of results available from Stahara et al. [1980]:

$$M_\infty = (2.0, \ 3.0, \ 5.0, \ 8.0, \ 12.0, \ 25.0)$$

$$B/R_0 = (0.01, \ 0.10, \ 0.25)$$

$$\bar{B}/R_0 = (0.10, \ 0.20, \ 0.25)$$

Also included in that reference are a few results for conditions well outside the range likely to be encountered at Venus but that are useful because they illustrate the extended capability of the present procedures.

Verification of the new procedures has been done in a variety of ways in addition to comparison with previous results for sets of conditions for which both sets of results could be determined. These include consideration of a variety of special test cases in which the location in the flow field and the incident interplanetary magnetic field orientation were systematically changed so as to produce both symmetric and antisymmetric changes in the resultant ionosheath magnetic field, as well as to reverse the roles of the perpendicular and normal components. All of these various permutations of the magnetic field calculations were successfully verified.

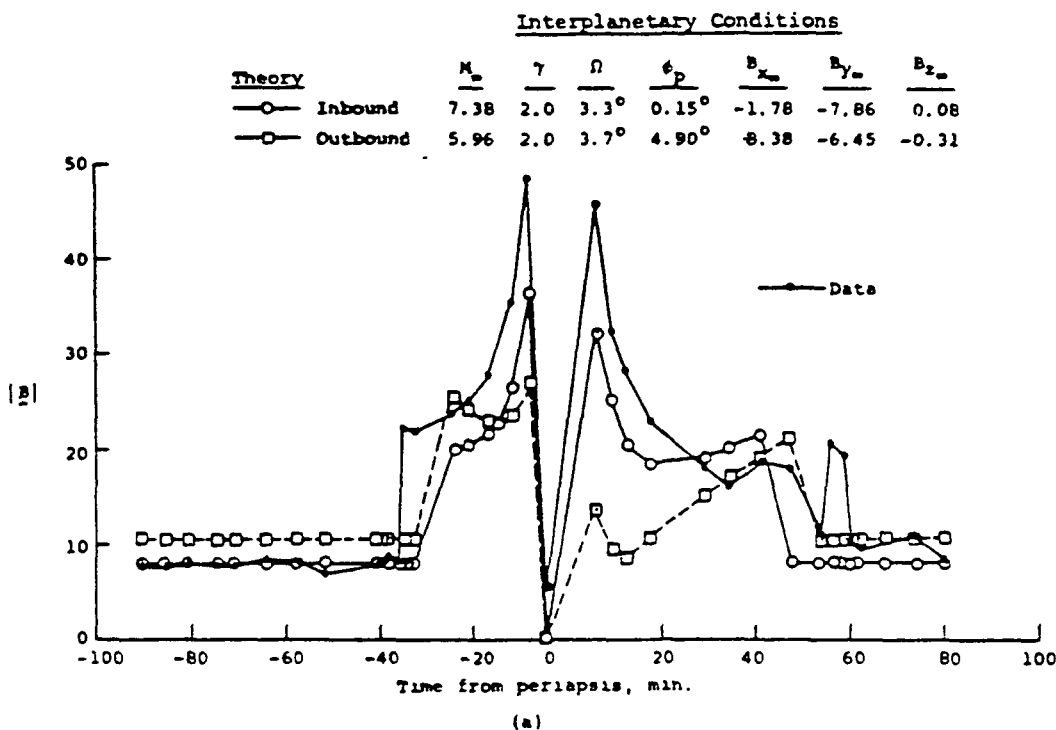The final and ultimate check of the theoretical

Fig. 16. Comparison of observed (OMAG) and theoretical time histories for the magnetic field for Pioneer Venus orbit 3 based on inbound and outbound interplanetary solar wind conditions using gasdynamic solutions M_∞ = 7.38, Υ = 2.0 for inbound and M_∞ = 5.96, Υ = 2.0 for outbound calculations. (a) Magnetic field magnitudes. (b) Magnetic field components.

model and numerical procedures lies in the comparison of the predicted results with data actually measured by a spacecraft. Attention is now turned, accordingly, to the results of preliminary comparisons with data obtained from orbits 3 and 6 of the Pioneer-Venus orbiter. These orbits were selected in conjunction with the experimenters on the basis of completeness of data and apparent steadiness of conditions during the time of interest for the study.

To perform calculations suitable for comparison with data from a particular orbit, it is necessary to specify appropriate conditions corresponding to those actually measured in both the ionosphere and in the oncoming interplanetary solar wind plasma. On the basis of data from the orbiter retarding potential analyzer (OPRA) indicating the ionospheric scale height to be approximately 200 km for orbits 3 and 6, a value of 0.03 was selected for H/R_0 or $\bar{H}/R_0$. For such small values the two ionospheric pressure models indicated by (20) and (21) yield essentially the same obstacle shape, as can be seen from Figure 2. With regard to oncoming interplanetary conditions it is required that values for the solar wind bulk velocity v_∞, density ρ_∞, temperature T_∞, and magnetic field B_∞ be specified. The first three are provided by the orbiter plasma analyzer (OPA), and the magnetic field is given by the orbiter flux gate magnetometer (OMAG). OPA provides either ion or electron data, but not both simultaneously. For orbits 3 and 6, ion measurements were available and have been employed. Data on the oncoming direction of the solar wind, as given in terms of the angles (Ω, ϕ_p), define the coordinate rotations required to align the gasdynamic calculation in the

free-stream solar wind direction; while information of solar wind speed, density, and temperature serve to define the free-stream gasdynamic Mach number M_∞.

Although it is known the temperatures of the ions and electrons may be substantially different in the solar wind plasma (a ratio T_e/T_i - 4 is often representative), they are assumed to be equal (T_e/T_i = 1) in the derivation of the single-fluid magnetohydrodynamic equations upon which the present calculations are based. Now that the theory has been put into a more readily usable form and more extensive data on the temperature of both electrons and ions are becoming available for comparative studies, steps should be taken to improve understanding of the relation between single- and multiple-component plasma theories for space plasma flows, and the calculative procedures refined as appropriate.

With this information the detailed gasdynamic and unit magnetic field calculations in the ionosheath region can be carried out. To provide an idea of the detail obtained by the present computational procedures, Figure 10 displays the flow field grid for one of the gasdynamic solutions used in the comparisons. Values for each of the plasma properties v/v_∞, ρ/ρ_∞, T/T_∞, $(B/B_\infty)_\shortparallel$, $(B/B_\infty)_\perp$ and $(B/B_\infty)_n$ are determined at each intersection of the grid lines, including the bow shock, stagnation streamline, and ionopause boundary. The final output of the calculation consists of these quantities and the coordinates of the bow shock and ionopause, expressed either in tabular form or as plotted contours, and also as time histories along a specified trajectory.

For comparisons with spacecraft data the time-
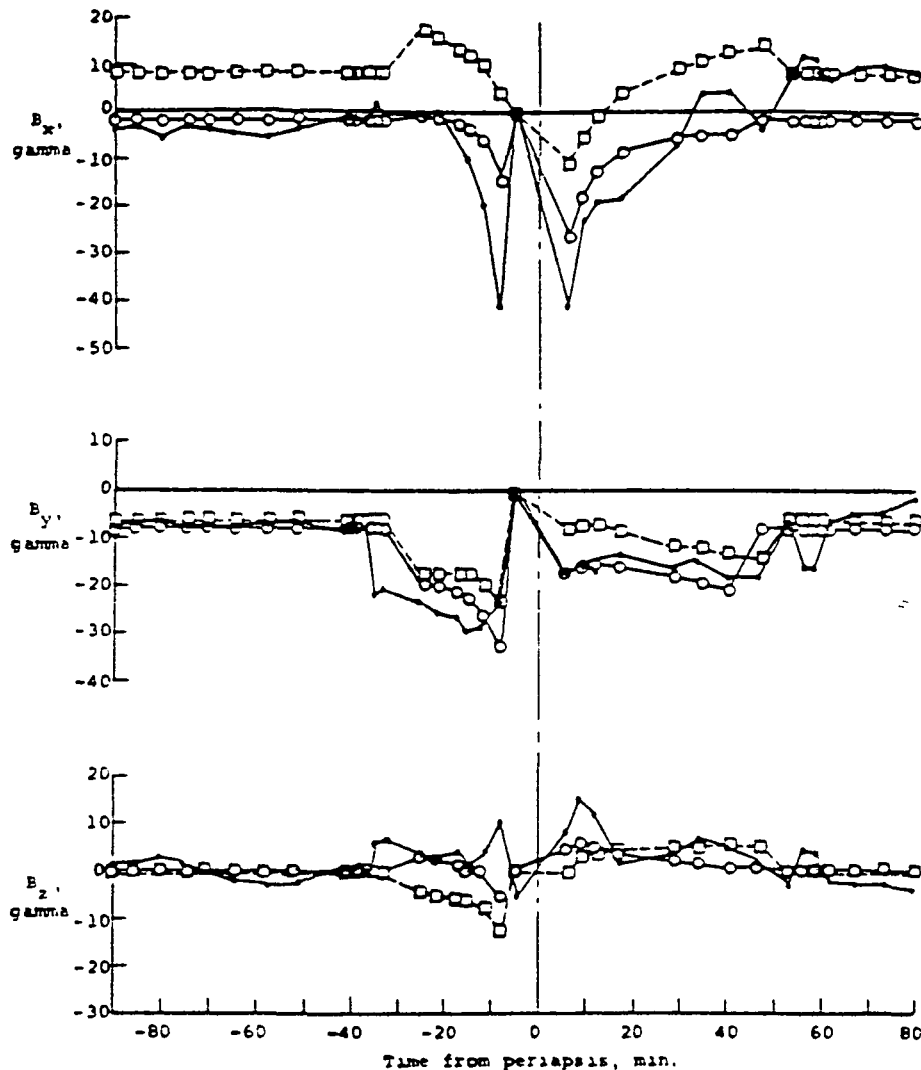
Fig. 16. (continued)

history predictions are the most convenient. For the theoretical predictions, two sets of results are usually generated on the basis of the last/ first interplanetary solar wind properties measured before/after bow shock inbound/outbound crossing.

Figure 11 displays some overall flow field results for orbit 6. Indicated are bow shock locations for the three combinations of M_∞ and plasma specific heat ratio γ, i.e., (M_∞, γ) = (13.3, 5/3), (13.3, 2), (3.0, 5/3) for flow about an ionopause with $\bar{E}/R_0$ = 0.03. Also indicated are two sets of points (solid lines with circles, and dashed lines with squares) representing the spacecraft trajectory as viewed in two solar wind oriented coordinate systems. The trajectory indicated by the solid lines and circles is that based on the last measured direction (Ω, ϕ_p) = $(6.5°, -1.4°)$ of the interplanetary solar wind just prior to crossing the bow shock on the inbound leg, while the dashed lines and squares denote the trajectory based on the first measured direction (Ω, ϕ_p) = $(4.9°, 7.6°)$ of the solar wind immediately after crossing the bow shock on the outbound leg. These results illustrate the extremely large dependence of spatial position of

a trajectory point, as viewed in solar wind coordinates, on solar wind direction. For the particular angles indicated, the shift in X coordinate of a trajectory point can be as great as a quarter of the Venusian planetary radius and obviously results in substantial differences in predicted flow and magnetic field properties. Although Spreiter and Rizzi [1972] noted the importance of such an effect in the interpretation of the data from Mariner 4 in its flyby of Mars, the effects of angular shifts in the solar wind direction are usually ignored in most discussions of the interaction. The present results, however, indicate that this purely geometrical effect can be very significant, even for directional shifts of less than 5°, and must be accounted for in any quantitative comparison of theoretical and observational results.

The selection of values for M_∞ and γ in Figure 11 represents an attempt to resolve the uncertainty in the appropriate values for these parameters. Because only solar wind ion temperatures from the OPA were available for orbit 6, the initial calculations of M_∞ were based on the assumptions that T_e = T_i, which leads to M_∞ = 13.3 and γ = 5/3, as appropriate for a gas with parti-

Interplanetary Conditions

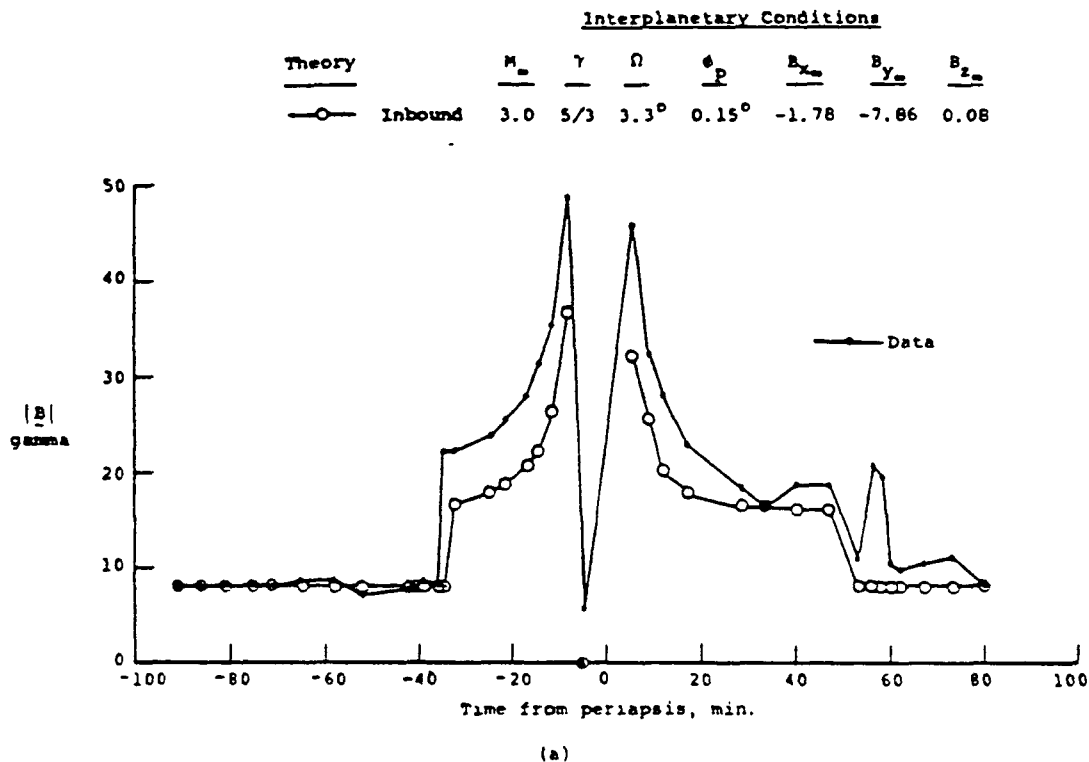| Theory		M_∞	γ	Ω	ϕ_p	B_{x_∞}	B_{y_∞}	B_{z_∞}
—O—	Inbound	3.0	5/3	3.3°	0.15°	-1.78	-7.86	0.08

(a)

Fig. 17. Comparison of observed (OMAG) and theoretical time histories of the magnetic field for Pioneer Venus orbit 3 based on inbound solar wind interplanetary conditions using a gasdynamic solution for $M_\infty = 3.0$, $\gamma = 5/3$. (a) Magnetic field magnitude. (b) Magnetic field components.

cles possessing 3 degrees of freedom for their molecular motion. The resulting location for the shock wave is not in good agreement with the observations. To investigate whether changing the value for γ to 2, which corresponds to a gas with 2 degrees of freedom as might be supposed to occur if the magnetic field sufficiently aligns the molecular motion, the calculations were repeated with $M_\infty = 13.3$ and $\gamma = 2$. The results, indicated by the dashed line, are in improved, but still not completely satisfactory, agreement with the observed shock locations. Finally, if it is assumed that the oncoming interplanetary electron temperature is not equal to the ion temperature but is substantially higher, we are led to consider low values of the order of 3-5 for M_∞. Results for $M_\infty = 3.0$, $\gamma = 5/3$ are indicated in Figure 11 by the solid line. It may be seen that results calculated for these values and for the inbound solar wind direction are in very good agreement with the theoretical results. These comparisons make evident both the possibilities and the uncertainties in the use of the theory at the present level of understanding of the parameter selection process.

Figure 12 displays the time history comparisons of the predicted bulk plasma density, speed, and temperature with OPA data. The solid lines with circles correspond to results based on inbound interplanetary conditions, while the dashed lines with squares correspond to outbound conditions. While the one data point in the ionosheath for each quantity is in general agreement with the theoretical calculation, the lack of more detailed plasma data prevents a definitive conclusion. The OPA requires approximately 9 min to acquire suffi-

cient data to enable determination of the bulk plasma quantities. This time interval usually presents no problem when the spacecraft is in the interplanetary solar wind, but the large resolution time effectively averages the plasma quantities in the ionosheath over such a large spatial range that only overall comparisons of the bulk plasma properties are possible with this instrument.

The situation is quite different for the magnetic field, since the OMAG provides essentially instantaneous measurements. Figure 13 displays a comparison of the data from orbit 6 with two sets of theoretical results based on the inbound and outbound interplanetary conditions. In these comparisons both sets of predictions exhibit good agreement with the data for the appropriate part of the trajectory. Thus, on the inbound leg the predictions based on the inbound interplanetary conditions are in good agreement with the data, while the outbound-condition predictions are notably inferior, particularly with regard to shock crossing; and conversely. Since steadiness of the interplanetary conditions was a criterion used in the selection of orbit 6 for these comparisons, the results of Figure 13 serve to illustrate the need for simultaneous measurements of interplanetary conditions and planetary flow field conditions in more definitive evaluations of the theory.

Results for corresponding comparisons for orbit 3 are given in Figures 14, 15, and 16. In Figure 14, bow shock locations are presented for five different combinations of M_∞ and γ. The Mach numbers $M_\infty = 7.38$ and 5.96 correspond to the inbound and outbound interplanetary conditions,
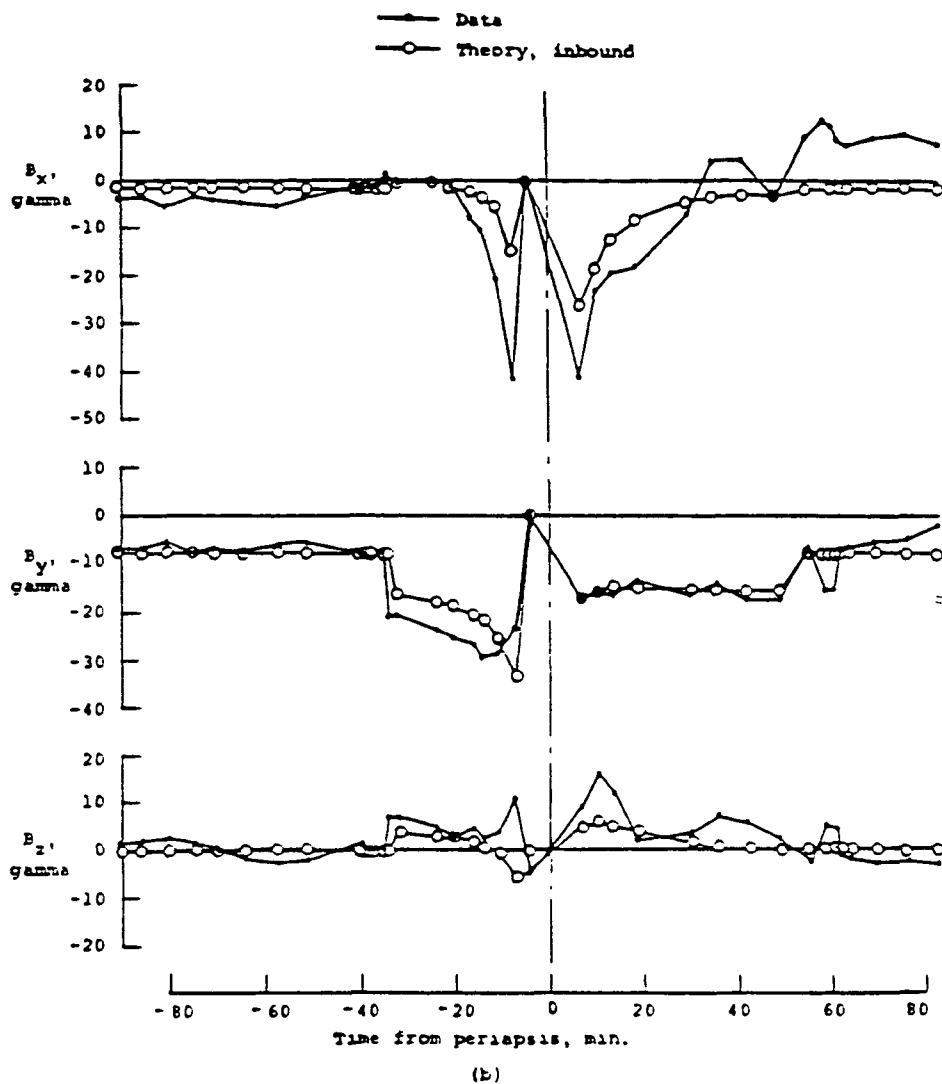
Fig. 17. (continued)

respectively, for $|\underline{V}_\infty|$, ρ_∞, and T_∞ as measured for the ions by the OPA; the two values for $\gamma = 5/3$, 2 are indicative of present uncertainty about the effective ratio of specific heats for the solar wind plasma. The bow shock location for $M_\infty = 3$ and $\gamma = 5/3$ given previously in Figure 11 for orbit 6 is also included, because once again it is closer to the observed shock crossings. Also provided in Figure 14 are the orbital trajectories as viewed in solar wind coordinates for the inbound $(\Omega, \psi_p) = (3.3°, 0.15°)$ and outbound $(\Omega, \psi_p) = (3.7°, 4.9°)$ solar wind directions.

The comparisons for the bulk plasma properties for orbit 3 shown in Figure 15 are marked again by the paucity of observational data. What information there is suggests agreement for the plasma speed and density but a notable discrepancy for the temperature. This is thought to be indicative of the manner in which the bulk properties from the theoretical model are interpreted in relation to the observational measurements; i.e., the theoretical values correspond to those for a single-component plasma in which it is considered that the electrons and ions have equal temperatures, whereas the measurements are for the ions only in a multicomponent plasma in which the ion and

electron temperatures are usually quite different. A more penetrating analysis of the meaning of the temperature in the theory and its relation to that deduced by the experimenters from their data appears to be a necessary and important subject for future study.

Results for the magnetic field comparisons are displayed in Figure 16, which provides time histories of the magnitude and individual components based on both inbound and outbound interplanetary conditions. Although the shock crossings are somewhat in disagreement, since the calculated results are for $M_\infty = 7.56$, 6.96 and $\gamma = 2$, the general trends displayed by the calculated and observed results are notably similar, particularly if account is taken of the drift with time along the trajectory of the transition from the calculations based on inbound conditions to ones based on the outbound conditions.

To demonstrate the improvement obtained in magnetic-field results when a gasdynamic flow field solution is employed which more closely agrees with the observational bow shock location, the magnetic field time histories from orbit 3 are compared in Figure 17 using gasdynamic results for $M_\infty = 3.0$, $\gamma = 5/3$, and the directions $(\Omega, \psi_p) =$
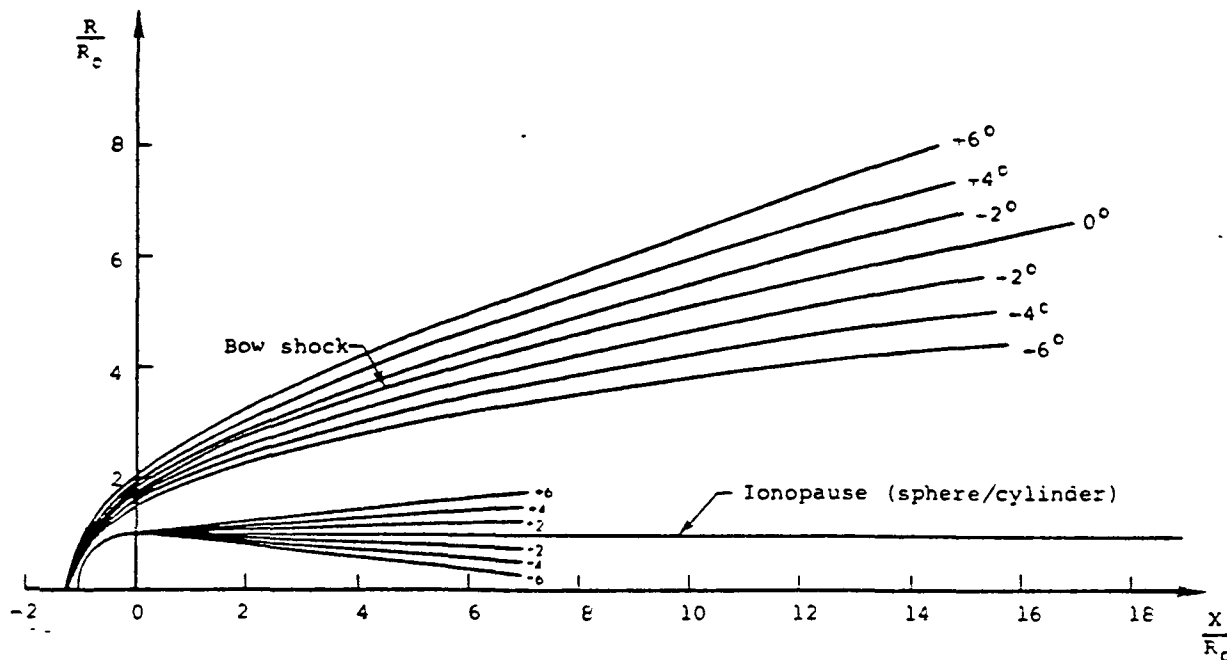
Fig. 18. Illustration of effect on bow shock location of variability of oncoming solar wind direction; $M_\infty = 8.0$, $\gamma = 5/3$ flow past a sphere/cylinder ionopause obstacle.

(3.3°, 0.15°) measured at the inbound shock crossing. As can be seen, there is a marked improvement in the agreement near the bow shock and quite good agreement throughout the ionosheath for both the magnitude and the individual magnetic field components. In addition to illustrating again that further study needs to be made of the parameter selection process required to relate the calculated and observational results optimally, these comparisons emphasize once again the need to account in the calculations for the actual direction of the interplanetary solar wind flow.

To illustrate the significance of this point, Figure 18 has been prepared to show that even a modest change of ±6° in the direction of the incident solar wind can have substantial effects on the location of the ionopause and bow wave, as viewed in a coordinate system aligned with the Sun-Venus direction which is typical of most presentations of observational data. It would be of considerable interest to determine how much of the scatter of data for the location of the bow wave may be attributable to this simple factor.

A further point of growing concern is associated with effects of significant changes downstream of the terminator of the ionopause shape from that calculated herein. More detailed comparisons will have to be reserved for future studies, but the results of Figure 19 for the theoretical characteristic lines emanating from the intersection of the ionopause and the terminator define the region of influence of a small inward or outward taper of the ionopause profile downstream of the terminator. For the entire region displayed extending downstream to more than 16 Venus radii, these results indicate that there is no accompanying change in the location of the bow wave. It may also be noted that the point designated by number 2 in the Mariner 5 data from Venus (see Spreiter and Alksne [1970] for an earlier comparison with theory), where the ionosheath plasma changes from comparatively quiet

to disturbed, is remarkably close to the characteristic line from the terminator. Such behavior could result from unsteady fluctuations of the ionopause surface beginning approximately at the terminator. The data from Pioneer Venus should be examined to determine whether this is a general property of the plasma in the vicinity of these characteristic lines or perhaps just the result of some passing transient occurring at the time of the Mariner 5 encounter.

Concluding Remarks

The present application of advanced computational procedures to the modeling of solar wind flow past Venus was undertaken to improve the accuracy and utility of the theoretical predictions. Starting with the steady, dissipationless, magnetohydrodynamic model for axisymmetric, supersonic, super-Alfvénic solar wind past a nonmagnetic planet with a shielding ionosphere, a number of important theoretical extensions have been developed and implemented. These include the capability for treating lower interplanetary gasdynamic Mach numbers M_∞ down to about 2 and a wider variety of ionopause shapes including a new family of shapes which includes the effect of gravitational variation in the scale height. Additionally, the capability for determining the plasma gasdynamic and magnetic field properties along any arbitrary trajectory, accounting for an arbitrary oncoming direction of the solar wind, has been established. All of these developments have been incorporated into a current computational model to enable detailed calculations of the solar wind interaction with Venus. The model has been comprehensively described by Stahara et al. [1980]. Also included in that account is an extensive catalog of results for a wide range of flow conditions and ionopause shapes representative of those that might be anticipated at Venus or at
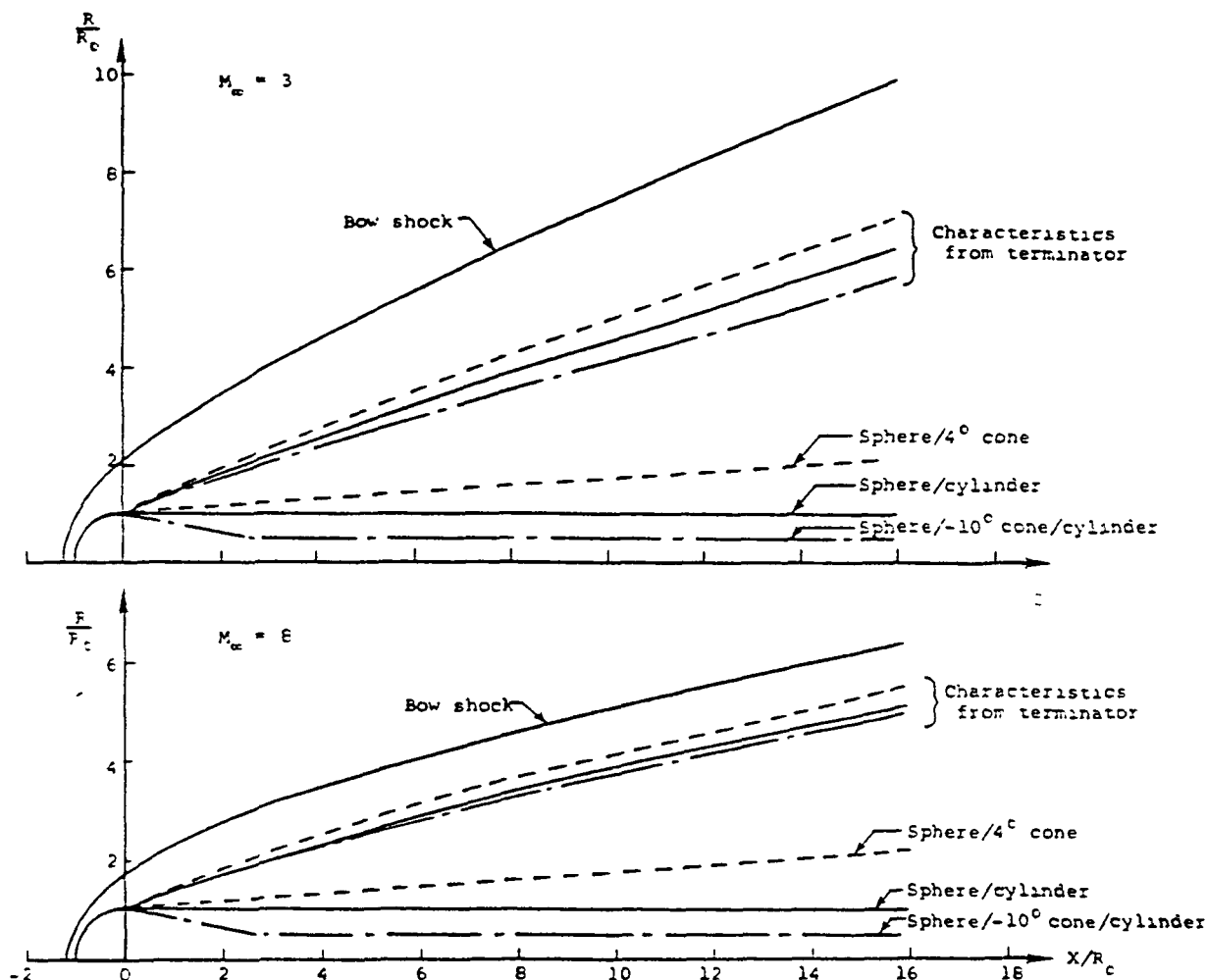
Fig. 19. Illustration of effect of various wake shapes on bow shock location and characteristics from terminator; $\gamma = 5/3$, $M_\infty = 3$ and 6.

some other nonmagnetic planet with a shielding ionosphere.

Finally, theoretical results determined from the model have been compared with data from two of the early orbits of the Pioneer Venus orbiter. These comparisons have indicated the importance, heretofore largely neglected, of the directional variability of the oncoming solar wind. These results, taken in toto, serve to verify the basic theoretical model and the effectiveness of the numerical solution, although it is evident that further study should be applied to certain questions relating to interpretation of plasma quantities like the temperature. The results demonstrate also the value of the present theoretical procedures as a research tool capable of routinely providing--at small computational cost and in a form directly compatible with observations--details of the solar wind/planetary atmosphere interaction process not previously attainable.

With regard to future uses as well as improvements of the present model, the obvious need for a detailed study involving comparison between theory and observations for a large number of orbits of the Pioneer Venus orbiter is clear. On the basis of the preliminary comparisons for orbits 3 and 6 the calculated magnetic field appears to be remarkably accurate for relatively

quiettime conditions. Similar comparisons of the plasma properties indicate a need for an improved interpretation of the results from the single-fluid theory in terms of multicomponent measurements. Questions regarding the possible suppression by the interplanetary magnetic field of the number of degrees of freedom of the plasma require further study and could be clarified through systematic comparisons with data. Additionally, observations from the Pioneer Venus orbiter of the nightside ionosphere of Venus have revealed a more complex and dynamic structure than suspected. These observations point, in particular, toward the need for improvement of the simple model used in the present method for the determination of the ionosphere boundary downstream of the terminator. This improved determination would involve an iterative procedure in which a balance of the sum of the solar wind gasdynamic and magnetic pressures along the ionopause surface would be maintained against the ionospheric pressure, not necessarily assumed to be spherically symmetric. The present method, which balances the extended Newtonian gas plus magnetic pressure distribution against the ionospheric pressure, might represent the first step of such an iteration; but it is also possible that dynamic effects associated with intermittently passing volumes of magnetized plasma torn from more upstream regions

of the ionopause might greatly impair the general utility of any stationary model for the ionopause downstream of the terminator. This is another important topic awaiting further study.

References

Alksne, A. Y., and D. L. Webster, Magnetic and electric fields in the magnetosheath, Planet. Space Sci., 18, 1203-1212, 1970.

Beam, R. M. and R. F. Warming, An implicit finite-difference algorithm for hyperbolic systems in conservation-law form, J. Comput. Phys., 22, 87-110, 1976.

Brace, L. H., H. A. Taylor, Jr., P. A. Cloutier, R. E. Daniell, Jr., and A. F. Nagy, On the configuration of the nightside Venus ionopause, Geophys. Res. Lett., 6, 345-348, 1979.

Brace, L. H., R. F. Theis, W. R. Hoegy, J. H. Wolfe, C. T. Russell, R. C. Elphic, and A. F. Nagy, The dynamic behavior of the Venus iono-sphere in response to solar wind interactions, J. Geophys. Res., this issue.

Chaussee, D. S., T. Holtz, and P. Kutler, Inviscid supersonic/hypersonic body flow fields and aerodynamics from shock-capturing technique calculations, Pap. 75-837, Amer. Inst. of Aeronaut. and Astronaut., New York, 1975.

Dryer, M., and R. Faye-Petersen, Magnetogasdynamic boundary condition for a self-consistent solu-tion to the closed magnetopause, AIAA J., 4, 246-254, 1966.

Dryer, M., and G. R. Heckman, Application of the hypersonic analogy to the standing shock of Mars, Solar Phys., 2, 112-120, 1967.

Intriligator, D. S., H. R. Collard, J. P. Mihalov, R. C. Whitten, and J. H. Wolfe, Electron obser-vation and ion flows from the Pioneer-Venus Orbiter plasma analyzer experiment, Science, 205, 116-119, 1979.

Kentzer, C. P., Discretization of boundary con-ditions on moving discontinuities, Proceedings of the Second International Conference on Numerical Methods in Fluid Dynamics, Lect. Notes Phys., 8, 108-113, 1970.

Knudsen, W. C., K. Spenner, J. R. Spreiter, K. L. Miller, and V. Novak, Thermal structure and major ion composition of the Venusian iono-sphere: First RPA results from Venus Orbiter, Science, 203, 757-763, 1979a.

Knudsen, W. C., K. Spenner, R. C. Whitten, J. R. Spreiter, K. L. Miller, and V. Novak, Thermal structure and energy influx to the day- and nightside Venus ionosphere, Science, 205, 105-107, 1979b.

Kutler, P., W. A. Reinhardt, and R. F. Warming, Numerical computations of multi-shocked three-dimensional supersonic flow fields with real gas effects, Pap. 72-702, Amer. Inst. of Aeronaut. and Astronaut., New York, 1972.

Kutler, P., W. A. Reinhardt, and R. F. Warming, Multi-shocked, three-dimensional supersonic flow fields with real gas effects, AIAA J., 11, 657-664, 1973.

MacCormak, R. W., The effect of viscosity in hypervelocity impact cratering, Pap. 69-354, Amer. Inst. of Aeronaut. and Astronaut., New York, 1969.

Russell, C. T., R. C. Elphic, and J. A. Slavin, Initial Pioneer Venus magnetic field results: Dayside observations, Science, 203, 745-745, 1979a.

Russell, C. T., R. C. Elphic, and J. A. Slavin, Initial Pioneer Venus magnetic field results: Nightside observations, Science, 205, 114-116, 1979b.

Spreiter, J. R., Magnetohydrodynamic and gas-dynamic aspects of solar-wind flow around terrestrial planets: A critical review, NASA Spec. Publ., SP-397, 135-150, 1976.

Spreiter, J. R., and A. Y. Alksne, Solar wind flow past objects in the solar system, Annu. Rev. Fluid Mech., 8, 313-354, 1970.

Spreiter, J. R., and W. P. Jones, On the effect of a weak interplanetary magnetic field on the interaction between the solar wind and the geomagnetic field, J. Geophys. Res., 68, 3555-3564, 1963.

Spreiter, J. R., and A. W. Rizzi, Aligned magnetohydrodynamics solution for solar wind flow past the earth's magnetosphere, Acta Astronaut., 1, 15-35, 1974.

Spreiter, J. R., A. Y. Alksne, and A. L. Summers, Hydromagnetic flow around the magnetopause, Planet. Space Sci., 14, 223-253, 1966.

Spreiter, J. R., A. Y. Alksne, and A. L. Summers, External aerodynamics of the magnetosphere, in Physics of the Magnetosphere, edited by R. L. Carovillano, J. F. McClay, and H. R. Radoski, pp. 304-378, D. Reidel, Hingham, Mass., 1968.

Spreiter, J. R., A. L. Summers, and A. W. Rizzi, Solar wind flow past nonmagnetic planets – Venus and Mars, Planet. Space Sci., 18, 2181-2189, 1970.

Stahara, S. S., D. S. Chaussee, B. C. Trudinger, and J. R. Spreiter, Computational techniques for solar wind flows past terrestrial planets – Theory and computer programs, NASA Contract. Rep., CR-2924, 1977.

Stahara, S. S., D. Klenke, B. C. Trudinger, and J. R. Spreiter, Application of advanced com-putational procedures for modeling solar-wind interactions with Venus – Theory and computer code, NASA Contract. Rep., CR-3267, 1980.

Thomas, P. D., M. Vinokur, R. Bastionon, and R. J. Conti, Numerical solution for the three-dimensional hypersonic flow field of a blunt delta body, AIAA J., 10, 887-894, 1972.

Wolfe, J., D. S. Intriligator, J. Mihalov, H. Collard, D. McKibbin, R. Whitten, and A. Barnes, Initial observations of the Pioneer Venus Orbiter solar wind plasma experiment, Science, 203, 750-752, 1979.

Comparison of Gas Dynamic Model With Steady Solar Wind Flow Around Venus

J. D. MIHALOV

Theoretical and Planetary Studies Branch. NASA Ames Research Center. Moffett Field, California 94035

J. R. SPREITER

Division of Applied Mechanics, Stanford University, Stanford, California 94305

S. S. STAHARA

Nielsen Engineering and Research, Inc., Mountain View, California 94043

A gas dynamic model for solar wind flow around Venus has been compared with Pioneer Venus orbiter plasma analyzer measurements from times when the solar wind flow seemed steadiest. The comparisons were made near the terminator. When the observed and model bow shock locations are matched, the model agrees fairly well with the observed parameters: the components of the flow velocity and magnetic field, and the proton number density and isotropic temperature. However, the Mach numbers required to fit the observed bow shock locations are less than 2/3 those estimated from the measured parameters of the free-stream flow, because the bow shock locations (near the terminator) are farther from Venus than expected. Sometimes the measured flow speeds appear to be retarded near the ionopause.

1 INTRODUCTION

The Pioneer Venus orbiter spacecraft [Colin, 1980], launched on May 20, 1978, carries plasma analyzer [Intriligator et al., 1980] and magnetometer [Russell et al., 1980] experiments that produce data that permit study of the flow of solar wind plasma around Venus. The plasma analyzer experiment uses 90° electrostatic deflection followed by current measurement throughout each spacecraft rotation, in five different angular sectors, using separate electrometer tubes. This study compares ionosheath data from five orbits with calculated values from the gas-dynamic model of *Spreiter and Stahara* [1980a, b]. Because of the highly inclined orbit, with periapsis initially well within the ionosphere, the data are generally acquired in the polar regions.

2. FLOW-FIELD DATA FROM VENUS' IONOSHEATH

Solar wind plasma proton parameters are obtained from the Pioneer Venus orbiter plasma analyzer data by least-squares fits of an isotropic temperature, convecting Maxwellian velocity distribution, to flight currents. When the spacecraft's periapsis is on the nightside of Venus, relatively distinct inbound and outbound crossings of Venus' bow shock are expected. For orbits with periapsis on the dayside, on the other hand, extended time intervals within the ionosheath and wake are expected, so that it becomes more difficult to judge the steadiness of the free-stream plasma flow. Consequently, data from nightside periapsis orbits only, through the first four 'eclipse seasons' to orbit 803, were examined for relatively constant solar wind proton velocity (including the flow direction), number density, and temperature. For the relatively constant cases, the amount

of ionosheath data available, and the steadiness of the interplanetary magnetic field also had to be checked. Finally, five orbits were selected as those with the steadiest interplanetary conditions, most suitable for detailed comparison with the gas dynamic model. Table 1 gives interplanetary conditions for the orbits used here.

In Table 1, v is the measured proton bulk speed (spacecraft reference frame), n is the proton number density, T_p is the isotropic proton temperature, B is the magnetic field magnitude, $M_s = v/[\gamma R(T_e + T_p)/m]^{1/2}$ is used for the sonic Mach number, with the ratio of specific heats, $\gamma = 5/3$, except as noted, and the mean molecular weight $m = 1$; $M_a = v/[B/(\mu_0 n m_p)^{1/2}]$; $M_{f\perp}$ is the perpendicular fast magnetosonic Mach number [*Clemmow and Dougherty*, 1969]: and $\beta_p = n k T_p/(B^2/2\mu_0)$ is the ratio of proton gas pressure to magnetic pressure. In addition. k is Boltzmann's constant. R is the universal gas constant, μ_0 is the vacuum permeability, and m_p is the proton mass. The electron temperature, T_e, is not directly measured during these periods, but has been estimated by using the measured proton and approximated helium number densities, together with an empirical expression of *Sittler and Scudder* [1980], $\log_{10} T_e(K) = (0.185 \pm 0.016)\log_{10} n_e(cm^{-3}) + (4.74 \pm 0.003)$. Here T_e is a temperature for the 'core' of the electron velocity distribution, and n_e is the electron number density. We use $T_e \sim T_c$ and $n_e \sim n + 2 n_o$, and n_o is a helium number density estimate. Estimates of n_o/n vary from 0.02 (orbit 63) to 0.07 (orbit 582), as a result, the effect of solar wind helium on the values of M_s and M_a is less than $\pm 13\%$, and thus is negligible.

In Table 1, the column labeled M_x gives the Mach numbers for which the gas dynamic model shock crossing locations agreed with those observed, as discussed below. The column of 'comments' in Table 1 gives a rough descriptive indication of the solar wind stream regime at the times used here. The solar wind flow is apparently much steadier for the ionosheath traversals discussed here, than for orbits 3

TABLE 1. Free-Stream Solar Wind Conditions

Orbit	v, km/s	n, cm^{-3}	T_p, °K	B, nT	M_a	M_s (est.)	$M_{f\perp}$	M_π	β_p	Comments
63 inbound	360	13.4	63.000	8.8	6.9	7.8	5.2	2.8	0 38}	Low-amplitude
63 outbound	362	14.3	53.200	8.8	7.1	8.1	5.4	3.4	0.34}	speed maximum
66*	280	43.0†	80.000†	10.8	≥7.8	≤5.4	~4.5	2.65	≥1.0	Trough between moderate speed streams
68 inbound	377	21.5	157.000	11.2	7.2	6.3	4.7	2.55	0.93}	Low maximum in
68 outbound	366	21.8	181.000	10.3	7.6	5.9	4.7	2.55	1.3 }	speed
129* $\gamma = 5/3$	334	29.0	53.500	10.6	7.8	7.2	5.3	2.65	0.48	Trough between higher speeds
$\gamma = 2$						6.5	5.0	3.2		
582 inbound	382	~13.0	~125.000	8.2	7.7	7.0	5.2	3 1	0.84}	Trough between
582 outbound	389	~13.0	~100.000	7.4	8.7	7.6	5.7	2.4	0.82}	high-speed streams

*Steadiest solar wind, comparison with model should be most reliable.
†Nonthermal portion of proton-velocity distribution not included in these values

and 6. for which *Spreiter and Stahara* [1980b] compared flight data with the same gas dynamic model.

The locations of the plasma data samples used in the present comparisons. in an axisymmetric coordinate system with the free-stream solar wind flow direction as the axis, are shown in Figure 1. These locations may be characterized as lying generally in the terminator region of the ionosheath.

3. DESCRIPTION OF GAS DYNAMIC MODEL

The time dependent dissipationless magnetohydrodynamic equations for conservation of mass, momentum, energy, and magnetic field, ignoring heat conductivity, viscosity, and electrical resistivity [*Spreiter et al.*, 1966; *Spreiter and Alksne*. 1970: *Spreiter and Stahara*, 1980b], excluding gravitational terms, are used here for calculation of model ionosheath flow fields for comparison with the spacecraft data. These equations are

$$\frac{\partial \rho}{\partial t} + \frac{\partial}{\partial x_k} (\rho v_k) = 0 \tag{1}$$

$$\frac{\partial}{\partial t} (\rho v_i) + \frac{\partial}{\partial x_k} \left(\rho v_i v_k + p\delta_{ik} - \frac{B_i B_k}{\mu_0} + \frac{B^2}{2\mu_0} \delta_{ik} \right) = 0 \tag{2}$$

$$\frac{\partial}{\partial t} \left(\frac{\rho v^2}{2} + \rho e + \frac{B^2}{2\mu_0} \right) + \frac{\partial}{\partial x_k} \left[\rho v_k \left(\frac{v^2}{2} + e + \frac{p}{\rho} \right) + S_k \right] \tag{3}$$

and

$$\frac{\partial B_i}{\partial t} = \frac{\partial}{\partial x_k} (v_i B_k - v_k B_i) \qquad \frac{\partial B_i}{\partial x_i} = 0 \tag{4}$$

where the Poynting vector is $S_i = (1/\mu_0)(v_i B^2 - B_i v_k B_k)$. and the ideal gas equation of state, $p = \rho RT/m$ is used Here ρ, p, v_i, T, and e refer to density, pressure, velocity component, temperature, and internal energy per unit mass, respectively. The value $m = 1/2$ is used for fully ionized hydrogen, and B is the magnetic field vector.

In the momentum and energy equations above, the assumption that M_a is high is invoked, so that the magnetic terms in (2) and (3) are disregarded as small. The mechanical portions of the magnetohydrodynamic equations thereby reduce to those of gas dynamics [*Spreiter et al.*, 1966,

Spreiter and Alksne, 1970]. and the magnetic field is subsequently determined by using the velocity and density as known quantities. Because (1)–(4) are dissipation-free, discontinuities in ρ, v, p, T, and B are permitted in the solutions The properties of the discontinuities are implicit in (1)–(4) because they are expressed in conservation form, and correspond to the generalized magnetohydrodynamic Rankine-Hugoniot shock-jump equations, if no approximations are introduced. Similarly. (1)–(4) correspond to those of gas dynamics and the limiting case of high Alfvén Mach number when the magnetic terms are omitted from (2) and (3) [*Spreiter et al.*, 1966; *Spreiter and Alksne*, 1970: *Spreiter and Rizzi*, 1974; *Spreiter and Stahara*, 1980b] With this approximation, (1)–(4) are then solved for the axisymmetric flow and magnetic field and the shock location. The boundary conditions applied are (1) the gas dynamic shock jump equations at the shock, (2) supersonic flow along a downstream surface, oriented normal to the axis of symmetry, and (3) flow parallel to both the ionopause surface. and to the stagnation streamline [*Spreiter and Stahara*, 1980a].

The axisymmetric obstacle shape (ionopause) is obtained by integrating an ordinary differential equation obtained from the Newtonian approximation for pressure balance across the boundary,

$$p_{st} \cos^2 \psi = p_{in} \exp \left[\frac{-(R_i - R_{in})}{h} \right] \tag{5}$$

by taking $p_{st} = p_{in}$ [*Spreiter et al.*, 1970]. Here p_{st} is the stagnation pressure of the solar wind at the nose of the ionopause, and ψ is the angle between the outward normal to the ionopause boundary and the free-stream solar wind flow direction.

The ionopause altitude at the nose of the ionosphere is specified, and an isothermal upper atmosphere with gravitationally varying scale height. $h = RT/mg$. is assumed [*Spreiter and Stahara*, 1980b] Here. $g = g_s(R_s/r)^2$ is the local acceleration of gravity. a subscript s denotes a value at Venus' surface. R_i is the radial location of the ionopause surface. and r is the radial distance from the center of the planet. T is the ionospheric temperature. and R_{in} is a constant reference radius. taken here to be $R_i - H$. with H the ionopause altitude at the ionopause nose Both T and m are assumed to be constant in the ionospheric region of interest Effects of electric currents within and at the bound-
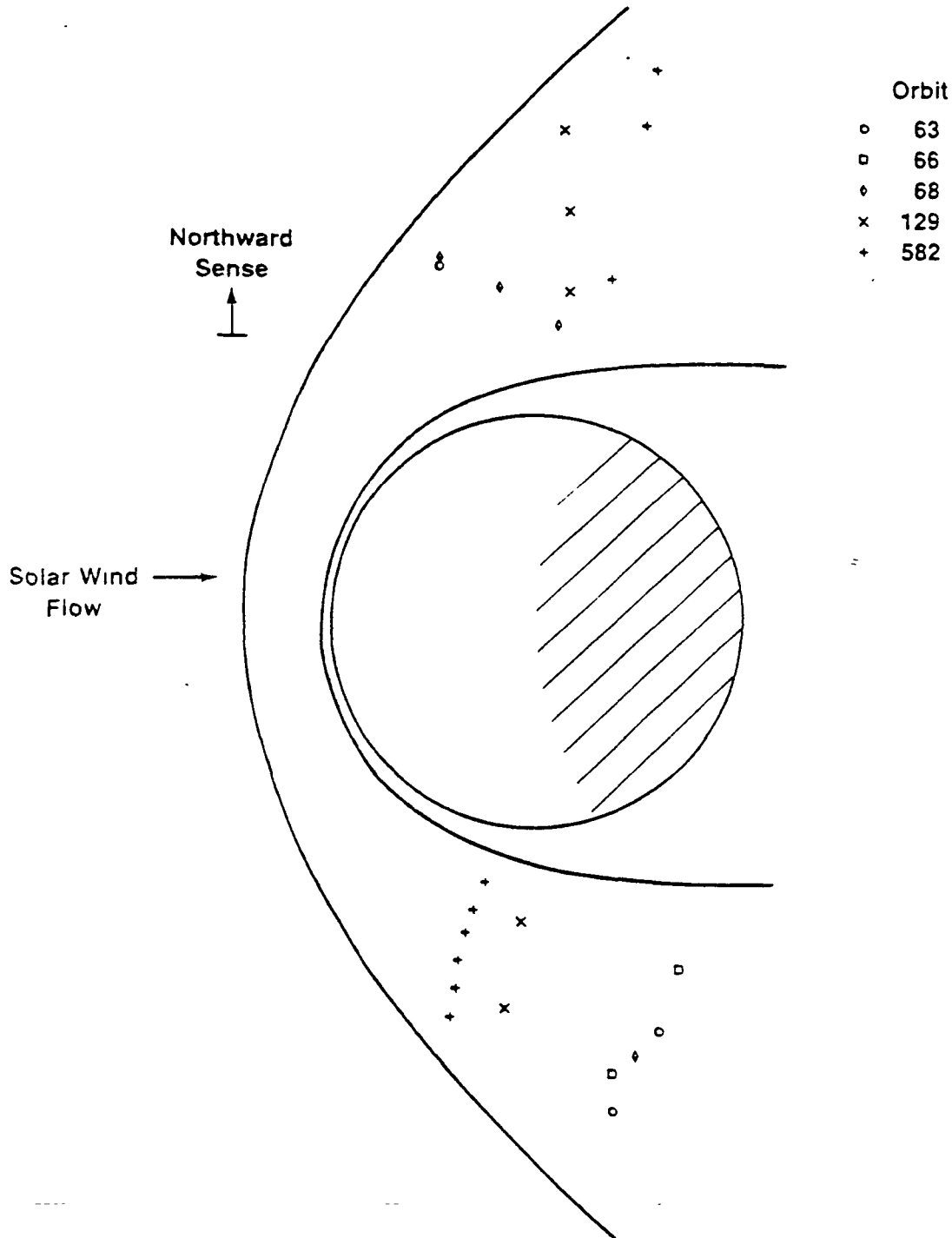
Fig. 1   Locations of samples of ionosheath plasma data used in this study, plotted in a cylindrical coordinate system with the axial coordinate aligned with the free-stream solar wind flow direction. The bow shock shape matches shock crossing locations for the outbound leg of orbit 582 (M_a = 2.4), with the ionopause determined from (5).

any of the ionosphere are assumed to be negligible in determining the pressure profile of the ionosphere.

Spreiter and Stahara [1980a] have described the computational methods used to calculate the flow field. In the nose region extending downstream to the vicinity of the terminator, both subsonic and supersonic flow occurs. Here, the fluid properties are calculated by using the second-order accurate, noniterative finite difference algorithm of *Beam and Warming* [1976], with Euler time differencing, to solve time dependent, Eulerian gas dynamic equations for axisymmetric flow, derived from equations (1) to (3) with the magnetic terms deleted. The computational mesh points are located every 4° from the stagnation point to the terminator, and at 17 intervals between the ionopause and the bow shock. Further description of the way that the boundary conditions are imposed is given by *Spreiter and Stahara* [1980b]

Downstream from the region in which all subsonic flow is found, the time independent form of the same axisymmetric, gas dynamic flow equations is solved by using the shock-capturing, marching method of *Kutler et al.* [1973]. At least 15 steps are used proceeding downstream from the terminator to 1 R_1, with mesh points at 17 intervals, again, between the ionopause and the bow shock.

The comparison of calculated and observed values was done for flow fields with Mach numbers for which the model shock locations agreed with those observed, as well as for Mach numbers estimated from upstream measurements. In the case of multiple bow shock crossings, the innermost ones were used to compare locations with the model. The Mach numbers required for agreement with the observed shock locations are given in Table 1 in the column headed M_a. These flow-field calculations use $h_s/R_{in} = 0.03$, as did *Spreiter and Stahara* [1980b], except for one case described below. This value corresponds to a scale height of the dayside ionosphere of about 200 km, in agreement with the measured ion and electron temperatures of about 2000°K and 3000°K, respectively [*Miller et al.*, 1980]. An alternative method for calculating the ionopause shapes has been presented by *Knudsen et al.* [1982]. The flow field using this shape was also calculated for one leg (orbit 582 outbound) and the results compared with those obtained by using the earlier ionopause shape

Small variations of the ionopause nose distance, R_{in}, were introduced for the flow-field calculations for the various orbits, by using for ionopause nose altitude, $R_{in} - R_s$, the ionopause altitude obtained from the empirical expression of *Brace et al.* [1980]. The measured free-stream proton convective pressure was substituted in the empirical expression for the magnetic field pressure measured at the outer boundary of the ionosphere. The nose altitudes used ranged from 296 km for orbit 66 (an upper limit) to 343 km for orbit 63 (inbound)

The streamlines for the case of orbit 582 outbound, with the ionopause shape as described by (5), are given in Figure 2.

4. COMPARISON OF OBSERVATIONS WITH CALCULATED RESULTS

Of the five steady orbits (Table 1), comparison with model calculations is first shown for orbit 129 inbound (particularly steady) and orbit 582 outbound (larger number of samples during the ionosheath traversal), in Table 2. In this table, X and R_c refer to the locations of the observations in a cylindrical coordinate system, in units of Venus radii (1 R_V = 6051 km). The axial coordinate X is along the sun-Venus direction and positive toward the sun. (Figure 1, on the other hand, is a plot in cylindrical coordinates $(X_{sw}; R_{sw})$, with the upstream solar wind flow direction as an X_{sw} axis, of the locations of the comparisons.) The gas dynamic calculations used the sonic Mach numbers M, estimated from free-stream measurements (Table 1) Proton convective pressures, $nm_p v^2$, of 5.4 × 10^{-8} and 3.3 × 10^{-8} dynes cm^{-2} for the free stream are used to deduce ~300 and ~330 km ionopause altitudes at the nose for orbits 129 and 582, respectively. One immediately finds, as did *Spreiter and Stahara* [1980b] for two other orbits that the calculated bow shock locations lie well within the observed locations. Also, the calculated speeds and proton number densities tend to be larger than the observed values. For orbit 582 (outbound), the calculated magnetic field magnitudes tend to increase as the bow shock is approached, whereas the observed values have an opposite trend.

Further comparisons are now given for flow fields with lower Mach numbers for which the model shock locations agree with those observed. *Spreiter and Stahara* [1980b] argued that such lower implied Mach numbers might arise

from elevated electron temperatures in the free stream. Table 3 gives a detailed comparison of observed and calculated values for orbit 129, one of the cases with the steadiest solar wind.

Least-squares fitting uncertainties are given in separate columns of Table 3 for the proton bulk speeds ($\sigma_{f,v}$) and the polar and azimuthal flow direction angles ($\sigma_{f,pol}$ and $\sigma_{f,az}$); for the proton number densities and isotropic temperatures the corresponding uncertainties are given in the same columns. These uncertainties, which are the changes in value of one plasma parameter that results in an increase of χ^2 by one, are taken as one standard deviation [see *Bevington*, 1969] and should represent only part of the total uncertainties. Response function uncertainties are one source of error not accounted for by the uncertainties in the plasma parameters given in Tables 2, 3, and 4. The 1, 2, and 3 components of the bulk velocity (magnitude v) are positive in the antisolar direction, the direction of planetary motion, and the northward direction normal to Venus' orbital plane, respectively; these components make up a right-handed, orthogonal system. The velocity components have been corrected for tips of the spacecraft spin axis away from an ecliptic north-south direction, for the inclination of Venus' orbit to the ecliptic plane and for the spacecraft velocity relative to Venus.

The observed and calculated temperatures in the table are not directly comparable. The observed temperatures are obtained from flight data under the assumption of isotropic proton temperatures. The theoretically calculated temperatures are obtained from the one-fluid gas dynamic model described above; they are used for the sum of the proton and electron temperatures.

The resolution of the basic magnetic field measurements is ±1/16 nT [*Russell et al.*, 1980] For orbit 129, a high-resolution (~100 samples per min) plot was supplied, and the average magnetic field component values were obtained by eye from the plot. For the other orbits, the magnetic-field data were made available as tabulations of averages over 64 s. The three components of the magnetic field make up a right-handed, orthogonal system, with component 1 positive in the solar direction, and component 3 positive northward in the direction normal to Venus' orbital plane.

For orbit 129, five ionosheath plasma samples are available; the upstream plasma parameters appear similar to those for the other orbits considered for this study, but the proton temperature is at the low end of the range. To a greater extent than for most of the other cases, use here of expected values for electron temperatures results in a calculated sonic Mach number too large to permit fitting the observed shock crossings, the calculated shock locations would fall inside of those observed. By matching the gas dynamic shock location to the observed shock locations, it is found that the calculated shock for a Mach number of 2.65 (and a 297-km ionopause nose altitude) can both match the last inbound bow-shock crossing (of three crossings) observed in the magnetometer data, and fall just a few seconds earlier than the first of three prominent bow-shock crossings observed in the plasma analyzer data, on the outbound leg. The second of these three outbound bow-shock crossings is only ~70 s later than the first. (It is difficult to obtain an inbound shock crossing time from the plasma analyzer data because a pronounced deflection of the polar flow angle is not observed.)
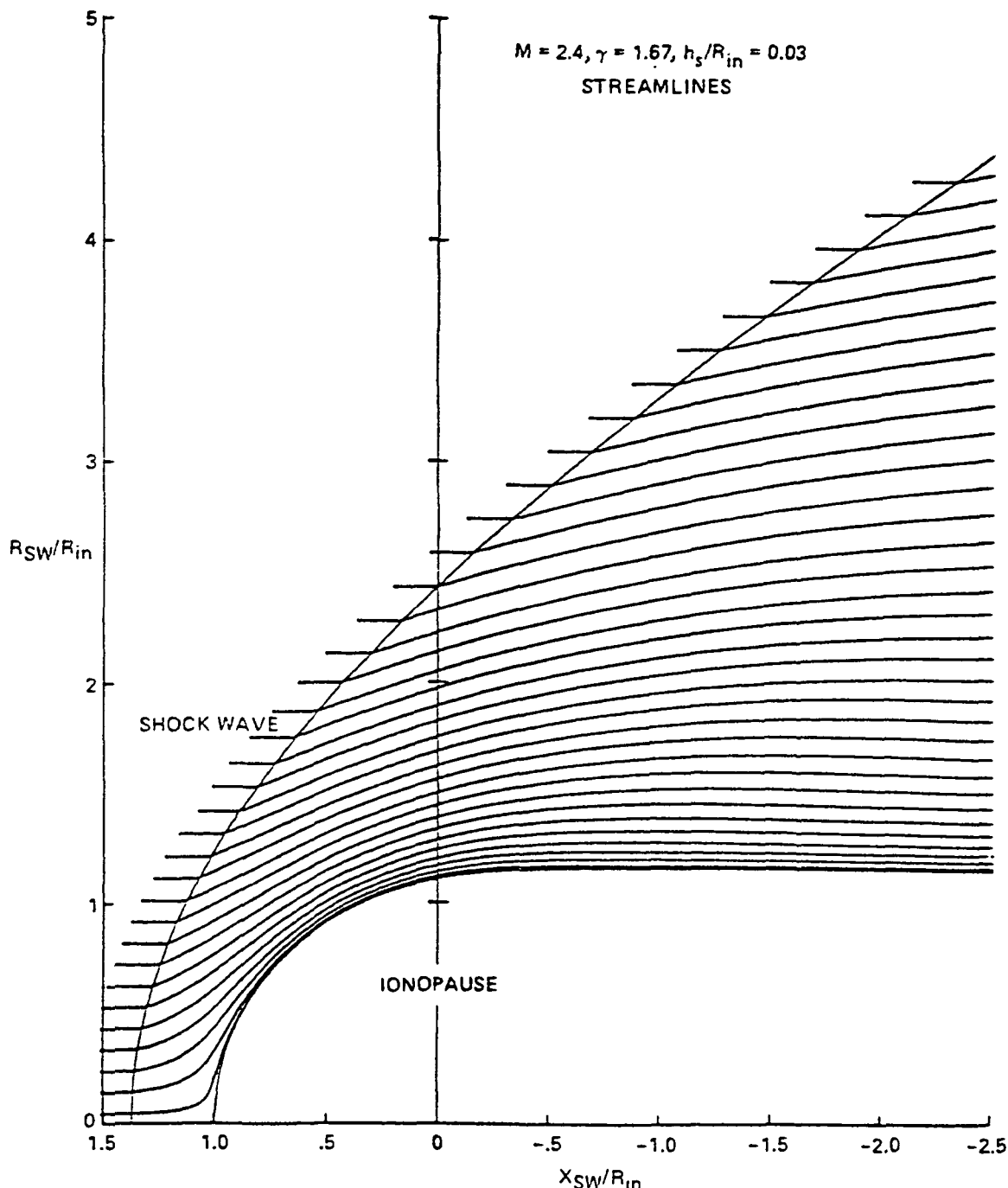
Fig. 2. Streamlines from the gas dynamic model for the outbound leg of orbit 582.

Except for the final speed sample, near the outbound bow shock, the orbit 129 ionosheath speeds remain lower than the calculated values. In particular, the speed sample closest to the ionopause on the inbound leg is only about half the calculated value. The calculated proton number densities are all within the fitting uncertainties of the measured values, given in Table 3. The observed proton fluxes for this orbit are not given in the table, however, they generally agree with the calculated values, within fitting uncertainty.

The ionosheath plasma flow deflections, observed generally in the polar regions, are typically less than the calculated values in the northward-southward direction (component 3) and greater than the calculated values in a plane perpendicular to the northward-southward direction (except for the sample closest to the ionopause on the inbound leg). This observation seems to suggest an asymmetric obstacle.

The calculated magnetic-field magnitudes for this orbit are now consistently less than the measured values (for the inbound leg sample closest to the ionopause, the two values are quite close, however). Except close to the ionopause, a similar tendency is present for all of the other orbits. This is similar to the earlier results of *Spreiter and Stahara* [1980b] (orbits 3 and 6). As an approximate description for orbit 129, the calculated northward-southward magnetic field component tends to agree with the observations; the calculated magnetic-field component along the sunward direction tends to be less than the observed values; and the remaining orthogonal magnetic-field component is observed to be both greater than (outbound leg) and less than (inbound leg) the calculated values.

If γ, the ratio of specific heats, is assumed to be 2 rather than 5/3, a gas-dynamic Mach number of 3.2 is found to fit

TABLE 2. Comparison of Observed and Calculated Values (M, Used in Model)

X, R_V	R_Z, R_V	v, km/s	v_{calc}, km/s	n, cm^{-3}	n_{calc}, cm^{-3}	B, nT	B_{calc}, nT
Orbit 129 Inbound, $M_s = 7.2$							
-0.507	2.327	238	*	63 ± 10	*	22.3	*
-0.447	1.936	238	280	42 ± 8	84	21.0	28.1
-0.365	1.559	-136	271	144 ± 91	46	18.7	21.5
Orbit 582 Outbound, $M_s = 7.6$							
0.342	1.250	272	285	12 ± 5	23	26.0	23.1
0.385	1.372	271	286	13 ± 3	30	25.5	22.3
0.418	1.493	266	292	15 ± 6	36	25.2-24.2	23.5
0.447	1.631	254	303	26 ± 7	46	24.8-24.1	26.1
0.470	1.764	251	*	40 ± 15	*	20 4	*
0.490	1.908	304	*	40 ± 6	*	17.8-16 4	*

*Outside of calculated bow shock.

the observed shock locations. *Spreiter and Stahara* [1980b] noted that such an assumption caused model shock locations near the terminator to move outward and match better their observed locations. The results for calculated parameters for this case are also given in Table 3: the changes from the γ = 5/3 cases are negligible, except that the calculated temperatures increased by about 30–50%.

The observed and calculated bulk speeds, number densities. and magnetic field strengths for the other orbits of this study are compared in Table 4 The speeds are presented in the reference frame moving with Venus. Since the magnetic field data were supplied as tabulations of averages over 64 s, there are cases in which the times of these averages do not coincide well with the times specified for the plasma data For those cases, values for these averages on both sides of the plasma data times are given. (The plasma data usually require at least 90 s for acquisition.) The values in parenthe-

ses for orbit 582 (outbound) in the table result from a calculation using the ionopause shape of *Knudsen et al.* [1982]: they are discussed later

In Tables 2. 3. and 4, the calculated speeds are generally larger than the observed values. The calculated number densities and magnetic field magnitudes tend to be smaller than the observed values The comparisons are discussed in the next section. Also, when the model shock locations match those observed, there is a slight tendency for the measured proton flux (nv) to be larger than the calculated value, excluding orbit 582: namely, of 14 flux values from these earliest four orbits, four measured values are larger than the calculated values, including the fitting uncertainties of the density, and only one measured value is similarly smaller than the calculated value For orbit 582, only the outbound portion has well-defined density measurements. and the observed flux values rise by a factor of about 3.

TABLE 3. Comparison of Measured and Model Values for Orbit 129

X, R_1	R_Z, R_1	v, km/s	σ_{f1}, km/s	v_{calc}, km/s	$\sigma_{f,az}$, deg	$\sigma_{f,pol}$, deg	v_1, km/s	$v_{1,calc}$, km/s	v_2, km/s	$v_{2\,calc}$, km/s	v_3, km/s	$v_{3,calc}$, km/s
Inbound												
-0.507	2.327	238	5	275 (278)	0.8	1.2	234	271 (274)	30	15 (15)	13	42 (42)
-0.447	1.936	238	6	278 (280)	0.7	1.9	234	275 (276)	28	0 (-1)	10	44 (45)
-0.365	1.559	-136	26	286 (289)	5 7	4.6	135	283 (285)	~0	-24 (-24)	--2	38 (40)
Outbound												
0.301	1.441	236	6	272 (276)	0.8	1.1	199	244 (247)	-102	-75 (-76)	-80	-95 (-97)
0.428	1.835	259	8	263 (266)	0.9	2.1	243	233 (237)	-62	-49 (-50)	-70	-111 (-111)

n, cm^{-3}	n_{calc}, cm^{-3}	T, °K	T_{calc}, °K	B, nT	B_{calc}, nT	B_1, nT	$B_{1,calc}$, nT	B_2, nT	$B_{2\,calc}$, nT	B_3, nT	$B_{3,calc}$, nT
Inbound											
63 ± 10	56 (55)	≤242,000	276 000 (404,000)	22.3	19 9 (19.8)	11 4	7 0 (7 0)	-7.2	-9 1 (-9 2)	-17 7	-16 3 (-16 1)
42 ± 8	48 (47)	≤208,000	270,000 (394,000)	21 0	18 4 (18 1)	13 8	8 1 (8 0)	-7.2	-9 3 (-9 2)	-14 1	-13 6 (-13 4)
144 ± 91	37 (36)	≤393,000	254,000 (359,000)	18.7	17.0 (16 5)	16 5	11 3 (10 8)	-2 5	-8 5 (-8 4)	-8 3	-9 4 (-9 2)
Outbound											
--	42 (41)	≤259,000	319,000 (413,000)	30 7	21.6 (21 1)	-7 6	-4 7 (-4 4)	-18 8	-11 6 (-11 4)	-23 1	-17 7 (-17.2)
--	55 (54)	<249,000	297,000 (450,000)	23.2	17 9 (17.5)	-4 7	-3 1 (-3 0)	-14 5	-8 8 (-8 7)	-17.5	-15.2 (-14 9)

Calculated Values M_s = 2 65 γ = 5/3. and in parentheses M_s = 3 2 γ = 2

TABLE 4. Comparison of Observed and Calculated Values

Orbit	X, R_v	R_z, R_v	v, km/s	v_{calc}, km/s	n, cm^{-3}	n_{calc}, cm^{-3}	B, nT	B_{calc}, nT
63 inbound	0.4525	1.719	≥260	271	≥64 ± 23	29	data gap	15.2
63 outbound	−0.4645	2.035	311	313	30 ± 8	22	12.9–16.7	16.0
63 outbound	−0.206	2.397	314	305	76 ± 11	32	22.0	18.5
66 outbound	−0.635	1.711	236	256	52 ± 6	44	13.1	13.5
66 outbound	−0.300	2.207	220	236	97 ± 11	72	23.2–23.5	18.4
68 inbound	0.477	1.766	328	282	~74 ± 13	45	≥25 4	18.2
68 inbound	0.180	1.618	284	298	75 ± 15	36	~22.7	16.8
68 inbound	−0.116	1.431	272	328	26 ± 14	25	14.7–13.1	15.3
68 inbound	−0.318	2.153	302	315	56 ± 8	33	19.1	15.1
582 inbound	−0.744	2.659	<418	326	>7.2	27	11.3–13.2	11.5
582 inbound	−0.673	2.405	~395	327	>64	24	13.2	10.2
582 inbound	−0.399	1.634	262	331	≥12 ± 9	16	6 0	5 4
582 outbound	0.342	1.250	272	310 (322)	12 ± 5	19 (17)	26.0	18 9 (18.1)
582 outbound	0.385	1.372	271	299 (307)	13 ± 3	21 (20)	25.5	16 8 (16.3)
582 outbound	0.418	1.493	266	294 (300)	15 ± 6	23 (22)	25.2–24.2	16.2 (15.8)
582 outbound	0.447	1.631	254	292 (297)	26 ± 7	24 (23)	24.8–24.1	15 9 (15.5)
582 outbound	0.470	1.764	251	292 (297)	40 ± 15	25 (24)	20 4	15.6 (15.3)
582 outbound	0.490	1.908	304	293 (298)	40 ± 6	26 (25)	17 8–16 4	15.4 (15 0)

M_∞ is used in model.

proceeding from the ionopause to the shock, and straddle the calculated values, which only increase by 30% as the same distance is traversed.

5. DISCUSSION AND SUMMARY

The comparisons of measured and model parameters for flow around Venus have shown generally good agreement when the observed and calculated shock locations are matched. There are two other important results from this study: first, that the bow shock locations are farther from Venus than expected (considering the gas dynamic solutions appropriate to the estimated free-stream Mach numbers), and second, that there are trends with substantial disagreements between the observed and calculated plasma parameters in Venus' ionosheath near the terminator.

Because the shock locations near the terminator are systematically farther from Venus than predicted from the gas dynamic model, the model ionosheath width was increased by lowering the Mach number. This characteristic appeared in the earlier study (two orbits) of Spreiter and Stahara [1980b]. The resulting situation with regard to the model and measured Mach numbers has been given in Table 1. Theis et al. [1981] also found that a relatively low Mach number (~3.8) was appropriate for a mean location of 475 Pioneer Venus shock locations. The locations of the bow shock crossings, used to determine model gas dynamic Mach numbers for the five steady orbits studied here, tend to straddle the locus of the published least-squares fit elliptical bow shock shape [Slavin et al., 1980; see also Slavin and Holzer, 1981]. The gas dynamic bow shock shapes that fit those crossings are more blunt than the fitted ellipse, and typically stand off a few hundred kilometers higher at the nose, compared with the least-squares fit ellipse. The greatest stand-off distances correspond to the lowest Mach numbers.

Possibly the bow shock is pushed away from Venus at the flanks as a result of mass addition to the ionosheath flow, from the ionosphere. Mihalov and Barnes [1981] have given evidence for such mass addition at and forward of the terminator plane. Taylor et al. [1980] have reported a layer of flowing ions outside the ionopause, resulting from 'solar

wind acceleration' of thermal ions in the upper ionosphere. Mass addition might result in decreasing the ionosheath wave speeds. The preliminary study of Slavin et al. [1979] remarked on the possibility of 'alteration of the magnetosheath flow' in connection with the solar wind-Venus interaction. The enhanced generation of whistler-mode wave energy at Venus' bow shock [Scarf et al., 1980] could be pertinent, also. For the aligned MHD case, reduction of M_∞ alone results in an increased shock distance at the flank [Spreiter and Rizzi, 1974], but the calculated magnitudes of these effects are insufficient to account for the differences observed by Pioneer Venus.

The effect of magnetic stress on boundary regions in plasma flow around planets has been estimated by Zwan and Wolf [1976]. This effect might cause discrepancies between observations and results from gas dynamic calculations: increased magnetic field strengths and reduced plasma densities near the boundary (body) are expected. Since the magnetic stress has been described as eliciting a squeezing out of plasma along magnetic field lines near the body, a transverse transport of momentum (a component normal to the undisturbed flow direction) would be introduced into the flow field.

The model ionosheath flow speeds tend to be larger than the observed values (18 out of 23 cases with matched observed and calculated shock locations). Part of the discrepancy between observed and calculated ionosheath flow speeds can be described as the difference between the tendencies for the calculated speed to increase and for the observed speed to decrease noticeably, both as the ionopause is approached. The difference between these trends might be due to transverse momentum flow induced by magnetic stresses. A decreased flow speed near the wake boundary has been inferred from Mariner 5 data also (see Pérez-de-Tejada [1979], Russell [1979], Spreiter and Alksne [1970], and Rizzi [1971]). Mass additions near the boundary might occur so as to slow the flow speed there. This effect has been analyzed for the case of Titan by Hartle et al. [1982]. In naive terms, the observed flow sometimes seems to act as if some type of boundary layer were present, so that the flow is retarded. The five plasma data samples with

observed flow speeds greater than model values are all adjacent to bow shock crossings. Such examples indicate smaller speed jumps at the shock, that is, a weaker shock, than that given by the model.

Usually the calculated proton number density is less than that observed (13 out of 14 cases with matched shock locations, excluding orbit 582) but is within the fitting uncertainty. For the outbound leg of orbit 582, the calculated number densities gradually increase by 40% from near the ionopause to the vicinity of the shock, with the observed and calculated shock locations matched, whereas the measured values increase by 3 1/3 times, from about 2/3 of the calculated value near the ionopause, to about 1 1/2 times the calculated value near the shock. The effect predicted from consideration of magnetic stress, a density depletion near the boundary (ionopause), relative to values from a gasdynamic model [Zwan and Wolf, 1976], is not unambiguously detected in our study.

The comparison of observed and calculated proton flux values has been described. The measured flux values seem to be slightly larger than the calculated values when the observed and calculated shock locations are matched, as described earlier. Additionally, the orbit 582 outbound comparison seems to indicate redistribution of the observed ionosheath flux away from the inner boundary, toward the shock, in comparison with the model. Because the observed values used here tend to have been acquired near the polar regions, one may speculate that nonaxisymmetry has resulted in an equatorial region with depleted fluxes. MHD effects will introduce asymmetry, some of the limited observational evidence currently available for Venus has been summarized by Russell and Vaisberg [1982].

In principle, it is possible that some type of time aliasing of the ionosheath plasma measurements could cause the measured number densities to be too large, because the current measurements are peak values during various sampling times. Then the measured flux values would be erroneously high. To date, such an effect has not been established to be significant.

The calculated magnetic field magnitudes tend to be appreciably lower than those observed, when the observed and calculated shock locations are matched. The closer agreement of the two sets near the ionopause in most of these cases is due to a drop of the measured values near the boundary, and so does not suggest the effect of the boundary layer due to magnetic stress, as described by Zwan and Wolf [1976], an increase of the measured values near the boundary would be expected as a result of that effect. Instead, most of the comparisons suggest a substantial modification of the ionosheath flow compared with the gas-dynamic model, which has been used with artificially low Mach numbers (~3) in order to match the shock locations. For orbit 582 outbound, matching the observed and calculated shock locations has resulted in reversing the gradient of the calculated magnetic field magnitudes from the case when the upstream Mach number model was used (Table 2), so that the field magnitude decreases as the shock is approached, in agreement with the observations.

Russell et al. [1979] reported that Venus' bow shock is weaker than the terrestrial bow shock, with magnetic field magnitude jumps across the shock that are less than expected from a gas dynamic model with a Mach number of 6. The results of this study indicate greater ionosheath magnetic

field magnitudes than for gas dynamic models with Mach numbers near 3. This is obviously a matter that warrants further study.

The calculated and observed flow directions and magnetic field orientations have been compared, for cases with the calculated and observed shock locations matched, in an attempt to understand better the differences between the measurements and the gas dynamic model. Except for orbit 582, the observed plasma flow deflections in the east-west direction seem larger than the calculated deflections, the observed and calculated flow deflections in the north-south direction seem comparable. The observed east-west and north-south components of the inclination of the ionosheath magnetic field seem greater than the calculated values, except for orbit 129. The upstream magnetic field is most inclined out of the ecliptic plane for orbit 129.

Knudsen et al. [1982] have presented a new method for calculating a shape of Venus' ionopause that agrees well with observations. This method uses Pioneer Venus results for the dependence of ionospheric density with solar zenith angle and for the altitude dependence of ionospheric electron and ion temperature. A converging ionopause shape downstream from Venus is achieved by maintaining a transverse ionosheath pressure near the terminator; the flow downstream from the terminator is described by two-dimensional supersonic expansion around a corner of an ideal gas [Liepmann and Roshko, 1957]. A problem with this representation is that the empirical ionosphere temperature and density model cannot balance a free-stream pressure greater than 4×10^{-6} dynes cm^{-2} [Knudsen et al., 1982], whereas the observed free-stream proton pressure for only two (orbits 63 and 582) of the five orbits used in our study was less than ($\sim 3 \times 10^{-8}$ dynes cm^{-2}) this limiting value. The low Mach number case ($M = 3$, $h/R_v = 0.1$) ionopause shape given by Knudsen et al. was used in the gas dynamic calculation for the orbit 582 outbound conditions (low free-stream pressure), to examine the changes of the calculated values. The Mach number required to fit the observed shock location had to be reduced from 2.4 to 2.3. The results are given in parentheses in Table 4. Except near the ionopause, where the maximum changes from the case with the ionopause derived from (5) are a 4% increase in flow speed, a 7% decrease in number density and a 4% decrease in magneticfield magnitude, the changes in the calculated parameters are small. The changes near the Knudsen ionopause might be expected because that surface is contracted around the planet (lower altitude ionopause), in comparison with the one derived from (5).

In summary, the gas dynamic model for solar wind flow around Venus gives results that agree fairly well with the observed flow velocities, proton number densities and isotropic temperatures, and vector magnetic fields, for five orbits with steady flow, when the calculated and observed shock locations are matched. The disagreements that have been found—principally a tendency for the flow field to exhibit higher number densities and magnetic field strengths than the model, together with the more distant shock locations than expected—suggest some significant differences between the actual and model flow fields. Some of the differences may be due to the selection of the artificially low Mach numbers for the calculations in order to match the observed shock locations. The comparisons all are in the vicinity of the terminator. The ionosheath seems to have

slower speeds and be more 'compressed' than the model, with greater proton densities and magnetic field strengths, when the low Mach numbers are used to match the shock locations. The data also appear to provide some evidence for further retardation of the flow speed near the body (ionopause). This may be indicative of the presence of a boundary layer, or the incorporation of ionospheric material in the flow, or both. Finally, it should be noted that since the comparisons of this study are for the vicinity of the terminator, some of the conclusions might be altered if conditions elsewhere were examined similarly.

REFERENCES

Beam. R M and R. F Warming. An implicit finite-difference algorithm for hyperbolic systems in conservation law form. *J. Comput. Phys.*, 22, 87–110, 1976

Bevington, P. R. *Data Reduction and Error Analysis for the Physical Sciences*, McGraw-Hill, New York, 1969.

Brace L H., R F Theis, W R Hoegy, J. H Wolfe, J D Mihalov, C. T. Russell R C Elphic, and A F. Nagy. The dynamic behavior of the Venus ionosphere in response to solar wind interactions. *J. Geophys. Res.*, 85, 7663–7678, 1980

Clemmow, P C., and J. P. Dougherty. *Electrodynamics of Particles and Plasmas* Addison-Wesley, Reading, Mass., 1969.

Colin, L . The Pioneer Venus program. *J Geophys. Res.*, 85, 7575–7598, 1980

Hartle, R E., E C. Sittler, Jr., K W Ogilvie, J. D. Scudder, A. J. Lazarus, and S K Atreya. Titan's ion exosphere observed from Voyager 1. *J. Geophys. Res.*, 87, 1383–1394, 1982.

Intriligator, D S., J. H. Wolfe, and J. D. Mihalov. The Pioneer Venus orbiter plasma analyzer experiment. *IEEE Trans. Geosci. Remote Sensing, GE-18,* 39–43, 1980

Knudsen, W. C., K. L. Miller, and K Spenner. Improved Venus ionopause altitude calculation and comparison with measurement. *J Geophys Res.*, 87, 2246–2254, 1982.

Kutler, P., W. A Reinhardt, and R. F. Warming. Multishocked, three-dimensional supersonic flowfields with real gas effects. *AIAA J.*, 11, 657–664, 1973.

Liepmann, H W., and A. Roshko. *Elements of Gas Dynamics.* John Wiley, New York, 1957

Mihalov, J D. and A. Barnes. Evidence for the acceleration of ionospheric O⁻ in the magnetosheath of Venus. *Geophys. Res. Lett.*, 8, 1277–1280, 1981

Miller, K L, W C. Knudsen, K Spenner, R C. Whitten, and V. Novak. Solar zenith angle dependence of ionospheric ion and electron temperatures and density on Venus. *J. Geophys. Res.*, 85, 7759–7764, 1980

Perez-de-Tejada, H., On the viscous flow behavior of the shocked solar wind at the Venusian ionopause. *J Geophys. Res.*, 84, 1555–1558, 1979

Rizzi, A., Solar wind flow past the planets earth, Mars and Venus, Ph.D. thesis, Stanford Univ., Stanford, Calif., 1971.

Russell, C. T., The interaction of the solar wind with Mars Venus and Mercury, in *Solar System Plasma Physics.* Chap. II.5, edited by C. F. Kennel, L. J. Lanzerotti, and E. N. Parker, North-Holland, Amsterdam, 1979.

Russell, C. T., and O. Vaisberg. The interaction of the solar wind with Venus, in *Venus,* edited by D M. Hunten, L. Colin, and T. M. Donahue, University of Arizona Press, Tucson, in press, 1982.

Russell, C. T., R. C. Elphic, and J. A. Slavin, Pioneer magnetometer observations of the Venus bow shock, *Nature, 282,* 815–816, 1979

Russell, C. T., R. C. Snare, J. D. Means, and R. C. Elphic, Pioneer Venus orbiter fluxgate magnetometer. *IEEE Trans. Geosci Remote Sensing, GE-18,* 32–35, 1980

Scarf, F. L., W. W L Taylor, C. T. Russell, and R. C. Elphic, Pioneer Venus plasma wave observations. The solar wind-Venus interaction. *J Geophys. Res.,* 85, 7599–7612, 1980.

Sittler, Jr. E C., and J D Scudder, An empirical polytrope law for solar wind thermal electrons between 0 45 and 4 76 AU: Voyager 2 and Manner 10. *J Geophys. Res.,* 85, 5131–5137, 1980

Slavin, J. A., and R E Hoizer Solar wind flow about the terrestrial planets. 1, Modeling bow shock position and shape. *J. Geophys. Res.,* 86, 11401–11418, 1981

Slavin, J. A, R C Elphic, C. T Russell, J H Wolfe, and D S Intriligator Position and shape of the Venus bow shock Pioneer Venus orbiter observations. *Geophys Res Lett* 6, 901–904, 1979

Slavin, J A., R C Elphic, C T Russell, F L. Scarf, J. H. Wolfe, J. D. Mihalov, D S Intriligator, L H Brace, H. A. Taylor Jr., and R E Daniell Jr. The solar wind interaction with Venus Pioneer Venus observations of bow shock location and structure. *J Geophys Res.* 85, 7625–7641 1980

Spreiter, J R, and A Y Alksne. Solar-wind flow past objects in the solar system. *Ann Rev Fluid Mechanics,* 2, 313–354, 1970

Spreiter, J R. and A W Rizzi, Aligned magnetohydrodynamic solution for solar wind flow past the earth s magnetosphere *Acta Astronaut.,* 1, 15–35, 1974

Spreiter, J R. and S S Stahara. A new predictive model for determining solar wind-terrestrial planet interactions. *J Geophys. Res ,* 85, 6769–6777, 1980a.

Spreiter, J R., and S S Stahara. Solar wind flow past Venus: Theory and comparisons. *J. Geophys Res.,* 85, 7715–7738, 1980b.

Spreiter, J R., A L. Summers, and A. Y. Alksne. Hydromagnetic flow around the magnetosphere *Planet Space Sci., 14,* 223–253, 1966.

Spreiter, J. R., A L Summers, and A W. Rizzi, Solar wind flow past nonmagnetic planets—Venus and Mars, *Planet. Space Sci., 18,* 1281–1299, 1970

Taylor H. A., Jr, H. C. Brinton, S J Bauer, R. E. Hartle, P A. Cloutier, and R. E Daniell, Jr., Global observations of the composition and dynamics of the ionosphere of Venus. Implications for the solar wind interaction. *J Geophys Res.,* 85, 7765–7777, 1980.

Theis, R. F. L H Brace, K H Schatten C T. Russell, J A. Slavin, and J A Wolfe. The Venus ionosphere as an obstacle to the solar wind. *Adv Space Res, 1,* 47–60, 1981

Zwan, B J., and R A Wolf. Depletion of solar wind plasma near a planetary boundary. *J Geophys Res 81,* 1636–1648, 1976

Solar Wind Flow About the Terrestrial Planets
2.   Comparison with Gas Dynamic Theory and Implications for Solar-Planetary Interactions

J. A. Slavin,[1] R. E. Holzer,[2] J. R. Spreiter,[3] S. S. Stahara,[4] and D. S. Chaussee[5]

This study utilizes gas dynamic calculations in conjunction with observational bow shock models to investigate the solar wind flow patterns about the terrestrial planets. Average dayside bow shock position could be predicted for the earth by theory with an error of only ~2%, given the observed shape and location of the magnetopause. Accordingly, our findings confirm the validity of the single-fluid gas dynamic approximation for describing this major aspect of solar wind flow past the earth. Modeled using gas dynamic theory, the solar wind interactions with Venus and Mars exhibit very significant differences. At Mars the mean inferred altitude of the solar wind–obstacle interface varies from 510 km at the stagnation point to almost 1000 km near the terminator. The effective magnetic moment required to produce a magnetosphere of this size for average solar wind dynamic pressures and terrestrial-type internal current systems is $1.4 \pm 0.6 \times 10^{22}$ G cm^3. Gas dynamic modeling of the January 21, 1972, Mars 3 and July 20, 1976, Viking 1 lander particles and fields observations supports the conclusion that the Martian obstacle to the solar wind lies at altitudes too high for it to be associated with only an ionospheric or atmospheric interaction. In contrast with Mars, our modeling of the Venus observations has found that the bow wave is closer to the planet than would be expected for a purely ionospheric obstacle. The subsolar width of the Venus ionosheath in the Venera and PVO measurements is only 60% and 90%, respectively, of that predicted by the gas dynamic model. This result is attributed to the presence of solar wind–neutral atmosphere interactions in the lower ionosheath that are not included in the gas dynamic code.

Introduction

In this article we report upon the second of a two-part investigation of the solar wind flow about the terrestrial planets. The first portion was presented in the paper by *Slavin and Holzer* [1981], which we will henceforth refer to as paper 1. In that study, bow wave observations at Venus, Earth, and Mars were brought together and modeled by using a standard set of methods for determining and comparing their shock shapes and positions. Here we continue by employing the bow shock models of paper 1 as boundary conditions for gas dynamic calculations from which the flow fields about these bodies are constructed.

The principal objectives are threefold. First, the large data base available for the earth system is compared with the predictions of gas dynamic theory in order to test the method before its use at the other planets. where far fewer observations have been made. Second, the gas dynamic calculations are applied to the Pioneer Venus orbiter (PVO) and Venera 9 and 10 shock measurements with the intent of evaluating the degree to which flow about Venus may be modeled without including the effects of solar wind plasma–neutral atmosphere interactions above the ionopause. While the PVO observations have shown the Venus interaction to be primarily ionospheric [*Brace et al.*, 1980; *Elphic et al.*, 1980; *Brace*

et al., 1982], cometary processes (i.e., charge exchange and photoion pickup) in the ionosheath can exert a great influence over the flow [*Wallis*, 1972; 1973]. While passing through the inner solar system, most active comets are thought to deflect the solar wind at large distances through charge exchange and photoion-pickup-induced mass loading of the incident solar wind flow [*Biermann et al.*, 1967]. Clarification of the role played by the neutral atmosphere in the Cytherean interaction is critical to the use of Venus as an analog of the solar wind flow about comets. Third, at Mars we use gas dynamic models to infer the average height of the solar wind–obstacle interface and evaluate the controversial January 21, 1972, Mars 3 observations that show a possible encounter with an intrinsic field magnetosphere [e.g., *Dolginov*, 1978a, b, c; *Russell*, 1978a, b]. The question of whether Mars undergoes a Venus-type ionospheric interaction with the solar wind or possesses a significant planetary magnetic moment remains unresolved because of a lack of low-altitude particles and fields measurements. Until such time as new observations are made by an orbiter with a low periapsis, such as the proposed ESA Kepler Mars mission. the Martian solar wind interaction must be studied predominantly through modeling of the high-altitude (i.e., >1000 km) Soviet Mars satellite measurements.

Gas Dynamic Theory

The methodology and computational techniques employed in the gas dynamic modeling of flow about the planets are well documented in the literature [e.g., *Spreiter et al.*, 1966; *Dryer and Heckman*, 1967; *Spreiter and Alksne*, 1970; *Dryer*, 1970; *Rizzi*, 1971; *Spreiter and Stahara*, 1980a, b]. For purposes of this study it is necessary for us to consider only the general properties of the solutions. Figure 1 displays bow shock position, streamlines, and characteristic lines for a single-fluid gas dynamic calculation of flow about a theoretical magnetopause surface [*Spreiter et al.*, 1966]. Far upstream the solar wind is assumed to be an ideal MHD

[1] NRC-NASA Resident Research Associate. Jet Propulsion Laboratory California Institute of Technology, Pasadena, CA 91109
[2] Institute of Geophysics and Planetary Physics, University of California, Los Angeles, CA 91109
[3] Division of Applied Mechanics, Stanford University, Stanford, CA 94305
[4] Nielson Engineering and Research, Inc., Mountain View, CA 49043
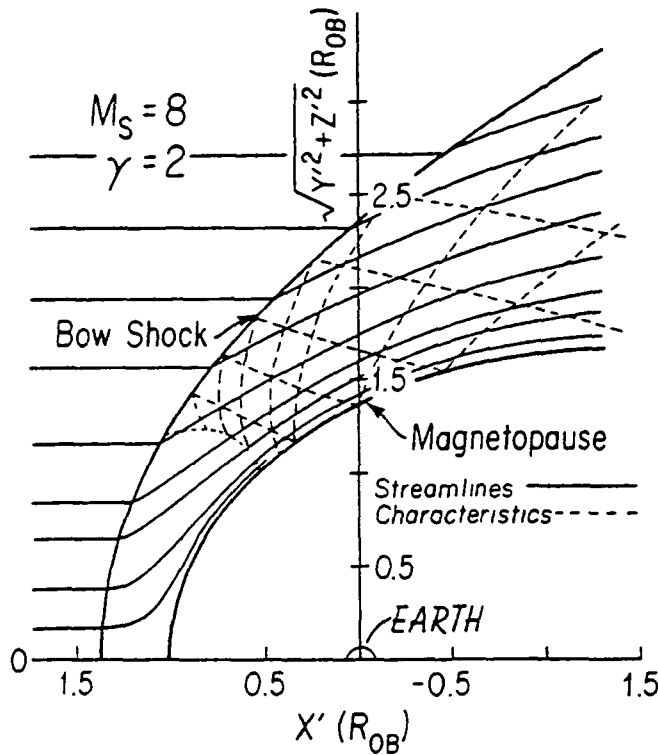[5] NASA Ames Research Center, Moffett Field, CA 94035

Fig. 1. Gas dynamic model of flow about a theoretical magnetopause for $M_s = 8$, and an adiabatic exponent of 2 from *Spreiter et al.* [1966] is displayed. Aberrated geocentric solar ecliptic coordinates are used as in paper 1.

fluid. It is completely described in the MHD equations by a sonic Mach number M_s, an Alfvenic Mach number M_A, and an adiabatic index γ for the equation of state. Previous theoretical examinations of this MHD problem [e.g., *Spreiter and Rizzi*, 1974; *Chao and Wiskerchen*, 1974] have shown that the bow shock jump conditions and the flow solutions are dependent separately upon M_s and M_A without any manipulation of these terms into a single Mach number being possible (although magnetosonic Mach number and β may be used instead of M_s and M_A; *Tidman and Krall* [1971]). For this reason there does not appear to be any theoretical support for the use of magnetosonic Mach numbers in studies of the dayside magnetosheath flow and bow shock position, as is sometimes done on intuitive grounds [e.g., *Russell*, 1977b]. In some cases the desire to use Mach numbers based upon the MHD fast-mode velocity appears to stem from the need to simplify the problem by making the Mach number that determines the distant downstream Mach cone the only Mach number in the flow calculations [e.g., *Dryer and Heckman*, 1967; *Shen*, 1971]. These difficulties are understandable when it is realized that no general theoretical solutions to this MHD problem have been found. Only in the specialized case of aligned flow (i.e., V∥B) has the problem of ideal MHD flow about an axisymmetric, blunt, magnetospheric obstacle been solved [*Rizzi*, 1971; *Spreiter and Rizzi*, 1974]. In that particular situation the MHD equations can be reduced to those of gas dynamics with a novel equation of state and solved numerically. However, the limit in which this MHD problem may generally be solved is that of a weak magnetic field in the sense of $M_A^2 = (\rho V^2/2)/(B^2/8\pi) \gtrsim 10^2$. This limit corresponds to the traditional 'gasdynamic approximation' [e.g., *Spreiter et al.*, 1966, *Dryer and Heckman*, 1967] in which the terms of the

MHD equations containing M_A are neglected on the grounds of their relative smallness. Solutions such as shown in Figure 1 are then obtained. Only in very recent times have any new attempts been made on the full MHD description [*Lyon et al.*, 1980; *Leboeuf et al.*, 1981; *Wu et al.*, 1981]. It is not yet clear when, or to what extent, these computational plasma physics codes will begin to contribute to our understanding of astrophysical plasma flow systems.

While the interplanetary magnetic field plays essential roles in almost all of the plasma processes taking place in the solar system (e.g., particle acceleration and transport), the magnetic energy in the solar wind is weak in comparison to the flow energy, and the gas dynamic approximation is usually valid (see, for example, Table 5 of paper 1). Still, the neglect of the IMF is widely felt to be the major limitation of the gas dynamic approach. It is not often appreciated that the more critical assumption in these calculations may be the use of a single-fluid description. Not only are the solar wind protons and electrons observed to have significantly different mean thermal speeds but their distribution functions and the processes influencing them are quite dissimilar [e.g., *Sittler and Scudder*, 1980]. Under these circumstances it is not physically reasonable to expect any single-fluid treatment to be able to predict the individual properties of these two different plasma species. However, it is possible for a single-fluid model to well represent the common, or shared, properties of a multispecies system. In this respect the problem of flow past a planet is like that of the expansion of the solar wind itself. Single-fluid models can be constructed to match the bulk speed and density at 1 AU but not the individual proton and electron temperatures [e.g . *Hundhausen*, 1972]. For this reason, in addition to introducing extended energy sources and other transport mechanisms, modern treatments of the solar wind often consider the protons and electrons as separate fluids. However, just as with the gas dynamic calculations in Figure 1, the magnetic field in the solar wind is still often regarded as frozen-in and dynamically unimportant once a given parcel of plasma is far from the initial acceleration region.

The need for a two-fluid model becomes even more apparent in the measurements across the shock. While the electrons and ions are shocked at about the same location relative to fluid length scales, the microphysics of the thermalization processes are different for the two species [e.g., *Greenstadt and Fredricks*, 1979]. The result is that the electron temperature increases by less than a factor of 2 [e.g., *Bame et al.*, 1979] as contrasted with a jump 2–4 times as great for the protons [e.g., *Montgomery et al.*, 1970]. Accordingly, the present gas dynamic models do no more than approximate the prediction of the individual species temperatures [e.g., *Mihalov et al.*, 1980, 1982]. With respect to the validity of the gas dynamic approach it is important to note that the model successfully predicts all of the shared properties: shock location [e.g., *Wolfe et al.*, 1966; this paper], velocity jump [e.g., *Burlaga and Ogilvie*, 1968; *Mihalov et al.*, 1980], density jump [e.g., *Howe and Binsack*, 1972], and total enthalpy [*Montgomery et al.*, 1970]. Hence, there is ample justification for the use of gas dynamic modeling as a tool in studying solar-planetary interactions once its limitations are recognized.

As discussed above, sonic and magnetosonic Mach numbers are the most commonly assumed ordering parameters for studies of bow shock location. Mach numbers based

upon the Alfven speed are also used sometimes for unstated reasons [e.g., *Harvey et al.*, 1981]. Observationally, the determination of the appropriate Mach numbers for this problem is not straightforward for a number of reasons. The high averge values and small spread in M_s and M_A [e.g., *Fairfield*, 1971; *Formisano*, 1979] and the dominance of solar wind dynamic pressure in setting bow wave position [*Fairfield*, 1971] make the variations in shock position and shape with changing Mach number difficult to detect. The lack of a Mach-number-independent means of determining the adiabatic exponent [*Dryer*, 1971] also introduces ambiguities into the application of gas dynamic theory to the problem. In this study the gas dynamic approximation is found to produce an accurate representation of the terrestrial bow shock/magnetopause system with a sonic Mach number

$$M_s = V_{sw}(2 \, k_b(1.08 \, T_p + 1.14 \, T_e)/1.16 \, m_p)^{-0.5} \quad (1)$$

based upon total plasma pressure [including 4% He^{++} with $T_{He}/T_H = 3.5$, see Table 5 of paper 1] and an adiabatic exponent of 2. Not only does the gas dynamic model that uses M_s computed in this way reproduce the average observations but M_s is also found to order the shock shapes and stand-off distances determined with the various earth-orbiting satellites in paper 1.

The effects of the choice of a γ value appear in the model jump conditions across the shock and in the resulting width of the magnetosheath. Figure 2 shows both the $\gamma = 5/3$ and 2 bow wave positions from *Spreiter et al.* [1966]. In this study we found that for a Mach number defined as in (1) an adiabatic exponent of 2 produces good agreement between gas dynamic theory and observation, although an optimum value might be very slightly lower. This result is in essential agreement with the VELA studies of *Gosling et al.* [1967] and *Montgomery et al.* [1970], the IMP investigation of *Fairfield* [1971], and the ISEE work of *Zhuang and Russell* [1981]. While a more detailed examination of this issue lies beyond the scope of our present investigation, further study of the problem is planned for the near future.

The variation of shock shape with obstacle shape is also addressed in Figure 2. Blunter bodies require thicker transition regions (i.e., more distant bow shocks) to accomplish the diversion of the incident flow than do more slender obstacles. It was, in fact, the one-to-one relationship between shock and body shape that formed the physical basis of the original inverse method for the calculation of hypersonic flow about obstacles [*Van Dyke*, 1958]. Shock shape would be iteratively varied until the resulting stagnation streamline coincided with the desired body shape. As shown in Figure 22 of paper 1, the bow waves of Venus, Earth, and Mars all possess different shapes in good qualitative agreement with their observed obstacle shapes and the aerodynamic relationships established by Van Dyke. For this reason, studies of flow about the planets require theoretical models with obstacle shape as an input variable. Fortunately, such codes now exist as a result of the work of *Spreiter et al.* [1970], *Chausee et al.* [1978], *Spreiter and Stahara* [1980a, b], and *Stahara et al.* [1980] on the solar wind interaction with Venus. Lacking in situ observations of ionopause shape, they performed pressure balance calculations with the ratio of ionospheric scale height to subsolar obstacle radius H/R_0 as a variable to obtain ionopause shape. The larger the assumed scale height the greater the bluntness of their tangential discontinuity obstacle. The increased
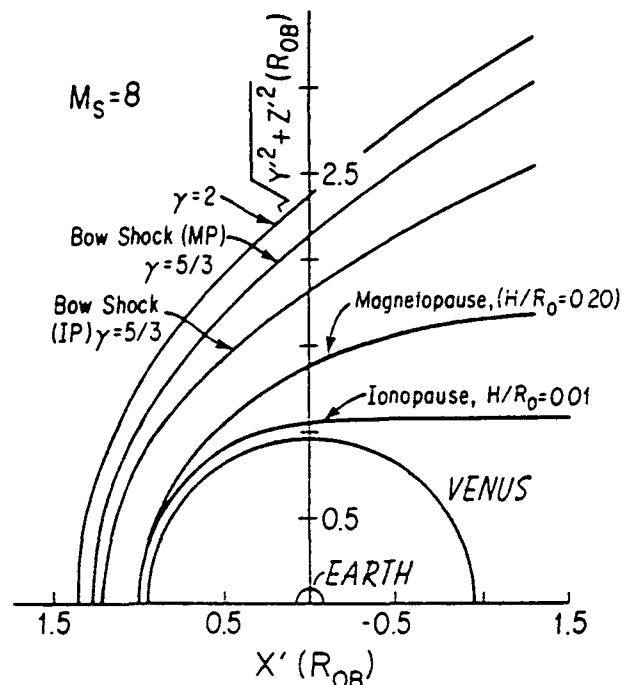

Fig. 2. Bow shock positions associated with theoretical earth (i.e., $H/R_0 = 0.20$) and Venus (i.e., $H/R_0 = 0.01$) obstacles for $M_s = 8$ and $\gamma = 2$ and 5/3 are compared. Note the increased width in the region between the shock and obstacle for blunter obstacles and larger adiabatic exponents.

bluntness is due to the large decline in external pressure between the nose and terminator coupled with the ionosphere's exponential pressure dependence upon scale height. The resulting flow models were then cataloged by M_s, γ, and H/R_0 [*Stahara et al.*, 1980]. Hence gas dynamic models are now available for a family of blunt obstacles parameterized by H/R_0.

MODELING RESULTS

Earth

In paper 1 the location of the terrestrial bow shock was modeled independently with the observations of IMP 3, IMP 4, Heos 1, and Prognoz 1 and 2. The results of that study are displayed in Figure 3, where they have been scaled, assuming the usual sixth root dipole–external pressure relation (e.g., equation (2)), to a common solar wind dynamic pressure of $1.16 \, m_p n_p V^2 = 2.1 \times 10^{-8}$ dynes/cm². As shown, the differences remaining among the four surfaces, while small, appear well ordered by the average observed upstream sonic Mach numbers. Both nose distance and eccentricity of the model surfaces vary monotonically with M_s. Such an ordering is not present when the models are compared with the average Alfvenic and magnetosonic Mach numbers listed in Table 5 of paper 1. Given the high average Alfvenic Mach number in the solar wind this result is in qualitative agreement with expectations based upon the gas dynamic approximation discussed earlier.

Figure 4 compares the average bow wave from paper 1 with the gas dynamic models of flow past a theoretical magnetopause surface by *Spreiter et al.* [1966]. Because it is our intent to predict the flow pattern behind the shock at Venus and Mars, we take this same approach here for the earth. In Figure 4 the forward portions of the theoretical and observed bow waves have been scaled to coincide. Magneto-
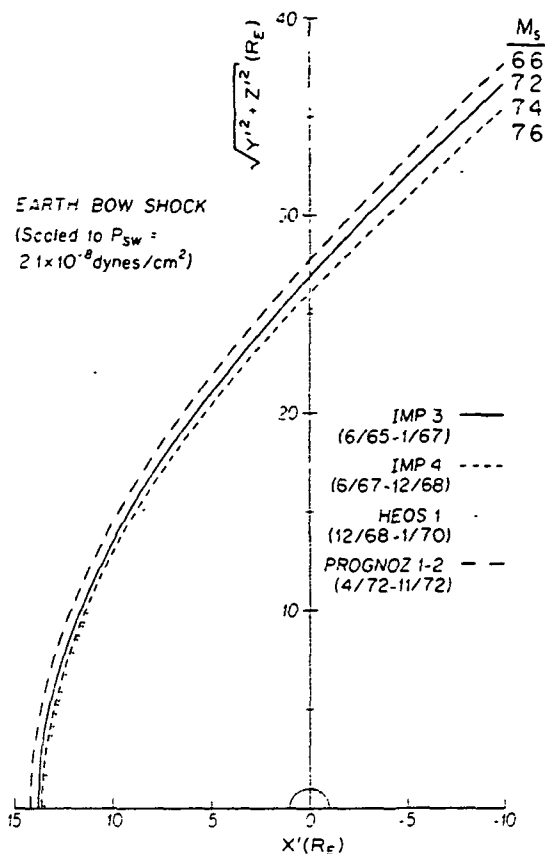
M_s

66
72
74
76

EARTH BOW SHOCK
(Scaled to P_{sw} =
2.1×10^{-8}dynes/cm^2)

IMP 3 ———
(6/65-1/67)

IMP 4 ----
(6/67-12/68)

HEOS 1 ·
(12/68-1/70)

PROGNOZ 1-2 — —
(4/72-11/72)

$X'(R_E)$

Fig. 3 The average shock surfaces from five earth orbiter missions obtained in paper 1 are displayed after being scaled to a common mean solar wind dynamic pressure.

EARTH BOW SHOCK AND MAGNETOPAUSE
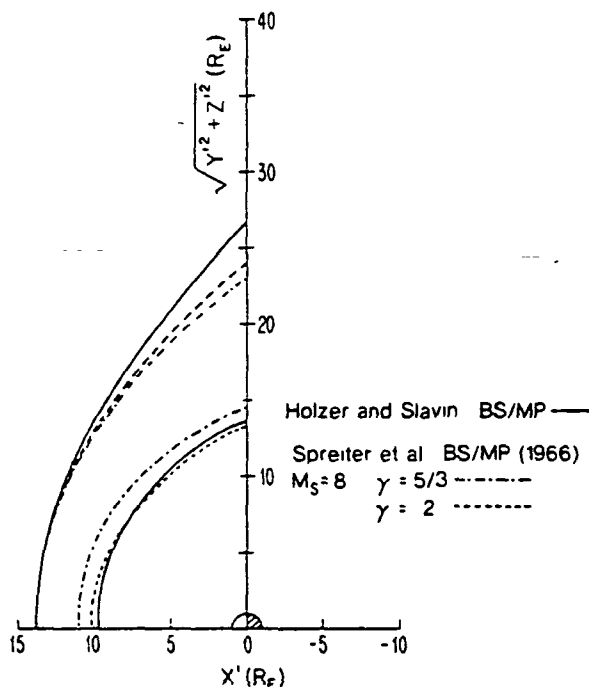(ALL SCALED TO P_{sw}= 2.1×10^{-8} dynes/cm^2)

Holzer and Slavin BS/MP ———

Spreiter et al BS/MP (1966)
M_s= 8 γ = 5/3 —·—·—
γ = 2 ········

$X'(R_E)$

Fig. 4 The average bow wave from paper 1 and the magnetopause from Holzer and Slavin [1978] are compared with the Spreiter et al. [1966] gas dynamic calculations.

pause position is then the predicted quantity. The observed magnetopause model with which the results are compared is the average model of Holzer and Slavin [1978] scaled to P_{sw} = 2.1 × 10^{-8} dynes/cm^2. This model surface was chosen because the study producing it considered the effects of solar wind dynamic pressure, and the observations upon which it is based were made near the center of the interval spanned by this investigation. In this way any effect of the solar cycle variation in geomagnetic activity on magnetopause position should be minimized. The shape of Holzer and Slavin magnetopause model is close to that of Fairfield [1971] but slightly less blunt than some of the others, such as Howe and Binsack [1972]. The gas dynamic bow shock/magnetopause positions displayed correspond to a sonic Mach number of 8 and adiabatic indices of 2 and 5/3. A sonic Mach number of 7.2, the mean in Figure 3, would have been preferred, but funding constraints limited us to using previously generated models in most cases. The error introduced by the use of M_s = 8 will be much less than the spread among the surface models in Figure 3. The spread in Figure 3 is larger than would be predicted by gas dynamic theory: this may be a result of the fitting uncertainties outlined in paper 1. However, the more important factors in Figure 4 are γ and obstacle shape. A value of γ = 5/3 is seen to predict a magnetosheath that is too narrow, whereas γ = 2 appears to be in near agreement with observation. The greatest discrepancy between the theoretical model and observational reality lies in their respective magnetopause shapes. This is a general failing of the various theoretical magnetopause calculations [e.g., Fairfield, 1971; Walker, 1979] believed to be caused by inaccuracies in their specification of the external pressure field and/or the internal magnetospheric current systems. Fluid calculations that use theoretical obstacle shape then produce a bow wave that is too slender and lies too close to the planet. We avoid this difficulty by selecting an obstacle surface in Figure 5 that is very near the average shape of the magnetopause as determined by actual observation. As shown, a H/R_0 = 0.35 obstacle is nearly midway between the slightly more slender magnetopause models of Fairfield and Holzer and Slavin and the blunter result of Howe and Binsack. Farther downstream the flat slope of the H/R_0 = 0.35 obstacle could become a source of error for comparisons with the observations, but we are concerned here with only the near portions of the bow wave.
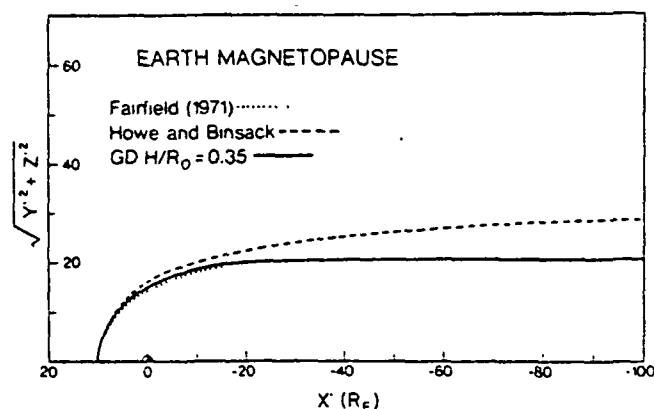

EARTH MAGNETOPAUSE

Fairfield (1971)········ ·
Howe and Binsack-----
GD H/R_0 = 0.35 ———

$X'(R_E)$

Fig. 5. A comparison of the empirical Fairfield [1971] and Howe and Binsack [1972] magnetopause models with the gas dynamic H/R_0 = 0.35 obstacle demonstrates the appropriateness of this theoretical surface for flow calculations.

In Figure 6 this $H/R_0 = 0.35$ obstacle has been used to calculate the flow pattern about the earth's magnetosphere. In order to compare the assumed obstacle shape with the Holzer and Slavin magnetopause, the radius of the obstacle has been chosen so that they share the same stagnation points. The agreement over the forward region of the magnetopause influencing the shock for the interval of interest (see the characteristic lines of the flow in Figure 1) is excellent. As expected from the discussion of the preceeding figure, the assumed obstacle is slightly blunter along the flanks than the Holzer and Slavin observational model but less so than Howe and Binsack. The resulting theoretical bow shock surface is in close agreement with paper 1's observational model as shown in the figure. The discrepancies near the nose and at the terminator amount to only ~2%. Error bars normal to the empirical shock and magnetopause surfaces provide a measure of the rms deviations of the observed boundary crossings about the model. As indicated, the differences between theory and observation appear much smaller than the rms spread in the data themselves and only somewhat larger than the fitting uncertainties discussed in paper 1. If the small overestimate in stand-off distance is real, then the optimum value of the adiabatic exponent may be slightly less than 2, as suggested by Fairfield. However, it is also possible that the small differences between the predicted and observed bow waves may be an MHD effect arising from the omission of the IMF in the gas dynamic calculations. For the special case of aligned flow, *Spreiter and Rizzi* [1974] have found that at Alfvenic Mach numbers greater than 5 (cf., the mean value for the observations in Figure 3 is 9.0; see Table 5 of paper 1) the shock surface is only slightly blunter than would be expected from gas

Fig. 7. The aligned MHD flow model of *Spreiter and Rizzi* [1974] is shown above. Future studies of low M_A conditions, using a larger data base than employed by this investigation, are planned to test these theoretical predictions.

dynamic calculations as detailed in Figure 7. Unfortunately, a much larger data set than the one employed by this study would be required to verify the results of their MHD model, given the modest rate of occurrence of low-M_A conditions.

Venus

The Cytherean bow wave has now been surveyed from orbit by Venera 9, Venera 10, and Pioneer Venus, as discussed in paper 1 [see also *Verigin et al.*, 1978; *Slavin et al.*, 1980; *Smirnov et al.*, 1980; *Russell and Vaisberg*, 1982]. Since the initial measurements of the Mariner 5 flyby and the Venera 4 descent probe in 1967 [*Bridge et al.*, 1967; *Dolginov et al.*, 1969; *Gringauz et al.*, 1968], a number of studies have compared bow wave position with the predictions of gas dynamics [*Gringauz et al.*, 1970; *Spreiter et al.*, 1970; *Rizzi*, 1971; *Vaisberg and Bogdanov*, 1974; *Ness et al.*, 1974; *Bridge et al.*, 1974; *Wallis*, 1974; *Vaisberg et al.*, 1976a; *Gringauz et al.*, 1976; *Russell*, 1977a, b; *Dolginov et al.*, 1978; *Romanov et al.*, 1978; *Verigin et al.*, 1978; *Wolfe et al.*, 1979; *Slavin et al.*, 1979a, b; *Mihalov et al.*, 1980; *Slavin et al.*, 1980; *Smirnov et al.*, 1980; *Spreiter and Stahara*, 1980b; *Taylor et al.*, 1980; *Theis et al.*, 1981]. General criticisms that can be leveled at many of these works may be listed under three main categories: they generally do not take into account measured ionopause and shock shape; the adiabatic exponent is commonly chosen to be 5/3 as opposed to the preferred (i.e., from the far more numerous earth observations) value of 2; and finally the possibility of nonideal gas dynamic processes such as charge exchange and photoion pickup influencing the flow is often ignored. With these points in mind the approach adopted here has been to match the observed shape of the bow wave with a gas dynamic model and then compare the predicted obstacle surface with existing ionopause measurements in the same way as Figure 4 does for the earth's magnetopause. An additional advantage to this method is that it predicts the solar wind flow field

EARTH BOW SHOCK AND MAGNETOPAUSE
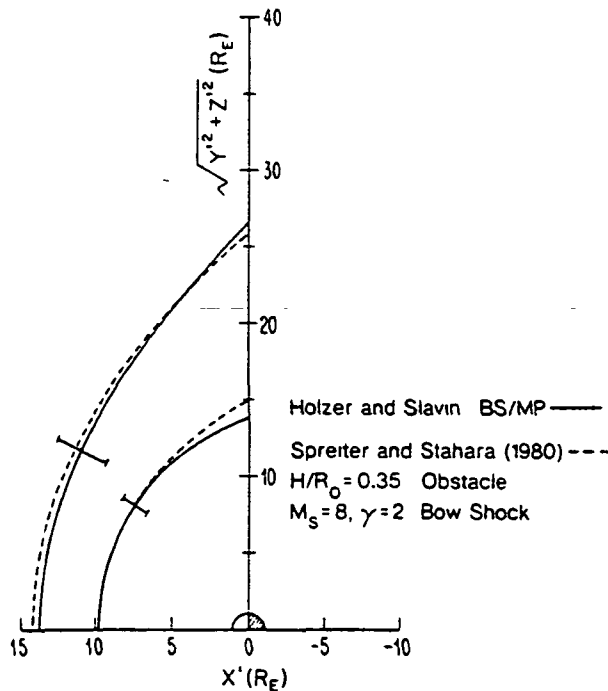### (ALL SCALED TO $P_{SW} = 2.1 \times 10^{-8}$ dynes/cm^2)

Fig. 6. The average observational boundary surfaces from Figure 5 are compared above with gas dynamic flow past a $H/R_0 = 0.35$ obstacle for $\gamma = 2$ and $M_s = 8$ upstream conditions. The error bars provide a measure of the rms spread in the spacecraft boundary crossings modeled in paper 1.
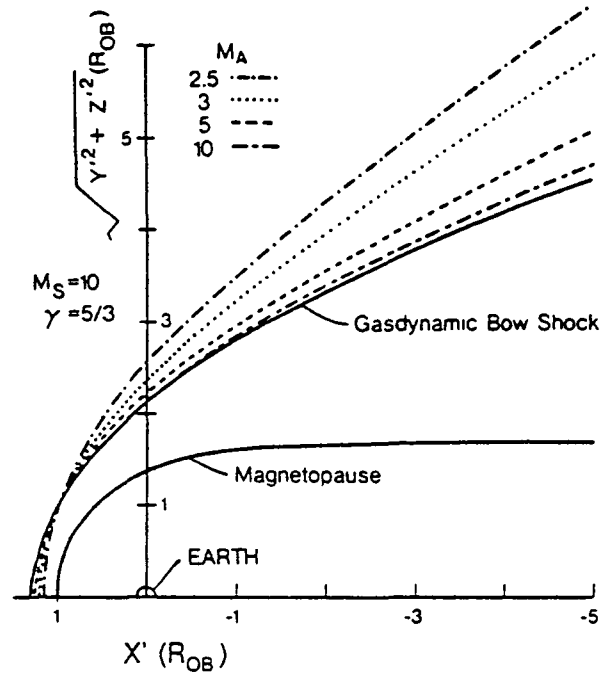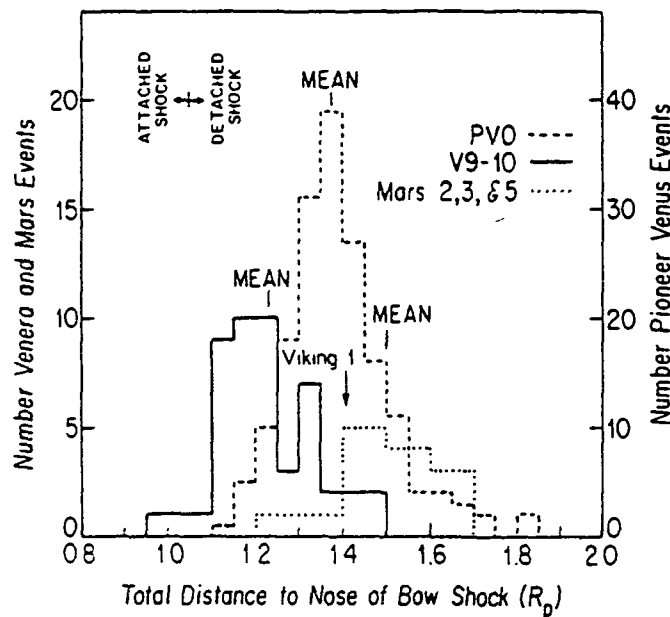
Fig. 8. The Venera 9 and 10. Pioneer Venus, and Mars 2, 3. and 5 bow shock crossings from paper 1 have all been mapped to zero-aberrated solar zenith angle by means of their average surface models in paper 1. The Viking 1 lander bow shock crossing has also been included by using the mean boundary shape derived from the orbiter measurements. In the upper left-hand corner the average height of the Venus subsolar ionopause has been marked to separate the attached and detached bow shock regimes.

from Venera and Pioneer Venus. The solutions are a function of the shape of the obstacle (e.g., $H/R_0 = 0.20$ corresponds to MP = classical Chapman-Ferraro magnetopause), the adiabatic exponent (5/3 or 2), the sonic Mach number, and the obstacle radius, which has been chosen so as to make the noses of the theoretical and observed bow shocks coincide. As in the terrestrial case a sonic Mach number of 8 was used, but again the error introduced should not be large in this hypersonic regime. The net effect of using 8 at Venus, as opposed to the $M_s = 6-7$ expected to be more typical of 0.7 AU (e.g., see Table 2 of paper 1), is to slightly underestimate the width of the ionosheath. For both the Venera and PVO observations it was found that an $H/R_0 = 0.20$ obstacle shape provided the best fit to the measured bow shock shape. In the subsolar region the observed distance between the shock and ionopause from the Venera and PVO measurements is only 60% and 90%, respectively, of that predicted by gas dynamics with $\gamma = 2$ For Venera, in fact, the effective obstacle surface passes beneath the surface of the planet. Further, the flanks of the gas dynamic obstacle needed to explain the shape of the shock flare out more than is observed for the Venus ionopause [Brace et al., 1980]. Based upon the ionospheric scale heights measured by PVO [Hartle et al., 1980], only an $H/R_0 = 0.01$ ionopause shape would have been expected. In the section devoted to solar-planetary interactions these findings will be interpreted in terms of significant cometary interactions in the low-altitude

behind the bow shock. Unlike at the earth, highly eccentric orbiters at Venus must pass through the low-altitude dayside regions at speeds sufficiently great to alias the plasma measurements [Mihalov et al., 1980, 1982]. For this reason it is highly desirable to be able to infer the flow field near the ionopause with a method that is independent of the low-altitude observations.

The Venera and PVO bow wave models are considered separately, owing to the very different altitudes at which they place the shock, as shown in Figure 8. The possible reasons for the difference in bow shock position between these missions, which we have discussed at length in paper 1 and Slavin et al. [1979b, 1980], are still the subject of controversy. Smirnov et al. [1980, 1981] and Romanov et al. [1978] favor an asymmetric shock cross section at Venus with the nonaxially symmetric IMF as the underlying cause. The near-polar-orbiting Pioneer Venus spacecraft then observes a more distant bow wave because the shock resides at higher altitudes over the poles than near the ecliptic plane where Venera 9/10 encountered it. However, as detailed in paper 1 and our earlier studies, we have found the trace of the shock surface in the aberrated terminator plane to be approximately circular at both the earth and Venus, independent of IMF orientation. Further, no anomalously large aberrations of the symmetry axis of the bow wave away from the solar wind flow direction have been observed. For this reason we favor a temporal cause for the discrepancy between Venera and PVO, with significant changes in the low-altitude solar wind interaction taking place between solar cycle minimum when the Venera measurements were taken and the solar maximum epoch of the PVO primary mission.

In Figures 9 and 10 a number of theoretical bow wave solutions are compared with the observed shock positions
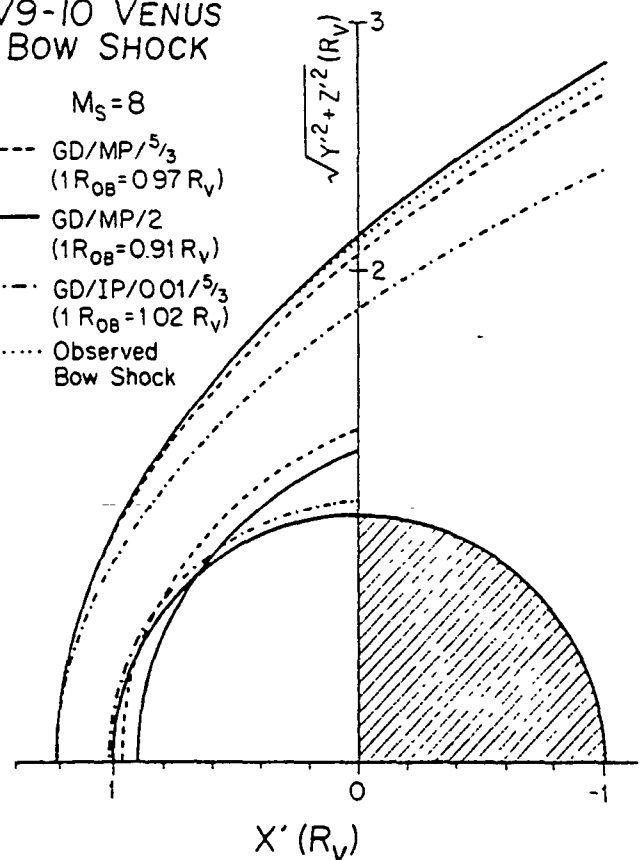

Fig. 9. The average Venera 9 and 10 bow shock model from paper 1 is compared with several gas dynamic models. They are labeled by calculation type (i.e., GD = gas dynamic), obstacle type (i.e., IP = ionopause; MP = magnetopause), H/R_0 value if IP, and the adiabatic exponent. Sonic Mach number appears at the top of the figure.

ionosheath. It will be suggested that at least for some modeling applications these processes may be regarded as. decreasing the adiabatic exponent behind the shock from the value of 2 appropriate to planets without large neutral populations extending into the solar wind. The term 'ionosheath' may then imply the presence of plasma-neutral atmosphere interactions as opposed to simply providing an alternate name for a magnetosheath surrounding a tangential discontinuity supported by an ionosphere. Finally, the evidence from all sources for such an ionospheric-cometary model of the Venus solar wind interaction will be reviewed.

Mars

In Figure 11 the Mars bow wave model surface from paper 1 is compared with a number of gas dynamic flow solutions [e.g., *Spreiter and Stahara*, 1980*a*, *b*; *Stahara et al.*, 1980] in the same manner that was employed at the earth and Venus. The best fit to the shape of the bow shock, indicated with a solid line, was produced with $M_s = 7.4$, $\gamma = 2$, and $H/R_0 = 0.03$. A sonic Mach number of 7.4 is about 20% lower than the expected mean at 1.5 AU. However, hypersonic flow in the near field (i.e., $x' > -1\ R_{ms}$) is relatively insensitive to changing Mach number beyond $M_s = 5$. The use of 7.4 because of its availability [e.g., *Spreiter and Stahara*, 1980*b*] should not be a significant source of error in the model calculation. In marked contrast with the situation at Venus, the best fit model in Figure 11 indicates that the average Martian obstacle to the solar wind ranges from 510 ($\pm 20\%$) at the subsolar point to nearly 1000 km near the terminator. The assumption of $\gamma = 5/3$, instead of $\gamma = 2$, would place the solar wind–obstacle interface at still greater altitudes. However, the small role of the neutral atmosphere in the solar
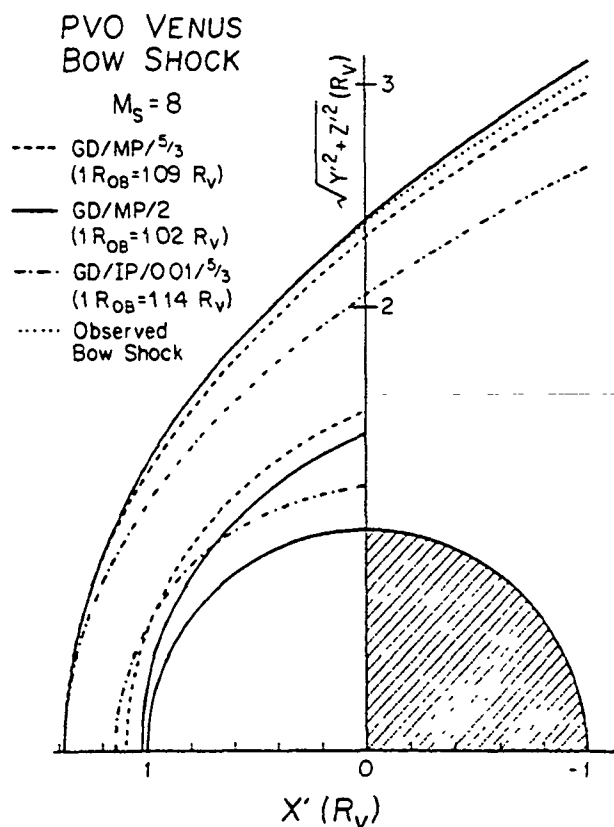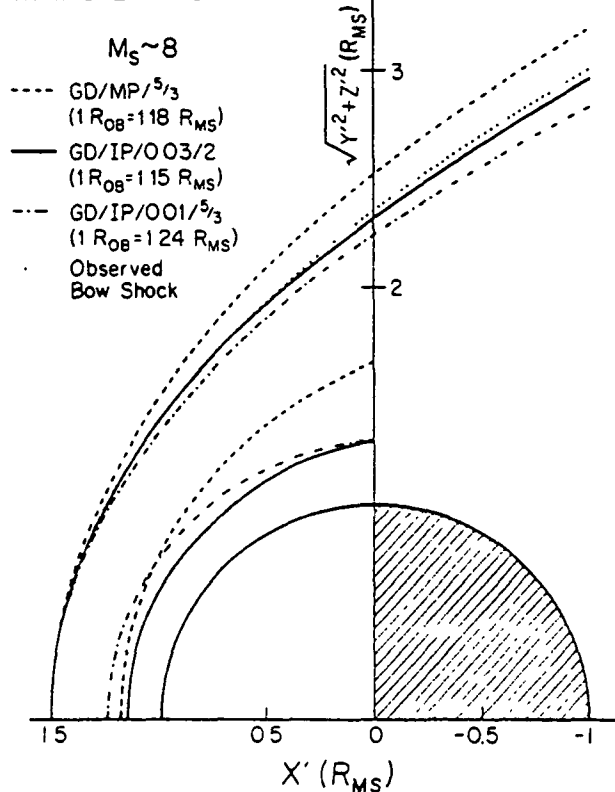

Fig. 11 The average Mars bow shock model from paper 1 is compared with a number of gas dynamic models, as in the two preceding figures.

Fig. 10. The average Pioneer Venus bow shock model from paper 1 is compared with a number of gas dynamic models, as in Figure 9.

wind interaction with Mars at altitudes above 300 km [*Cloutier et al.*, 1969] argues in favor of using the adiabatic exponent that best characterizes the flow about the earth as opposed to Venus. As treated by *Slavin and Holzer* [1982], the height of the Martian obstacle in Figure 11 appears to be far too great for this planet to be undergoing a Venus-type interaction with the solar wind. In a later section we will examine additional Mars orbiter observations with the aid of the theoretical flow models developed in the course of this study.

· This modeling of the Mars bow wave with a complete gas dynamic flow field represents an improvement over many of the earlier studies [e.g.. *Russell*, 1977*c*]. In most of those works the shock crossings were modeled empirically to determine the subsolar height of the bow wave. The Martian magnetosheath was then assumed to have the same relative thickness as that of the earth in order to infer the altitude of the stagnation point on the obstacle. However, the width of the magnetosheath is a function of obstacle shape, with thicker magnetosheath regions being necessary to redirect flow about blunter bodies [*Van Dyke*, 1958; *Spreiter and Stahara*, 1980*b*]. The model in Figure 11 shows an obstacle that is more slender than that of the earth. For this reason, previous investigations assuming the same relative magnetosheath thickness as the terrestrial case underestimate the height of the solar wind–obstacle interface by about 20%. By comparison with the other Mars studies that have used gas dynamic flow calculations [*Dryer and Heckman*, 1967; *Spreiter and Rizzi*, 1972; *Gringauz et al.*, 1973; *Bogdanov and Vaisberg*, 1975; *Breus and Verigin*, 1976; *Gringauz et al.*, 1976; *Dolginov et al.*, 1976; *Vaisberg et al.*, 1976*b*], we

have enjoyed the advantage of having a much larger number of flow models with which to work. The result has been the good fit to the shape of the bow wave in Figure 11 and hence the near field flow pattern In addition, we have based our modeling on only the adequately sampled portion of the Mars shock forward of $x' > -1 R_{ms}$. In this way the spatial biases inherent in the sparse downstream observations (e.g. see paper 1) have been avoided.

DISCUSSION

Earth

This study represents the first major comparison between gas dynamic theory and the position of the terrestrial bow shock since the *Fairfield* [1971] work conducted a decade ago. A detailed discussion of the data set and modeling techniques utilized by Fairfield is contained in paper 1. For the purposes of this investigation the main advantages of our observational shock model over that of Fairfield lie in the slightly larger fraction of a solar cycle sampled, 1965-1972 as contrasted with 1963-1968, and the greater availability of upstream parameters for the individual bow wave encounters. The shape and location of these two average bow shock models are, in fact, quite similar (see Figure 19 of paper 1).

In Fairfield the observational model of the shock was compared with the gas dynamic calculations of *Spreiter and Jones* [1963], which assumed $\gamma = 2$ and $M_s = 8.7$. Just as in this study, the theoretical magnetopause and bow shock shapes were determined to be slightly less blunt than the observations indicated. However, the Spreiter and Stahara codes now available allow for the choice of obstacle shape as an input parameter. Figure 6 displayed an excellent fit to the empirical model with $H/R_0 = 0.35$, $M_s = 8$, and $\gamma = 2$.

Accordingly, we concluded that our investigation has confirmed the good agreement between single-fluid gas dynamic theory and average dayside bow wave location obtained by Fairfield and many of the earlier works [e.g., *Gosling et al.*, 1967]. It is also important to note that both the Fairfield study and this investigation have found that the single-fluid gas dynamic models perform well when a sonic Mach number based upon total ion and electron plasma pressure and an adiabatic exponent close to 2 are used. Finally, we have found that the average shock position and shape models obtained from the individual missions of paper 1 are well ordered by M_s and not by magnetosonic or Alfvenic Mach numbers. All of these results support the validity of the gas dynamic approximation and the general applicability of fluid theory to the macroscopic description of solar wind flow past planetary size tangential discontinuity surfaces. Future investigations with a much larger data set are planned to examine quantitatively the gas dynamic predictions concerning the variation in shock position/shape with M_s; to study the limitations of the gas dynamic calculations farther downstream, where the position of the shock should be under the influence of the magnetosonic fast wave Mach cone; and, last, to document the expected gradual failure of these gas dynamic models as IMF strength increases and M_A decreases.

Venus

The problem of flow into and about a partially absorbing body in an astrophysical application was considered long ago in reference to the moon [*Tozer and Wilson*, 1967; *Sonett and Colburn*, 1968]. While there was little hope that the lunar surface material electrical conductivity could be high enough to provide for anything like the nearly total exclusion of the incident solar wind possible for a planetary ionosphere [e.g.. *Cloutier and Daniell*, 1973; *Zeleny and Vaisberg*, 1981], it was thought that sufficient deflection might occur to cause the formation of a bow shock. Under these circumstances the bow wave would remain strong in the sense that γ and upstream Mach number would determine the jump conditions, but it would move closer to the moon as the total amount of absorption increased. A sufficiently high rate of absorption could then result in the bow shock becoming 'attached' to the body with only 'limb' shocks remaining. It is now known that the moon absorbs almost all of the incident solar wind and thus prevents the development of a global shock wave [*Schubert and Lichtenstein*. 1974; *Spreiter et al.*, 1970] *Russell* [1977a] raised the possibility of a partial absorption of the solar wind at Venus in his interpretation of the Mariner 10 shock observations [*Bridge et al.*, 1974; *Ness et al.*, 1974]. In Russell's controversial analysis [*Ness*, 1977; *Russell*, 1977b], evidence that the Venus bow wave had been attached to the ionosphere during the time of the Mariner 10 flyby was presented. He estimated that the fraction of the incident flow being absorbed at that time was 33%. In Figure 8 of this study, both the Venera 9 and 10 and Pioneer Venus bow shock encounters from paper 1 were mapped to the nose position along the x' axis. The nominal top of the ionosphere is marked in the upper left-hand corner of the figure to separate the attached and detached regimes. None of the Pioneer Venus events, and only a statistically insignificant number of the Venera shock encounters, fall into the attached category. Accordingly, it is concluded that the Cytherean bow wave must nearly always be detached. However, during the solar minimum epoch of the Venera orbiter and the Mariner 10 flyby, the shock can indeed lie quite close to the planet.

The low-altitude flow field in the Venus ionosheath is examined further in Figures 12 and 13. The top panels of each figure display the exact streamline patterns from the best fit gas dynamic models in Figures 9 and 10. In both cases, although more so for the Venera model, a portion of the gas dynamic streamlines intersect the observed ionopause boundary. If there were no neutral atmosphere extending up into the ionosheath, then one might conclude that the particles on the streamlines crossing the ionopause were simply being lost to the ionosphere/atmosphere in a lunar-type interaction. However, such a conclusion would contradict the theoretical calculations indicating that the Cytherean ionosphere is a sufficiently good electrical conductor to exclude almost all of the solar wind [e.g.. *Cloutier and Daniell*, 1973; *Zeleny and Vaisberg*. 1981]. In fact. the neutral atmosphere does permeate the ionosheath [*Cravens et al.*, 1980; *Nagy et al.*, 1981]. These neutrals will interact with the solar wind plasma through charge exchange and photoion pickup to become mass/momentum/energy terms in the flow field that are not taken into account by the conventional gas dynamic calculations used in this investigation. As demonstrated in previous theoretical studies [*Biermann et al.*, 1967; *Cloutier et al.*, 1969; *Wallis*. 1973. Harel and Siscoe in *Bridge et al.*, 1976], the net result is to divert the incoming flow about the volume occupied by the neutral population. Accordingly, these interactions at Venus can result in a greater deflection of ionosheath flow at higher altitudes than would be expected from the thermal and

magnetic pressure gradients of a neutral atom free magneto-sheath [e.g., *Wallis*, 1982]. Charge exchange interactions will transfer momentum and energy from the solar wind to the hot neutral atoms they create while the pickup of cold ions created by both photoionization and charge exchange will add mass to the flow field and transfer flow energy to thermal energy. Although the detailed high time and spatial resolution particle distribution measurements required to model these processes will not be made for some time, it may be that one effect of these processes is to introduce additional degrees of freedom to the flow system. They could therefore lower the value of the adiabatic exponent (i.e., $\gamma = (n + 2)/n$ for a perfect gas) appropriate to the idealized equation of state in our gas dynamic model calculations. For these reasons it is probable that plasma-neutral atmosphere interactions, as opposed to a lunar-type absorption of a portion of the solar wind flux, are the main reasons for the small width of the Venus ionosheath relative to Earthlike magnetosheaths. The bottom panel of Figures 12 and 13 present a qualitative flow pattern that is consistent with the high-altitude gas dynamic results (i.e., top panels), the need for a general exclusion of the solar wind by the ionosphere, and the anticipated effects of plasma-neutral interactions discussed above. The solar wind plasma on the streamlines closest to the stagnation line penetrate the deepest into the

Gasdynamic Model of Flow About Venus at Solar Maximum
($M_S = 8$, $\gamma = 2$, $H/R_O = 0.20$, and 1 $R_{OB} = 101$ R_v)

Ionospheric - Cometary Model Venus Solar Wind Interaction

Solar Zenith Angle (deg.)

Fig. 13. The same as the preceding figure but for the Pioneer Venus modeling results.

Gasdynamic Model of Flow About Venus at Solar Minimum
($M_S = 8$, $\gamma = 2$, $H/R_O = 0.20$, and 1 $R_{OB} = 0.91$ R_v)

Ionospheric - Cometary Model Venus Solar Wind Interaction
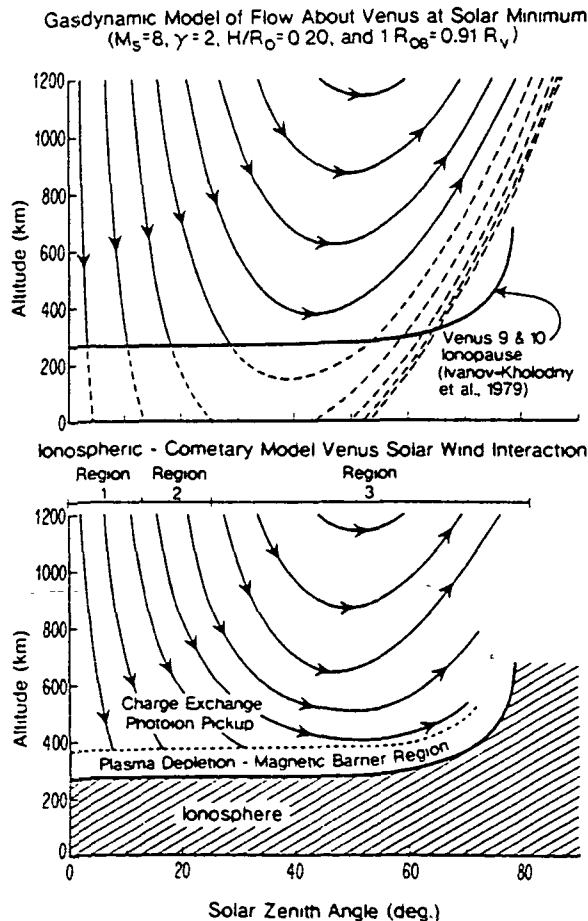
Solar Zenith Angle (deg.)

Fig. 12. In the top panel the gas dynamic flow field derived from the position and shape of the Venus bow wave measured by Venera are plotted in relation to their radio occultation ionopause [*Ivanov-Kholodny et al.*, 1979] A qualitative flow model, including the expected effects of charge exchange and photoion pickup, is displayed in the bottom panel
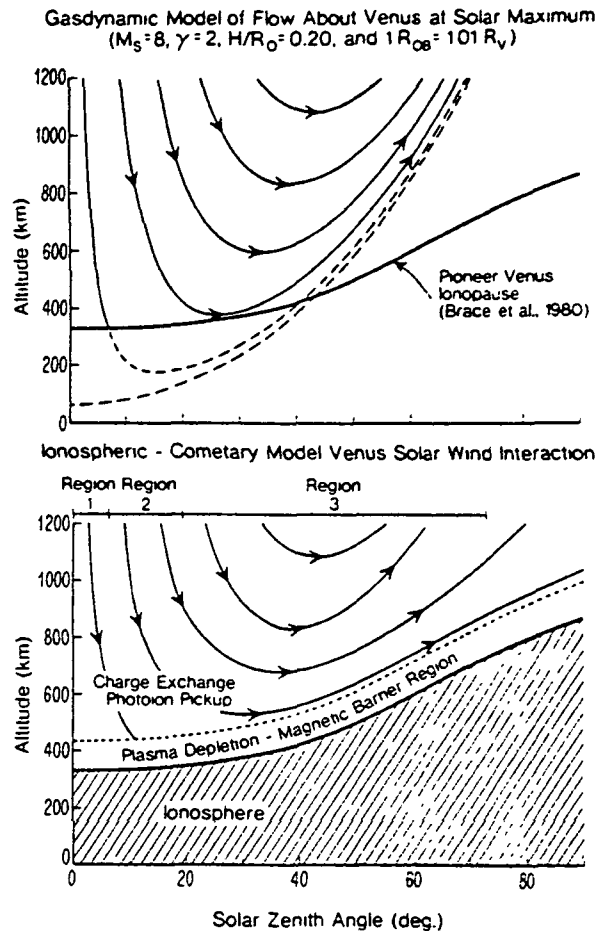
neutral atmosphere external to the ionopause and take the greatest amount of time to flow about the obstacle. These streamlines interact most strongly with the neutrals and are designated region 1 in the bottom panels. To what extent and in what manner the ionosheath plasma (i.e., solar wind + ionized neutrals + ionospheric plasma(?)) in this region flows downstream can only be determined by further observation and modeling of ionosheath phenomena (e.g., the recently discovered 'plasma clouds,' *Brace et al.* [1982]; *Russell et al.* [1982]). Region 2 is filled with the portion of the flow that interacts more weakly with the neutral atmosphere than region 1 because of its overall greater altitude. These streamlines have been drawn to follow the contour of the observed ionopause surface. Those streamlines residing at sufficiently great heights to be essentially unaffected, like the upstream flow, make up region 3. They correspond exactly to the gas dynamic results of the upper panels. The plasma depletion, or magnetic barrier, region [*Elphic et al.*, 1980] has somewhat arbitrarily been drawn as being a constant 100 km thick [*Zwan and Wolf*, 1976]. This region has not yet been well mapped observationally or intensively modeled with theory. Its actual extent and degree of depletion will vary in three dimensions. For these reasons, no attempt has been made to extrapolate the two-dimensional streamlines of Figures 12 and 13 into the depletion layer.

Figure 14 displays these same results, but from a different perspective, by showing the upstream mapping of the low-altitude flow field in the preceding two figures. The Venera 9

Venera 9 and 10
Solar Minimum Epoch

$\sqrt{X'^2 + Y'^2 + Z'^2}$

Mass Accretion
Boundary Layer

STREAMLINE
REGIONS

X' (R$_V$)

Pioneer Venus
Solar Maximum Epoch

$\sqrt{X'^2 + Y'^2 + Z'^2}$

Mass Accretion
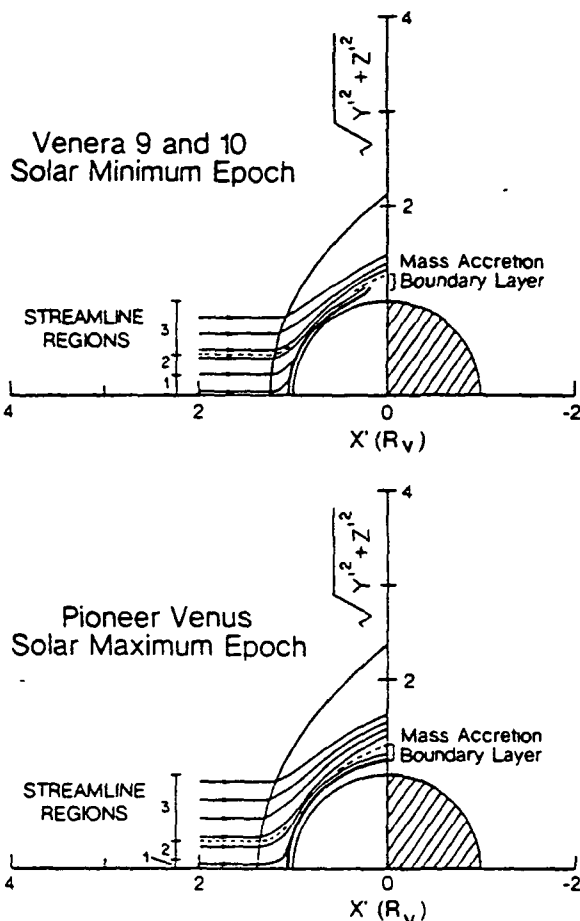Boundary Layer

STREAMLINE
REGIONS

X' (R$_V$)

Fig. 14 The results of the preceding two figures are displayed from a different perspective, which shows the fractions of the incident solar wind interacting directly with the planet and the global two-dimensional streamline pattern.

and 10 solar minimum flow field places 10% of the incident streamlines in region 1 and 10% in region 2. At solar maximum the PVO model shows a weaker interaction, with the neutrals producing a region 1 and region 2 with 1% and 9%, respectively, of the incoming streamlines. Hence, this study concludes that 10–20% of the solar wind streamlines incident over the dayside of Venus interact strongly with the planet. This result places an absolute upper limit on the mean electric potential drop across the ionosphere of approximately 0.15×60 kV = 9 kV pole to pole. However, the shielding effect of the high electrical conductivity of the ionosphere may reduce the actual drop to order 10 V or less [Cloutier and Daniell, 1973; Zeleny and Vaisberg, 1981]. Downstream, the region 1 and 2 streamlines will still be appreciably affected by the accretion of new ions and will make up the boundary layer region that has been previously observed (e.g., the Penumbra region, Gringauz et al. [1976], Vaisberg et al. [1976a]; mantle region, Spenner et al. [1980]).

As regards the factor of 2 variation in the fraction of the incident solar wind contained in regions 1 and 2, we propose that this phenomenon occurs directly as a result of the solar cycle modulation of ionopause height first discovered by Wolff et al. [1979]. In their model, ionopause altitude varies with the phase of the solar cycle. It is lowest at solar minimum because of the solar wind dynamic pressure peak and solar EUV emission trough that occur during the low portion of the cycle. Hence, near solar minimum the number

of atmospheric neutrals exposed to the solar wind will be maximized in relation to the rest of the cycle. Theoretical support for a factor of 2 increase in the strength of the cometary component of the Venus interaction caused by the relatively small change in ionopause altitude in Figures 12 and 13 is found in the calculations by Gombosi et al. [1981]. In their study a gas dynamic flow field was assumed, and the total number of charge exchange reactions in the ionosheath was computed by using Pioneer Venus neutral atmosphere models. They found that 1–16% of the incident protons underwent charge exchange as a function of the assumed height of the ionopause. Hodges and Tinsley [1981] have recently produced the same order of magnitude results as Gombosi et al. [1981] in a modeling study of the Venus exosphere. In the Gombosi et al. [1981] work a change in ionopause height of the amount shown in the figures produces a variation of only about 30% in the total number of charge exchange interactions. By comparison, we found a 100% growth in the solar wind flux in regions 1 and 2. However, since their model does not take into account photoion pickup, the modification of the flow field with mass addition, or the actual shape of the ionopause, the factor of 3 difference between our model of the observations and their theoretical calculations does not appear to be serious. In addition, McElroy et al. [1982] have estimated that ionosheath electron impact ionization will be a comparable or greater source of oxygen ions than photoionization. Hopefully, the Pioneer Venus orbiter will continue to be funded until its reentry in the early 1990's. In this event it should be possible to reach some definite conclusion about the existence and causes of the solar cycle ionosheath variations we have proposed.

On the basis of our modeling results it appears necessary to briefly review and evaluate the current state of theory and observation concerning the solar wind interaction with Venus. Prior to the Pioneer Venus mission, three factors were stressed as being of possibly great importance to the physics of the interaction: cometary processes involving the neutral atmosphere [Wallis, 1972, 1973; Bridge et al., 1976], ionospheric currents induced by the solar wind [Cloutier and Daniell, 1973; Cloutier et al., 1982], and the effects of any small intrinsic magnetic fields [Russell, 1976a, b]. Low-altitude nightside PVO measurements [Russell et al., 1980] have now confirmed the Venera 4 results of Dolginov et al. [1969], indicating no significant planetary magnetic field. The strong plasma-neutral atmosphere interaction with a large reduction in solar wind Mach number upstream of the bow wave, proposed by Wallis, has also failed to materialize [Mihalov et al., 1980, 1982; Slavin et al., 1980]. However, the more modest cometary interaction within the ionosheath, proposed by this study, appears consistent with the theoretical models of Harel and Siscoe (reported in Bridge et al. [1976]) as well as with the recent Gombosi et al. [1980, 1981] and L. M. Zeleny and O. M. Vaisberg (unpublished manuscript, 1981) calculations. Observationally, the presence of a suprathermal ion layer just exterior to the ionopause [Taylor et al., 1980] and discovery of O$^-$ ions being carried off by the solar wind in the downstream ionosheath [Mihalov et al., 1980; Mihalov and Barnes, 1981; Intriligator, 1982] along with clouds of apparently ionospheric plasma [Brace et al., 1982; Russell et al., 1982] indicate the presence of strong interactions in the low-altitude ionosheath. However, the exact role of the neutral atmosphere in

these processes has not yet been determined. It has not yet been demonstrated that sufficient mass is being picked up to account for the observed slowing of the solar wind near the flanks of the ionopause (*Mihalov et al.* [1982]; H. Perez-de-Tejada, unpublished manuscript, 1982). Finally, while many aspects of the interaction remain unresolved, the incident solar wind is indeed diverted about the planet by large induction currents within the ionosphere [*Elphic et al.*, 1980] as predicted by the Cloutier and Daniell models. Pioneer Venus has gone on to present the basic unipolar induction concept with a number of new phenomena to be incorporated, such as ionospheric flux ropes [*Elphic et al.*, 1980], a Zwan-Wolf plasma depletion layer exterior to the ionopause [*Zwan and Wolf*, 1976; *Elphic et al.*, 1980; *Vaisberg et al.*, 1980], occasional intervals of strong ionospheric magnetic fields [*Elphic et al.*, 1980; *Luhmann et al.*, 1980], and a boundary layer along the flanks of the ionopause [*Perez-de-Tejada*, 1980; *Spenner et al.*, 1980; *Taylor et al.*, 1980]. Definitive observations regarding many of these questions will probably require a large number of high time resolution measurements from a low-altitude orbit skimming the iono-sheath-ionosphere interface such as that being considered for VOIR.

Mars

The solar wind interaction with Mars has been the subject of controversy for over 15 years. As considered in the reviews by *Michel* [1971], *Hill and Michel* [1975], *Bauer* [1976], *Ness* [1979], *Russell* [1979], *Siscoe and Slavin* [1979], and *Gringauz* [1981], the very limited particles and fields measurements gathered by the Mariner 4 distant flyby and the Mars 2, 3, and 5 orbiters have not provided a definitive picture of the solar wind interaction with this planet. While the bow shock has been sampled on numerous occasions, none of these satellites probed the region below 1000 km where the solar wind interaction must take place. Further, the total number of observations were small, and the instruments were often turned off during the periapsis portions of their orbits [*Gringauz*, 1976]. Given the nature of the existing data, there has naturally developed a question over whether Mars is magnetized at all or stands off the solar wind through a Venus-type solar wind interaction.

For this reason it is important that the average flow pattern about Mars that is displayed in Figure 11 does not appear at all like that of Venus in Figures 9 and 10. Given the same adiabatic exponents, the Mars gas dynamic obstacle lies well above the ionosphere proper while the Venusian obstacle resides at or below the altitude of the ionosphere. Figure 8 further stresses this difference between Mars and Venus by comparing the nose positions of the Martian bow shock along with the Venera and PVO observations at Venus from paper 1. While all three distributions overlap to some degree, the Mars bow wave is indeed the most distant overall and is far removed from the attached regime. *Slavin and Holzer* [1982] have conducted a study of the Mars solar wind-obstacle interface in Figure 11 and the ability of the ionosphere to support it. Using PVO Venus interaction models, they showed that the Martian ionosphere could not stand off the average solar wind at these heights, even if it were always magnetized through the capture of IMF field lines, as happens only sometimes at Venus. Their results supported the general findings reached by some of the earlier studies, which did not consider induced magnetic fields
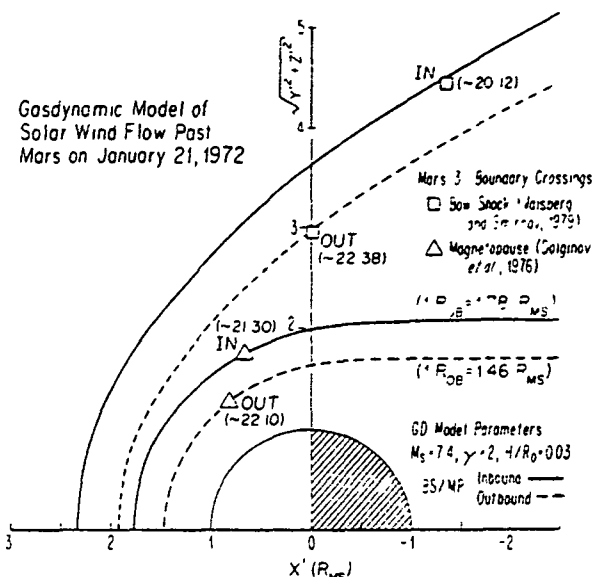

Fig. 15. The inbound and outbound January 21, 1972, Mars 3 bow shock and magnetopause crossings have been modeled separately with the same gas dynamic solution found to well represent the average Mars observations in Figure 12.

[*Gringauz*, 1976; *Intriligator and Smith*, 1979]. Slavin and Holzer further concluded that if Mars were in fact lacking a significant intrinsic magnetic field, then the solar wind would often push the ionosphere to altitudes below 300 km, where plasma-neutral atmosphere interactions would absorb and deflect the flow [*Cloutier et al.*, 1969]. Such an interaction with the tenuous atmosphere of Mars would produce a bow wave location lower than that of Venus. Figure 8 shows this not to be the case. Further, no such low-altitude 'iono-pauses' have been observed in the extensive Viking radio occultation measurements [*Lindal et al.*, 1979].

Using the scale heights measured by the Viking landers [*Hanson et al.*, 1977], Slavin and Holzer went on to show that ionospheric plasma pressure will make a negligible contribution to standing off the solar wind at the altitudes of the gas dynamic Mars obstacle in Figure 11. With this knowledge the effective dipole magnetic moment of Mars may be computed by using the classical relationship between magnetic moment and stand-off distance for a dipole in the solar wind under the assumption of terrestrial-type magnetospheric current systems [e.g., *Spreiter et al.*, 1966; *Holzer and Slavin*, 1978]

$$M = (2\pi P_{sw} R_s^6 \, k/f^2)^{1/2} \qquad (2)$$

where k/f^2 is a constant equal to 0.59, and R_s is the magnetopause stand-off distance, 3900 km. The result obtained by Slavin and Holzer was $1.4 \pm 0.6 \times 10^{22}$ G cm³, which is sufficient to produce a small magnetosphere at Mars.

Having briefly reviewed the analysis of Slavin and Holzer, this investigation makes further application of gas dynamic modeling to the Mars interaction problem by examining some individual events from the published Mars orbiter records. In particular, the January 21, 1972, observations of Mars 3 are considered in Figure 15. Those measurements have been interpreted by the magnetometer [*Dolginov et al.*, 1973] and Faraday cup [*Gringauz et al.*, 1974] experimenters as depicting a brief encounter with an intrinsic field magneto-sphere between approximately 21:30 and 22:10 (Moscow

Bow Shock Crossings

△ Mars 2
(20:09, 12/14/71)

O Mars 3
(02:33, 12/15/71)

GD Model

$M_S = 4.0$, $\gamma = 2$
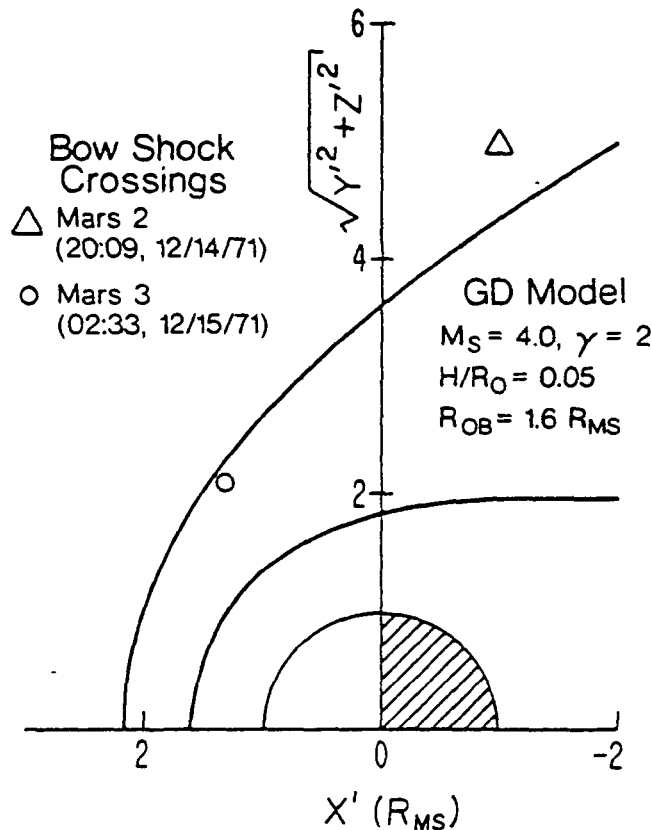$H/R_O = 0.05$
$R_{OB} = 1.6 \, R_{MS}$

X' (R_{MS})

Fig. 16 Both the study by *Bogdanov and Vaisberg* [1975] and paper 1 noted some unusually distant bow shock crossings by Mars 2 and 3 on December 14–15, 1971. These crossings are modeled with a low-Mach-number gas dynamic calculation by using an obstacle shape close to that determined in Figure 11.

time). *Wallis* [1975] and *Russell* [1978a, b] have disputed this analysis on numerous grounds, discussed in *Slavin and Holzer* [1982] and many of the review papers cited earlier. As shown, we have modeled the Dolginov/Gringauz magnetopause crossings and the Vaisberg and Smirnov shock encounters by using the average gas dynamic model from Figure 11. The agreement is excellent between the model and the observations when the inbound and outbound passes are considered separately, but good results are also apparent when only average magnetopause/bow shock positions are used. The first pair of boundary encounters are well matched with a subsolar obstacle radius of 1.78 R_{MS} (i.e., 1 R_{MS} = 3390 km) while a smaller $R_{ob} = 1.46 \, R_{MS}$ is required for the outbound encounters. Such a situation might occur if, for example, a pressure pulse in the solar wind (e.g., an interplanetary shock wave) arrived while Mars 3 was within the magnetosphere. The height of the magnetopause would then be depressed until the spacecraft again found itself in the magnetosheath. This scenario would also explain the lower altitude of the exit from the magnetosphere as compared with the entry identified by Dolginov/Gringauz.

Solar wind ion speeds were obtained from the plasma analyzer measurements, but no reliable densities and temperatures [*Dolginov*, 1978a]. *Bogdanov* [1975; see *Dolginov*, 1978a] has assembled solar wind dynamic pressure values for many of the Mars 2 and 3 passes near the planet by using the in situ ion speed measurements and densities extrapolated from IMP 6 at 1 AU. For the January 21, 1972, events the Mars 2 and IMP 6 parameters are $V_{sw} = 500$ km/s and $n =$

1.2 cm^{-3} to yield $P_{sw} = 0.6 \times 10^{-8}$ dynes/cm^2. While solar wind dynamic pressures determined in this manner are subject to significant errors, it is desirable to examine the planetary magnetic moments that may be derived from the obstacle sizes in Figure 15 by using (2). The effective dipole moments arrived at are 3.3×10^{22}, 1.8×10^{22}, and 2.5×10^{22} G cm^3 for the inbound, outbound, and average stand-off distances. These values are similar to, but slightly greater than, the 1.8×10^{22} G cm^3 *Dolginov* [1978a, b] determined by inversion of the magnetic field vectors near penapsis and the $1.4 \pm 0.6 \times 10^{22}$ G cm^3 obtained from gas dynamic modeling of bow shock shape/position by *Slavin and Holzer* [1982]. Hence, given the uncertainties in the solar wind dynamic pressure on January 21, 1972, our gas dynamic analysis of these Mars 3 observations support the conclusion that Mars possesses a significant intrinsic magnetic field and does not undergo a Venus-type ionospheric interaction with the solar wind.

In paper 1 a pair of shock crossings by Mars 2 and 3, separated by only about 7 hours on December 14–15, 1971, were seen to lie far outside of the average bow wave position. They were noted earlier by *Bogdanov and Vaisberg* [1975], who calculated a subsolar obstacle radius of 1.8 R_{MS} for the event. In the absence of upstream parameters, *Vaisberg* [1976] suggested that these crossings might be more the result of low solar wind Mach numbers producing a thicker-than-average magnetosheath than low dynamic pres-

MARS BOW SHOCK
$(X' > -1 \, R_{MS})$

△ Mars 2 (1971-2)
+ Mars 3 (1971-2)
□ Mars 5 (1974)
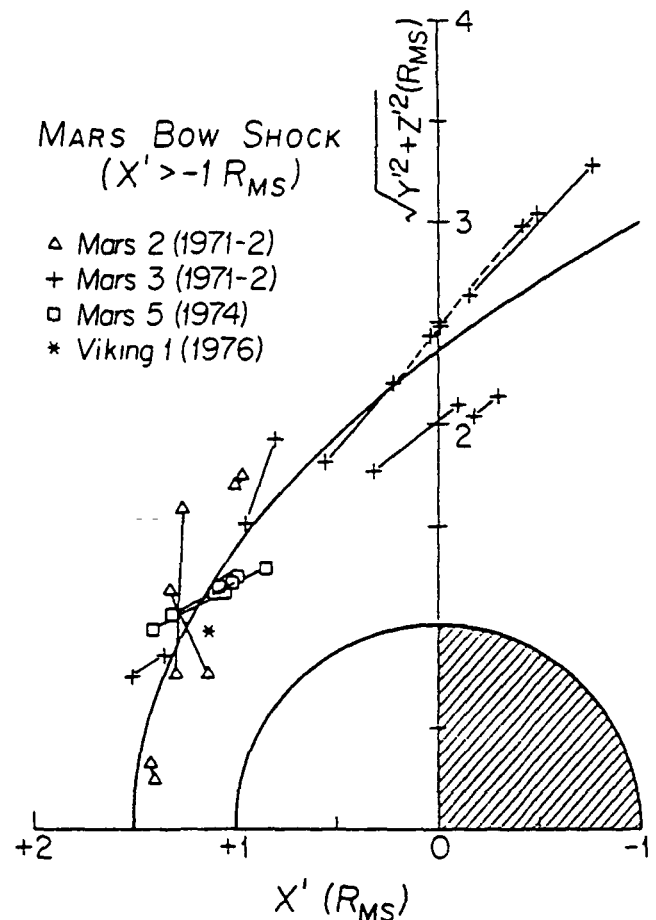* Viking 1 (1976)

X' (R_{MS})

Fig. 17. The Viking 1 lander bow shock crossing identified by *Cragin et al.* [1982] is plotted in aberrated coordinates and compared with the Mars 2, 3, and 5 bow wave encounters considered in paper 1.

sure causing an expansion of an intrinsic field magneto-
sphere. We examine this question in Figure 16 with a low-
Mach-number gas dynamic model based on an obstacle
shape similar to those utilized in Figures 11 and 15. The
$M_s = 4$ flow solution yields a moderately good fit to the
crossings but with a difference in flare angle that suggests a
sightly lower Mach number as being optimum. This point
was not pursued further because lack of funds prevented
production of lower-Mach-number models. However, the
important result is that the assumption of an unusually low
Mach number still does not negate the need for a solar wind
stand-off distance far in excess of the height at which an
ionopause might form. Hence, not only low-Mach-number
conditions but also a large-diameter obstacle, such as an
expanded intrinsic field magnetosphere, appear necessary to
explain the December 14–15, 1971, Mars orbiter bow wave
observations.

Recently, the high-altitude (i.e., 16,000 to 350 km) Viking
lander retarding-potential analyzer measurements have been
examined by *Cragin et al.* [1982]. As detailed in their paper,
a distinct peak in the rms deviations of Viking 1 lander RPA
electron fluxes was observed near the altitude of the mean
Mars bow shock determined by the Mars 2, 3, and 5 orbiters.
They suggest that this signature is associated with wave
particle interactions in the Martian foreshock. In Figure 17
we have aberrated and plotted the Cragin-et-al.-suggested
shock encounter at 1700-km altitude; this is relative to the
Soviet orbiter crossings modeled in paper 1. The agreement
is good with the Viking 1 lander datum, only somewhat
lower in altitude than the average as seen in Figure 8.
Further, there is no evidence for the larger solar maximum/
minimum variation very evident in the Venus shock observa-
tions. The Viking 2 lander followed a different trajectory,
which did not take it outside of the magnetosheath.

Figure 18 reproduces the Viking 1 electron current rms
deviation and mean value as a function of altitude from
Cragin et al. [1982] for comparison with our gas dynamic
Mars flow model in Figure 11. As shown by cross hatching at
the top and bottom of the figure, the gas dynamic model at a
solar zenith angle of 40° places the obstacle altitude at 490
km if the bow shock is assumed to lie near the sudden jump
in σ near 1850 km. Given the very limited nature of the
measurements, it may be argued that the shock could have
lain somewhere else between 3000 and 700 km. However, it
is interesting to note that the theoretical obstacle in Figure 18
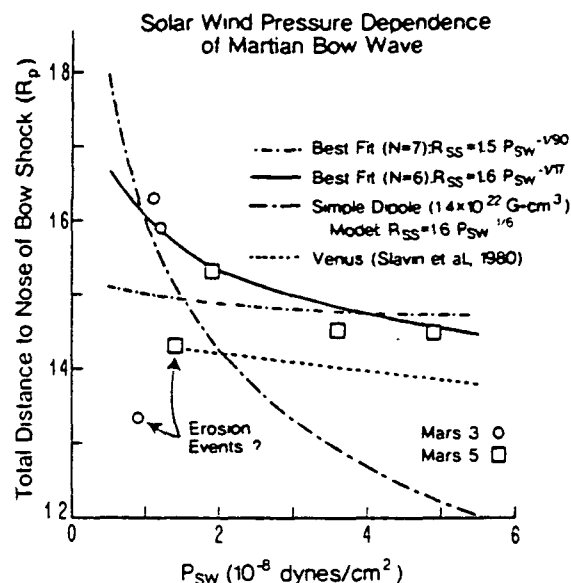
Fig. 19. Seven Mars 3 and 5 shock crossings for which reliable
solar wind dynamic pressure (i e.. $1.16 \, n_p/m_p V^2$) values exist have
been graphed against P_{sw}

falls 200–300 km below the rapid drop in electron flux near
700–800 km, which Cragin et al. suggest might indicate entry
into a plasma depletion layer similar to that at Venus. Such a
thickness is similar to that predicted for Mars by *Zwan and
Wolf* [1976] and observed by *Elphic et al.* [1980] at Venus.
In agreement with the results of *Intriligator and Smith* [1979]
and *Slavin and Holzer* [1982], Cragin et al. found that the
ionosphere of Mars could not have stood off the solar wind
on this occasion for any reasonable set of ionospheric
plasma conditions.

In Figure 19 the dependence of the height of the Mars bow
shock upon solar wind dynamic pressure is investigated. For
seven of the Mars shock crossings in paper 1 there exists
either in situ dynamic pressure measurements [i.e., Mars 5;
Dolginov, 1976] or good agreement between the 1 and 1.5
AU solar wind speed observations during the interval for
which density was extrapolated to Mars orbit [*Dolginov*,
1978a]. The average shape of the shock from paper 1 was
then used to map each of these four Mars 5 and three Mars 3
shock encounters down to the nose position with the results
plotted in Figure 19. The formal errors associated with these
mappings caused by the uncertainties in the mean surface
(see Table 7 of paper 1) and the locations of the crossings
average about 0.05 R_{MS}. For the sake of comparison with an
ionospheric interaction we have also displayed the distance
to the nose of the Venus bow wave as a function of upstream
dynamic pressure determined with the Pioneer Venus obser-
vations by *Slavin et al.* [1980]. The exponential variation of
ionospheric plasma pressure with altitude makes Venus a
relatively incompressible obstacle, as can be seen in the
small slope of the dashed line in the figure. The much
stronger pressure dependence of a simple magnetic dipole of
magnitude 1.4×10^{22} G cm^3 is plotted with a long-short
dashed line. While the few Mars data points do not contra-
dict this simple dipole relationship at low P_{sw}, there is only a
slight additional decrease in shock distance as pressure
increases above 2×10^{-8} dynes/cm^2. There are also two
crossings at relatively low pressures. To emphasize the
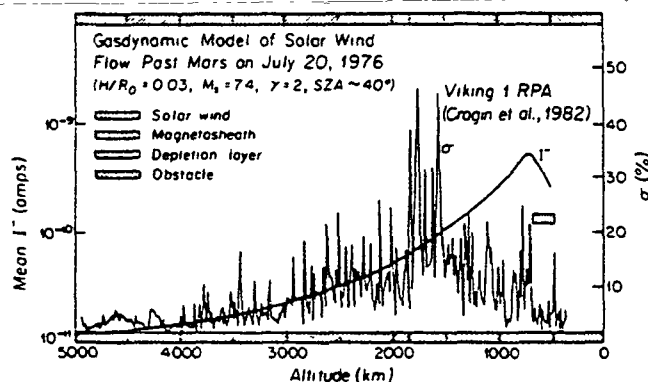potentially strong role of magnetic reconnection in determin-

Fig. 18. The gas dynamic flow model describing the average
Mars observations in Figure 12 is used to model the Viking 1 lander
RPA mean negative current and coefficient of variation measure-
ments of *Cragin et al.* [1982].

ing the configuration of a planetary magnetosphere with a high ionospheric electrical conductivity [*Rassbach et al.,* 1974], we have speculatively labeled these two points as erosion events. Best fits to all seven of the points, with the lowest excluded, are indicated. In both cases the pressure dependence is weaker than that of a simple dipole but stronger than at Venus. Although the presently available observations do not warrant additional modeling, we note for future investigations that ionospheric induction currents can be expected to stiffen the Martian dipole field lines to compression in a fashion analogous to that predicted for the small magnetosphere of Mercury [*Hood and Schubert,* 1979; *Suess and Goldstein,* 1979]. The results in Figure 19, suggesting a Venus-type dependence at higher dynamic pressures and an Earthlike response at lower pressures, may be quite reasonable for a small Martian magnetosphere.

CONCLUSIONS

1. The finding by *Fairfield* [1971] that the average position of the dayside bow shock/magnetopause boundaries is well predicted by single-fluid gas dynamic theory has been confirmed and extended. The new gas dynamic code of *Spreiter and Stahara* [1980a] is found to improve the agreement between theory and experiment by allowing for the specification of an obstacle shape based upon magnetopause observations as opposed to using less realistic theoretical models. The average locations and shapes of the forward bow shock determined by four different satellite missions have been found to be well ordered by solar wind dynamic pressure and sonic Mach number. A single-fluid adiabatic exponent of 2 produced better gas dynamic fits to the observed width of the magnetosheath than a value of 5/3. On the basis of these results it is concluded that the gas dynamic approximation to the fluid description of solar wind impingement on the terrestrial magnetosphere is generally valid for average upstream conditions.

2. Application of gas dynamic modeling to Venus has shown that the ionosheath is significantly narrower than would be predicted for a simple terrestrial-type magnetosheath of comparable shape. Further, the ionosheath is thinner at solar minimum in the Venera observations than at solar maximum as measured by Pioneer Venus. The most probable causes of both the overall thinness of the ionosheath and its apparent solar cycle modulation are the ionized neutral pickup and solar wind–exosphere charge exchange processes taking place in the ionosheath. The lower ionopause [*Wolff et al.,* 1979] during cycle minimum will enhance the number of atmospheric neutrals exposed to the solar wind by allowing the incoming flow to penetrate closer to the planet than is the case at solar maximum. From the Venera and PVO gas dynamic flow models it is estimated that 20% and 10%, respectively, of the incident solar wind streamlines are significantly modified by plasma-neutral particle interactions.

3. Gas dynamic modeling of the Mars interaction, unlike the situation at Venus, places the solar wind–obstacle interface well above the heights at which this planet could stand off the solar wind in the absence of an intrinsic magnetic field. It was found that the bow shock crossings observed by Mars 3 on January 21, 1972, were indeed consistent with this spacecraft having encountered a modest intrinsic field Martian magnetosphere near periapsis, as maintained by *Dolginov et al.* [1973] and *Gringauz et al.* [1974]. Because its

magnetic moment is small, the ionosphere and neutral atmosphere may be expected to sometimes participate directly in the solar wind interaction through induction and, more rarely, cometary processes when the solar wind dynamic pressure is high or the dayside magnetosphere is significantly eroded by reconnection. Possible evidence for such effects was found in the observed dependence of bow wave altitude upon upstream dynamic pressure.

REFERENCES

Bame, S. J., J. R. Asbridge, J. T. Gosling, M. Halbig, G. Paschmann, N. Sckopke, and S. Rosenbauer, High temporal resolution observations of electron heating at the bow shock, *Space Sci. Rev., 23,* 75, 1979.

Bauer, S. J., Solar wind control of the extent of planetary ionospheres, Solar Wind Interactions with the Planets Mercury, Venus, and Mars, *NASA SP-397,* edited by N. F. Ness, pp. 47–62, 1976.

Biermann, L., B. Brosowski, and H. U. Schmidt, The interaction of the solar wind with a comet, *Solar Phys., 1,* 254, 1967.

Bogdanov, A. V., Investigation of the ion component of plasma near the solar wind-Mars interaction zone, Doctoral thesis (in USSR), 1975

Bogdanov, A. V., and O. L. Vaisberg, Structure and variations of the solar wind-Mars interaction region, *J. Geophys. Res., 80,* 487, 1975.

Brace, L. H., R. F. Theis, W. R Hoegy, J. H Wolfe, J. D. Mihalov, C. T. Russell, R. C. Elphic, and A. F. Nagy, The dynamic behavior of the Venus ionosphere in response to the solar wind interaction, *J. Geophys. Res., 85,* 7663, 1980.

Brace, L. H., H. A. Taylor, T. I. Gombosi, A. J. Kliore, W. C. Knudsen, and A. F. Nagy, The ionosphere of Venus Observations and their interpretation, in *Venus,* edited by D. M Hunten, L. Colin, and T. M. Donahue, University of Arizona Press, Tempe, Ariz., 1982.

Brace, L. H., R. F Theis, and W. R. Hoegy, Plasma clouds above the ionopause of Venus and their implications, *Planet. Space Sci., 30,* 29, 1982.

Breus, T. K., and M. I. Vengin, Investigation of solar plasma near Mars, 4, Comparison of results of simultaneous plasma and magnetic measurements on Mars 2, *Cosmic Res., 14,* 359, 1980

Bridge, H. S., A. J. Lazarus, C. W. Snyder, E. J. Smith, L. Davis, P. J. Coleman, Jr., and D. E. Jones, Plasma and magnetic fields observed near Venus, *Science, 158,* 1669, 1967.

Bridge, H. S., A. J. Lazarus, J. D. Scudder, K. W. Ogilvie, R. E. Hartle, J. R. Asbridge, S. J Bame, W. C. Feldman, and G. L. Siscoe, Observations of the Venus encounter by the plasma science experiment on Mariner 10, *Science, 183,* 1293, 1974.

Bridge, H. S., R. E Hartle, A. J. Lazarus, K. W. Ogilvie, J. D. Scudder, G. L. Siscoe, and C. M Yeates, Interaction of the solar wind with Venus, Solar Wind Interaction With the Planets Mercury, Venus, and Mars, *NASA SP-397,* edited by N. F. Ness, pp. 63–79, 1976.

Burlaga, L. F., and K. W. Ogilvie, Observations of the magnetosheath-solar wind boundary, *J. Geophys. Res., 73,* 6167, 1968.

Chao, J. K., and M. J. Wiskerchen, The ratio of specific heats for postshock plasmas of a detached bow shock: An MHD model, *J. Geophys. Res., 79,* 4769, 1974.

Chaussee, D. S., S. S. Stahara, and J. R. Spreiter, Axisymmetric implicit blunt-body computation of solar wind flows past planets, *AIAA J., 16,* 647, 1978.

Cloutier, P. A., and R. E. Daniell, Ionospheric currents induced by

the solar wind interaction with planetary atmospheres, *Planet Space Sci.*, *21*, 463, 1973.

Cloutier, P. A., M. B. McElroy, and F. C. Michel, Modification of the Martian ionosphere by the solar wind, *J. Geophys. Res.*, *74*, 6215, 1969.

Cloutier, P A., T. F Tascione, R. E. Daniell, H A. Taylor, and R. S. Wolff, Physics of the interaction of the solar wind with the ionosphere of Venus: Flow/field models, in *Venus*, edited by D. M. Hunten, L Colin, and T M. Donahue, University of Arizona Press, Tempe, Ariz., 1982.

Cragin, B L., W B Hanson, and S Sanatani, The solar wind interaction with Mars as seen by the Viking retarding potential analyzers, *J Geophys. Res*, *87*, 4395, 1982.

Cravens, T. E., T. I. Gombosi, and A. F. Nagy, Hot hydrogen in the exosphere of Venus, *Nature*, *283*, 178, 1980.

Dolginov, Sh. Sh, E G Eroshenko, and L. N Zhuzgo, Magnetic field investigation with interplanetary station Venera 4, *Cosmic Res.*, *6*, 469, 1969

Dolginov, Sh Sh., The magnetosphere of Mars, in *Physics of Solar Planetary Environments*, edited by D J. Williams, pp. 872–888, AGU, Washington, D. C., 1976.

Dolginov, Sh Sh., On the magnetic field of Mars: Mars 2 and 3 evidence, *Geophys. Res Lett.*, *5*, 89, 1978a.

Dolginov, Sh. Sh., On the magnetic field of Mars: Mars 5 evidence, *Geophys. Res Lett.*, *5*, 93, 1978b.

Dolginov, Sh. Sh., The magnetic field of Mars, *Cosmic Res.*, *16*, 204, 1978c

Dolginov, Sh. Sh., E G. Eroshenko, and L. N. Zhuzgo, Magnetic field in the very close neighborhood of Mars according to data from the Mars 2 and 3 spacecraft, *J. Geophys. Res.*, *78*, 4779, 1973.

Dolginov, Sh. Sh., E R Eroshenko, L. N Zhuzgo, V. A. Sharova, K I. Gringauz, V V Bezukikh, T K. Breus, M I Vengin, and A. P. Remizov, Magnetic field and plasma inside and outside the Martian magnetosphere, Solar Wind Interactions With the Planets Mercury, Venus, and Mrs, edited by N. F. Ness, pp. 1–20, *NASA SP-397*, 1976.

Dolginov, Sh. Sh., L. N. Zhuzgov, V A. Sharnova, and V. B. Buzin, Magnetic field and magnetosphere of the planet Venus, *Cosmic Res.*, *16*, 657, 1978.

Dryer, M., Solar wind interactions-hypersonic analogue, *Cosmic Electrodvn.*, *1*, 115, 1970

Dryer, M., Comparison of experimental and gas dynamic jumps across the earth's shock, *J Geophys Res.*, *76*, 1070, 1971.

Dryer, M., and G R Heckman, On the hypersonic analogue as applied to planetary interactions with the solar plasma, *Planet. Space Sci.*, *15*, 515, 1967.

Elphic, R. C., C. T. Russell, J. A. Slavin, and L. H. Brace, Observations of the dayside ionopause and ionosphere of Venus, *J. Geophys Res.*, *85*, 7679, 1980

Fairfield, D. H., Average and unusual locations of the earth's bow magnetopause and bow shock, *J. Geophys. Res.*, *76*, 6700, 1971.

Formisano, V, Orientation and shape of the earth's bow shock in three dimensions, *Planet. Space Sci.*, *27*, 1151, 1979.

Gombosi, T. I., T. E. Cravens, A F. Nagy, R. C. Elphic, and C. T. Russell, Solar wind absorption by Venus, *J. Geophys. Res.*, *85*, 7747, 1980.

Gombosi, T. I., M Horanyi, T E Cravens, A. F. Nagy, and C. T. Russell, The role of charge exchange in the solar wind absorption by Venus, *Geophys. Res Lett.*, *8*, 1265, 1981.

Gosling, J. T., J. R. Asbridge, S. J. Bame, and I. B. Strong, Vela 2 measurements of magnetopause and bow shock positions, *J. Geophys. Res.*, *72*, 101, 1967.

Greenstadt, E. W., and R W Fredricks, Shock systems in collisionless space plasmas, in *Space Plasma Physics*, vol 2, edited by A G. W. Cameron, p. 807, National Research Council, Washington, D. C., 1979

Gringauz, K. I, Interaction of the solar wind with Mars as seen by charged particle traps on Mars 2, 3, and 5 satellites, *Rev. Geophys. Space Phys.*, *14*, 391, 1976.

Gringauz, K. I., A comparison of the magnetospheres of Mars, Venus, and Earth, *Advan. Space Res.*, *1*, 5, 1981.

Gringauz, K. I., V. V. Bezrukikh, L. S. Musatov, and T K. Breus, Plasma measurements in the vicinity of Venus by the space vehicle Venera 4, *Cosmic Res.*, *6*, 350, 1968.

Gringauz, K. I., V. V Bezrukikh, G. I. Volkov, L. S Musatov, and T K Breus, Interplanetary plasma disturbances near Venus

determined from Venera 4 and Venera 6 data, *Cosmic Res*, *8*, 393, 1970.

Gringauz, K. I., V. V. Bezrukikh, G. I. Volkov, T. K Breus, L. S. Musatov, L. P. Havkin, and G. F Sloutchenkov, Results of solar plasma electron observations on Mars 2 and Mars 3, *J Geophys Res.*, *78*, 5808, 1973.

Gringauz, K. I., V. V. Bezrukikh, T. K. Breus, M. I. Vengin, G. I Volkov, and A. V. D'yachkov, Characteristics of electrons along the orbits of artificial Mars satellites Mars 2 and Mars 3, *Cosmic Res.*, *12*, 535, 1974.

Gringauz, K. I., V. V. Bezrukikh, T K. Breus, T. Gombosi, A. P Remizov, M. I. Vengin, and A. I. Volkov, Plasma observations near Venus on board the Venera 9 and 10 satellites by means of the wide angle plasma detectors, in *Physics of Solar Planetary Environments*, edited by D. J. Williams, AGU, Washington. D C., 1976

Hanson, W. B., S. Santini, and D R. Zuccaro, The Martian ionosphere as observed by the Viking retarding potential analyzers, *J. Geophys. Res.*, *82*, 4351, 1977

Hartle, R. E., H. A Taylor, Jr., S J Bauer, L H. Brace, C. T. Russell, and R. E. Daniell, Jr., Dynamical response of the dayside ionosphere to the solar wind, *J. Geophys. Res.*, *85*, 7739, 1980.

Harvey, C. C., M B. Bavassano-Cattaneo, M Dobrowolny, S Orsini, A. Mangeney, and C. T. Russell, Correlated wave and particle observations upstream of the earth's bow shock, *J. Geophys. Res.*, *86*, 4517, 1981.

Hill, T. W., and F. C. Michel, Planetary magnetospheres, *Rev. Geophys. Space Phys.*, *13*, 967, 1975

Hodges, R. R., Jr., and B. A. Tinsley, Charge exchange and the Venus ionosphere as the source of hot exospheric hydrogen, *J. Geophys. Res.*, *86*, 7649, 1981.

Holzer, R. E., and J. A. Slavin, Magnetic flux transfer associated with expansions and contractions of the dayside magnetosphere, *J. Geophys. Res.*, *83*, 3831, 1978

Hood, L. L., and G. Schubert, Inhibition of solar wind impingement on Mercury by planetary induction currents, *J. Geophys. Res.*, *84*, 2641, 1979.

Howe, H C., and J. H. Binsack, Explorer 33 and 35 plasma observations of magnetosheath flow, *J. Geophys. Res.*, *77*, 3334, 1972.

Hundhausen, A. J., *Solar Wind and Coronal Expansion*, chap. 3, Springer-Verlag, New York, 1972.

Intriligator, D. S., Observations of mass addition to the shocked solar wind of the Venusian ionosheath, *Geophys. Res Lett.*, *9*, 727, 1982.

Intriligator, D. S., and E. J. Smith, Mars in the solar wind, *J. Geophys. Res.*, *84*, 8427, 1979.

Ivanov-Kholodny, G. S., et al., Daytime ionosphere of Venus as studied by Venera 9 and 10 dual-frequency radio occulation experiments, *Icarus*, *39*, 209, 1979.

Leboeuf, J. N., T. Tajima, C F Kennel, and J M. Dawson, Global simulations of the three dimensional magnetosphere, *Geophys. Res. Lett.*, *8*, 257, 1981.

Lindal, G. F., H. B. Hotz, D. N. Sweetnam, Z. Shippony, J. P. Brenkle, V. Hartsell, R. T Spear, and W H Michael, Jr., Viking radio occulation measurements of the atmosphere and topography of Mars: Data acquired during 1 Martian year of tracking, *J. Geophys. Res.*, *84*, 8443, 1979

Luhmann, J. G., R. C. Elphic, C. T. Russell, J. D. Mihalov, and J. H. Wolf, Observations of large steady magnetic fields in the dayside Venus ionosphere, *Geophys. Res. Lett.*, *7*, 917, 1980.

Lyon, J., S. H. Brecht, J A. Fedder, and P. Palmadesso, The effects on the earth's magnetotail from shocks in the solar wind, *Geophys. Res. Lett.*, *7*, 721, 1980.

McElroy, M. B., M. J. Prather, and J. M. Rodriguez, Loss of oxygen from Venus, *Geophys Res. Lett.*, *9*, 649, 1982.

Michel, F. C., Solar wind interactions with planetary atmospheres, *Rev. Geophys. Space Phys.*, *9*, 427, 1971.

Mihalov, J. D., and A. Barnes, Evidence for the acceleration of ionospheric O$^-$ in the magnetosheath of Venus, *Geophys. Res. Lett.*, *8*, 1277, 1981.

Mihalov, J. D., J. H. Wolfe, and D. S. Intriligator, Pioneer Venus observations of the solar wind-Venus interaction, *J. Geophys Res.*, *85*, 7613, 1980.

Mihalov, J. D., J. R. Spreiter, and S. S. Stahara, Comparison of gas dynamic model with steady solar wind flow around Venus, *J. Geophys. Res.*, in press, 1982.

Montgomery, M. D., J. R. Asbridge, and S. J. Bame, Vela 4 observations near the earth's bow shock, *J. Geophys. Res.*, *75*, 1217, 1970.

Nagy, A. F., T. E. Cravens, J.-H. Yee, and A. I. F. Stewart, Hot oxygen atoms in the upper atmosphere of Venus, *Geophys. Res. Lett.*, *8*, 629, 1981.

Ness, N. F., Comment on 'The Venus bow shock: Detached or attached?' by C. T. Russell, *J. Geophys. Res.*, *82*, 2439, 1977

Ness, N. F., The magnetic fields of Mercury, Mars, and the Moon, *Ann. Rev Earth Planet. Sci.*, *7*, 249, 1979.

Ness, N F., K. W Behannon, R. P. Lepping, Y. C. Whang, and K. H. Schatten, Magnetic field observations near Venus Preliminary results from Mariner 10, *Science*, *183*, 1301, 1974

Perez-de-Tejada, H., Evidence for a viscous boundary layer at the Venus ionopause from the preliminary Pioneer Venus results, *J. Geophys. Res.*, *85*, 7709, 1980

Rassbach, M. E., R. A. Wolf, R. E. Daniell, Jr., Convection in a Martian magnetosphere, *J. Geophys. Res.*, *79*, 1125, 1974.

Rizzi, A., Solar wind flow past the planets Earth, Mars, and Venus, Doctoral dissertation, Stanford Univ., Stanford, Calif., 1971.

Romanov, S. A., V. N Smirnov, and O. L. Vaisberg, Interaction of the solar wind with Venus, *Cosmic Res*, *16*, 1978

Russell, C. T., The magnetosphere of Venus: Evidence for a boundary layer and a magnetotail, *Geophys. Res. Lett.*, *3*, 589, 1976a.

Russell, C. T., The magnetic moment of Venus: Venera 4 measurements reinterpreted, *Geophys Res Lett*, *3*, 125, 1976b

Russell, C. T., The Venus bow shock: Detached or attached?, *J. Geophys. Res.*, *82*, 625, 1977a.

Russell, C T, Reply, *J. Geophys Res.*, *82*, 2441, 1977b.

Russell, C. T., On the relative locations of the bow shocks of the terrestrial planets, *Geophys. Res. Lett.*, *4*, 387, 1977c

Russell, C. T., The magnetic field of Mars: Mars 3 evidence reexamined, *Geophys. Res. Lett.*, *5*, 81, 1978a

Russell, C. T., The magnetic field of Mars: Mars 5 evidence reexamined, *Geophys. Res Lett.*, 1978b

Russell, C. T., The interaction of the solar wind with Mars, Venus, and Mercury, *Solar System Plasma Physics*, vol 2, edited by C. F. Kennel, L. J. Lanzerotti, and E. N. Parker, p. 208, North-Holland, Amsterdam, 1979

Russell, C. T., and O. L Vaisberg, The interaction of the solar wind with Venus, in *Venus*, edited by D. M. Hunten, L. Colin, and T. M. Donahue, University of Arizona Press, Tempe, Ariz., 1982.

Russell, C. T, R. C. Elphic, and J. A. Slavin, Limits on the possible intrinsic magnetic field of Venus, *J. Geophys. Res.*, *85*, 8319, 1980.

Russell, C. T., J. G Luhmann, R. C. Elphic, F. L. Scarf, and L. H. Brace, Magnetic field and plasma wave observations in a plasma cloud at Venus, *Geophys. Res. Lett.*, *9*, 45, 1982.

Schubert, G., and B. R. Lichtenstein, Observations of moon-plasma interactions by orbital and surface experiments, *Rev. Geophys. Space Phys.*, *12*, 592, 1974.

Shen, W.-W., Ratio of specific heats in the solar wind plasma flow through the earth's bow shock, *J Geophys Res.*, *76*, 8181, 1971

Siscoe, G. L., and J. A. Slavin, Planetary magnetospheres, *Rev. Geophys. Space Phys.*, *17*, 1677, 1979.

Sittler, E. C., Jr., and J D. Scudder, An empirical polytrope law for solar wind thermal electrons between 0.45 and 4 76 AU: Voyager 2 and Mariner 10, *J. Geophys Res.*, *85*, 5131, 1980.

Slavin, J A., and R. E. Holzer, Solar wind flow about the terrestrial planets, 1, Modeling bow shock position and shape, *J. Geophys. Res.*, *86*, 11,401, 1981.

Slavin, J. A., and R E Holzer, The solar wind interaction with Mars revisited, *J. Geophys Res.*, in press, 1982.

Slavin, J. A., R. C. Elphic, C. T. Russell, J. H. Wolfe, and D S. Intriligator, Position and shape of the Venus bow shock: Pioneer Venus orbiter observations, *Geophys. Res. Lett.*, *6*, 901, 1979a.

Slavin, J. A., R. C. Elphic, and C. T. Russell, A comparison of Pioneer Venus and Venera bow shock observations: Evidence for a solar cycle variation, *Geophys. Res. Lett.*, *6*, 905, 1979b.

Slavin, J. A., R. C. Elphic, C T. Russell, F. L. Scarf, J. H Wolfe, J. D. Mihalov, D S. Intriligator, L. H Brace, H. A. Talor, Jr., and R. E. Daniell, Jr., The solar wind interaction with Venus: Pioneer Venus observations of bow shock location and structure, *J Geophys Res*, *85*, 7625, 1980.

Smirnov, V. N., O. L. Vaisberg, and D S Intriligator, An empirical model of the Venusian outer environment, 2, The shape and location of the bow shock, *J. Geophys. Res*, *85*, 7651, 1980.

Smirnov, V. N., O. L. Vaisberg, S. A. Rominov, J. A. Slavin, C. T. Russell, and D. S. Intriligator, Three-dimensional shape and position of the Venus bow shock (in Russian), *Kosm. Issled.*, *19*, 613, 1981.

Sonett, C. P., and D. S. Colburn, The principle of solar wind induced planetary dynamos, *Phys. Earth Planet. Inter.*, *1*, 326, 1968.

Spenner, K., W. C. Knudsen, K. L. Miller, V. Novak, C. T. Russell, and R. C. Elphic, Observations of the Venus mantle. The boundary region between the solar wind and ionosphere, *J Geophys. Res.*, *85*, 7655, 1980

Spreiter, J. R., and A. Y. Alksne, Solar wind flow past objects in the solar system, *Ann Rev. Fluid Mech.*, *8*, 313, 1970

Spreiter, J. R., and W P. Jones, On the effect of a weak interplanetary magnetic field on the interaction between the solar wind and the geomagnetic field, *J. Geophys. Res.*, *68*, 3555, 1963.

Spreiter, J. R, and A. W. Rizzi, The Martian bow wave—Theory and observation, *Planet Space Sci.*, *20*, 205, 1972

Spreiter, J. R., and A. W Rizzi, Aligned flow solutions for solar wind flow past the earth's magnetosphere, *Acta Astronaut.*, *1*, 15, 1974.

Spreiter, J. R., and S. S. Stahara, A new predictive model for determining solar wind-terrestrial planet interactions, *J Geophys Res.*, *85*, 6769, 1980a.

Spreiter, J. R., and S. S. Stahara, Solar wind flow past Venus. Theory and comparisons, *J. Geophys. Res.*, *85*, 7715, 1980b

Spreiter J. R., A. L. Summers, and A. Y. Alksne, Hydromagnetic flow around the magnetosphere, *Planet. Space Sci.*, *14*, 223, 1966

Spreiter, J. R., M. C Marsh, and A. L. Summers, Hydromagnetic aspects of solar wind flow past the moon, *Cosmic Electrodyn.*, *5*, 1, 1970

Spreiter, J. R., A. L. Summers, and A. W Rizzi, Solar wind flow past nonmagnetic planets—Venus and Mars, *Planet. Space Sci.*, *18*, 1281, 1970

Stahara, S. S., D. Klenke, B. C. Trudinger, and J R. Spreiter, Application of advanced computational procedures for modeling solar wind interactions with Venus—Theory and computer code, *NASA CR-3267*, 1980.

Suess, S T., and B. E. Goldstein, Compression of the Hermaean magnetosphere by the solar wind, *J. Geophys. Res.*, *84*, 3306, 1979

Taylor, H. A., Jr., H. C. Brinton, S. J. Bauer, R. E. Hartle, P. A. Cloutier, and R. E. Daniell, Jr., Global observations of the composition and dynamics of the ionosphere of Venus: Implications for the solar wind interaction, *J. Geophys. Res.*, *85*, 7765, 1980.

Theis, R. F., L H. Brace, K. H. Schatten, C. T Russell, J. A Slavin and J H. Wolfe, The Venus ionosphere as an obstacle to the solar wind, *Advan. Space Res.*, *1*, 47, 1981.

Tidman, D. A., and N. A. Krall, *Shock Waves in Collisionless Plasmas*, pp. 15–16, Interscience, New York, 1971.

Tozer, D. C., and J. Wilson, The electrical conductivity of the moon, *Proc. R. Soc., Ser A.*, *296*, 320, 1967.

Vaisberg, O. L, Mars-plasma environment, in *Physics of Solar Planetary Environment*, edited by D J. Williams, pp. 854–871, AGU, Washington, D C., 1976

Vaisberg, O. L., and A V Bogdanov, Flow of solar wind around Mars and Venus—General principles, *Cosmic Res.*, *12*, 253, 1974.

Vaisberg, O L., S A Romanov, V. N Smirnov, I P. Karpinsky, B. I. Khazanov, B. V. Polenov, A. V. Bogdanov, and N. M. Antonov, Ion flux parameters in the solar wind-Venus region according to Venera 9 and 10, in *Physics of Solar Planetary Environments*, edited by D. J. Williams, pp 904–917, AGU, Washington, D. C., 1976a.

Vaisberg, O. L., A V. Bogdanov, V. N. Smirnov, and S A. Romanov, On the nature of the solar wind-Mars interaction, Solar Wind Interaction With the Planets Mercury, Venus, and Mars, *NASA SP-397*, edited by N. F Ness, pp. 21–40, 1976b.

Vaisberg, O L., D. S Intriligator, and V. N. Smirnov, An empirical model of the Venusian outer environment, 1, The shape of the dayside solar wind-atmosphere interface, *J. Geophys. Res.*, *85*, 7642, 1980

Van Dyke, M D., The supersonic blunt body problem—Review and extension, *J. Aerosp Sci.*, 485, 1958.

Verigin, M. I., K. I. Grngauz, T. Gombosi, T. K. Breus, V. V. Bezrukikh, A. P. Remizov, and G. I. Volkov, Plasma near Venus from the Venera 9 and 10 wide angle plasma analyzer data, *J Geophys. Res . 83*, 3721, 1978.

Walker, R J., Quantitative modeling of planetary magnetospheric magnetic fields, in *Quantitative Modeling of Magnetospheric Processes*, edited by W P Olson, pp 9–34, AGU, Washington, D. C., 1979

Wallis, M K., Comet-like interaction of Venus with the solar wind, *Cosmic Electrodyn., 3*, 45, 1972.

Wallis, M. K., Weakly shocked flows of the solar wind plasma through the atmospheres of comets and planets, *Planet. Space Sci., 21*, 1647, 1973.

Wallis, M. K., Solar wind interaction with Venus: Review, in *Solar Wind Three*, edited by C. T. Russell, p. 421, Institute of Geophysics and Planetary Physics, UCLA, Los Angeles, Calif., 1974.

Wallis, M K., Does Mars have a magnetosphere?, *Geophys. J R Astron Soc., 41*, 349, 1975.

Wallis, M. K., Comet-like interaction of Venus with the solar wind, 3, The atomic oxygen corona, *Geophys Res. Lett., 9*, 427, 1982.

Wolfe, J H., R. W. Silva, and M. A. Meyers, Observations of the solar wind during the flight of Imp I, *J Geophys Res., 71*, 1319, 1966.

Wolfe, J. H , D. S. Intriligator, J. D Mihalov, H Collard, D McKibben, R. Whitten, and A. Barnes, Initial observations of the Pioneer Venus orbiter solar wind plasma experiment, *Science, 203*, 750, 1979.

Wolff, R. S., B E. Goldstein, and S. Kumar, A model of the variability of the Venus ionopause altitude, *Geophys Res Lett , 6*, 353, 1979.

Wu, C. C., R. J. Walker, and J M. Dawson, A three-dimensional MHD model of the earth's magnetosphere, *Geophys. Res. Lett., 8*, 523, 1981.

Zhuang, H C., and C T. Russell, An analytical treatment of the structure of the bow shock and magnetosheah, *J Geophys. Res , 86*, 2191, 1981.

Zwan, B. J., and R. A. Wolf, Depletion of solar wind plasma near a planetary boundary, *J Geophys. Res., 81*, 1636, 1976.

PLANETARY MACH CONES: THEORY AND OBSERVATION

J.A. Slavin[1], R.E. Holzer[2], J.R. Spreiter[3], and S.S. Stahara[4]

[1] Jet Propulsion Laboratory, California Institute of Technology,
   Pasadena, CA 91109
[2] Institute of Geophysics and Planetary Physics, University of
   California, Los Angeles, CA 90024
[3] Division of Applied Mechanics, Stanford University, Stanford,
   CA 94305
[4] Nielsen Engineering and Research, Mountain View, CA 49035

ABSTRACT

This study uses observations by a number of spacecraft to investigate the asymptotic behavior of planetary bow shocks. Toward this end a single standard method has been used to model distant bow shock position and shape. Mach cone angles of 13.9 ± 2°, 11.4 ± 3°, and $8.1 \pm 4_{o}$ at Venus, Earth, and Mars, respectively, were determined from the observational shock models. These cone angles and their decrease with growing distance from the sun are generally consistent with downstream bow shock position being limited by the MHD fast mode Mach number. Gasdynamic solutions for solar wind flow about Venus, Earth, and Mars were computed up to 50 R_{OB} (i.e. obstacle radii) behind the planets and compared with observed bow shock location. In each case the position of the shock was well predicted up to a certain distance downstream: -4 R_{OB} at Venus, -6 R_{OB} at Earth, and -10 R_{OB} at Mars. Beyond this point the observed shock position lies farther from the aberrated sun-planet line than the gasdynamic model with the discrepancy greatest at Venus and least at Mars. The better agreement between gasdynamic theory and observation with growing distance from the sun is attributed to an increase in the accurancy of the gasdynamic approximation with decreasing IMF strength. These results suggest that gasdynamic theory will be most accurate in describing flow about large bodies in the outer solar system.

Introduction

Previous studies (Fairfield, 1971; Slavin et al., 1983) have shown that the position and shape of planetary bow shocks forward of about one obstacle radius behind the planet are well predicted by single fluid gasdynamic theory (Spreiter et al., 1966; Spreiter and Stahara, 1980). In these theoretical models the presence of the interplanetary magnetic field is neglected on the grounds of its smallness in the sense $M_A^2 = \rho v^2/(B^2/8\pi) \sim 100$. The flow field is then completely determined by upstream sonic Mach number, M_s, adiabatic exponent, γ, and the obstacle shape/position.

While this approach is mathematically valid as an approximation to the numerically intractable MHD equations, the requirement that the ambient magnetic field be neligible is not met everywhere. For example, investigations of the regions just exterior to the Venus ionopause (Elphic et al., 1980), Earth magnetopause (Crooker et al, 1979), and Saturn magnetopause (Smith et al., 1980) have discovered a thin layer of compressed magnetic field adjacent to these obstacles from which the solar wind plasma has been lost via field aligned flows. These layers are not present in gasdynamic theory, but were predicted by one dimensional (Lees, 1964) and quasi-two dimensional (Zwan and Wolf, 1976) MHD studies of the stagnation region.

Another place where the gasdynamic approximation may be a poor representation is near the distant downstream bow shock. In this region the characteristic lines start to intersect the shock at small angles, as shown in Figure 1, indicating that the shock is approaching its "Mach cone" limit (e.g. Landau and Lifshitz, 1959). Gasdynamic models may not be able to accurately predict shock location in this region because the gasdynamic approximation, $M_A \gtrsim 10$, becomes invalid as the shock weakens. Mach number in the shock frame decreases as less deflection of the flow is required and the wave begins to propagate more across than against the solar wind flow direction. The bow shock continues to weaken until the Mach number in the shock frame goes to unity and it decays into a compressional wave. Hence, at some intermediate distance downstream the gasdynamic approximation becomes invalid and the agreement between theory and observation may deteriorate.

This study investigates the asymptotic behavior of planetary bow shocks and the ability of gasdynamic theory to describe it. Spacecraft observations at Venus, Earth, and Mars are used to model the shapes and positions of their distant bow waves utilizing a standard method. The measured planetary Mach cone angles are compared with the mean sonic and MHD fast wave Mach numbers at 0.7, 1.0, and 1.5 AU to assess the downstream influence of the interplanetary magnetic field. Finally, numerical gasdynamic flow solutions extending up to 50 obstacle radii behind the planets are obtained and tested against the observed location of the downstream bow shock.

Modeling Bow Shock Position

The bow shocks of Venus and Mars have been modeled using the three parameter second order method of Slavin et al. (1980;Slavin and Holzer, 1981). The terrestrial shock was not modeled because the techniques applied by Fairfield (1971) have already been shown to be quite similar to those employed here (Slavin and Holzer, 1981). The fitting

parameters are the surface eccentricity, $\mathcal{E}$, the semi-latus rectum, L, and the location of the focus along the x' axis, x_0. The shock itself is assumed to possess cylindrical symmetry about the solar wind direction which is taken to be opposite the aberrated planet centered solar ecliptic x axis (i.e. $\vec{V}_{sw}/|\vec{V}_{sw}| = -\hat{x}'$). All modeling is performed in the aberrated coordinates using either in situ solar wind speed or a mean value of 430 km/sec.

The near planet bow shock has been found previously to be highly symmetric about the x' direction in agreement with the predictions of gasdynamic theory (Slavin et al., 1980; Slavin and Holzer, 1981; Tatrallyay et al., 1983). Farther downstream the asymmetric nature of the MHD fast wave Mach cone may become significant. However, the effect should be small and there are too few distant shock obervations to model this region as a function of the upstream IMF orientation. Uncertainties introduced by our assumption of cylindrical symmetry for the downstream shock will be discussed in a later section.

The equation for the model surface is

$$r = L/(1 + \mathcal{E}\cos\theta) \qquad (1)$$

where r is radial distance from the focus (i.e. $x'=x_0$) and θ is measured about the focus from the positive x' axis direction. When the eccentricity in (1) is greater than unity, as is the situation in studies of the distant shock, the resultant curve is a hyperbola. For any hyperbola asymptotes exist which bound its position and correspond to the Mach cone for shock waves. They depend only upon the eccentricity and yield an expression for experimentally determined Mach cone angle

$$\alpha_{OBS} = \tan^{-1}((\mathcal{E}^2-1)^{1/2}) \qquad (2)$$

This expression can be differentiated to obtain the uncertainty in Mach cone angle, $\delta\alpha_{OBS}$, as a function of the error in the model eccentricity

$$\delta\alpha_{OBS} = (\delta\mathcal{E}/\mathcal{E})/(\mathcal{E}^2-1)^{1/2} \qquad (3)$$

Figure 2 displays typical orbits for Venera 9/10 and the Pioneer Venus Orbiter, PVO, in relationship to an extrapolated near planet model surface (Slavin et al., 1980). While PVO provides some excellent coverage of the forward shoch when periapsis is on the nightside, it is a very poor source of information on the location of the distant bow wave because of its tendency to parallel the shock (see discussion of these problems in Slavin and Holzer, 1981; Tatrallyay et al., 1983). Small variations in the flare angle of the shock appear in the PVO observations as boundary crossings at larger or smaller values of the x' coordinate. For this reason we have not used the PVO observations in modeling the downstream Venus shock. The lower inclination and less eccentric nature of their orbits make the Venera 9 and 10 shock crossings (Smirnov et al., 1981) better suited for modeling the distant Venus shock. Near planet shock crossings by Pioneer Venus were also not included because of the possibly solar cycle related variation in the altitude of the forward Cytherean shock discovered by Slavin et al. (1979;1980). With the exception of the Mariner 5 and Venera 4/6 downstream crossings, the Venus bow shock model produced by this study is based on solar minimum measurements.

In $1/r,\cos(\theta)$ coordinates centered on the geometric focus second order curves become straight lines (see equation 1). Linear least square fitting techniques may thus be applied. Figure 3 displays Mariner 5 (Bridge et al., 1967; Russell, 1977), Venera 4 and 6 (Gringauz et al., 1970), Mariner 10 (Bridge et al., 1974; Russell, 1977), and Venera 9 and 10 (Smirnov et al., 1980) bow shock crossings in these "conic" coordinates along with a least square best fit. The focus location on the x' axis was then systematically varied until the root-mean-square deviation of the crossings measured normal to the best fit surface was minimized. Figure 4 plots the Venus crossings in the conic coordinates again, but with the focus now centered on the optimum $x_o = +0.45$ R_v. The rms deviation in $x,(y'^2+z'^2)^{1/2}$ space is decreased by a factor of 2.6 in going from $x_o = 0$ to $x_o = 0.45$ R_v. Figure 5 displays the shock crossings and best fit model surface in the more usual aberrated cylindrical coordinates. The uncertainties in the model eccentricity and semi-latus rectum are approximately $\pm 1\%$. This is somewhat less than was found for the near planet Venera 9/10 and Pioneer Venus models by Slavin and Holzer (1981) because the inclusion the downstream observations permits less variation in the fitting parameters. The Mach cone determined from our shock model and equations (2) and (3) is $13.9^{\circ} \pm 2^{\circ}$. This result is intermediate between the 10.8° and 15.4° cone angles implied by the PVO distant shock model of Tatrallyay et al. (1983) and Venera 9,10 model by Smirnov et al. (1980). The next section will compare this result to the sonic and MHD Mach cones expected on the basis of average solar wind parameters.

In passing it is noted that the more extensive investigation of the distant Pioneer Venus distant shock crossings by Tatrallyay supports the preliminary finding of Slavin et al. (1980) that no decrease in solar wind Mach number took place bewteen the Venera 9,10 and PVO intervals of observation. If anything, Mach number appears to have been higher during the 1979-81 period. A large decrease in solar wind Mach number would have provided an alternate explanation for the change in forward bow shock position betweem 1975-6 and 1978-79 attributed to the effect of solar cycle changes in solar EUV and solar wind dynamic pressure by Slavin et al. (1980; Slavin and Holzer, 1983).

Observations of the terrestrial bow shock downstream of $x' = -60$ R_e have been made by only a few missions: Explorer 33 (Howe and Binsack, 1972; Mihalov, 1974), Pioneer 7 (Villante, 1976), and Pioneer 8 (Bavassano et al., 1971). The shock crossings in the better sampled $x' > -60R_e$ region have been modeled by Fairfield (1971) with a second order method comparable to the procedure employed here. As discussed in Slavin and Holzer (1981), the Fairfield best fit to the aberrated shock data was a hyperbola with $\mathcal{E} = 1.02$, $L = 22.3$ R_e, and $x_o = +3.4$ R_e. The corresponding Mach cone angle is $11.4^{\circ} \pm 3^{\circ}$ (assuming $\pm 1\%$ fitting errors) or 2.5° less than observed for Venus. While the Mach cones inferred from the more distant Pioneer and Explorer observations will be discussed in the next two sections, we have adopted the Fairfield aberrated shock surface for all comparisons with our models of the Venus and Mars bow shocks.

The Martian bow shock has been observed by the Mars 2, Mars 3 and Mars 5 orbiters and the Mariner 4 fly-by (see reviews by Russell, 1979; Gringauz, 1980; Slavin and Holzer, 1982). Sample trajectories for the three Soviet orbiters are displayed in Figure 6 along with the locations at which they crossed the Martian bow shock (O.L. Vaisberg and V.N.

Smirnov,private communication, 1979; see Slavin and Holzer, 1981). While the Mars 2 and 3 orbits parallel the downstream shock surface, the more perpendicular crossings of Mars 5 at about $x' = -5\ R_{OB}$ allow us to model the distant shock. Mariner 4 provides an additional shock encounter at approximately twice that distance (Smith, 1969).

Figure 7 displays our best fit to the Mars shock observations. The shape and location of the model surface is well determined with $\varepsilon = 1.01$ ($\pm 1\%$), $L = 1.68\ R_{MS}$ ($\pm 1\%$), and $x_o = +0.7 R_{MS}$. The Mach cone angle is $8.1^\circ \pm 4^\circ$ which is 3.3° less than the Earth value and 5.8° degrees below the Venus result. No other Martian shock model using observations from all four of these missions has been published. However, comparison with the Bogdanov and Vaisberg (1975) Mars 2/3 and Mariner 4 model demonstrates the importance of the Mars 5 crossings. In the absence of the intermediate distance Mars 5 shock data, their model eccentricity was approximately 7% larger and far more uncertain than determined here.

Mach Cone Angles

Table 1 compares the Mach cone angles at Venus, Earth, and Mars determined in the preceeding section with conditions in the interplanetary medium. In particular, the radial scalings for solar wind sonic and Alfvenic Mach number discussed in Slavin and Holzer (1981) have been adopted and the 0.7, 1.0, and 1.5 AU values listed. The limiting Mach cone angle in gasdynamic theory is that associated with the sonic wave speed

$$\alpha_s = \sin^{-1}(1/M_s) \qquad (4)$$

Following Table 1, as mean sonic Mach number increases from 6.6 to 7.9 the cone angle decreases from 8.7° at 0.7 AU to 7.3° near 1.5 AU.

While no general MHD solutions for flow about a blunt obstacle have been found (Spreiter and Rizzi, 1974), Mach cone type arguments using the MHD fast wave speed may be applied to predict asymptotic bow shock position in MHD theory (Michel, 1965). Unlike the situation for compressional disturbances in an unmagnetized isotropic plasma, fast mode wave speed is a function of propagation direction relative to the ambient magnetic field. The fast mode propagates faster perpendicular to B than parallel to it. Mach number based on the perpendicular fast mode speed is

$$M_{ms} = M_A M_s / (M_A^2 + M_s^2)^{1/2} \qquad (5)$$

so that

$$\alpha_{\perp} = \sin^{-1}((M_A^2 + M_s^2)^{1/2}/M_A M_s) \qquad (6)$$

Since the perpendicular fast mode speed is significantly larger than the sonic speed, the $\alpha_{\perp}$ values are $2-3^\circ$ greater than α_s as shown in Table 1. The parallel fast mode propagation speed is the greater of the sonic and Alfven speeds. Hence, the parallel MHD Mach number is simply equal to M_s due to the average $M_A > M_s$ conditions in the solar wind. At oblique propogation angles the fast mode speed lies in between the 0° and 90° values listed in the table.

The angle the local shock propagation direction (i.e. the shock normal) makes with the magnetic field is function of location on the shock surface. Both the mean spiral configuration of the IMF and the three dimensional curved nature of the bow shock contribute to the lack of symmetry. Over the poles and on the dusk side of the shock surface, the tendency is toward quasi-perpendicular geometries with limiting angles approaching $\alpha_\perp$. Quasi-parallel conditions are more probable on the dawn side where the cone angle should be closer to $\alpha_\parallel \approx \alpha_s$. These asymmetries in the MHD Mach cone were first quantitatively modeled by Michel (1965). It was his conclusion that the variations in MHD Mach cone angle with respect to the x' axis are about 1° overall, but generally less than 0.5° for the regions near the ecliptic where most of the spacecraft observations used in this study were made. For this reason it does not appear that any significant additional errors have been introduced by our earlier assumption of axial symmetry given the $2-4^\circ$ uncertainties in the observational determinations of Mach cone angle. In addition, the the larger Mach numbers in the outer solar system can be expected to produce distant shock shapes that are nearly parabolic given the Mars fitting results in this study. From equation (3) it is clear that a very large number of observations will be needed to accurately measure the smaller Mach cone angles at Jupiter and Saturn.

The observed Mach cone angles in Table 1 decrease with distance from the sun as predicted by both gasdynamic and MHD theory, but the variation is larger than expected. The observed Mach cone angle lies between $\alpha_\perp$ and $\alpha_\parallel$ only in the case of Mars although the error bars on α_{OBS} for the Earth also fall in that range. The measured cone angle at Venus lies well above the sonic Mach cone angle, but the lower bar is only slightly greater than the perpendicular fast mode prediction. Accordingly, the observed locations of the distant bow shocks appear to be more consistent with the larger MHD Mach cone than the smaller gasdynamic value. The Mach numbers used in calculating the predicted cone angles are based upon long term averages of interplanetary conditions (Slavin and Holzer, 1981). Hence they may not be the optimum values for the various portions of the solar cycle when the Venera and Mars orbiters bow shock observations were made. However, no long term variation in solar wind Mach number has been found in the solar wind records (Slavin et al., 1979) and the Earth observations used by Fairfield covered approximately half a solar cycle.

As mentioned earlier, bow shock encounters downstream of $x'=-60$ R$_e$ involving Explorer 33, Pioneer 7, and Pioneer 8 have taken place. Mach cone angles have been estimated in these cases by modeling of the shock surface and examination of the shock normals inferred from jump conditions. The distant bow shock model of Howe and Binsack (1972) based upon only the Explorer 33 and 35 observations has an asymptote of 17.7°. This value is greater than all of the Mach angles determined by this study and would imply a mean solar wind Mach number of only 3.3. However, the modeling method used in that study was never fully described and inspection of the fit shows a marked tendency to underestimate the altitude of the forward shock The result is an enhanced flare angle which is not present in the Fairfield model. Shock normals determined for Pioneer 7 and 8 implied Mach cone angles of 20° (Villante, 1976) and 22° (Bavassano et al., 1971), respectively. The Mach numbers implied by the Pioneer 7/8 cone angles are 2.7-2.9. These

values are much smaller than the average MHD and sonic Mach numbers listed in Table 1. The reason for the large Mach cone angles inferred from the shock normal analyses is unclear, but could be associated with either unusually low solar wind Mach numbers during the Pioneer encounters or waves on the shock boundary.

Gasdynamic Models

The Spretier and Stahara (1980; Stahara et al., 1980) gasdynamic code has been modified to produce solutions as far as 50 R_{OB} downstream. Figures 8, 9, and 10 display the calculated bow shock locations for the Venus, earth, and Mars body shapes determined by the Slavin et al. (1983) study and sonic Mach numbers of 4 and 8. These two Mach numbers were chosen because they correspond to the largest and smallest Mach cone angles in Table 1 (i.e. 7.9 from from α_{OBS} at Venus and 4.2 from α_s at Mars). The ability of the gasdynamic solutions to predict forward shock position has already been demonstrated by Slavin et al. (1983). However, the planetary Mach cones inferred from the shock observations in the preceeding section indicate that downstream the bow shocks are limited by larger Mach cones than predicted by gasdynamic theory. Below we investigate where these departures start and their magnitude.

The gasdynamic models of flow past Venus are displayed in Figure 8. The near shock is well represented by the $M_s=8$ theoretical shock forward of approximately $x'=-4$ R_{OB}. Farther downstream the bow shock continues to flare outward until its slope nearly matches that of the $M_s=4$ gasdynamic shock. Figure 9 performs this same comparison with the earth shock model of Fairfield (1971). The results are similar, but with the disagreement between theory and observation being less severe and starting farther behind the planet near $x'=-6$ R_{OB}. Finally, Figure 10 presents the Mars observations. In this case the $M_s=8$ theoretical model does not begin to seriously diverge from the observational model until $x'=-10$ R_{OB} is reached, and then only by a modest amount.

These results are generally consistent with both the expected limitations of the gasdynamic approximation and the uncertainties in the experimentally determined Mach cones. In all three cases the planetary bow shocks approach Mach cones that are greater than predicted by gasdynamic theory, but by only a small amount at Mars where $\alpha_s < \alpha_{OBS} < \alpha_L$. The trend as a function of distance from the sun is also much as would be expected from Table 1. Gasdynamic theory is more accurate and may be used farther downstream at greater distances from the sun where the IMF is weaker and the Alfvenic Mach number higher. The implications are that gasdynamic theory will be least useful at Mercury, but highly accurate for dscribing the flow of solar wind about Jupiter, Saturn, and the outer planets.

Conclusions

The distant bow shocks of Venus, Earth, and Mars have been modeled using a standard method. Mach cone angles determined from the best fit shock models are generally consistent with the MHD fast mode speeds measured in the solar wind as a function of distance from the sun. The finding by earlier studies that gasdynamic theory can accurately predict the location and shape of the forward bow shock has been extended and quantified. At Venus the bow shock position and orientation is poorly

represented by gasdynamic theory much beyond $x'=-4$ R_{OB}. The disagreement is smaller at the Earth and begins farther downstream near $x'=-6$ R_{OB}. Finally, at Mars the gasdynamic bow wave lies quite close to the observed shock surface with small discrepancies becoming evident only downstream of $x'=-10$ R_{OB}. The better agreement between gasdynamic theory and observation with increasing distance from the sun is attributed to the decrease in IMF strength with distance making the gasdynamic approximation more accurate.

TABLE 1. Predicted and Observed Mach Cones

Planet	R	M_A	M_S	α_S	$M_{ms\perp}$	$\alpha_\parallel$	$\alpha_\perp$	α OBS
Venus	0.7 AU	7.9	6.6	8.7°	5.1	8.7°	11.3°	13.9°± 2°
Earth	1.0 AU	9.4	7.2	8.0°	5.7	8.0°	10.1°	11.4°± 3°
Mars	1.5 AU	11.1	7.9	7.3°	6.4	7.3°	9.0°	8.1°± 4°

References

Bavassano, B., F. Mariani, U. Villante, and N.F. Ness, Multiple crossings of the earth's bow shock at large geocentric distances, J. Geophys. Res., 76, 5970, 1971.

Bridge, H.S., A.J. Lazarus, C.W. Snyder, E.J. Smith, L. Davis, Jr., P.J. Coleman, Jr., and D.E. Jones, Plasma and magnetic fields observed near Venus, Science, 158, 1669, 1967.

Bridge, H.S., A.J. Lazarus, J.D. Scudder, K.W. Ogilvie, R.E. Hartle, J.R. Asbridge, S.J. Bame, W.C. Feldman, and G.L. Siscoe, Observations at Venus encounter by the plasma science experiment on Mariner 10, Science, 183, 1293, 1974.

Crooker, N.U., T.E. Eastman, and G.S. Stiles, Observations of plasma depletion in the magnetosheath at the dayside magnetopause, J. Geophys. Res., 84, 869, 1979.

Elphic, R.C., C.T. Russell, J.A. Slavin, and L.H. Brace, Observations of the dayside ionopause and ionosphere of Venus, J. Geophys. Res., 85, 7679, 1980.

Fairfield, D.H., Average and unusual locations of the earth's magnetopause and bow shock, J. Geophys. Res., 76, 6700, 1971.

Gringauz, K.I., V.V. Bezrukikh, G.I. Volkov, L.S. Mustov, and T.K. Breus, Interplanetary disturbances near Venus determined from Venera 4 and 6 data, Cosmic Res., 8, 1970.

Gringauz, K.I., A comparison of the magnetospheres of Mars, Venus, and Mars, Adv. Space Sci., 1, 5, 1981.

Howe, H.C., Jr., and J.H. Binsack, Explorer 33 and 35 plasma observations of magnetosheath flow, J. Geophys. Res., 77, 3334, 19.

Landau, L.D., and E.M. Lifshitz, Fluid Mechanics, pp. 310-313, Pergamon Press, New York, 1959.

Lees, L., Interaction between the solar plasma wind and the geomagnetic cavity, AIAA J., 2, 1576, 1964.

Michel, F.C., Detectaability of disturbances in the solar wind, J. Geophys. Res., 70, 1, 1965.

Mihalov, J.D., Distant bow shock observations by Explorer 33, Astrophys. and Space Sci., 30, 447, 1974.

Russell, C.T., On the relative locations of the bow shocks of the terrestrial planets, Geophys. Res. Lett., 4, 387, 1977.

Russell, C.T., The interaction of the solar wind with Mars, Venus, and Mercury, Solar Wind Plasma Physics, eds. C.F. Kennel, L.J.Lanzerotti, and E.N. Parker, pp. 208-252, North-Holland Pub., Amsterdam, 1979.

Slavin, J.A., R.C. Elphic, and C.T. Russell, A comparison of Pioneer Venus and Venera observations: Evidence for a solar cycle variation, Geophys. Res. Lett., 6, 905, 1979.

Slavin, J.A., R.C. Elphic, C.T. Russell, F.L. Scarf, J.H. Wolfe, J.D. Mihalov, D.S. Intriligator, L.H. Brace, H.A. Taylor, Jr., and R.E. Daniell, Jr., The solar wind interaction with Venus: Pioneer Venus observations of bow shock location and structure, J. Geophys. Res., 85, 7625, 1980.

Slavin, J.A., and R.E. Holzer, Solar wind flow about the terrestrial planets 1. Modeling bow shock position and shape, J. Geophys. Res., 86, 11,401, 1981.

Slavin, J.A., and R.E. Holzer, The solar wind interaction with Mars

Revisited, J. Geophys. Res., 87, 10,285, 1982.

Slavin, J.A., R.E. Holzer, J.R. Spreiter, S.S. Stahara, and D.S. Chaussee, Solar wind flow about the terrestrial planets 2. Comparison with gasdynamic theory and implications for solar-planetary interactions, J. Geophys. Res., 88, 19, 1983.

Smirnov, V.N., O.L. Vaisberg, and D.S. Intriligator, An empirical model of the Venusian outer evironment 2. Shape and location of the bow shock, J. Geophys. Res., 85, 7651, 1980.

Smith, E.J., L. Davis, Jr., D.E. Jones, P.J. Coleman, Jr., D.S. Colburn, P. Dyal, and C.P. Sonett, Saturn's magnetosphere and its interaction with the solar wind, J. Geophys. Res., 85, 5655, 1980.

Spreiter, J.R., and A.W. Rizzi, Aligned MHD solution for solar wind flow past the earth's magnetosphere, Acta Astronautica, 1, 15, 1974.

Spreiter, J.R., A.L. Summers, and A.Y. Alksne, Hydromagnetic flow around the magnetosphere, Planet. Space Sci., 14, 223, 1966.

Spreiter, J.R., and S.S. Stahara, A new predictive model for determining solar wind-terrestrial planet interactions, J. Geophys. Res., 85, 6769, 1980.

Stahara, S.S., D. Klenke, B.C. Trudinger, and J.R. Spreiter, Application of Advanced Computational Procedures for Modeling Solar Wind Interactions with Venus - Theory and Computer Code, NASA Contract Rep. 3267, 1980.

Tatrallyay, M., C.T. Russell, J.D. Mihalov, and A. Barnes, Factors controlling the location of the Venus bow shock, submitted to J. Geophys. Res., 1983.

Villante, U., Evidence for a bow shock structure at 400 R_e: Pioneer 7, J. Geophys. Res., 81, 1441, 1976.

Zwan, B.J., and R.A. Wolf, Depletion of solar wind plasma near a planetary boundary, J. Geophys. Res., 81, 1636, 1976.

Figure Captions

1. Gasdynamic models of flow about the earth for an adiabatic exponent of 2 and sonic Mach numbers of 4 and 8 are displayed. Obstacle shape in the Spreiter and Stahara (1980) numerical codes is parameterized in terms a quantity H/R_0. The coordinates used are aberrated geocentric solar ecliptic (i.e. $\vec{V}_{sw}/|\vec{V}| = -\hat{x}'$) in units of obstacle radii, R_{OB}.

2. Sample Venera 9, 10 and Pioneer Venus orbits are shown in Venus solar ecliptic coordinates relative to the bow shock.

3. Mariner 5, Venera 4, Venera 6, Mariner 10, and Venera 9, 10 bow shock crossings are displayed in planet-centered "conic" cooridnates along with a linear best fit.

4. The same as the preceeding figure, but with the conic focus moved to $x_0 = +0.45 \ R_v$ to improve the fit.

5. The Venus bow shock crossings and best fit are displayed in aberrated planet centered solar ecliptic coordinates.

6. Sample Mars 2, 3, and 5 orbital trajectories are plotted in relation to the observed crossings of the bow shock.

7. Mariner 4, Mars 2, Mars 3, and Mars 5 bow shock crossings are plotted in planet centered solar ecliptic coordinates. The best 3 parameter second order least square fit to the boundary is also displayed.

8. The observed location of the Venus bow shock is compared with two gasdynamic models of flow about the planet.

9. The terrestrial bow shock model of Fairfield (1971) is comapred with two models of flow about the earth.

10. The observed location of the Mars bow shock is compared with two models of flow about the planet.

GASDYNAMIC MODEL OF FLOW PAST
A PLANETARY OBSTACLE

Bow Shock $\gamma = 2$ $M_S = 4$ — — —
                        $M_S = 8$ ·—·—·

Characteristic Lines ··········

$\sqrt{Y'^2 + Z'^2}$

Magnetosphere $(H/R_O = 0.20)$

$X'\ (R_{OB})$

FIG. 1

FIG. 2

MARINER AND VENERA VENUS BOW SHOCK
CROSSINGS IN ABERRATED PLANET CENTERED
CONIC COORDINATES

△ Mariner 5 (1967)
○ Venera 4 (1967)
□ Venera 6 (1969)
◇ Mariner 10 (1974)
+ Venera 9,10 (1975-6)

Best Fit
$X = 0.00 \ R_V$
$\varepsilon = 0.92$
$L = 2.24 \ R_V$
2-D NORMAL RMS $= 0.81 \ R_V$

$1/r \ (R_V^{-1})$

cos (SVS)

FIG. 3

FIG. 4

MARINER AND VENERA VENUS BOW SHOCK CROSSINGS (1967 - 1976)

Mariner 5 (1967) △
Venera 4 (1967) ○
Venera 6 (1969) ▢
Mariner 10 (1974) ◇
Venera 9, 10 +
    (1975 - 6)

$\sqrt{Y'^2 + Z'^2}$

X' (R_V)

Best Fit All Crossings
$X_0 = +0.45\ R_V$
$\mathcal{E} = 1.03$
$L = 1.68\ R_V$
2-D Normal RMS = 0.31 R_V

FIG. 5

MARS ORBITER BOW SHOCK CROSSINGS

Mars 2 (1971-2) △
Mars 3 (1971-2) ○
Mars 5 (1974) □

FIG. 6

MARINER AND MARS CROSSINGS OF MARS BOW SHOCK (1965-1974)

Mariner 4 (1965) ◇
Mars 2 (1971-2) △
Mars 3 (1971-2) ○
Mars 5 (1974) □

$\sqrt{Y'^2 + Z'^2}$

X' (R_{MS})

Best Fit
$X_0 = +0.7\ R_{MS}$
$\varepsilon = 1.01$
$L = 1.68\ R_{MS}$
2-D Normal RMS = 0.37 R_{MS}

FIG. 7

VENUS BOW SHOCK : 1967-76

Observed ——————
GD ($\gamma = 2$, $M_S = 4$) — — —
GD ($\gamma = 2$, $M_S = 8$) — · — ·

Magnetosphere ($H/R_O = 0.20$, $1\,R_{OB} = 0.91\,R_V$)

$\sqrt{Y'^2 + Z'^2}$

$X'\,(R_V)$
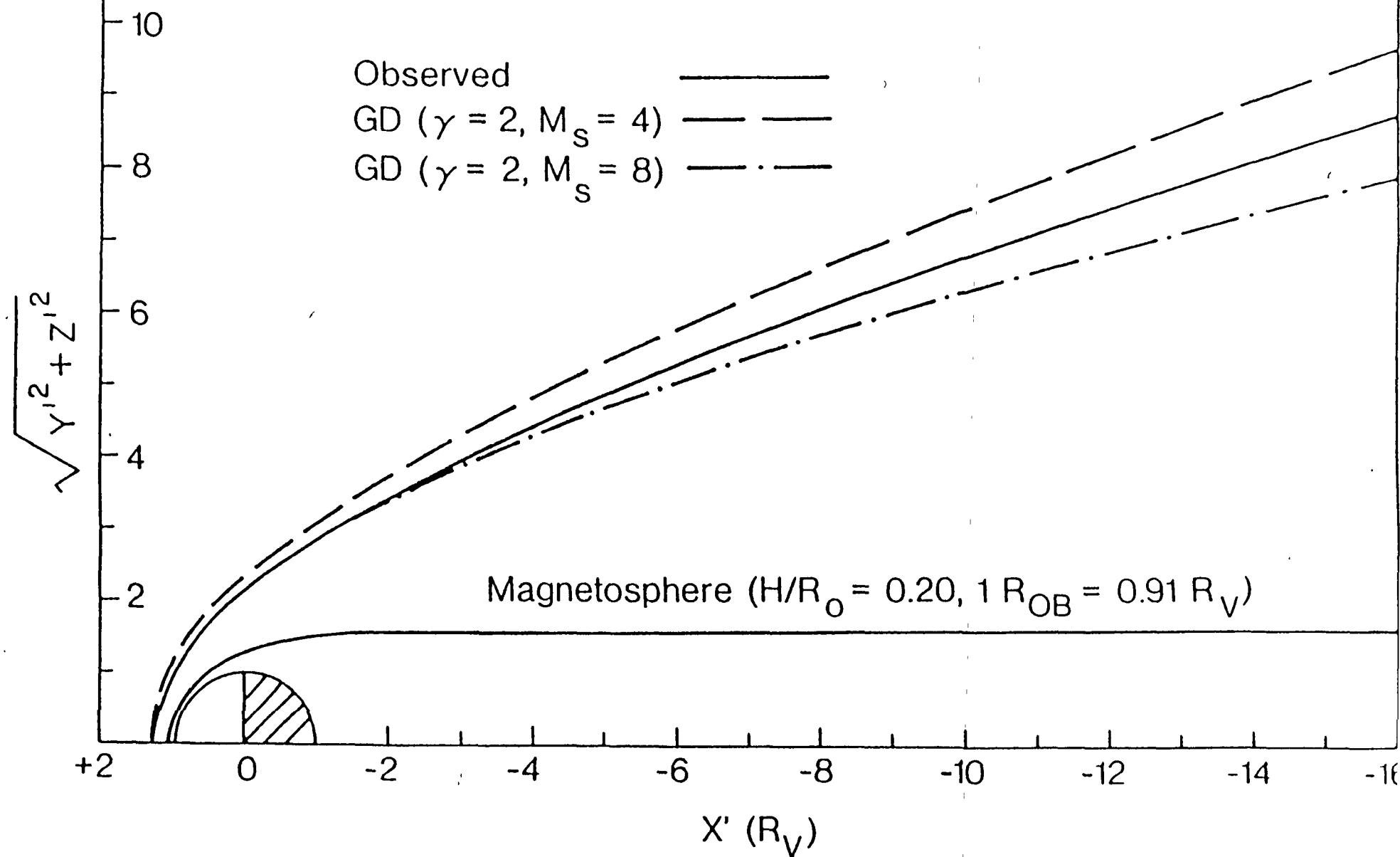
FIG. 8

EARTH BOW SHOCK: 1963-68

Observed (Fairfield, 1971) ——
GD ($\gamma = 2$, $M_S = 4$) — —
GD ($\gamma = 2$, $M_S = 8$) ·—·—·
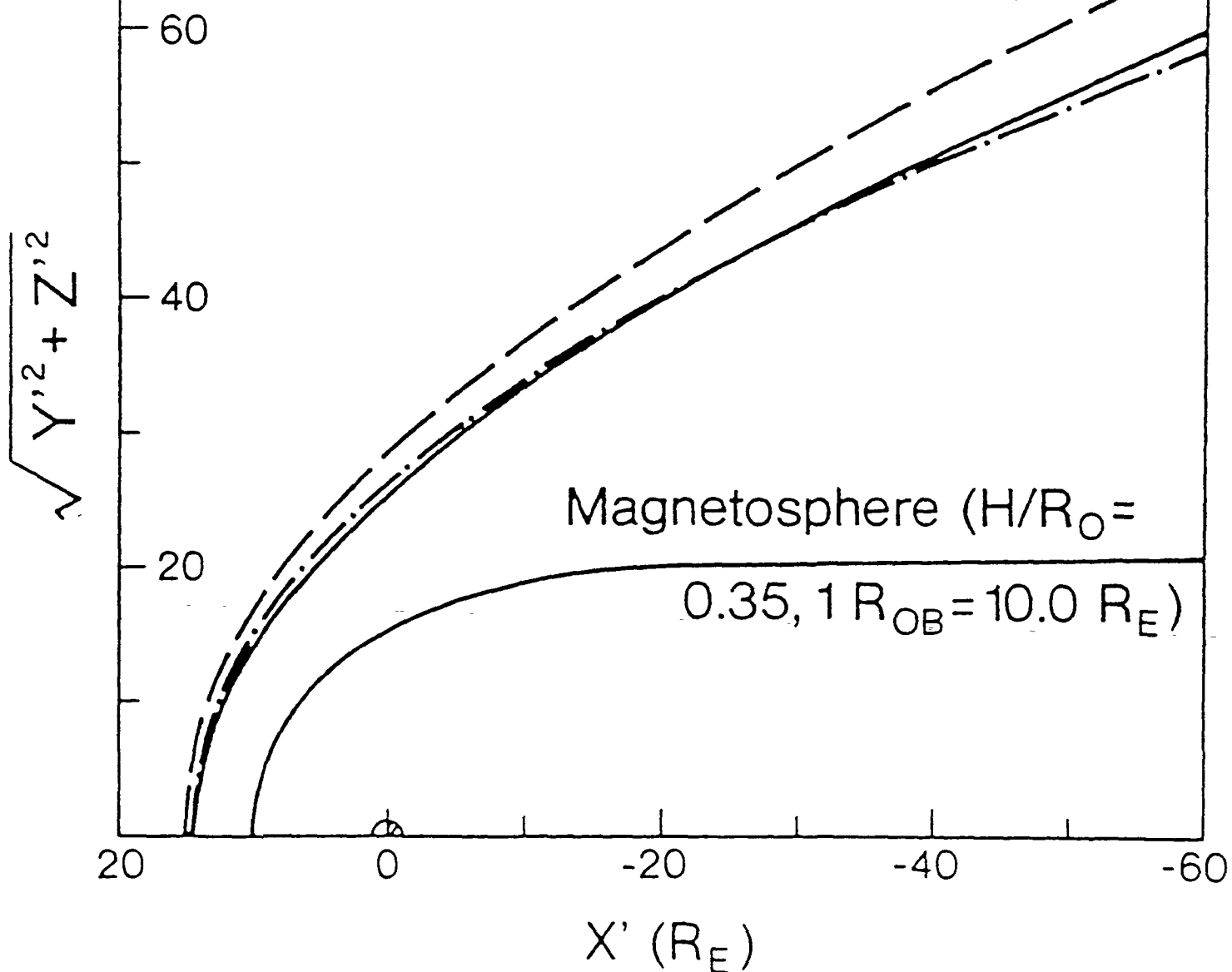
Magnetosphere ($H/R_O =$
0.35, 1 $R_{OB} = 10.0$ R_E)

$\sqrt{Y'^2 + Z'^2}$

X' (R_E)

FIG. 9

MARS BOW SHOCK: 1965 - 1974

Observed ———
GD ($\gamma = 2$, $M_S = 4$) — —
GD ($\gamma = 2$, $M_S = 8$) —·—·

$\sqrt{Y'^2 + Z'^2}$

Magnetosphere ($H/R_O = 0.05$, $1\,R_{OB} = 1.15\,R_{MS}$)

X' (R_{MS})
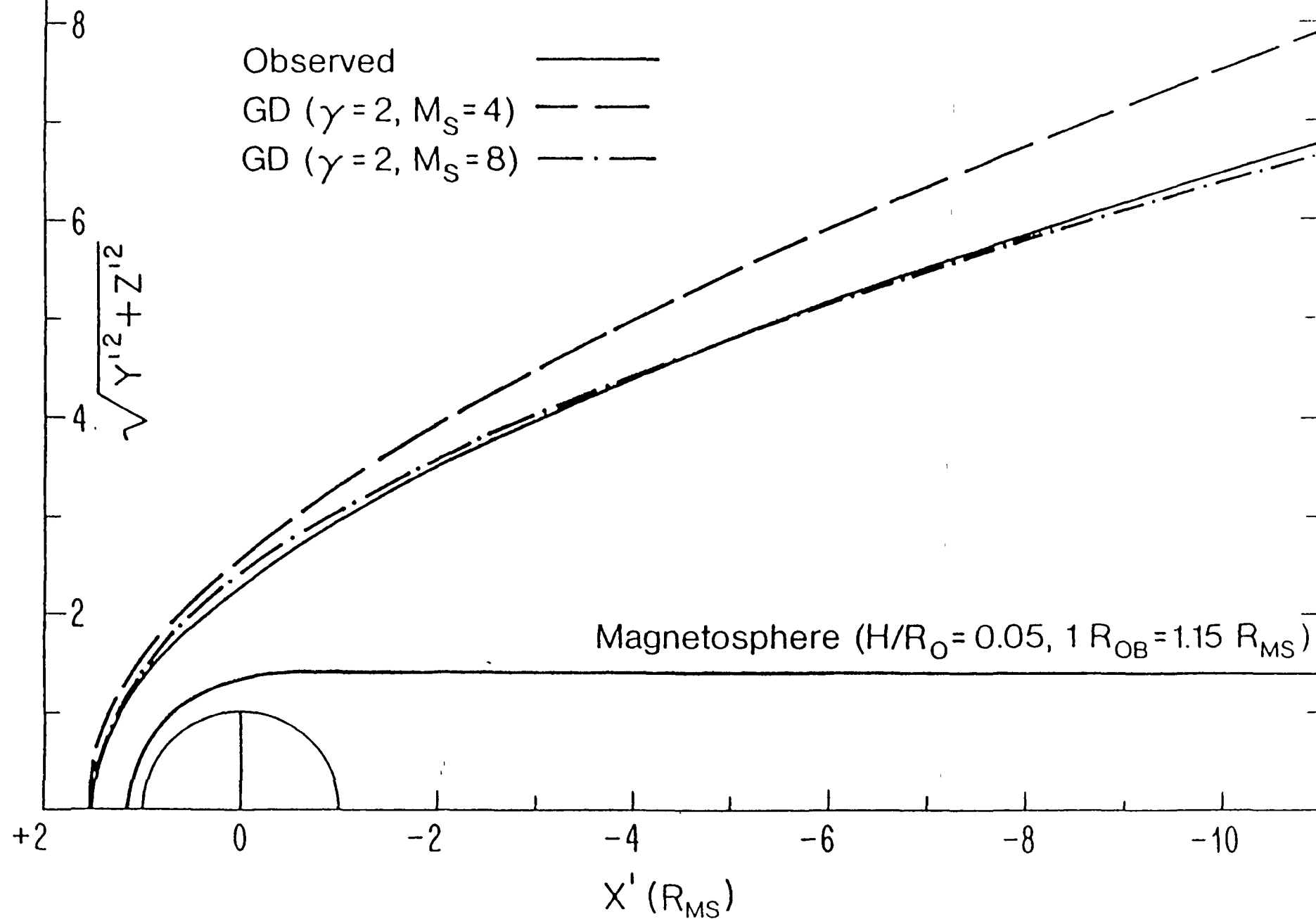
Characteristics of the Magnetospheric Source

of Interplanetary Energetic Particles

J.G. Luhmann, R.J. Walker, C.T. Russell

Institute of Geophysics and Planetary Physics
University of California
Los Angeles, California   90024

N.U. Crooker

Department of Atmospheric Sciences
University of California
Los Angeles, California   90024

J.R. Spreiter

Department of Applied Mechanics
Stanford University
Stanford, California   94305

S.S. Stahara

Neilsen Engineering and Research, Inc.
Mountain View, California   94043

D.J. Williams

Applied Physics Laboratory
Johns Hopkins University
Laurel, Maryland 20707

Abstract

The earth's bow shock is frequently cited as an example of an astrophysical shock where particle acceleration is observed. However, because energetic particles observed upstream of the bow shock may be accelerated within the magnetosphere, it is important to understand the properties of the magnetospheric source. A first order picture of the spatial distribution of magnetospheric particles in the magnetosheath and upstream is obtained by mapping those magnetic field lines which drape over the magnetopause through the bow shock. Subsets of these field lines that connect to potential sites of magnetic merging on the magnetopause are also traced in the event that leakage occurs preferentially where normal components of the field are present across that boundary. The results can be used to determine whether the so-called "diffuse" particles observed upstream are accelerated locally or within the magnetosphere.

Introduction

The energetic particles that are observed in interplanetary space are attributed to a variety of sources, both nonlocal and local. The primary nonlocal sources are the as yet uncertain sources of the galactic cosmic rays, while the more numerous local sources include solar flares, corotating interaction regions, interplanetary shocks, and planetary bow shocks. In recent years, much attention has been focussed on the $\gtrsim 50$ keV ions detected upstream of the earth's bow shock because of their implications for shock acceleration of galactic cosmic rays in the interstellar medium (cf. Axford, 1981). While the question of the contribution of magnetospheric particles to this population has been addressed by a number of authors (i.e., Scholer et al., 1981), it is still a relatively unsettled issue. Yet, if planetary bow shocks are to be used as astrophysical laboratories, it is important to understand the nature of the magnetospheric source.

Ions and electron beams with energies a few times that of solar wind particles have been traced back to the quasiperpendicular bow shock (cf. Gosling et al., 1981). The origin of these few keV particles is most likely related to the reflection of a small fraction of the incident solar wind from the bow shock as first suggested by Sonnerup (1969). These beams are probably also responsible for the generation by a beam-plasma instability of the MHD waves that are observed in the same upstream region (Barnes, 1970; Gary, 1981; Russell and Hoppe, 1983). A more energetic, (>50 keV) less directed population, the so-called "diffuse" particles which are observed downstream of these beams (cf. Ipavich et al., 1981; Anderson, 1981; Mitchell et al., 1983) has been explained as beam particles which are stochastically accelerated by the Fermi process in the regions where the upstream magnetic field fluctuations produced by the beam are convected against the shock (cf. Jokipii, 1967; Lee, 1982). Indeed, both West and Buck (1976) and Crooker et al. (1981) found an energetic ion population in the magnetosheath that appeared to be convected, together

with fluctuating magnetic fields, along plasma stream lines from the region of the bow shock where the diffuse particles are observed upstream.

On the other hand, very energetic (MeV) Jovian electrons observed in the interplanetary medium have been attributed to a magnetospheric source (McDonald et al., 1975), and Zwickl et al. (1981) found heavy ions of unmistakably magnetospheric origin in the upstream particles near Jupiter. Still, it may be argued that the region of space near the planets is contaminated by cold planetary ions which are then accelerated at the planetary bow shock, as proposed for the earth's upstream diffuse particles.

These things considered, it is relevant to review what has been observed near the terrestrial magnetopause through which the particles must exit the magnetosphere. Williams et al. (1981) have examined the behavior of energetic particles at the magnetopause boundary. These authors demonstrated that bite-outs occur in the trapped pitch angle distributions at large pitch angles, which is what one expects if some of the drifting trapped population is lost to the magnetosheath. Also, West and Buck (1976), Asbridge et al. (1978) and Bieber and Stone (1981) have all reported observations of layers of energetic particles in the magnetosheath near the magnetopause. Scholer et al. (1981) showed that the flux in the magnetosheath is comparable to the 90° trapped flux which is feeding the leakage. At least some of these particles observed near the magnetopause must end up in interplanetary space.

The distinction between magnetospheric particles and those accelerated upstream of the terrestrial bow shock was attempted experimentally by Scholer et al. (1981) who argued that magnetospheric ions are more energetic and are accompanied by electrons. In another observational study, Bieber and Stone (1981) pointed out that upstream magnetospheric electron events usually occur in conjunction with geomagnetic activity on the ground. Yet it seems that some of the confusion surrounding this matter of magnetospheric sources can be cleared up most effectively by a model that describes where those particles which are observed to leak out of the magnetopause go.

A global picture of the magnetospheric particle source can be expected to exhibit certain characteristics. The particles are presumably accelerated within the magnetosphere either in the routine manner of the permanently trapped outer zone population, or in transient events in the magnetotail. Proceeding outward, there are two mechanisms by which these particles can exit the magnetopause based on the current understanding of its structure. One possibility is that a turbulent . boundary layer (cf. Russell and Greenstadt, 1983) can scatter an adiabatically drifting trapped magnetospheric particle onto magnetosheath field lines. Provided that the boundary layer is large in areal extent, this type of leakage would occur over practically the entire magnetopause, with perhaps a preference for dawn and dusk where the sunward drifting electrons and protons, respectively, cross the terminator. Alternatively, the particles may leak out preferentially at areas on the magnetopause where merging of the magnetospheric and magnetosheath fields occurs (Crooker, 1979; Luhmann et al., 1983) because there normal components of the magnetic field allow adiabatic motion from one region to the other (Speiser et al., 1981; Daly, 1983).

Next, one must trace the particle motion through the magnetosheath from the magnetopause to the bow shock. Here there is a question of whether the particle motion is adiabatic or diffusive. If along its path a particle encounters magnetic fluctuations of substantial amplitude which satisfy the condition for gyroresonance when Doppler shifted to the particle's reference frame (cf. Jokipii, 1967), it will be scattered by the fluctuations. In this case the magnetospheric particles will "diffuse" outwards towards the shock. Moreover, if the magnetic fluctuations have some net motion, say in the direction of the convecting magnetosheath plasma, the isotropized particles will exhibit a similar bulk motion. If the scattering is strong, few magnetospheric particles will be able to reach the upstream region.

Rather, they will be carried antisunwards along the flanks of the magnetopause with the magnetosheath plasma in which the magnetic fluctuations are embedded. However, if the magnetic fluctuations are in a frequency range that does not affect the particles of interest, or if the magnetic field is fairly undisturbed, the gyrocenters of the energetic particles will approximately follow magnetosheath field lines through the bow shock to interplanetary space. While displacement of the gyrocenters from the field lines will be caused by the motional (VXB) electric field drift associated with the convection of the magnetized magnetosheath and solar wind plasma, this can probably be neglected for >50 keV ions (cf. Anderson, 1981; Mitchell et al., 1983). Thus, field line tracing from the magnetopause through the magnetosheath will, under conditions of nearly adiabatic particle motion, give information (to within a gyroradius) about the volume that should be populated with magnetospheric particles.

While some combination of diffusive and adiabatic behavior is probably a more realistic description of the particle motion in the magnetosheath, several studies (i.e., Palmer, 1981) suggest that the mean free path for scattering in the magnetosheath can be long. In this paper emphasis is placed on the characteristics of the magnetospheric source that would be expected for adiabatic behavior of the particles within the magnetosheath, although some discussion of the effects of magnetosheath turbulence is included in the final section. Toward this end, magnetosheath magnetic field lines that either pass within ~ 1 R_e (~ 1 particle gyroradius) of the magnetopause (for modeling widespread leakage) or at potential sites of magnetopause reconnection where the magnetosheath and magnetosphere fields are antiparallel, are traced outward to interplanetary space. The magnetosheath field model used here is derived from the gasdynamic treatment of the solar wind flow around the magnetosphere (Spreiter and Stahara, 1964, 1982). In this model, the

magnetic field configuration is calculated on the assumption that the interplanetary magnetic field is frozen in the diverted solar wind plasma. Thus, the "beams" of magnetospheric particles are found to have distinctive shapes and locations that depend on the interplanetary field orientation.

Description of the Model

The gasdynamic magnetosheath magnetic field model has been described elsewhere by its originators (Spreiter and Stahara, 1964, 1982). As mentioned above, this model assumes that the interplanetary magnetic field is frozen in the flow. Although few comparisons of this model with observations have been carried out for the earth (cf. Fairfield, 1976), several detailed analyses have been done for the Venus magnetosheath (Spreiter and Stahara, 1980). The fact that the Venus ionospheric obstacle is much less compressible than the earth's magnetosphere, and is scaled much smaller, is an advantage for comparisons with the steady state model. The time scale for variations in the interplanetary field is typically short compared to the time (several hours) it takes a spacecraft to travel through the dayside magnetosheath at the earth. But the interplanetary field can be quite steady during the time interval of the Pioneer Venus orbiter traversal of the Venus magnetosheath ($\sim.5$ hr). The magnetosheath magnetic field model based on gasdynamics agrees quite well with the observed magnetic field at Venus. Although here the object of interest is the less well-behaved earth, it is considered that an idea of the magnetosheath field line geometries can be obtained from an examination of constant scale models with constant interplanetary fields. A sonic Mach number of 6 and a magnetopause shape derived from the Hedgecock and Thomas magnetosphere model (cf. Walker, 1976) were used in the gasdynamic calculation to produce the magnetosheath fields used here.

To determine the locations of magnetic merging on the magnetopause, the magnetospheric field at the magnetopause was presumed to be given by the Hedgecock and Thomas (cf. Walker, 1976) model. As described elsewhere (Luhmann et al., 1983) the

locations where this internal field was within ∿10° of antiparallel to the magneto-
sheath field were then defined as merging sites.

Routes for magnetospheric particle leakage are approximated by magnetosheath
field lines which either drape against the dayside magnetopause, for the case of
widespread leakage, or by field lines which originate at the magnetopause at the
aforementioned merging sites.

Figures 1 and 2 illustrate the results of the modeling in the same format for
the cases of widespread leakage and localized reconnection site leakage, respectively.
These figures display projected views of the three-dimensional magnetosheath field
line configuration for different interplanetary field orientations. The underlying
magnetosheath draping is shown as fine lines. These field lines start at 49 points
in interplanetary space on a square grid oriented perpendicular to the interplanetary
field. The heavy lines in Figure 1 are projected views of field lines which pass
within ∿1 earth radius of the magnetopause at the terminator plane at equispaced
intervals of ∿10°. These produce a three-dimensional picture of the volume of
flux tubes which would be populated by magnetospheric particles if the particles
leak out over a large area of the dayside magnetopause. The shapes of the volumes
are notably different for each interplanetary field configuration, appearing as
sheets for interplanetary fields perpendicular to the flow, and as a cylindrical
tube for radial magnetic field. Subsets of these volumes are connected to merging
sites, as defined above, on the magnetopause. The heavy lines in Figure 2 identify
groups of field lines which originate near those sites, which are shown on the
magnetopause from the viewpoint of the sun in Figure 3. Figure 2 illustrates the
importance of southward interplanetary field in obtaining large amounts of magneto-
spheric particle leakage if merging at the magnetopause is a necessary factor.
Finally, Figure 4 shows the cross-sections of several of the volumes of flux tubes
from Figures 1 and 2 at various planes in interplanetary space. This diagram gives

a feeling for the sizes of the volumes of magnetospheric particles that a spacecraft might traverse while located beyond the bow shock.

Discussion and Conclusions

In the introductory section the effects of scattering of the particles by magnetic fluctuations and of drifts produced by the motional electric field ($\overline{E} = \overline{V} X \overline{B}$ where V = plasma velocity, B = magnetic field) were mentioned. Anderson (1981) has given a complete description of trajectory dispersion by the VXB field in interplanetary space where V and B are uniform. However, the drift effects in the magnetosheath are not so simply described because of the complicated magneto-sheath velocity field and the magnetic field, which varies with the interplanetary field orientation. Figure 5 shows several examples of particle trajectories originating near the subsolar magnetopause, drifting in the $\overline{V}X\overline{B}$ and $\overline{B}$ fields from the gasdynamic magnetosheath model. As discussed by Anderson (1981) for the upstream region, the particle gyrocenter trajectories are dispersed antisunward from magnetic field lines according to their parallel (to $\overline{B}$) velocities. Particles with small parallel velocities are swept into the flow, in the limit of zero parallel velocity their gyrocenters following streamlines. At the opposite extreme, particles with large parallel velocities have gyrocenter paths that lie practically along magnetic field lines. Most observations are of particles with intermediate behavior. Thus, some spatial dispersion of particles of different energies in the magnetosheath and upstream regions is to be expected. The anticipated spatial gradients, with low energies mostly antisunward, should be considered in interpreting delays in the onsets of fluxes at successively higher energies as observed from spacecraft moving from dawn toward noon. This spreading of the magnetospheric beam will distort the spatial distributions suggested by Figures 1-2 for particles with low parallel velocities. However, for energies >50 keV and pitch angles >45° field-aligned gyrocenter motion is probably a fair approximation.

On the subject of scattering, it has been established that magnetic fluctuations in the magnetosheath, apart from the turbulent boundary layer near the magnetopause (Hones, 1983), are confined to streamlines of magnetosheath plasma flow that are connected to the quasiparallel bow shock (Greenstadt et al., 1983, Russell and Luhmann, 1983). Figure 5 illustrates how sections of the trajectories of the magnetospheric particles intersect the regions (shaded) of fluctuating magnetic fields behind the quasiparallel bow shock on their way through the magnetosheath. The spectrum of the magnetosheath field fluctuations, which has been studied by Greenstadt et al. (1983) is similar in shape, and at least equivalent in power, to the spectrum of the waves upstream from the bow shock. The latter has been shown by Lee (1982) to often justify the use of the diffusion equation in describing the transport of upstream energetic particles. The upstream patterns for magnetospheric particle leakage shown in Figures 1 and 2 will under such circumstances be smeared out by the diffusing regions in the magnetosheath. However, some properties of the leakage patterns, such as the local time sector of the transmitted population, may be roughly preserved. An important point in connection with this geometry is that the upstream leakage frequently occurs through the region of the quasiparallel bow shock, where the so-called "diffuse" particle populations, consisting of nearly isotropic energetic ions, are observed (Ipavich et al., 1981, Paschmann et al., 1981, Bonifazi and Moreno, 1981). The present results suggest that caution should be exercised when interpreting these diffuse populations as ions locally accelerated in the upstream region. Other properties of the observed energetic diffuse ions that a magnetospheric source would explain are the apparent limiting fluxes, which are similar to the trapped flux near the magnetopause, the time constants for flux buildup after a sudden change in the interplanetary field, which may be the leakage and travel times to the upstream observing point, and the K_p dependence of the

energetic upstream population (West and Buck, 1976), since the trapped population at the magnetopause as well as the rate of leakage through reconnection sites (i.e., the areal extent of merging regions) will be greater under the conditions that produce high K_p. The observed frequent absence of energetic upstream electrons together with the diffuse ions can be attributed to leakage efficiencies and propagation differences for the two species, partly due to their very different gyroradii.

One obvious test that could be performed to determine the effeciency of upstream acceleration without contamination by the magnetospheric source is to measure energetic particles upstream of the bow shocks of planets with weak intrinsic fields like Venus and Mars. However, although magnetic field measurements are available for these planets, energetic particles were not measured on the spacecraft missions to them. In any case, the present study suggests that in interpreting observations of energetic particles near planetary bow shocks, one must consider not only whether the local magnetic field lines connect to the bow shock, but also whether they connect to the magnetopause.

Acknowledgments

Figure Captions

Figure 1. Projections (in the GSE coordinate system) of magnetosheath field lines
(fine lines) and field lines passing within $\sim$1 R_e of the magnetopause in
the terminator plane (heavy lines) for various interplanetary field orientations:
(a) northward or southward (Z-directed), (b) dawn or dusk (Y-directed), (c)
Parker Spiral (45° to X and Y axes, parallel to X-Y plane, (d) radial
(X-directed). · The gyrocenters of energetic particles which leak out of the
magnetosphere over a large area of the magnetopause will follow paths roughly
within the volumes defined by the heavy lines.

Figure 2. Same as Figure 1, but here the heavy lines originate near potential
merging sites on the magnetopause (see Fig. 3), and the interplanetary field
is: (a) southward, (b) northward, (c) Y-directed, (d) radial, (e) and (f)
Parker Spiral toward and away, respectively.

Figure 3. Projection of the magnetopause surface (in the GSE Y-Z plane) showing
where the magnetospheric and magnetosheath model fields are within 10° of
antiparallel at the magnetopause. Reconnection or merging is presumed to
occur between the two fields at these sites. Merging produces normal components
of the field on the boundary, allowing the adiabatic motion of particles from
the magnetosphere to the magnetosheath. The field orientations are (a) radial,
(b) southward, (c) Y-directed, (d) Parker Spiral away, (e) northward, (f)
Parker spiral toward.

Figure 4. Cross-sections of some of the volumes defined by the heavy lines in
Figures 1 and 2 at various planes parallel to the GSE coordinate axes. The
light shading shows the areas within which widespread leakage (see Fig. 1)
would be observed, while the dark shading shows these areas for localized,
reconnection site leakage (see Fig. 2). The X, Y, or Z positions and inter-
planetary field orientations are indicated in the upper right.

Figure 5. Examples of particle trajectories in the model magnetosheath magnetic
and electric (VXB) field. On the left, the interplanetary field is perpendic-
ular to the flow. The light lines show the streamline and background field
line geometry in the plane of symmetry. The particles launched near the
subsolar magnetopause with 45° pitch angle, have energies of 1 keV, 5 keV
and 50 keV from left to right. The shading shows where magnetosheath turbulence,
which can scatter the particles, is expected behind the quasiparallel shock.
On the right a similar diagram illustrates 1 keV and 5 keV particles for a
Parker Spiral interplanetary field.

(a)

(b)

(c)

(d)

(a)　　　　　　　　(b)　　　　　　　　(c)

(d)　　　　　　　　(e)　　　　　　　　(f)
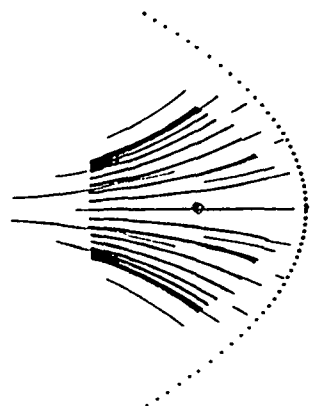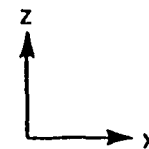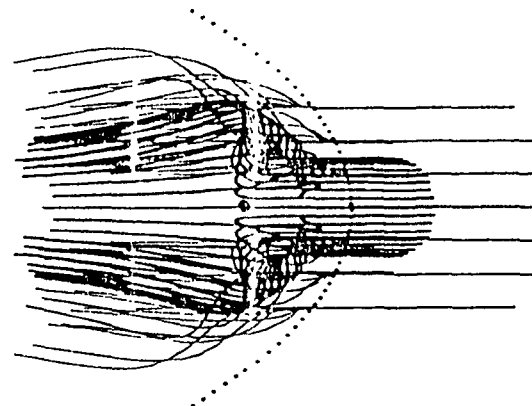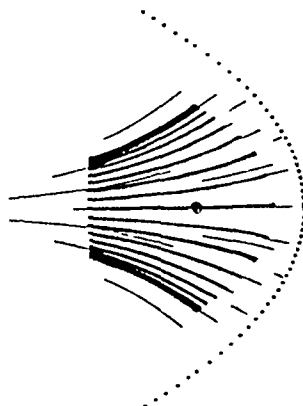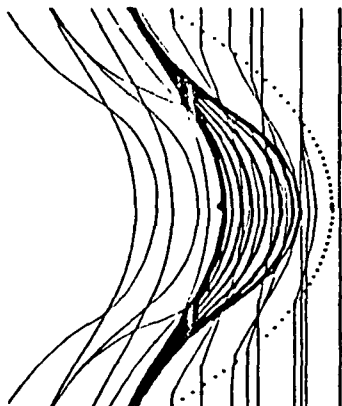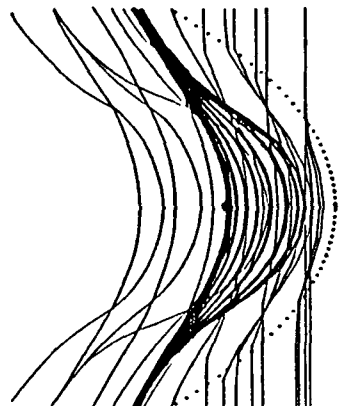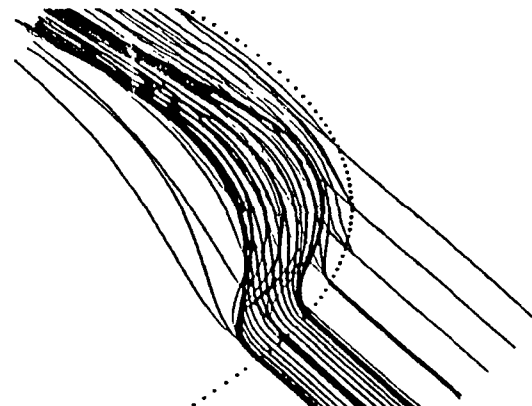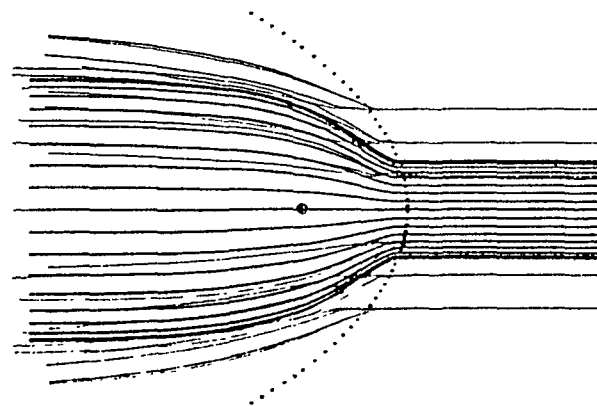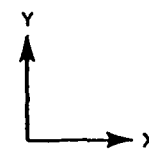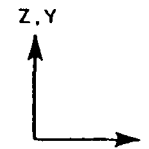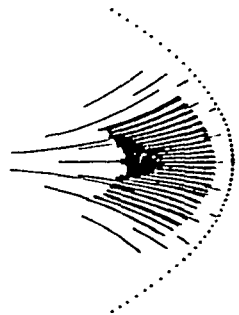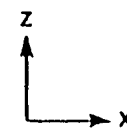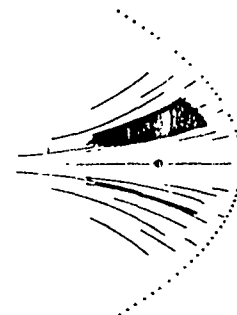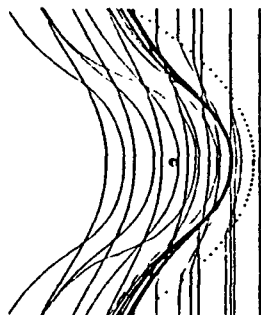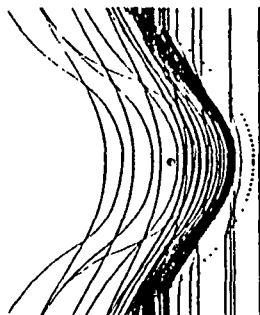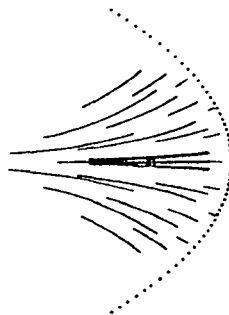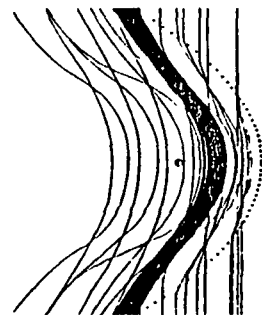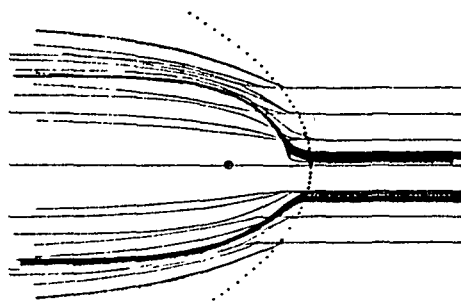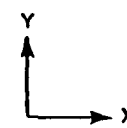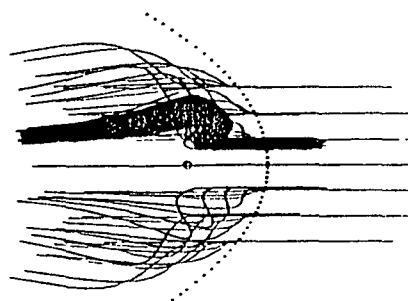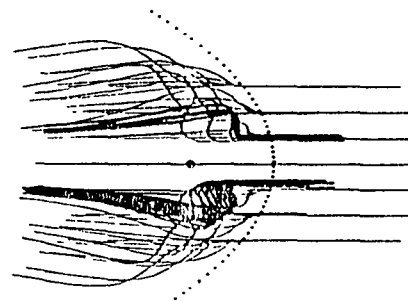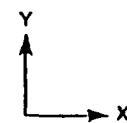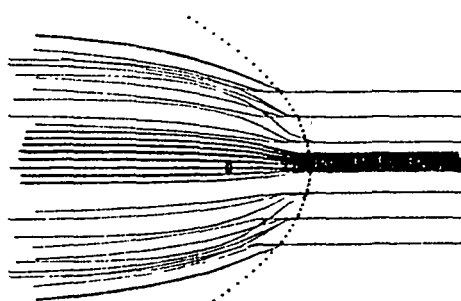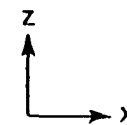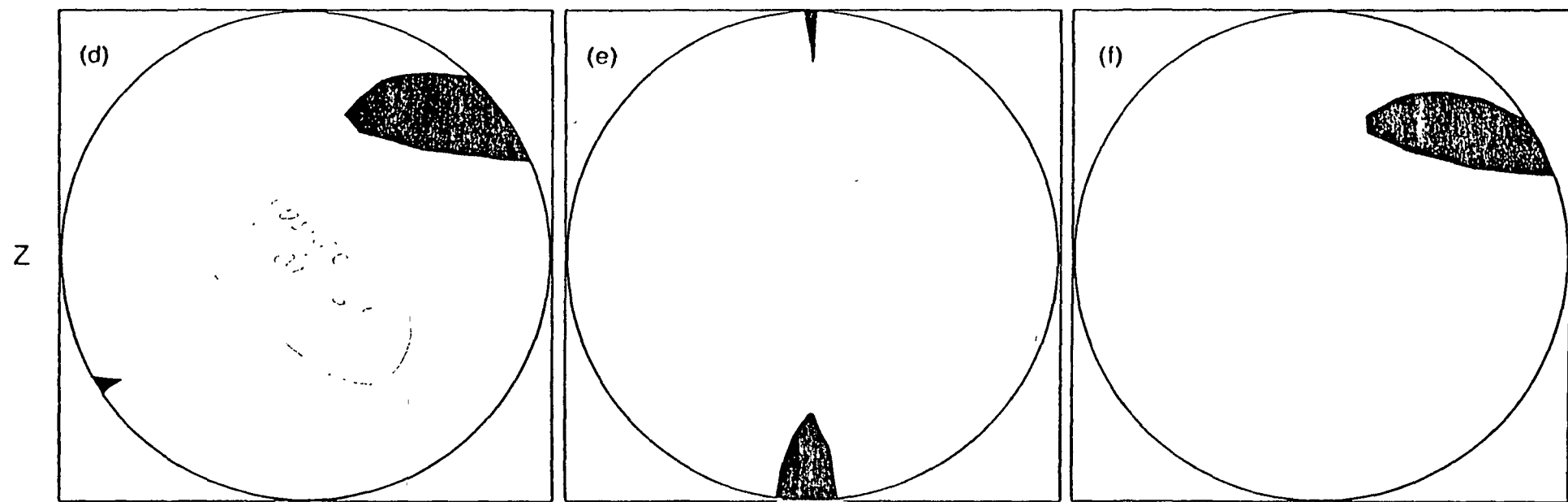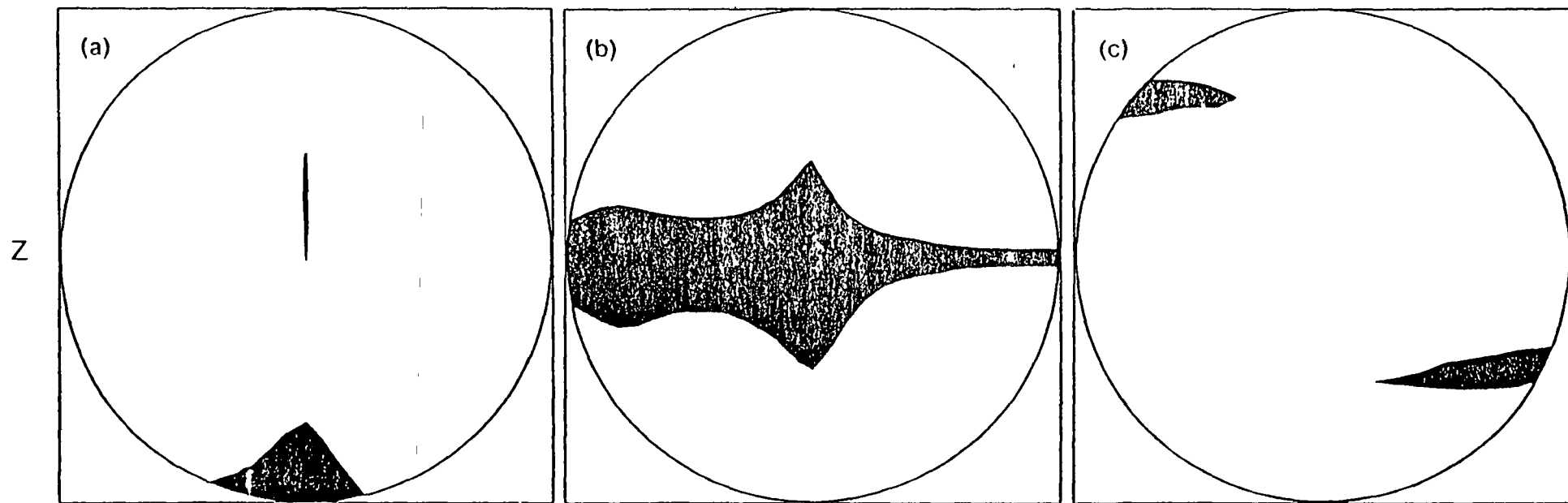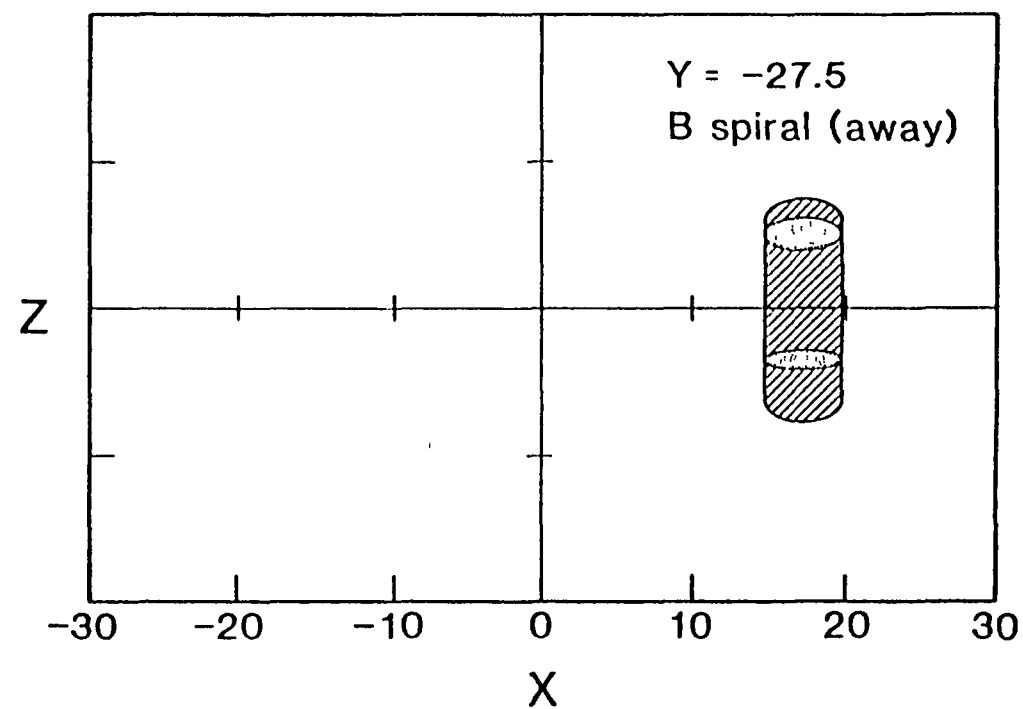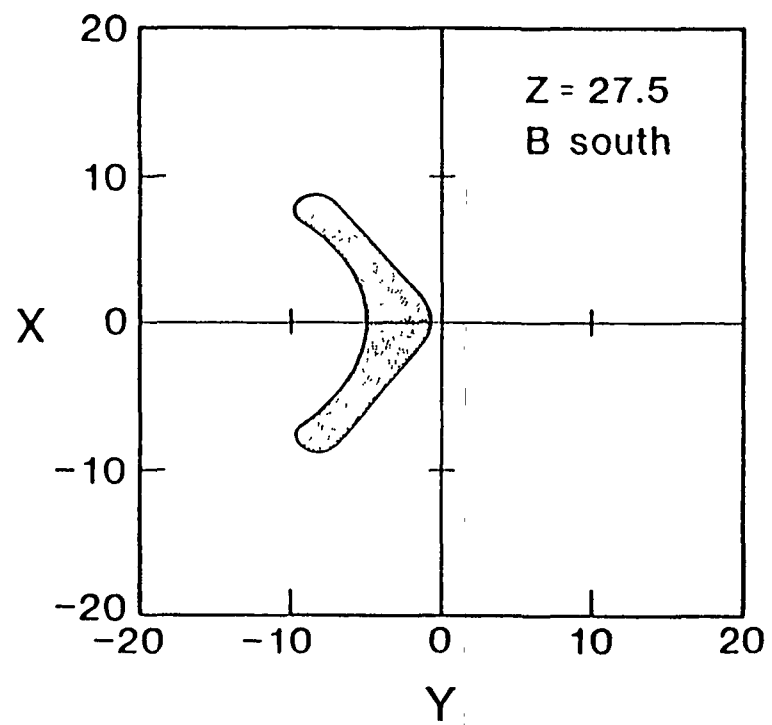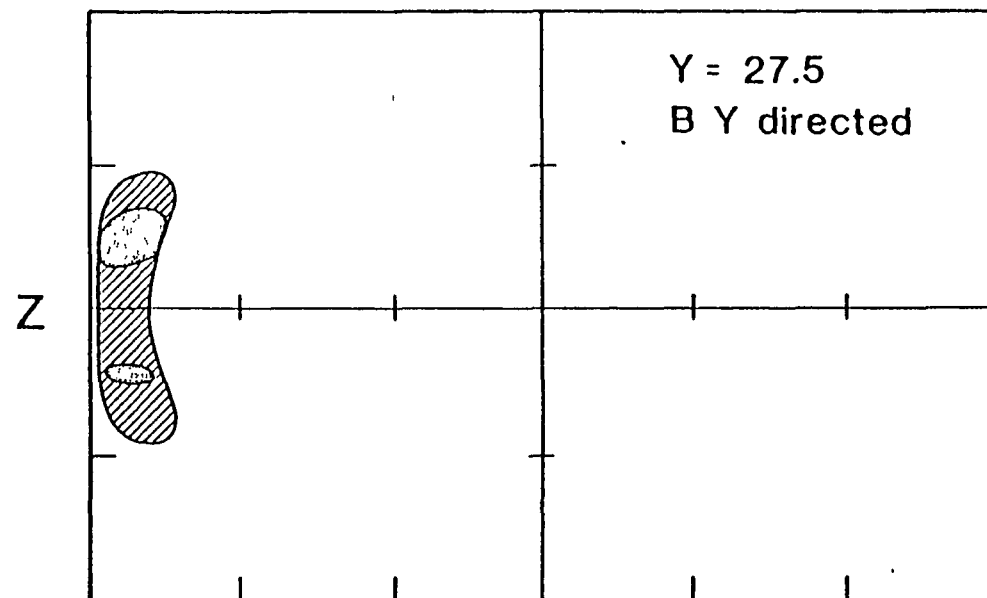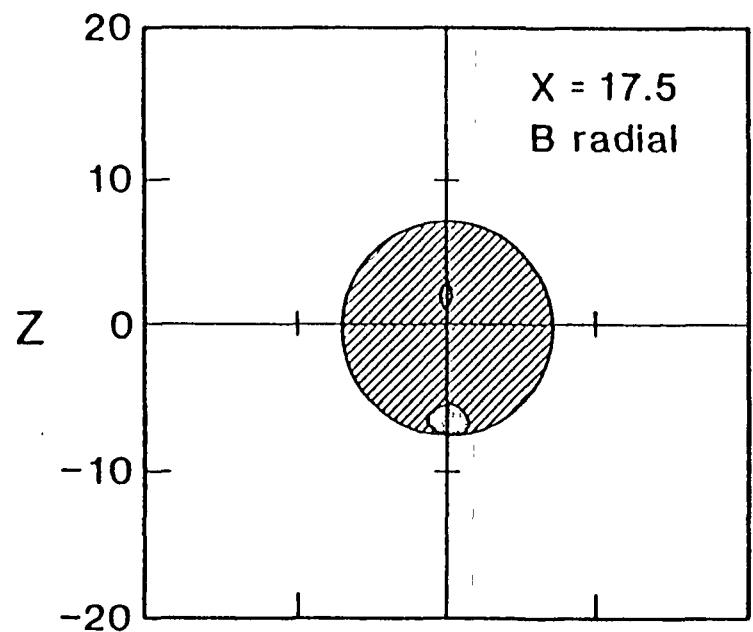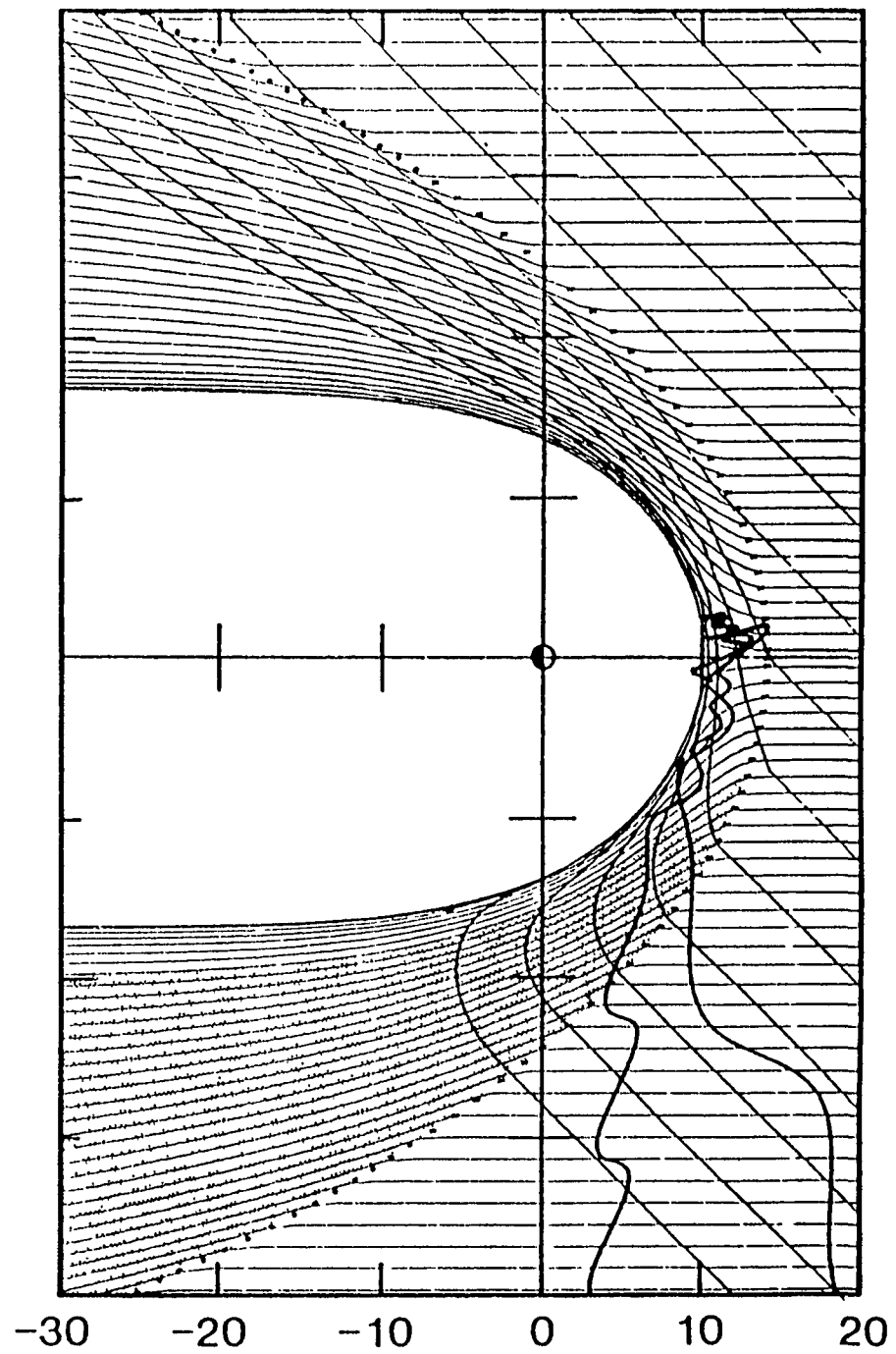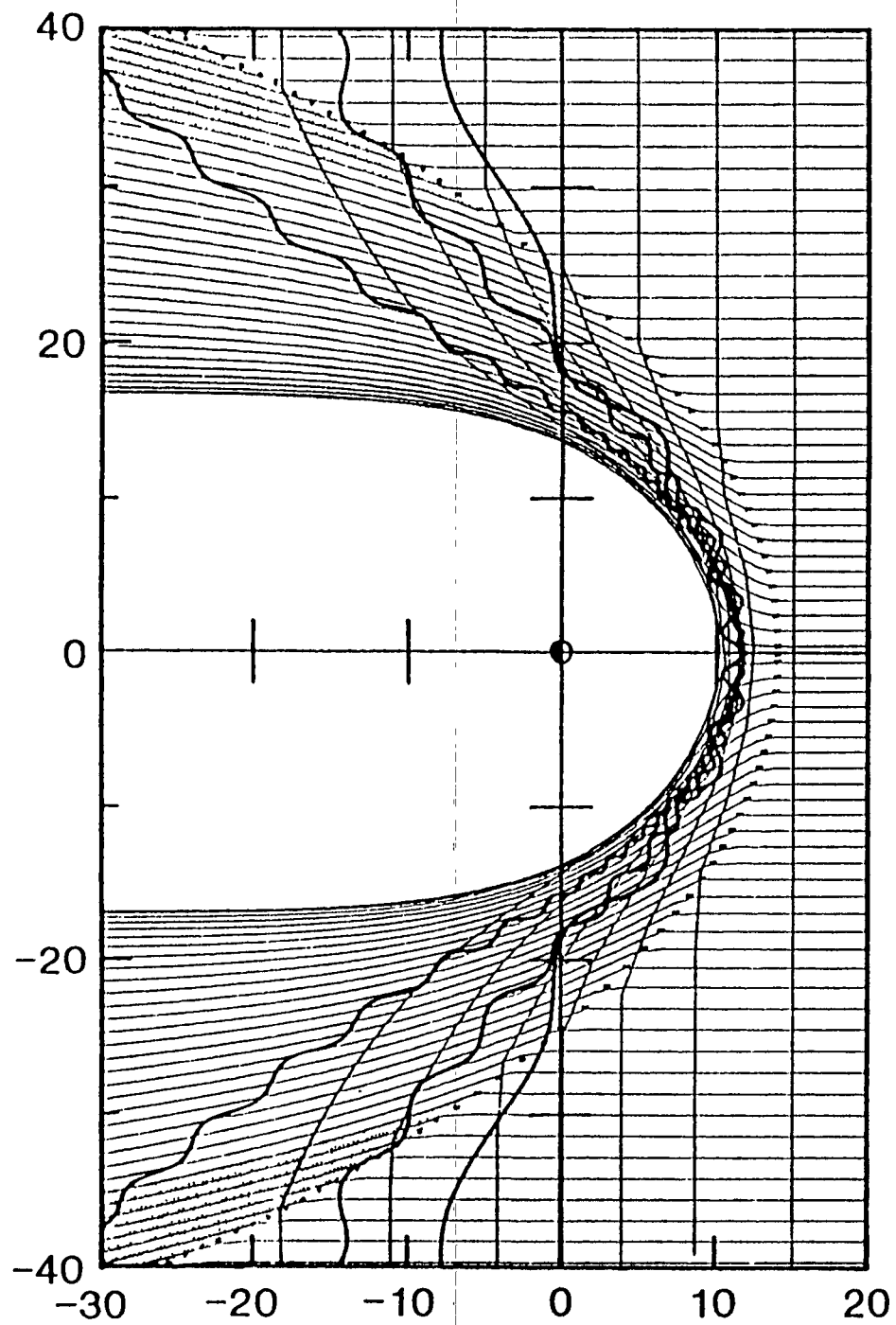
Patterns of Magnetic Field Merging Sites

on the Magnetopause

J.G. Luhmann, R.J. Walker, C.T. Russell

Institute of Geophysics and Planetary Physics

University of California

Los Angeles, California 90024

N.U. Crooker

Department of Atmospheric Sciences

University of California

Los Angeles, California 90024

J.R. Spreiter

Department of Applied Mechanics

Stanford University

Stanford, California 94305

S.S. Stahara

Neilsen Engineering and Research, Inc.

Mountain View, California 94043

May, 1983

Abstract

Models of the magnetospheric and magnetosheath magnetic fields are used to determine the relative orientations of the two near the dayside magnetopause for the purpose of locating potential merging sites. Areas on the magnetopause with various degrees of antiparallelness for different interplanetary field orientations are displayed as contour diagrams. For southward and GSE-Y interplanetary field, the patterns obtained are consistent with those envisioned by Crooker in an earlier analysis which used simplified representations for the magnetic field geometry. Here, the application of realistic models shows the locations of areas where any antiparallel component occurs. Merging sites for radial interplanetary fields are also illustrated. The results suggest that the geometrical configuration of the field is suitable for merging over a large fraction of the magnetopause for interplanetary fields that are either primarily southward, GSE-Y, or radial (GSE-X) in direction.

Introduction

There is considerable interest in the question of where reconnection or magnetic field merging occurs in the magnetosphere (cf. Russell, 1976). Several years ago Crooker (1979) presented a qualitative model of the sites of magnetic field merging on the magnetopause. This analysis was based on a conceptual picture of the magnetopause and a superposed overlying uniform field, perpendicular to the earth-sun line, which was taken to represent the magnetosheath field at its inner boundary. The latter was rotated to mimic the effect of different interplanetary field directions. Reconnection or merging lines were defined as the locus of points for which these approximate magnetospheric and magnetosheath fields were antiparallel when projected onto a plane (the GSE Y-Z plane). The major point arising from this analysis was the role of the cusp in locating potential merging sites. However, the author also qualified the results by pointing out that merging can occur where only components of the two fields are antiparallel (cf. Cowley, 1976), and that the draping geometry of the magnetosheath field over the magnetopause is not necessarily well represented by a uniform field in the GSE Y-Z plane projected onto the magnetopause. The present study extends the ideas put forth in this earlier effort by employing realistic models of the magnetospheric and magnetosheath fields to locate antiparallel fields at their magnetopause interface. The new aspects of this analysis include the location of fields with only components that are antiparallel, and the treatment of radial (GSE-X) interplanetary fields which were not considered previously.

Description of the Model

The Hedgecock and Thomas model (cf. Walker, 1976) was selected to represent the magnetospheric field at the dayside magnetosheath because it has a fairly realistic cusp geometry. This model also has north-south asymmetries caused by the uneven distribution of the data that went into its construction, rather than by true

asymmetry. It was therefore assumed that the more heavily sampled northern section was the more accurate, and a mirror image of the model north of the equator was used to represent the southern magnetosphere. Possibly real dawn-dusk asymmetries in this northern section were retained. The dipole axis of the model was assumed to coincide with the GSE-Z axis for this study. Although the seasonal variation of the dipole tilt with respect to this axis will modify the magnetospheric field at the magnetopause, the complication introduced by the use of a tilted model precluded the study of this effect.

The magnetosheath field was modeled using the assumption that the interplanetary field is frozen into the medium in the gasdynamic treatment of supersonic flow around an axisymmetric obstacle (cf. Spreiter and Stahara, 1982). The shape of the obstacle was presumed to follow the shape of the Hedgecock and Thomas model magnetopause in the noon-midnight meridian. For the purpose of the present analysis, the aberration of the solar wind flow was neglected. A free-stream sonic Mach number of 6.0 was used in the gasdynamic code, with which magnetosheath fields at a distance of approximately .5 earth radii from the surface of the obstacle were computed for a variety of interplanetary field orientations. (The field determined with the gasdynamic code becomes inaccurate near the stagnation streamline that bathes the obstacle surface.)

The angle between the two modeled fields was found over the surface of the dayside magnetopause at the grid points shown in Figure 1. Contour diagrams of the cosine of this angle were then constructed to display the regions of different degrees of antiparallelness as viewed from the Sun.

Results

Figure 2 contains the contour diagrams described above for various interplanetary magnetic field orientations (ie. magnetosheath models). The shaded areas, representing fields that are within 10° of being antiparallel, are roughly consistent with

Crooker's (1979) merging lines for interplanetary field orientations perpendicular to the solar wind velocity. New sites arise when there is a substantial GSE-X or radial component of the interplanetary field. As expected, the southward directed interplanetary field produces the largest area of nearly antiparallel fields on the magnetopause, while the northward interplanetary field produces the smallest area. However, the regions for which there is some component of the magnetosphere and magnetosheath fields antiparallel cover a large region of the magnetopause for most interplanetary field orientations.

Discussion and Conclusions

For several reasons, the patterns shown in Figure 2 must be considered with some measure of caution when comparing with observations at the magnetopause. First, the interplanetary field is typically variable on the time scale of plasma convection through the dayside magnetosheath. Except under circumstances of exceptionally steady interplanetary field orientation, the actual pattern of antiparallel fields projected on the magnetopause must be predicted from the field observed in the solar wind at earlier times. (The convection time is several minutes from the subsolar shock to the nose of the magnetopause.) Second, currents near the magnetopause and MHD effects such as that described by Zwan and Wolf (1979) will affect the field geometry at that boundary. Third, the possible dependence of the merging rate on the local plasma velocity has not been folded into these patterns. If slow flow is necessary for merging then those regions near the subsolar stagnation point will be favored. Similarly, the possible role of the field magnitudes was neglected here. Finally, reconnection itself may cause the reconnected field lines to be pulled over the magnetopause, disrupting any pattern imposed purely by the magnetospheric and magnetosheath fields. (The boundary layer may be a manifestation of the latter process.) Yet, the patterns shown in Figure 2 may provide a picture of the initial conditions set up by a sudden change in interplanetary field orientation.

Recent statistical studies of the spatial distribution of flux transfer events near the magnetopause (Berchem and Russell, 1983) show a double-banded distribution which flanks the equator. These authors have argued that their results are consistent with the preferred occurrence of reconnection at the equator where quasi-steady merging has been predicted for southward interplanetary field (Dungey, 1961, Sonnerup, 1976). However, their distributions are also consistent with a super-position of the patterns for southward field and for GSE-Y fields as shown in Figure 2. In fact in their study, some events occurred in association with practically GSE-Y directed fields. Also, because the highest geomagnetic latitudes were not covered in their sample, the merging poleward of the cusps predicted for north-ward directed fields (see Fig. 2) could not have been observed. Still, separation of their data into events associated with steady, primarily southward interplanetary fields and GSE-Y fields may produce the distinctive patterns shown in Figure 2 for these two cases. One would expect the GSE-Y fields to produce events in opposing corners along a diagonal through the subsolar point, while southward fields would produce a broad latitudinal band including the equator.

In conclusion, the present analysis represents the extent to which one can practically go in using static magnetic field models to understand the global picture of reconnection sites on the magnetopause. Time-dependent, 3-dimensional MHD models of the solar wind interaction with the magnetosphere, such as that developed by Wu et al. (1980) and Fedder et al. (1981) will, of course, be the ultimate tool for the investigation of merging sites.

Figure Captions

Figure 1. A view, in the GSE X-Z plane, of the grid points on the Hedgecock-Thomas model magnetopause at which the dot-product of the magnetospheric field model and the gasdynamic magnetosheath field model was computed in this analysis. Also shown are the magnetospheric model field lines in the noon meridian.

Figure 2. Contours on the magnetopause (viewed from the sun, i.e., the GSE Y-Z plane projection) of equal value of the cosine of the angle between the magnetospheric and magnetosheath model fields. Only contours with negative values, implying some antiparallel component, are shown. Values at the contours, starting with the contour filled with shading, are -.98, -.95, -.9, -.8, -.7, -.6, -.5, -.4, -.3, -.2, -.1, 0. The interplanetary field orientations are as follows: (a) radial (+X-directed), (b) southward, (c) Y-directed (toward dusk), (d) Parker Spiral toward, (e) northward, (f) Parker Spiral away, (g) equal Y and Z components, no X-component, (h) equal X, Y, and Z components, (i) equal and opposite Y and Z components, no X-component.
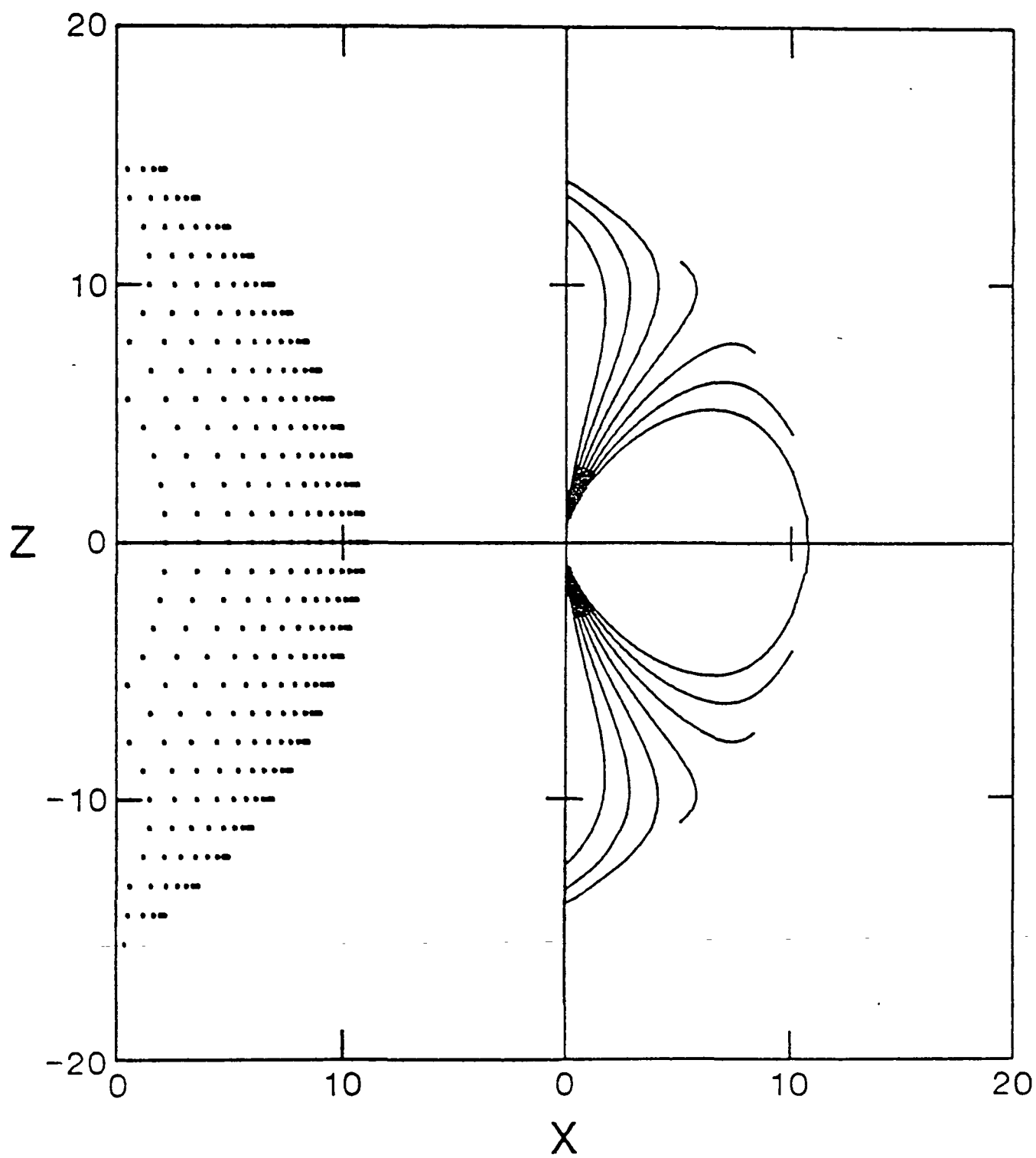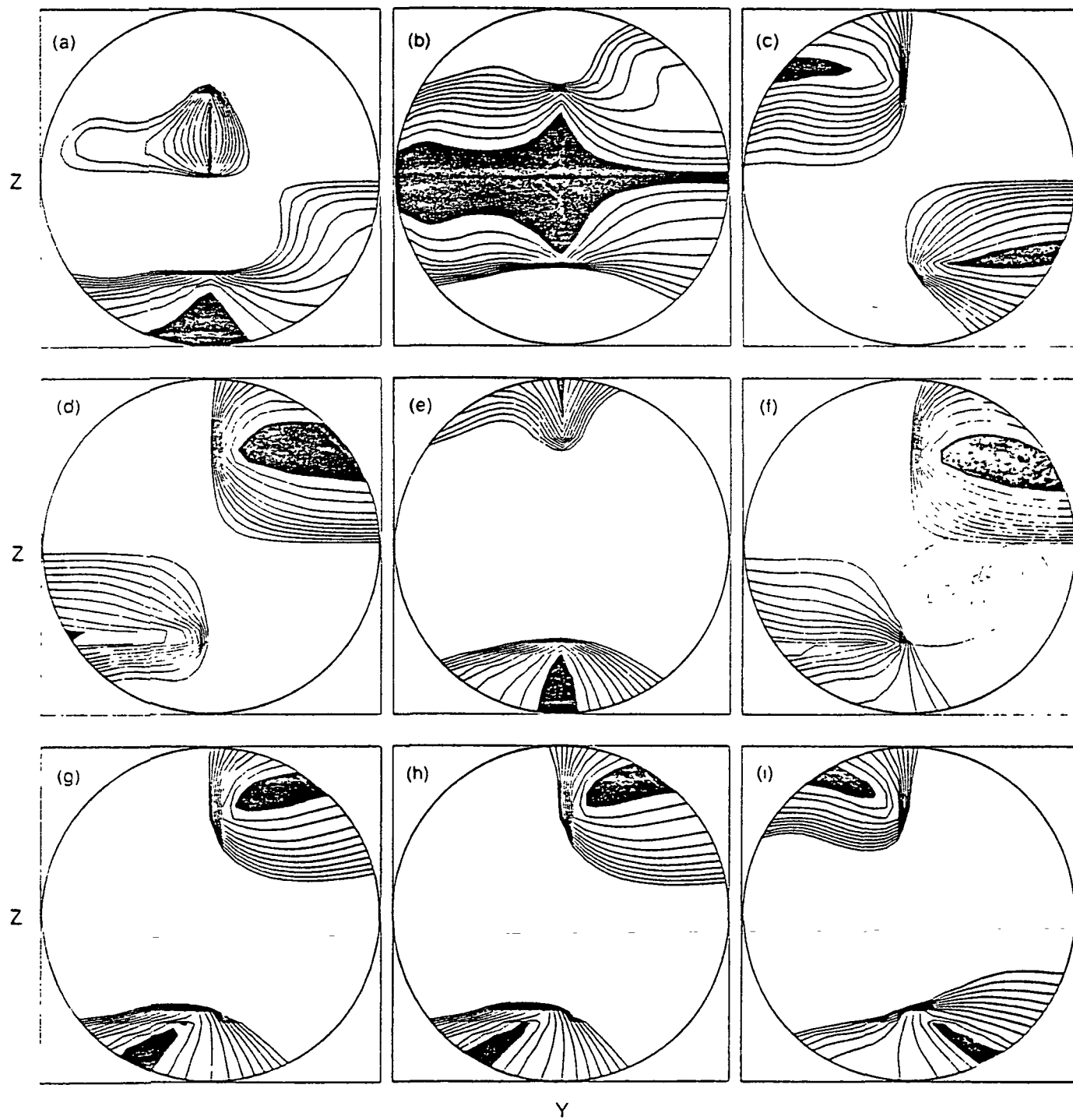
THE MAGNETIC FIELD OF MARS:
IMPLICATIONS FROM GAS DYNAMIC MODELING

C.T. Russell[1] and J.G. Luhmann
Institute of Geophysics and Planetary Physics
University of California, Los Angeles
Los Angeles, California 90024

J.R. Spreiter
Division of Applied Mechanics
Stanford University
Stanford, California 94305

S.S. Stahara
Nielson Engineering and Research, Inc.
Mountain View, California 94043

[1]Also Department of Earth and Space Science, UCLA

ABSTRACT

On January 21, 1972 the Mars-3 spacecraft observed a variation in the magnetic field during its periapsis passage over the dayside of Mars that was suggestive of entry into a Martian magnetosphere. We have obtained the original data and trajectory (Sh. Sh. Dolginov, personal communication, 1983), and have attempted to simulate the observed variation of the magnetic field using a gasdynamic simulation. In the gasdynamic model we first generate a flow field and then use this flow field to carry the interplanetary magnetic field through the Martian magnetosheath. The independence of the flow field and magnetic field calculation allows us to converge rapidly on an IMF orientation which would result in a magnetic variation similar to that observed by Mars-3. There appears to be no need to invoke an entry into a Martian magnetosphere to explain these observations.

Of the magnetic fields of the four terrestrial planets, the magnetic field of Mars is least understood, even though Mars has been visited by many spacecraft. The reason for this gap in our understanding is that of the many U.S. spacecraft to Mars, only the first, Mariner 4, in 1965, carried a magnetometer, and on this mission the flyby distance was so great that only brief encounters with the planetary bow shock and magnetosheath were observed. At least three Soviet Martian orbiters have carried magnetometers, but none of these spacecraft have provided low altitude (<1000 km) data or measurements directly behind the planet. Nevertheless, some of these measurements have been interpreted as indicative of the existence of an intrinsic planetary magnetic field. The Mars 5 measurements behind, but not directly behind, the planet have been inter- preted as indicating a tail (Dolginov et al, 1976). The Mars 2 measure- ments have been interpreted as indicating a dipole movement with its axis in the equatorial plane (Smirnov et al, 1978). The Mars 3 measurements have been interpreted to indicate, on one occasion, an entry into a Martian magnetosphere (Dolginov, et al, 1973; Gringauz et al, 1974). However, for this interpretation to be correct, the dipole moment : would have to be aligned with the spin axis.

These interpretations have been criticized on several counts. The size of the magnetic moment consistent with the reported Mars 5 tail encounters is smaller than that reported from the dayside Mars 3 entry (Russell, 1978a). Further, the putative tail entries are suspect because of the direction of the field in the region inferred to be "tail". The Mars 2 inferences are inconsistent with the Mars 3 inferences, but are consistent with the magneto- tail being due to draped interplanetary magnetic field lines (Russell, 1981).

We note that Venus has no discernible intrinsic field, yet still has a magnetotail formed from the interplanetary magnetic field (Russell et al, 1981a). Finally, the Mars 3 measurements have been interpreted as passage through a magnetosheath, rather than a magnetosphere (Wallis, 1975; Russell, 1978b). Wallis (1975) suggested that the region that Dolginov et al (1973) had identified as magnetosheath could equally well be interpreted as the foreshock region. Russell (1978b) suggested that the putative magnetospheric field had the draping pattern of magnetosheath field lines. At that time there was no convenient means to test the hypothesis. However, code development since that time now permits a relatively simple test of this hypothesis, and it is the purpose of this note to perform such a test.

GASDYNAMIC MODELING

Numerical models of the solar wind interaction with planetary obstacles have now been in use for nearly two decades (cf. Spreiter et al, 1966). Code developments and technological change since that time have decreased the cost and increased the speed and flexibility of the models (Spreiter and Stahara, 1980a, b), and provided the capability of intercomparing observations and models along actual spacecraft trajectories. A feature of the gasdynamic model makes the model ideally suited for the task at hand. The flow solution is not affected by the magnetic field. The magnetic field is obtained by stretching the original upstream magnetic field with the derived flow field, but neither the magnetic tension nor the magnetic pressure react back on the flow. The flow solution is affected only by the upstream Mach number, the ratio of specific heats, γ, and the shape of the obstacle.

We use this magnetic field independence in our investigations below in the following manner. First, we calculated the flow field around the obstacle for a given Mach number, γ, and shape. We choose a magnetosonic Mach number of 7.7 as being appropriate for average solar wind conditions at Mars (Russell et al 1982b). For an obstacle shape we use a Venus shape with an ionospheric scale height of 0.025. The solution is quite insensitive to this latter quantity as long as it is smaller than about 0.1. The choice of γ, the ratio of specific heats, is not a simple matter. Fairfield (1971) and Zhuang and Russell (1981) both deduced that a value $\gamma = 2$ gives the best fit to the terrestrial magnetosheath thickness. Slavin et al (1983) have found good agreement for Mars using $\gamma = 2$, and Tatrallyay et al (1983) have found that $\gamma = 1.9$ provides the best fit for Venus. However, Tatrallyay et al also find an Alfvenic Mach number depend-

ence for the value of γ and that the best fit value of γ is 1.6 above an Alfvenic Mach number of 7. Thus, we might expect that the best fit for Mars might not be the same as the terrestial and Venus best fits. On the other hand, the magnetic field strength at Mars, on the day being considered herein, is large and hence one might expect that the Mach number was lower than usual. In the absence of knowledge of the plasma density and bulk velocity, we will use the average Mach number 7.7 and the previously determined best-fit γ -value of 2.

After the flow field solution is obtained, we can calculate the magnetic field along the trajectory of the spacecraft as if the magnetic field lines were dye lines in a fluid flow. This calculation is rapid and can be repeated at small cost in computing time. Thus, it is feasible to hunt for a suitable IMF direction, flow observation angle, or obstacle size.

Previous work has used the gasdynamic simulation to determine whether the bow shock location of Mars implies an obstacle of the size of the planet plus ionosphere or somewhat larger (Russell 1977; 1970; Slavin et al, 1983). Once that obstacle size is determined, one has the further problem of whether the ionosphere is strong enough to stand off the solar wind. In this study, we use the gasdynamic simulation in a different way. We wish to examine whether we can replicate the Mars 3 magnetic field observations, which were claimed to indicate a magnetospheric entry, with a trajectory passing solely through magnetosheath. This argument has been made in the past (Russell, 1978b), but not as quantitatively as is now possible.

CALCULATIONS

The magnetic field observations that we are attempting to model are
shown in Figure 1. Panel (a) shows the time series and panel (b) shows the
field vectors and trajectories projected into the Y-Z plane. The field
values and the trajectory have been supplied in tabular form by Sh. Sh.
Dolginov (personal communication, 1983) to whom we are very grateful. The
trajectory is very similar to that originally derived by Russell (1978b; 1979).
However, use of investigator-supplied values removes the uncertainty
associated with the original interpolation process and a possible source of
error. Table 1 lists the position of Mars-3 at selected times. The magnetic
field values also closely resembled those published by Gringauz et al. (1974)
and Russell (1978b; 1979) as well as those in the early publications by
Dolginov and coworkers. However, there is ambiguity and inconsistency in the
various descriptions of the coordinate system used to display the Mars-3 magnetic
field data. We use herein the latest definition (Dolginov, 1978) in which
the direction of the Y-component is in the direction of planetary motion. As
we show below this definition of coordinates provides internal consistency
in the behavior of the data. We emphasize that we must judge consistency in
terms of the variations in the data, since the zero levels of the Mars-3
magnetometer are not known. Our modeling provides an estimate of these
uncertainties and they prove to be large.

If we assume that the Mars-3 magnetometer's zero levels remained unchanged
during its periapsis passage on 1/21/72, we can use the field variations to
initialize our simulation effort. It is both our hypothesis and Wallis' (1975)
that an inbound shock crossing occurred at 2129 $\pm$ 2 (across an unfortunately
timed data gap of 4 minutes duration) and an outbound crossing occurred at 2259.

The latter time was also given as the outbound shock crossing by Dolginov et al. (1975). However, there is little change in the vector field direction there. This fact suggests that the outbound shock is a quasi-parallel shock, i.e., the IMF is parallel to the shock normal at this point. The inbound shock has a more rapid increase, as if it were a quasiperpendicular shock.

Table 2 lists the median magnetic field vectors from 2115 to 2145 Moscow time across the feature we interpret to be the inbound shock crossing. The Mars-3 magnetometer returned 8 values of the magnetic field in rapid succession every 2 minutes only some of which were successfully recovered. The right-hand column labelled N lists the number of values available at each recording interval. Assuming that the noise on the measurements, both due to the ambient medium and due to the spacecraft, were randomly positive and negative, we used the median values in each telemetry interval as our best estimate. Medians have been used because mean values are sensitive to occasional very inaccurate values whereas medians are not.

For our first estimate of the IMF field, we take the jump in field across the inbound shock divided by three and assume this to be the IMF value. As shown in Table 2, the upstream values are "noisy". However, since we are merely attempting to determine a starting value we will simply use the value at 2127 as the upstream value and the value at 2131 as the downstream value. One-third of this difference is (-1.5, -4.5, 0.9) which provides our first estimate of the upstream field corrected for zero level errors. Figure 2 panel (a) shows the time series derived using this vector as input and an ionopause altitude of 430 km. The inbound shock crossing occurs about 8 minutes early and the outbound shock about 22 minutes early. If we rotate the flow 9° in the direction of aberration expected from planetary motion, we obtain the time series shown in Figure 2 panel (b). A 9° aberration angle is

only about 5° larger than that expected due to Mars' orbital motion transverse to the solar wind flow and well within the known amplitude of solar wind directional variations. We note that other flow directions will also reproduce the observed shock locations for example a total aberration angle of 7° and a flow from the south of 4° will do as well.

The model time series of Figure 2 resemble the variations seen in Figure 1. However, the model variations are smaller than the observations, especially in the B_z component. Further, the jump in the magnetic field at the outbound shock seems larger in the models than in the data. Hence we need to make the IMF larger, more negative along the Z-direction and more aligned with the outbound shock normal. Figure 3 shows the results of using an input value of (-4, -4.5, -3) nT and an aberration of 7 degrees with the flow coming from 4° below the ecliptic plane. The panel on the right shows the model and on the left the observations with the baselines corrected so that the average IMF readings agree. The qualitative behavior of each of the corresponding traces agrees. The magnitude of the variations are equal but the traces differ in the exact timing of the peaks and the rapid variations in direction. There are many possible reasons for such differences. There are questions of the appropriate choice of γ and M_{MS} for this day and of the accuracy of the gasdynamic simulation of an MHD problem. We may not have made the best choice of the IMF orientation. Further, it is certain that the IMF did not remain steady during the Mars flyby, as assumed in the simulation.

In order to determine whether our solution is, in fact, a reasonable one, Figures 4, 5 and 6 compare individual vectors from the observations and model. Figure 4 shows the solar ecliptic plane projection. The field vectors to the right and left of Mars agree quite well. Only during the subsolar

passage is there a major disagreement. There is certainly no hint in these data that a magnetosphere has been entered. Figure 5 shows the vectors projected in the dawn-dusk plane. There is very good agreement in this projection except near the inbound shock crossing, where there is some apparent temporal variation. Finally, in Figure 6, we show the two solar-cylindrical projections. Again, the agreement is very good, except for obvious temporal fluctuations and in a region near closest approach. This latter distortion is a pulling of the field toward the antisolar direction as if there were some drag on the flow in this region. Such a drag could be provided by mass-loading. However, calculations suggest that mass-loading is weak at Mars (Russell et al., 1983).

Earlier, we speculated that the inbound shock was a quasiperpendicular shock and the outbound shock was quasiparallel. This is, of course, implicit in the solutions we have derived, but it is of some interest to check this assumption. We can use the coplanarity assumption to derive the shock normal from the model field values. These normals are (.144, -.624, -.442) and (.618, .705, .347). Since the IMF value input to the model was (-4, -4.5, -3), these correspond to θ_{BN} values of 77° and 12°, respectively, for the inbound and outbound shocks. These values are those of a quasiperpendicular shock and a quasiparallel shock, as we originally assumed.

DISCUSSION AND CONCLUSIONS

The model values do not perfectly replicate the data. Part of the differences are certainly due to temporal variations in the interplanetary magnetic field. Some of the difference may be attributable to non-gasdynamic effects, such as magnetic forces and mass loading. In view of the existence of so many reasons why there should be differences, the observed agreement is heartening. We have found a magnetosheath magnetic field along the Mars-3 trajectory which resembles the Mars-3 observations. Thus, the Mars-3

data do not provide unambiguous evidence for an intrinsic Martian magnetic field. Our best fit obstacle size is also quite consistent with an ionospheric obstacle. Not only is the solar wind much weaker at Venus than at Mars, but also the Mars gravitational field is weaker. Hence, the upper atmosphere and ionosphere of Mars will have much greater scale heights than at Venus, all else being equal. On the other hand, in situ measurements of both the field and plasma of the Martian ionosphere will be necessary before the exact nature of the ionopause is determined. This study says only that any planetary field did not extend much above 400 km on 2/21/71, and certainly not to 1,200 km, the location of Mars-3.

Finally, we have shown that the gasdynamic simulation provides a powerful tool for interpreting magnetic measurements obtained in planetary magnetosheaths. In the past this important capability has not been fully exploited.

REFERENCES

Dolginov, Sh. Sh., The magnetic field of Mars, Kosmich. Issled., 16, 257-268, 1978.

Dolginov, Sh. Sh., Ye. G. Yeroshenko and L.N. Zhuzgov, Magnetic field in the very close neighborhood of Mars according to data from the Mars-2 and -3 spacecraft, J. Geophys. Res., 78, 4779, 1973.

Dolginov, Sh. Sh., Ye G. Yeroshenko and L.N. Zhuzgov, The magnetic field of Mars from Mars-3 and Mars-5 data, Kosmich. Issled., 13, 108-122, 1975.

Dolginov, Sh. Sh., Ye. G. Yeroshenko, L.N. Zhuzgov, V.A. Sharova, K.I. Gringauz, V.V. Bezrukikh, T.K. Breus, M.I. Verigin and A.P. Remizov, Magnetic field and plasma inside and outside of the Martian magneto-sphere, in Solar-Wind Interaction with the Planets Mercury, Venus and Mars, pp. 1-18, NASA SP 397, Washington, D.C., 1976.

Fairfield, D.H., Average and unusual locations of the Earth's magnetopause and bow shock, J. Geophys. Res., 76, 6700, 1971.

Gringauz, K.I., V.V. Bezrukikh, T.K. Breus, M.I. Verigin, G.I. Volkov and A.V. Dyachkov, Study of solar plasma near Mars and on Earth-Mars route using charged particle traps on a Soviet spacecraft in 1971-1973 II. Characteristics of electrons along orbits of artificial Mars satellites Mars-2 and Mars-3, Kosmich. Issled., 12, 585-599, 1974.

Russell, C.T., On the relative locations of the bow shocks of the terrestrial planets, Geophys. Res. Lett., 4, 387-390, 1977.

Russell, C.T., The magnetic field of Mars: Mars-5 evidence re-examined, Geophys. Res. Lett., 5, 85-88, 1978a.

Russell, C.T., The magnetic field of Mars: Mars-3 evidence re-examined, Geophys. Res. Lett., 5, 81-84, 1978b.

Russell, C.T., The Martian magnetic field, Phys. Earth Planet Inter., 20, 237-246, 1979.

Russell, C.T., The magnetic fields of Mercury, Venus and Mars, Adv. Space Res., 1, 3-20, 1981.

Russell, C.T., J.G. Luhmann, R.C. Elphic and F.L. Scarf, The distant bow shock and magnetotail of Venus: Magnetic field and plasma wave observations, Geophys. Res. Lett., 8, 843-846, 1981.

Russell, C.T., M.M. Hoppe and W.A. Livesey, Overshoots in planetary bow shocks, Nature, 296, 45-48, 1982.

Russell, C.T., T.I. Gombosi, M. Horanyi, T.E. Cravens and A.F. Nagy, Charge-exchange in the magnetosheaths of Venus and Mars: A comparison, Geophys. Res. Lett., 10, 163-164, 1983.

Slavin, J.A., R.E. Holzer, J.R. Spreiter, S.S. Stahara and D.S. Chausee, Solar wind flow about the terrestrial planets, 2. Comparison with gas dynamic theory and implications for solar-planetary interactions, J. Geophys. Res., 88, 19-35, 1983.

Smirnov, V.N., A.N. Omel'chenko and O.L. Vaisberg, Possible discovery of cusp near Mars, Kosmich. Issled., 16, 864-869, 1978.

Spreiter, J.R. and S.S. Stahara, A new predictive model for determining solar wind-terrestrial planet interactions, J. Geophys. Res., 85, 6769, 1980a.

Spreiter, J.R. and S.S. Stahara, Solar wind flow past Venus: Theory and comparisons, J. Geophys. Res., 85, 7715, 1980b.

Spreiter, J.R., A.L. Summers and A.Y. Alksne, Hydromagnetic flow around the magnetosphere, Planet Space Sci., 14, 223, 1966.

Tatrallyay, M., C.T. Russell and J.G. Luhmann, On the proper Mach number ratio of specific heats for modelling the Venus bow shock, $\underline{J}$. $\underline{Geophys}$. $\underline{Res}$., submitted, 1983.

Wallis, M.K., Does Mars have a magnetosphere?, $\underline{Geophys}$. $\underline{J}.\underline{R}$. $\underline{Astron}$. $\underline{Soc}$., $\underline{41}$, 349, 1975.

Zhuang, H-C. and C.T. Russell, An analytic treatment of the structure of the bow shock and magnetosheath, $\underline{J}$. $\underline{Geophys}$. $\underline{Res}$., $\underline{86}$, 2191-2205, 1981.

Table 1. Mars-3 Trajectory

Moscow Time	XSE	YSE	ZSE
2101	$-0.177 \, R_M$	$-2.788 \, R_M$	$-0.747 \, R_M$
2131	0.659	-1.313	-1.042
2201	0.956	0.758	-0.639
2231	0.240	2.198	0.499
2301	-0.641	2.927	1.557

Table 2. Median Magnetic Field Vectors

Moscow Time	BX SE[+]	BY SE[+]	BZ SE[+]	N
2115	-0.6	3.3	-6.2	6
2117	-2.4	3.9	-7.8	8
2119	-2.3	3.9	-5.5	8
2121	-2.0	4.5	-6.2	8
2123	-2.6	5.5	-5.2	3
2125	-3.9	7.8	-7.8	5
2127	-3.9	5.2	-7.8	1
2129	-6.2*	-1.6*	-6.5*	0
2131	-8.4	-8.4	-5.2	3
2133	-9.1	-10.4	-7.8	2
2135	-11.0	-13.0	-9.1	8
2137	-10.4	-13.0	-13.6	3
2139	-10.4	-12.6	-16.9	8
2141	-10.4	-12.3	-20.2	5
2143	-10.4	-8.4	-23.4	5
2145	-8.1	-5.2	-22.1	4

[+]Zero levels unknown

*Interpolated value

Figure 1. Magnetic field observed by the Mars 3 spacecraft on 01/21/72.
(a) Time series in solar ecliptic coordinates.
(b) Vectors along the trajectory projected into the Y-Z solar ecliptic
plane. No zero level corrections have been applied.

Figure 2. Magnetic field calculated along Mars 3 trajectory using a
ratio of specific heats, γ, of 2 a magnetosonic Mach number
of 7.7, and an ionopause altitude of .430 km, with an IMF of
(-1.5, -4.5, 0.90) nT.
(a) Model A with no aberration of the solar wind.
(b) Model B with a 9° aberration of the solar wind in the direction of
the average expected solar wind observation.

Figure 3. Magnetic field along the Mars 3 trajectory
(a) Panel on left shows observations corrected so that average IMF is
same as IMF in model C.
(b) Panel on right shows model C. All parameters are the same as in
models B, except IMF has been changed to (-4, -4.5, -3).

Figure 4. Ecliptic plane projection of magnetic field along Mars 3
trajectory.
(a) Corrected observations.
(b) Model C.

Figure 5. Dawn-dusk plane projection of magnetic field along Mars 3
trajectory.
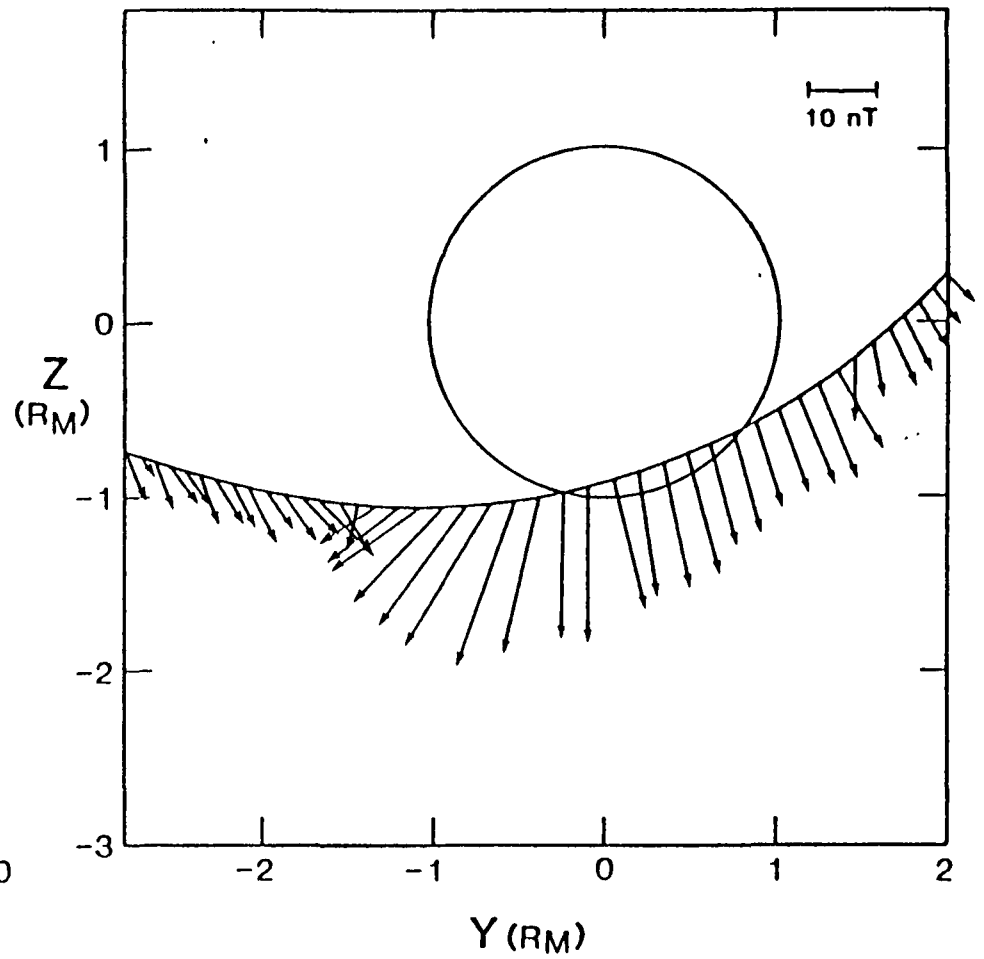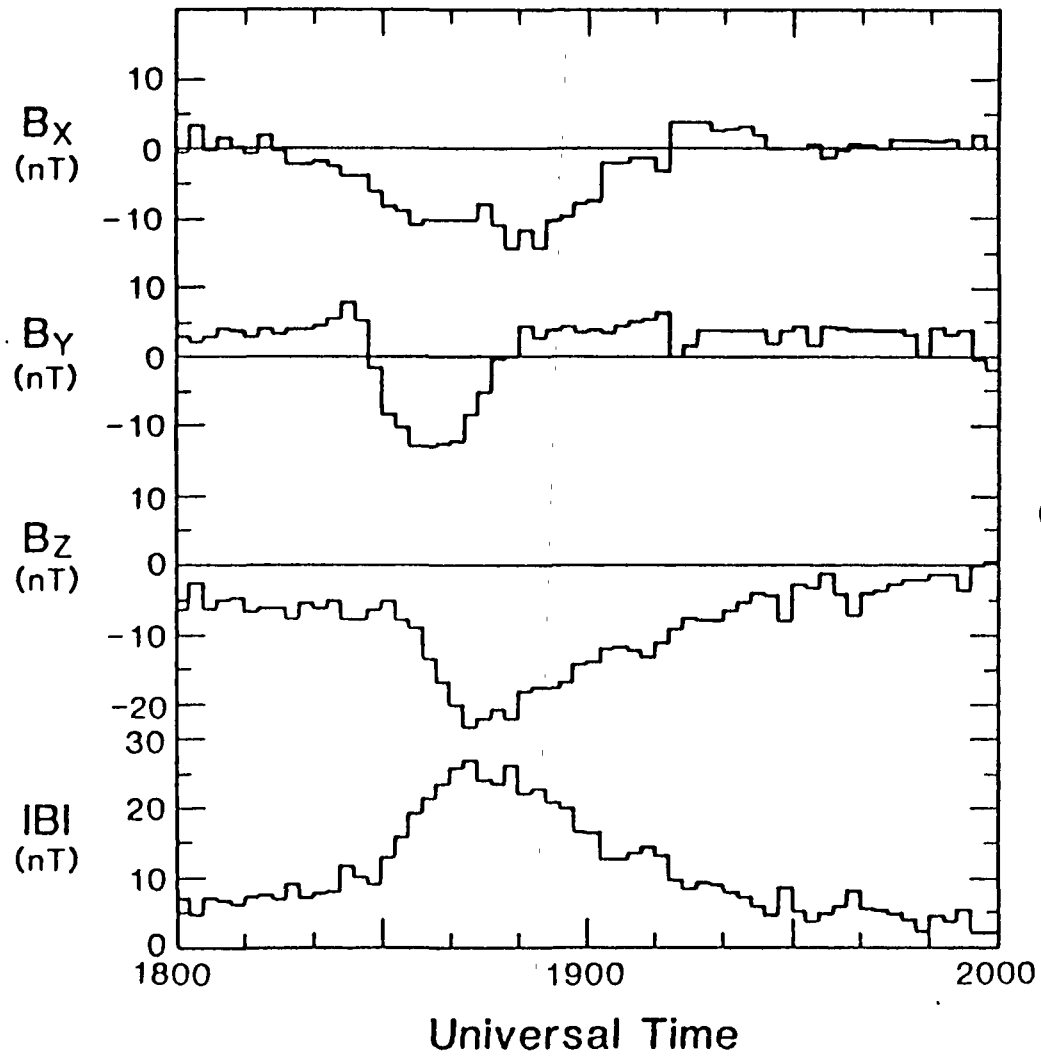(a) Corrected observations.
(b) Model C

Figure 6. Solar-cylindrical projection of magnetic field along Mars 3
trajectory.
(a) Corrected observations.
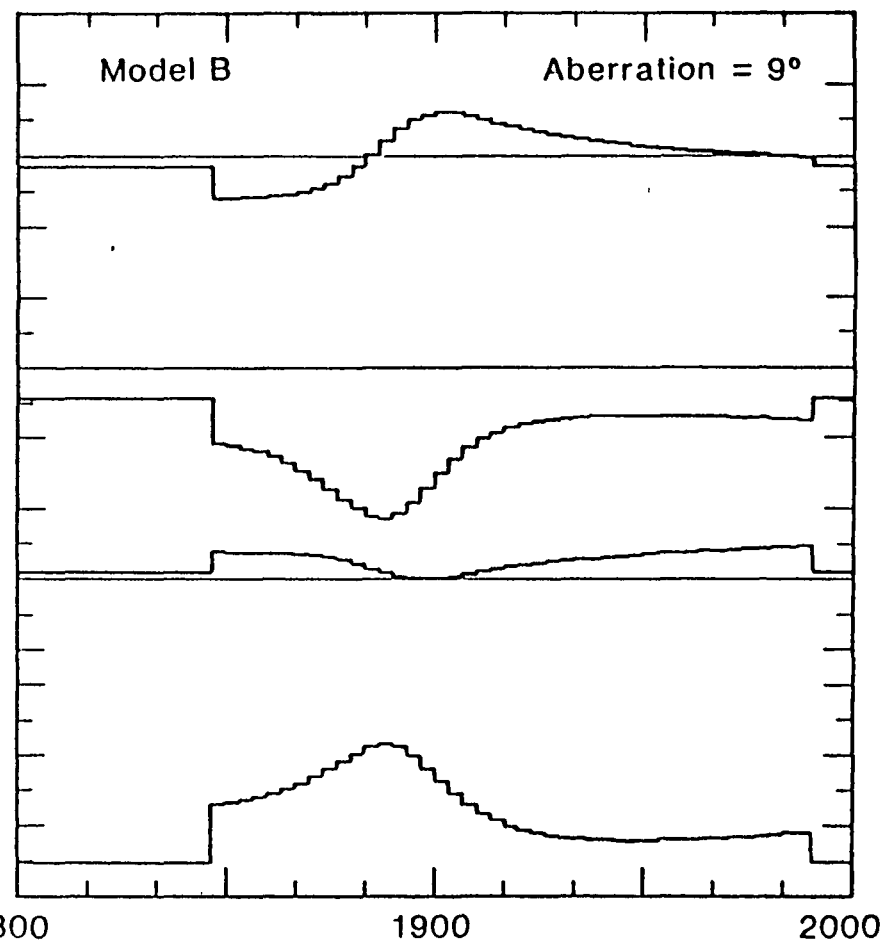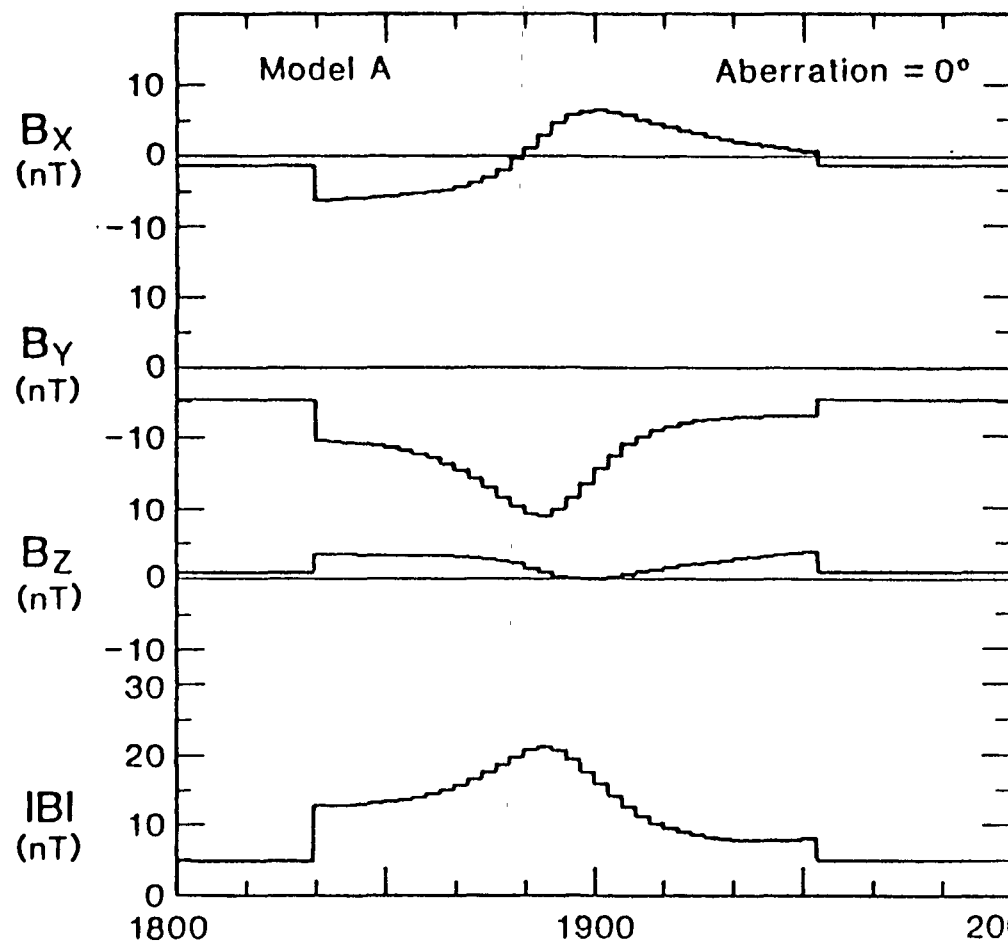(b) Model C.

Original Data

$M_{MS} = 7.7 \quad B_{IMF} = (-1.5, -4.5, 0.9) \text{ nT}$
$\gamma = 2.0 \quad \text{Ionopause Altitude} = 430 \text{ km}$

Model A — Aberration = 0°

Model B — Aberration = 9°

B_X (nT)

B_Y (nT)

B_Z (nT)

|B| (nT)

Universal Time

$M_{MS} = 7.7$
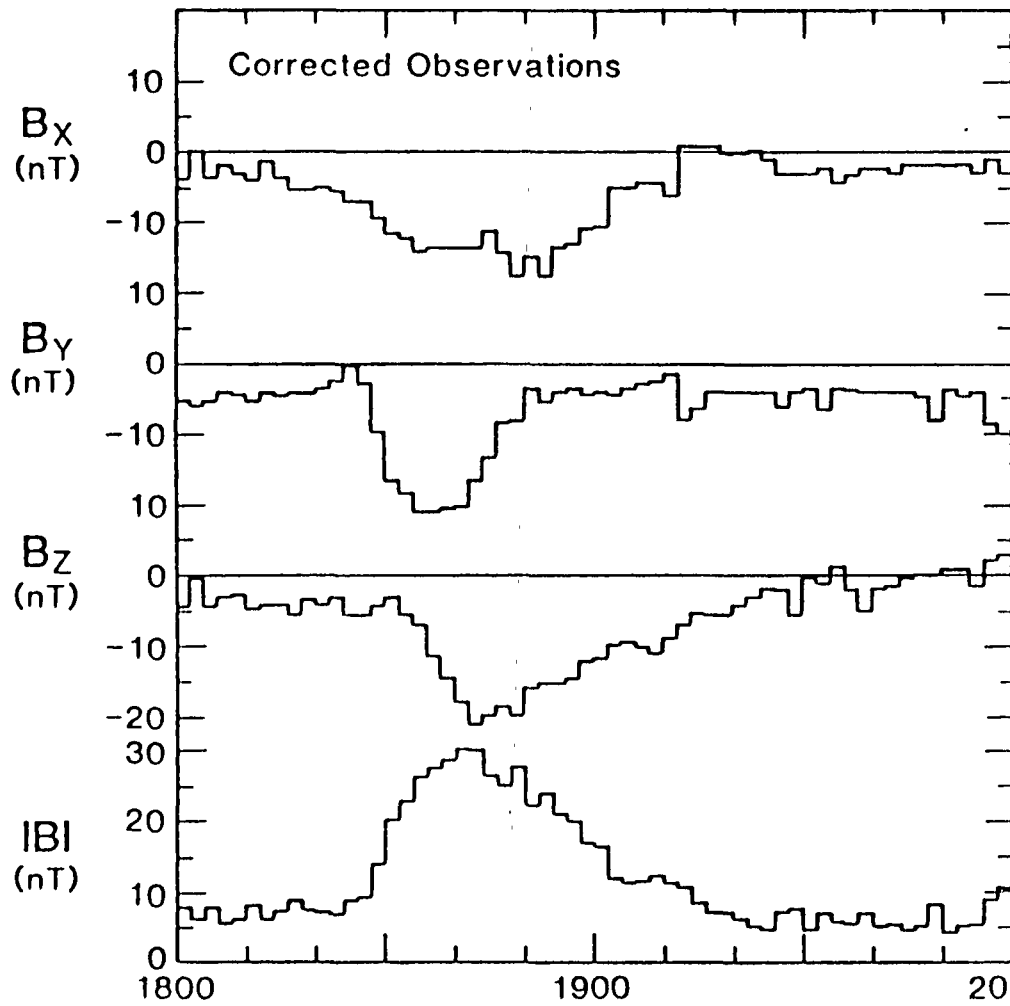
$\gamma = 2.0$

$B_{IMF} = (-4, -4.5, -3)\text{nT}$

Aberration = $9°$

Ionopause

Altitude = 430 km

Corrected Observations

Model C

B_X (nT)

B_Y (nT)

B_Z (nT)

$|B|$ (nT)

Universal Time

Corrected
Observations
Aberrated 9°

⊢ 10 nT ⊣

Model C
Aberrated 9°

⊢ 10 nT ⊣

Distance from Solar Wind–Mars Line (R$_M$)

Distance Along Solar Wind–Mars Line (R$_M$)